Doctoral theses at NTNU, 2016:140

Yared Worku Bekele

Isogeometric Analysis of Coupled Problems in Porous Media

Simulation of Ground Freezing

NTNU
Norwegian University of
Science and Technology

Doctoral thesis

Yared Worku Bekele

ISBN 978-82-326-1618-3 (printed ver.)
ISBN 978-82-326-1619-0 (electronic ver.)
ISSN 1503-8181

NTNU
Norwegian University of
Science and Technology

Thesis for the Degree of
Philosophiae Doctor
Faculty of Engineering Science and Technology
Department of Civil and Transport Engineering

NTNU
Norwegian University of
Science and Technology

Doctoral theses at NTNU, 2016:140

NTNU

Yared Worku Bekele

Isogeometric Analysis of Coupled Problems in Porous Media

Simulation of Ground Freezing

Thesis for the Degree of Philosophiae Doctor

Trondheim, May 2016

Norwegian University of Science and Technology
Faculty of Engineering Science and Technology
Department of Civil and Transport Engineering

NTNU
Norwegian University of
Science and Technology

NTNU
Norwegian University of Science and Technology

Thesis for the Degree of Philosophiae Doctor

Faculty of Engineering Science and Technology
Department of Civil and Transport Engineering

ISBN 978-82-326-1618-3 (printed ver.)
ISBN 978-82-326-1619-0 (electronic ver.)
ISSN 1503-8181

Doctoral theses at NTNU, 2016:140

Printed by NTNU Grafisk senter

Contents

Abbreviations and Acronyms

AGF	Artificial Ground Freezing
BVP	Boundary Value Problem
CAD	Computer Aided Design
FEA	Finite Element Analysis
GRID	Global Resource Information Database
GTR	Generalized Trapezoidal Rule
HM	Hydro-mechanics/mechanical
IGA	Isogeometric Analysis
LHS	Left Hand Side
LR	Locally Refined
NURBS	Non-Uniform Rational B-Splines
PDE	Partial Differential Equation
RHS	Right Hand Side
SAMCoT	Sustainable Arctic Marine and Coastal Technology
THM	Thermo-hydro-mechanics/mechanical
UNEP	United Nations Environment Program

Nomenclature

Latin Capital Letters

$\bar{\mathcal{H}}$	Refined knot vector
$\hat{V}$	Weighting function space
$\hat{V}_h$	Finite weighting function space
$\mathbb{I}$	Fourth-order identity tensor
$\mathcal{H}$	Knot vector
$\mathcal{L}$	Differential operator
$\mathcal{Z}$	Knot vector
$\overline{T}$	Prescribed temperature
$B_{\Xi,\mathcal{H}}$	Bivariate B-Spline based on knot vectors Ξ and $\mathcal{H}$
B_{Ξ}	Univariate B-Spline based on knot vector Ξ
E	Young's modulus
E^{α}	Internal energy of phase α
$E^{\beta\alpha}$	Internal energy exchange from phase β to phase α
H^1	Sobolev space
H^{α}	Rate of heat energy for phase α
K^{α}	Kinetic energy of phase α
K_{f}	Bulk modulus of fluid
K_{o}	Bulk modulus of porous medium
K_{s}	Bulk modulus of solid
K_{w}	Bulk modulus of water
L	Specific latent heat
L^2	Space of square integrable functions
$L_{k,r}$	B-Spline basis function k of polynomial degree r
M^{α}	Mass of phase α
$M^{\alpha\beta}$	Mass exchange from phase α to phase β
$M^{\beta\alpha}$	Mass exchange from phase β to phase α
$M_{j,q}$	B-Spline basis function j of polynomial degree q
N	Number of phases in porous medium
$N_{i,p}$	B-Spline basis function i of polynomial degree p
Q	Total heat supply to porous medium
Q^{α}	Heat supply to phase α
Q^{f}	Heat supply to fluid
Q^{s}	Heat supply to solid
R_i^p	Univariate rational basis functions of polynomial degree p
$R_{i,j,k}^{p,q,r}$	Trivariate rational basis functions of polynomial degrees p, q and r
$R_{i,j}^{p,q}$	Bivariate rational basis functions of polynomial degrees p and q
S^{α}	Entropy of phase α
T	Absolute temperature of porous medium
T^{α}	Absolute temperature of phase α
T_{o}	Initial temperature
V	Trial solution space
V^{s}	Volume of solid
V_h	Finite trial solution space
W	Weighting function
W^{α}	Rate of mechanical energy for phase α

Latin Capital Letters (Bold)

$\bar{\boldsymbol{P}}$	Refined control points
$\boldsymbol{A}^{\alpha}$	Lagrangian acceleration of phase α
$\boldsymbol{B}$	Strain-displacement matrix
$\boldsymbol{C}$	B-Spline/NURBS curve
$\boldsymbol{C}_{\mathrm{pp}}$	Compressibility matrix
$\boldsymbol{C}_{\mathrm{pu}}$	Hydro-mechanical coupling matrix
$\boldsymbol{C}_{\mathrm{TT}}$	Internal energy matrix
$\boldsymbol{C}_{\mathrm{up}}$	Mechanical-hydraulic coupling matrix
$\boldsymbol{C}_{\mathrm{uT}}$	Mechanical-thermal coupling matrix
$\boldsymbol{C}_{\mathrm{uu}}$	Stiffness matrix
$\boldsymbol{D}$	Constitutive tangent stiffness tensor
$\boldsymbol{D}^{\alpha}$	Rate of deformation tensor
$\boldsymbol{F}^{\alpha}$	External forces on phase α
$\boldsymbol{G}$	Arbitrary matrix
$\boldsymbol{H}^{\alpha}$	Angular momentum of phase α
$\boldsymbol{I}$	Identity matrix
$\boldsymbol{J}$	Jacobian matrix
$\boldsymbol{K}$	Global LHS matrix
$\boldsymbol{K}_{\mathrm{e}}$	Element LHS matrix
$\boldsymbol{K}_{\mathrm{pp}}$	Permeability matrix
$\boldsymbol{K}_{\mathrm{TT}}$	Thermal matrix
$\boldsymbol{L}$	Differential operator stresses in Voigt notation
$\boldsymbol{L}^{\alpha}$	Spatial velocity gradient of phase α
$\boldsymbol{L}^{\mathrm{f}}$	Spatial velocity gradient of fluid
$\boldsymbol{L}^{\mathrm{s}}$	Spatial velocity gradient of solid
$\boldsymbol{M}^{\alpha}$	Moment of external forces on phase α
$\boldsymbol{N}$	Basis functions
$\boldsymbol{N}_{\mathrm{p}}$	Pressure basis functions
$\boldsymbol{N}_{\mathrm{T}}$	Temperature basis functions
$\boldsymbol{N}_{\mathrm{u}}$	Displacement basis functions
$\boldsymbol{P}$	Control points
$\boldsymbol{P}^{\alpha}$	Linear momentum of phase α
$\boldsymbol{P}^{\beta\alpha}$	Linear momentum exchange from phase β to phase α
$\boldsymbol{R}$	Residual vector
$\boldsymbol{S}$	B-Spline/NURBS surface
$\boldsymbol{T}^{\mathrm{c}}$	Control point temperature values
$\boldsymbol{V}$	B-Spline/NURBS volume
$\boldsymbol{V}^{\alpha}$	Lagrangian velocity of phase α
$\boldsymbol{W}^{\alpha}$	Spin tensor
$\boldsymbol{X}$	Vector of unknown field variables
$\boldsymbol{X}^{\alpha}$	Reference position of phase α

$\tilde{\boldsymbol{D}}$	Constitutive tangent matrix for stresses in Voigt notation
$\tilde{\boldsymbol{I}}$	Identity vector for stresses in Voigt notation

Greek Small Letters

$(\tilde{\xi}, \tilde{\eta}, \tilde{\zeta})$	Coordinates of parent element
(ξ, η, ζ)	Coordinates of parameter space
α	Phase number/Biot's coefficient/Coefficient value or function
α_o	Thermal expansion coefficient of porous medium
α_s	Thermal expansion coefficient of solid
α_w	Thermal expansion coefficient of water
$\bar{\eta}$	Inserted knot value
$\bar{\xi}$	Inserted knot value
β	Coefficient value or function
χ^α	Phase distribution function
$\delta\boldsymbol{u}$	Vector-valued test function
δp	Scalar test function
δT	Scalar test function
η	Knot value
γ	Scalar weight
γ_f	Unit weight of fluid
γ_w	Unit weight of water
λ	Effective thermal conductivity coefficient
λ_s	Thermal conductivity of solid
λ_w	Thermal conductivity of water
μ	Viscosity of fluid
μ^α	Chemical potential of phase α
μ^β	Chemical potential of phase β
ν	Poisson's ratio
ψ^α	Helmholtz free energy of phase α
ρ	Total density of porous medium
ρ^α	Partial density of phase α
ρ^β	Partial density of phase β
ρ^s	Partial density of solid
ρ_α	Real density of phase α
ρ_f	Real density of fluid
ρ_s	Real density of solid
ρ_w	Real density of water
ρ_wo	Initial density of water
θ	Time integration parameter
ξ	Knot value
ζ	Knot value

Greek Capital Letters

$\bar{\Xi}$	Refined knot vector
Δt	Time step size
Ξ	Knot vector

Greek Letters (Bold)

$\boldsymbol{\kappa}$	Permeability matrix
$\boldsymbol{\lambda}$	Effective thermal conductivity matrix
$\boldsymbol{\sigma}$	Total stress tensor of porous medium
$\boldsymbol{\sigma}^\alpha$	Stress tensor of phase α
$\boldsymbol{\sigma}'$	Effective stress
$\boldsymbol{\sigma}^\mathrm{f}$	Partial stress tensor of fluid
$\boldsymbol{\sigma}^\mathrm{s}$	Partial stress tensor of solid
$\boldsymbol{\sigma}_\mathrm{f}$	Pore fluid stress
$\boldsymbol{\varepsilon}$	Total strain tensor
$\boldsymbol{\varepsilon}^\mathrm{c}$	Creep strain tensor
$\boldsymbol{\varepsilon}^\mathrm{o}$	Strain tensor not associated with effective stress
$\boldsymbol{\varepsilon}^\mathrm{T}$	Thermal strain tensor
$\boldsymbol{\varepsilon}_\mathrm{v}^\mathrm{s}$	Volumetric strain tensor

Latin Small Letters

(x, y, z)	Coordinates of physical space
$\mathrm{d}V$	Control volume element
$\overline{h}$	Specified value of field variable u on a Robin boundary
$\overline{p}^\mathrm{w}$	Prescribed pore water pressure
$\overline{q}$	Specified normal derivative of field variable u on a Neumann boundary
$\overline{q}^\mathrm{T}$	Heat flux
$\overline{q}^\mathrm{w}$	Water flux
$\overline{u}$	Specified value of field variable u on a Dirichlet boundary
c	Specific storage coefficient
c_f	Specific heat capacity of fluid
c_s	Specific heat capacity of solid
c_w	Specific heat capacity of water
d	Spatial dimension
e^α	Specific internal energy of phase α
e^f	Specific internal energy of fluid
e^s	Specific internal energy of solid
f	Arbitrary scalar function
g	Gravitational acceleration
h^α	Partial energy source of phase α
k_r	Relative permeability coefficient
m	Multiplicity of knot
n	Porosity
n^α	Volume fraction of phase α
n^f	Volume fraction of fluid
n^s	Volume fraction of solid
p	Polynomial degree
p^f	Fluid pressure
p^s	Average pressure on solid
p^w	Pore water pressure
p_o^w	Initial pore water pressure
p_p	Polynomial degree of pressure basis functions
p_T	Polynomial degree of temperature basis functions
p_u	Polynomial degree of displacement basis functions
s^α	Specific entropy of phase α
s^β	Specific entropy of phase β
t	Current time
t_o	Initial time
u_h	Galerkin approximation of field variable u
v^α	Specific volume of phase α
v^β	Specific volume of phase β
w	Test function/Weighting coordinate

Latin Small Letters (Bold)

$\boldsymbol{a}$	Total acceleration of porous medium
$\boldsymbol{a}^\alpha$	Acceleration of phase α
$\boldsymbol{a}^\mathrm{s}$	Acceleration of fluid
$\boldsymbol{a}^\mathrm{fs}$	Relative acceleration between fluid and solid
$\boldsymbol{b}$	Total body force of porous medium
$\boldsymbol{b}^\alpha$	Body force of phase α
$\boldsymbol{f}$	Global RHS vector
$\boldsymbol{f}^\alpha$	Arbitrary vector function
$\boldsymbol{f}_\mathrm{e}$	Element RHS vector
$\boldsymbol{f}_\mathrm{p}$	External flow vector
$\boldsymbol{f}_\mathrm{T}$	External heat vector
$\boldsymbol{f}_\mathrm{u}$	External force vector
$\boldsymbol{k}$	Hydraulic conductivity matrix
$\boldsymbol{n}$	Outward unit normal vector
$\boldsymbol{p}^\mathrm{c}$	Control point pressure values
$\boldsymbol{q}$	Total heat flux vector for porous medium

$\boldsymbol{q}^{\alpha}$	Partial heat flux vector of phase α	$\boldsymbol{v}^{\mathrm{f}}$	Velocity of fluid
$\boldsymbol{q}^{\mathrm{f}}$	Partial heat flux of fluid	$\boldsymbol{v}^{\mathrm{s}}$	Velocity of solid
$\boldsymbol{q}^{\mathrm{s}}$	Partial heat flux of solid	$\boldsymbol{v}^{\beta\alpha}$	Relative velocity between phase β and phase α
$\boldsymbol{r}$	Position vector		
$\boldsymbol{t}^{\alpha}$	Traction forces for phase α	$\boldsymbol{v}^{\mathrm{sf}}$	Relative velocity between solid and fluid
$\boldsymbol{u}$	Displacement vector	$\boldsymbol{w}$	Darcy's velocity
$\boldsymbol{u}^{\mathrm{c}}$	Control point displacement values	$\boldsymbol{x}$	Position vector
$\boldsymbol{u}_{\mathrm{o}}$	Initial displacement vector	$\boldsymbol{x}^{\alpha}$	Position vector of phase α
$\boldsymbol{v}^{\alpha}$	Velocity of phase α	$\overline{\boldsymbol{t}}$	Surface traction
$\boldsymbol{v}^{\beta}$	Velocity of phase β	$\overline{\boldsymbol{u}}$	Prescribed displacement

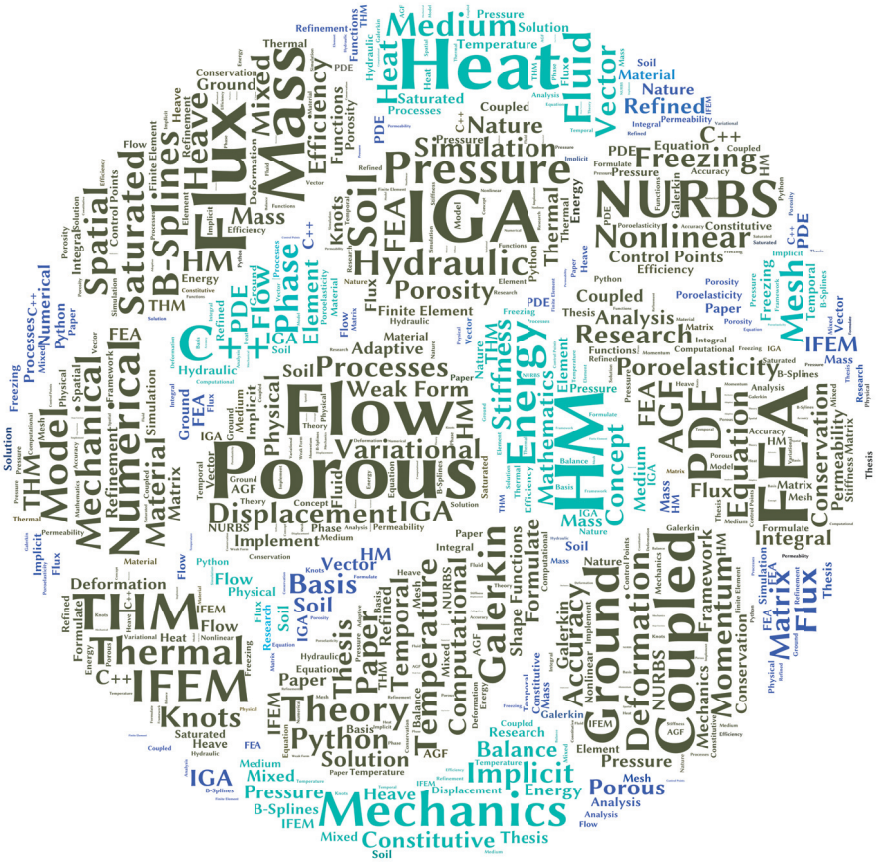

See the forest for the trees!

Abstract

Computational modeling of coupled problems in porous media is essential in various disciplines of science and engineering. The porous media of interest here are soils subjected to different physical processes. In particular, hydraulic (H), coupled hydro-mechanical (HM) and thermo-hydro-mechanical (THM) processes are addressed. Development of a fully-coupled THM numerical model targets ground freezing phenomena as the main application problem. The governing equations for the various processes are derived based on porous media theory. The fundamentals of this theory are presented in a general form and discussed by focusing on soils and the application problems. Isogeometric analysis (IGA) is adopted for implementing the governing equations, leading to the development of a code for numerical simulations. One of the main reasons for choosing IGA as a computational framework is the smoothness of the basis functions, which is attractive for better continuity of field variables. The main concepts behind IGA, including its advantages compared to traditional finite element analysis (FEA), are briefly discussed.

The first problem studied is steady-state groundwater flow governed by Darcy's law. Numerical challenges occur in the simulation of groundwater flow problems due to complex boundary conditions, varying material properties, presence of sources or sinks in the flow domain or a combination of these. Adaptive IGA using locally refined (LR) B-Splines is applied to address some of these problems. A posteriori error estimates are calculated to identify which B-Splines should be locally refined. The error estimates are calculated based on recovery of the L_2-projected solution. The adaptive analysis method is first illustrated by performing simulation of benchmark problems with analytical solutions. Numerical applications to two-dimensional groundwater flow problems are then presented. The problems studied are flow around an impervious corner, flow around a cutoff wall and flow in a heterogeneous medium. The convergence rates obtained with adaptive analysis using local refinement were, in general, observed to be of optimal order in contrast to simulations with uniform refinement.

Classical problems in poroelasticity are next addressed using mixed IGA, i.e. using different polynomial degrees for displacement and pore pressure. The finite element method has been widely applied to such problems and the numerical behavior of the governing equations has been discussed by several researchers. Equal order

IGA has recently been applied to poroelasticity. Pressure oscillations at small time steps have been known to be an issue in the simulation of poroelasticity problems. The performance of mixed IGA for smaller time steps is investigated by revisiting Terzaghi's classical consolidation problem. A numerical study is also performed on the consolidation of a layered soil where a very low permeability layer is known to cause pressure oscillations. It is observed from the numerical studies that mixed IGA improves the accuracy of the pore pressure results compared to equal order simulations, as is known from traditional FEA. The pressure oscillations, however, are not completely removed but were observed to decrease with increasing polynomial degrees. Mixed simulations with a graded mesh refinement were observed to reduce the pore pressure oscillations, revealing the potential of adaptive refinement for such problems.

Fully coupled THM processes in ground freezing are then studied using mixed IGA. The governing linear momentum, mass and energy balance equations are formulated by assuming saturated conditions. Strain due to phase change is incorporated into the linear momentum balance equation. This is attained through a simple thermoelastic constitutive equation with temperature dependent strength parameters. The supplementary equations that complete the model include the soil-water characteristic curve and a hydraulic conductivity model. After spatial and temporal discretization, the governing and supplementary equations result in a strongly coupled and highly nonlinear system of equations, which are solved using Newton-Raphson iteration. Numerical studies are performed on one-dimensional freezing and a frost heave problem where experimental data is available. Good agreements were observed between the mixed IGA based simulation of a THM coupled problem in frost heave and the corresponding experimental data found from literature. The continuity of the basis functions in mixed IGA of THM coupled problems implies that prediction of derived quantities, such as fluxes, across knot spans (analogous to elements in traditional FEA) can be controlled and improved.

In general, the numerical implementation work resulted in H, HM and THM frameworks for simulation of poro/geomechanics problems using IGA. The frameworks are developed based on IFEM - an object-oriented isogeometric toolbox for the solution of partial differential equations. The developed numerical codes may be used and extended further. In addition to the various application problems studied, the numerical work mainly initiates application of IGA to THM coupled problems in porous media. The features of IGA that are computationally attractive in this context, such as the ability to perform higher-order simulations with ease, can thus be utilized.

Preface

This thesis work has been part of the Material Modeling work package (WP2) under the research project SAMCoT - Sustainable Arctic Marine and Coastal Technology. The work is carried out at the Department of Civil and Transport Engineering, NTNU and at the Department of Applied Mathematics, SINTEF ICT, in Trondheim. The numerical implementation work is performed by using IFEM as a platform. IFEM is an object-oriented toolbox for implementing finite element solvers for linear and nonlinear partial differential equations using B-Splines and NURBS as basis functions. IFEM is developed at the Department of Applied Mathematics, SINTEF ICT, Trondheim and is available as an open-source software. The adaptive refinement capability of IFEM depends on the LR B-Splines package developed by Dr. Kjetil A. Johannessen. Details of other thrid-party software that IFEM depends on may be referred from the official repository page on GitHub.

The journal papers, published and submitted, are included in the thesis in their original form. Due to the independent nature of the manuscripts, some text and equations in the main document are found repeated in the papers. The nomenclature is mainly generated for the chapters and appendices of the thesis. Most of the notations also apply to the papers with the exception of a few different symbols.

Trondheim, Norway Yared W. Bekele

Acknowledgements

The financial support from the Research Council of Norway and industrial partners through the research project SAMCoT is greatly acknowledged. Many people have contributed directly or indirectly to the realization of this thesis. I would first like to thank my supervisor Prof. Steinar Nordal for taking me as his PhD student, for his feedback and for introducing me to the key connections that later became invaluable to my work. I am grateful to my co-supervisor Prof. Trond Kvamsdal for introducing me to the world of isogeometric analysis and for welcoming me to his research group at SINTEF. I have learned a lot from your advice on how to approach problems and I am grateful for your continuous motivation and feedback. Thanks also to Prof. Thomas Benz for initially opening the door to my PhD career. My gratitude also goes to Prof. Knut Høyland for being a very supportive work package leader.

Acknowledging the help I received from Dr. Arne Morten Kvarving in a few sentences feels too inadequate. None of this would have been possible without your relentless help in the numerical implementation work in IFEM. In addition to that, you still made time for reviewing the papers and proofreading the thesis. I am immensely grateful for everything you did. The visit of Dr. Hiroyuki Kyokawa to NTNU as a postdoctoral researcher could not have been any more timely for my research. I am indebted to him for his help in the theoretical development of the THM framework. Thank you for your cooperation and motivation. It has been great to work on poroelasticity with Dr. Eivind Fonn. You have been a pleasure to work with and thank you for your contribution.

Working in the Applied Mathematics Department of SINTEF ICT has been a very enriching experience. I would like to thank Dr. Knut Morten Okstad for being there to answer my questions regarding IFEM. It has been gratifying to discuss IFEM, computation and what not with Dr. Timo van Opstal and Dr. Kjetil A. Johannessen; thank you both. Thanks also to the rest of the group for being friendly and for creating a great research environment.

The long journey towards completing this thesis hasn't been an all smooth ride. There was a time around the beginning when I felt strayed. My then colleague and friend Dr. Anteneh Biru was there to listen to all my frustrations. All the discussions we had were of great influence in helping me think more clearly and

find my focus. I am very grateful for this and also for your insightful feedback on our paper. My gratitude also goes to Dr. Emilie Guegan for patiently sharing MY office over the years. Thank you for the uplifting conversations on work and life. I would also like to thank Dr. Seyed A. G. Amiri for the interesting discussions and comments on our paper and Ashenafi Lulseged for helping with the proofreading of the thesis.

The last four years at the Department of Civil and Transport Engineering have been enjoyable because of wonderful colleagues, both current and past. To my colleagues in the Geotechnical Division, thank you all for the work related interactions, the good times during social activities and the diverse entertaining chats in the lunch room. Thanks to Marit Skjåk-Bræk for her help in the administrative matters. Thanks also to all SAMCoT colleagues.

Family and friends remind you that life is not all about work by being there for a much needed balance. I am grateful for having great friends - near and far, old and new. To all my friends in Trondheim, I am thankful for the good times I shared with you. From the simple hangouts to sharing important moments in each others lives, it has been an enjoyable life experience and I will cherish the memories. All my friends farther from here, I am appreciative of having you in my life and thank you for your great friendship. Last but not least, I am grateful for having a wonderful family. Your unconditional love, belief and pride in me have been a prominent source of motivation that kept me pushing forward. This is for you Abaye, Emaye, Selam, Erma, Betty, Zee, Ash and TGye; I love you all.

Trondheim, Norway Yared W. Bekele

Part I

Primer

"If we knew what it was we were doing, it would not be called research, would it?"

– Albert Einstein

Chapter 1

Introduction

In this introductory chapter, the organization of the thesis is first described. The background and motivation for the thesis, with focus on the application problems to be studied, is then discussed. The objectives of the thesis and the research methodology are highlighted.

1.1 Organization of Thesis

The thesis is organized into three main parts and an appendix: Part I, Part II, Part III and Part IV, the Appendix.

Part I: Primer - is an introductory part containing three chapters, including the current chapter.

- **Chapter 1**: The background and motivation for the thesis work is conferred. The research strategy followed to achieve the objectives is discussed.
- **Chapter 2**: Porous media theory is briefly presented in this chapter. The discussion covers the basics of porous media theory with a main focus on conservation laws. Other laws that complete the mathematical model for a porous material are also dealt with. Derivation of the governing conservation equations is first presented in a general form. Specific governing equations for hydraulic, hydro-mechanical and thermo-hydro-mechanical processes, with focus on the application problems here, are then derived.
- **Chapter 3**: The fundamentals behind isogeometric analysis (IGA), the computational method applied here, are highlighted. A brief discussion on spline basis functions and geometries is presented. The refinement capabilities of IGA are discussed and a comparison with the finite element method is made. A general discussion on the application of IGA to boundary value problems is presented.

Part II: Papers - presents the main results from the research work in the form of accepted and submitted publications.

- **Paper 1**: Application of IGA to porous media flow problems is presented. Specifically, IGA with adaptive refinement is applied to steady-state groundwater flow problems. The performance of adaptive IGA for this class of problems is demonstrated through relevant numerical studies.
- **Paper 2**: Hydro-mechanically (HM) coupled problems are studied in this paper by applying mixed IGA. Classical elastic consolidation problems are revisited under the new computational framework and numerical studies are performed with a focus on the accuracy of the solution at small time steps.
- **Paper 3**: Thermo-hydro-mechanically (THM) coupled problems in ground freezing are studied in this paper. The governing equations are developed such that strain due to phase change is incorporated into the equilibrium equation. Mixed IGA is applied and the resulting highly nonlinear system of equations are solved iteratively. Numerical verification and validation is performed by considering a case where experimental data is available.

Part III: Summary - contains a chapter summarizing the research work.

- **Chapter 4**: A summary of the papers in Part II is presented. The main findings of the research work are highlighted and conclusions are drawn. A list of recommendations for future work is made under the theoretical and numerical aspects of the research.

Part IV: Appendix - presents miscellaneous material related to the thesis work.

- **Appendix A**: The simplest case of a THM coupled problem, an intermediate implementation in the development of the final THM framework, is presented. In particular, THM coupled processes in a saturated porous medium (thermoporoelasticity) are studied using IGA. The results presented are only preliminary. A detailed investigation showing the advantages of IGA for this class of problems is a subject for a future work.
- **Appendix B**: A quick reference to integral theorems, which are mentioned and used throughout the thesis, is given.
- **Appendix C**: Conference papers and presentations related to the thesis are listed.

1.2 Background and Motivation

The benefits of computational modeling in various disciplines of science and engineering cannot be understated. Computational models can improve the understanding of physical phenomena in different ways such as by providing a deeper

insight into complex physical phenomena which are otherwise difficult to deal with and by shedding light on counterintuitive seeming outcomes. With the advancement of computing power, problems that are insoluble by traditional methods can be tackled through computational modeling.

Computational poro/geomechanics has a wide range of applications and is the main theme of the current research. The focus of this thesis is on coupled problems in porous media. Materials that are composed of a solid matrix and pores (or voids) that may be filled with one or more fluids are referred to as porous media. Porous material can be either natural, such as soils and rocks, or artificial, such as foams. The main porous media of interest for the applications in this thesis are soils subjected to different physical processes. The theoretical formulations and computational aspects are, however, presented in a general form which may be applicable to other porous materials.

Coupled problems in porous media are studied here. A *coupled problem* is a physical problem which involves a multi-way interaction of physical processes or computational components; see Felippa et al. (2001). According to this definition, the interaction of two or more physical processes in a porous medium resulting in a mathematical formulation that needs to be solved sequentially or simultaneously results in a coupled problem. In some cases, a single physical process may be governed by multiple equations with coupled computational components to be solved for simultaneously. The problems that are studied here are fluid flow in a porous medium, hydro-mechanics (coupled fluid flow and deformation) and thermo-hydro-mechanics (coupled heat transfer, fluid flow and solid deformation). These are discussed further and examples of relevant application problems are listed in the following sections.

Hydraulics (H)

Porous media flow is what we refer to as hydraulics here. The flow of fluid through porous media is relevant in different applications such as groundwater flow or reservoir engineering. The flow could either be single-phase, a single fluid phase occupying the pore spaces, or multi-phase, multiple fluid phases flowing simultaneously. The study here focuses on single-phase flows. The governing equations for a single-phase porous media flow problem usually have computationally coupled components such as pressure and velocity.

In the computational modeling of porous media flow problems, a wide range of analytical and numerical methods exist. Numerical studies have been performed over the past several decades. In the current study, IGA is applied to single-phase porous media flow and the numerical properties of the governing equation are investigated. In particular, steady-state groundwater flow problems governed by Darcy's law are revisited with a view to examining the accuracy of the solution with respect to spatial discretization.

Hydro-Mechanics (HM)

The flow of fluid coupled with solid deformation in porous media is what we refer to as hydro-mechanics here. The mathematical formulations governing hydro-mechanically coupled problems in porous media constitute the backbone of computations in poromehcanics/geomechanics. There are a wide range of natural and man made materials that are studied under this framework. The application areas are also diverse; examples include geomechanics, biomechanics, oil and gas reservoir engineering and earthquake engineering.

Computational modeling of hydro-mechanically coupled problems in porous media is not a new endeavor. In fact, it has been studied in the past several decades for diverse applications using various computational methods. Poroelasticity, a classical hydro-mechanical problem, is revisited here with a view to assessing the numerical properties of the governing equations under the computational method applied here.

Thermo-Hydro-Mechanics (THM)

The coupled interaction of heat transfer, fluid flow and solid deformation in porous media results in what we refer to as thermo-hydro-mechanics. This class of problems may be categorized into two groups: high temperature and low temperature regime problems. A typical application in the low temperature regime is ground freezing and thawing, which may occur naturally or artificially. These are discussed in the next section. Other applications in the high and low temperature regimes are briefly discussed afterwards.

Natural Ground Freezing

It is estimated that permafrost accounts for about 20-25% of our planet's total land area in the Northern Hemisphere, French (1999). In Figure 1.1, the distribution of naturally frozen ground in this region is shown. The increasing socioeconomic activities in such areas lead to the construction and installation of various infrastructure which directly or indirectly interact with the ground. These activities call for a better understanding of the behavior of frozen ground for a safe and economic design of infrastructure. The most common challenge associated with construction in frozen ground is damage to structures such as roads, buildings and pipelines due to frost heave and thaw settlement related to seasonal variation of temperature; see Andersland and Ladanyi (2004).

The physical processes that occur in frozen ground are complex and strongly coupled. Computational modeling of these processes requires a detailed mathematical formulation and a robust numerical implementation.

Artificial Ground Freezing

Artificial ground freezing (AGF) is a construction technique which has been used in civil engineering for more than a century, Harris (1995). Some applications of AGF include ground stabilization in the construction of tunnels of various purposes,

Figure 1.1: Distribution of naturally frozen ground in the Northern Hemisphere. Image credit: Philippe Rekacewicz, 2005, UNEP/GRID-Arendal Maps and Graphics Library.

creation of a temporary support for excavation, stabilization during mining in an unstable ground, support for foundations near excavations, limitation of contaminant transport in the ground, structural underpinning for foundation improvement and arrest of landslides. An example of AGF in tunneling is shown in Figure 1.2. Compared to other ground improvement techniques, AGF is very environmentally friendly. Numerical simulation of AGF is essential in planning an optimum freezing technique and predicting the expected outcome.

Recent applications of AGF include construction of the Oslofjord underground tunnel in Norway (Eiksund et al. (2001)), the Bothnia railway line in Sweden (Johansson (2009)), the Naples subway in Italy (Colombo et al. (2008)) and the Guangzhou subway tunnel in China (Li et al. (2006)). Another example application of AGF is the containment of radioactive waste transport in the ground at the Fukushima Power Plant in Japan, which is an ongoing project.

Other Applications

THM coupling in the high temperature regime has several applications in various disciplines of science and engineering. Some examples include geothermal energy extraction, safety assessment of nuclear waste repositories, oil and gas reservoir engineering, underground energy storage and CO_2 sequestration. See Paper III for references to such application areas.

Freezing and thawing in porous media has other applications besides natural and artificial ground freezing. Some example application areas include food processing (see Rebellato et al. (1978) and Moraga and Salinas (1999)) and biomechanics (see Rubinsky and Pegg (1988) and Deng and Liu (2004)).

The research work in this thesis aims to contribute to the better understanding

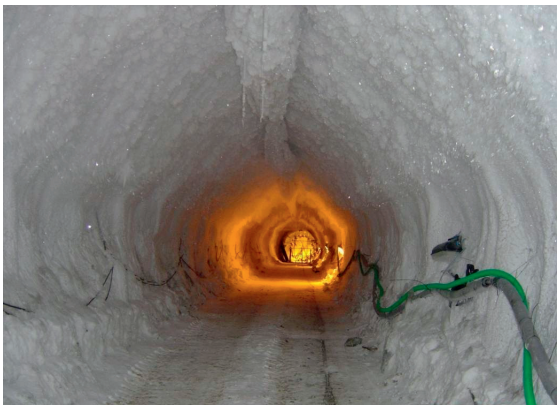

Figure 1.2: Artificial ground freezing in tunneling. Image credit: MMM Hydropower.

and improvement of the computational modeling of the application problems highlighted above. IGA is adopted for the numerical study of these problems.

Why IGA?

The reasons for choosing IGA as a computational framework include:

- The basis functions in IGA are the same as those used in computer aided design (CAD). Thus, analysis can be performed on 'exact' CAD geometries, which are only approximated in finite element analysis (FEA) through mesh generation.
- The smoothness of the spline basis functions in IGA, compared to Lagrange polynomial based basis functions in FEA, is found attractive for better continuity of field variables.
- Better continuity of field variables means improvement in the accuracy of derived quantities such as stresses, strains, fluid fluxes and heat fluxes.

Other specific advantages of IGA over traditional FEA are discussed in Chapter 3.

Objectives

A general aim of the research is to serve as a contribution towards robust and efficient methods in computational poro/geomechanics. The specific objectives of the research work include:

- To develop a robust computational tool for the simulation of coupled problems in porous media where the main application is THM coupling during ground freezing.
- To investigate the accuracy of the numerical solution of the governing equations in classical hydro-mechanically coupled problems.

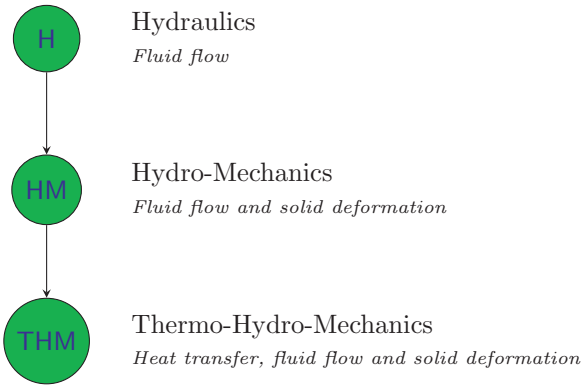

Figure 1.3: Hierarchical development of the IGA based computational framework.

- To investigate the accuracy of using IGA for fluid flow computations in porous media governed by Darcy's law.

1.3 Research Strategy

The numerical implementation work leading to a fully coupled THM code for ground freezing is performed in a hierarchical way. Application of IGA as the computational method here is investigated at each step of the numerical study. The implementation starts with porous media flow under isothermal conditions and a constant porosity in the medium i.e. no deformations. The results from this work are reported in Paper I. The next step is to couple fluid flow with solid deformation i.e. hydro-mechanics. In particular, poroelasticity is revisited under the IGA framework and the results are reported in Paper II. Thermo-hydro-mechanical coupling is then studied starting with the simplest case of thermoporoelasticity. Phase change is then incorporated into the governing and supplementary equations. The intermediate results from thermoporoelasticity are given in Appendix A and the application to ground freezing is presented in Paper III.

The numerical implementation work is performed using IFEM as a platform - an isogeometric toolbox for the solution of partial differential equations, under development at SINTEF ICT, Applied Mathematics Department in Trondheim, Norway. In addition to the promising reasons for choosing IGA, this created an opportunity to combine the competencies of different scientific groups at NTNU. The open source nature of IFEM also has the advantage of avoiding a 'black box' approach to the finite element simulations targeted here. These aspects are utilized to create a numerical tool that may be used and developed further, with full access to the understanding of the mathematical formulations and the source code. This creates a platform for H, HM and THM problems in geomechanics. The THM framework is tailored to solve ground freezing problems.

"I learned very early the difference between knowing the name of something and knowing something."

– Richard Feynman

Chapter 2

Porous Media Theory

In this chapter, fundamental concepts and formulations in porous media theory are presented. The discussion starts with a brief history of porous media theory. The volume fraction concept and kinematic relations are then presented. Conservation laws are derived in a general form which may be applicable to any porous material subjected to different physical processes. Thermodynamic formulations and phase transitions in porous media are briefly discussed. Formulations that complete the mathematical model for a given porous material, such as constitutive laws, are also discussed. The main porous materials of interest in this thesis are soils and specific conservation equations are derived for hydraulic, hydro-mechanical and thermo-hydro-mechanical processes by making the necessary assumptions for particular application needs.

2.1 Background

The study of porous materials is essential in various disciplines of science and engineering such as soil mechanics, oil and reservoir engineering, biomechanics, material sciences and chemical engineering. The porous materials studied under porous media theory can either occur naturally, such as soils and rocks, or may be artificial, such as sponges and synthetic polymers. The physical and mechanical properties of such materials have been studied experimentally and mathematically over several decades by a number of researchers. Modern porous media theory, which will be discussed in detail in later sections, developed over a long period of time to reach to what is known today. The historical development of the theory is documented in some publications such as de Boer and Ehlers (1988) and de Boer (2003).

There are some important milestones in the development of porous media theory, as presented in de Boer (1998). In the earliest stages of the theory, Leonhard Euler presented the first discussion on the geometry of a porous medium and indirectly contributed to the formulation of the axioms of continuum mechanics. The intro-

duction of the volume fraction concept by Reinhard Woltman in the 19th century proved to be a fundamental contribution. This concept was further discussed by Achille Delesse. The development of mixture theory, a branch of porous media theory, was initiated by Adolph Fick. An important mathematical relation describing the motion of a fluid in a porous medium was derived by Henry Darcy, which we refer to today as Darcy's law. In early 20th century, Paul Fillunger and Karl von Terzaghi made seminal contributions to the theory of liquid-saturated porous solids. Fillunger developed equations for uplift forces while studying the stresses acting on concrete and masonry gravity dams. Terzaghi also studied uplift forces independently of Fillunger and further made contributions to the understanding of capillary pressure, the concept of effective stresses and soil consolidation theory. The effective stress concept was discussed earlier by Fillunger. After mid 20th century, the theory of porous media started taking shape to become what we know today. Some of the contributions in this period include work on the theory of mixtures by Green and Naghdi (1967), without using the volume fraction concept, the study of fluid motion in porous media by Whitaker (1969), modeling of simultaneous heat, mass and momentum transfer by Whitaker (1977), the treatment of the mechanics of continuous porous media by Prévost (1980), a theory of immiscible and structured mixtures by Bedford and Drumheller (1983) and a generalized approach to the derivation of balance laws by Hassanizadeh (1986). Application of the theory of mixtures to the modeling of incompressible and compressible porous media was presented by Bowen (1980) and Bowen (1982), respectively. A discussion relating mixture theory and Biot's approach to porous media theory can be found in Coussy et al. (1998).

In the following sections, the basic components of porous media theory are presented. The volume faction concept, a fundamental concept in porous media theory, is first discussed. The conservation laws of mass, momentum and energy are then presented in a general form for a porous medium with any number of constituents. The mechanics of phase change in a porous medium and how it affects the conservation laws is then treated. Constitutive equations that govern the constituents of the porous medium are required to complete the theory and these are discussed afterwards. These sections are presented in a brief way here and a detailed presentation of the topics may be referred from modern treatments of porous media theory such as in Coussy (2004), Vadász (2008) and Ehlers and Bluhm (2013).

2.2 Volume Fraction Concept

One of the most important concepts in the development of porous media theory is the volume fraction concept. This concept is used to a idealize a porous medium with multiple constituents as a homogeneous continuum. An important assumption in the volume fraction concept is that the solid constituent of the porous medium is considered as a reference volume such that only the fluid constituents can enter or leave the reference volume; see Bluhm and de Boer (1997).

Consider a porous medium composed of N constituents. Let V be the total volume of the porous medium and V^α be the volume of phase α. Let $\mathrm{d}V$ be a control volume

element in the total volume and $\boldsymbol{x}$ be its position vector in a global coordinate system at a given time t. Similarly, let $\boldsymbol{r}$ be the position vector of a microscopic volume element $\mathrm{d}V_\beta$ inside $\mathrm{d}V$. The volume of constituent α within the control volume can be determined by first defining a phase distribution function χ^α such that

$$\chi^\alpha(\boldsymbol{r},t) = \begin{cases} 1 & \text{for} \quad \boldsymbol{r} \in \mathrm{d}V_\beta \\ 0 & \text{for} \quad \boldsymbol{r} \in \mathrm{d}V_\gamma, \quad \beta \neq \gamma. \end{cases} \tag{2.1}$$

Thus, the partial volume of constituent α in the control volume can be written as

$$\mathrm{d}V^\alpha(\boldsymbol{x},t) = \int_{\mathrm{d}V} \chi^\alpha(\boldsymbol{r},t)\mathrm{d}V_\beta. \tag{2.2}$$

The volume fraction n^α of phase α can now be defined as

$$n^\alpha(\boldsymbol{x},t) = \frac{\mathrm{d}V^\alpha}{\mathrm{d}V} = \frac{1}{\mathrm{d}V}\int_{\mathrm{d}V} \chi^\alpha(\boldsymbol{r},t)\mathrm{d}V_\beta. \tag{2.3}$$

The position vector $\boldsymbol{r}$ may be written in terms of the global position vector $\boldsymbol{x}$ by introducing a local reference system $\boldsymbol{\xi}$ with origin at $\boldsymbol{x}$, such that $\boldsymbol{r} = \boldsymbol{x} + \boldsymbol{\xi}$. The individual volumes of the constituents and their volume fractions satisfy the conditions

$$\sum_{\alpha=1}^{N} \mathrm{d}V^\alpha = \mathrm{d}V \quad \text{and} \quad \sum_{\alpha=1}^{N} n^\alpha = 1. \tag{2.4}$$

The volume fractions can now be used to describe the relationship between the densities of the constituents of the porous medium at microscopic and macroscopic levels. We denote the intrinsic real density of constituent α by ρ_α and the partial density at macroscale by ρ^α, following the notations according to Prévost (1980). The relationship between these two densities in terms of the volume fraction of the phase under consideration is given by

$$\rho^\alpha(\boldsymbol{x},t) = n^\alpha(\boldsymbol{x},t)\rho_\alpha(\boldsymbol{x},t). \tag{2.5}$$

The total density of the mixture ρ is then the sum of the partial densities of all constituents i.e.

$$\rho(\boldsymbol{x},t) = \sum_{\alpha=1}^{N} \rho^\alpha(\boldsymbol{x},t). \tag{2.6}$$

2.3 Kinematics

Kinematic relations describing the relative motions of the phases in a porous medium are briefly discussed here. These relations will be used later in deriving the conservation laws for a porous medium. A detailed presentation may be referred from Lewis and Schrefler (1998).

According to the volume fraction concept, a porous medium composed of N constituents is approximated as a homogeneous continuum. Thus, a material point

defined by the position vector $\boldsymbol{x}$ is simultaneously occupied by all phases. Let $\boldsymbol{X}^\alpha$ be the reference position of phase α at time $t = t_\mathrm{o}$. The position of each material point $\boldsymbol{x}^\alpha$ of phase α at time t may be written in a Lagrangian description as

$$\boldsymbol{x}^\alpha = \boldsymbol{x}^\alpha(\boldsymbol{X}^\alpha, t). \tag{2.7}$$

An Eulerian description of motion may be written for a non-singular Lagrangian description as

$$\boldsymbol{X}^\alpha = \boldsymbol{X}^\alpha(\boldsymbol{x}^\alpha, t). \tag{2.8}$$

For a particle of phase α with a defined path, Lagrangian descriptions of the velocity and acceleration are

$$\begin{aligned} \boldsymbol{V}^\alpha &= \frac{\partial \boldsymbol{x}^\alpha(\boldsymbol{X}^\alpha, t)}{\partial t} \\ \boldsymbol{A}^\alpha &= \frac{\partial^2 \boldsymbol{x}^\alpha(\boldsymbol{X}^\alpha, t)}{\partial t^2}. \end{aligned} \tag{2.9}$$

Eulerian description of the velocity and acceleration may be derived by using (2.8) in (2.9). Given an Eulerian description of the velocity $\boldsymbol{v}^\alpha(\boldsymbol{x}^\alpha, t)$, the Eulerian acceleration $\boldsymbol{a}^\alpha$ may be derived by evaluating the time derivative of the velocity where the Lagrangian coordinates are held constant. That is, by applying the chain rule

$$\boldsymbol{a}^\alpha = \frac{\partial \boldsymbol{v}^\alpha}{\partial t} + \nabla \boldsymbol{v}^\alpha \cdot \boldsymbol{v}^\alpha. \tag{2.10}$$

For any differentiable function f^α describing some physical property of phase α in the porous medium, the *material time derivative* (also called *convective derivative* or *Lagrangian derivative*) is introduced to describe its rate of change relative to a chosen phase. If the Eulerian description of $f^\alpha = f^\alpha(\boldsymbol{x}^\alpha, t)$ is given, its material time derivative with respect to a moving particle of phase α is defined by

$$\frac{\mathrm{D}_\alpha f^\alpha}{\mathrm{D}t} := \frac{\partial f^\alpha}{\partial t} + \nabla f^\alpha \cdot \boldsymbol{v}^\alpha. \tag{2.11}$$

The material time derivative of f^α with respect to a moving particle of another phase, say phase β, is defined as

$$\frac{\mathrm{D}_\beta f^\alpha}{\mathrm{D}t} := \frac{\partial f^\alpha}{\partial t} + \nabla f^\alpha \cdot \boldsymbol{v}^\beta. \tag{2.12}$$

Equations (2.11) and (2.12) result in the relation

$$\frac{\mathrm{D}_\beta f^\alpha}{\mathrm{D}t} = \frac{\mathrm{D}_\alpha f^\alpha}{\mathrm{D}t} + \nabla f^\alpha \cdot \boldsymbol{v}^{\beta\alpha} \tag{2.13}$$

where

$$\boldsymbol{v}^{\beta\alpha} = \boldsymbol{v}^\beta - \boldsymbol{v}^\alpha \tag{2.14}$$

is the relative velocity of a particle of phase β with respect to phase α.The material time derivative may be applied to either a scalar or a vector quantity.

In porous media theory, we often require the rate of change of volume averaged quantities. For a vector physical property $\boldsymbol{f}^\alpha$ of phase α per unit volume, the total time derivative over a volume V is given according to Reynold's transport theorem by

$$\begin{aligned}\frac{d}{dt}\int_V \boldsymbol{f}^\alpha \mathrm{d}V &= \int_V \left(\frac{\partial \boldsymbol{f}^\alpha}{\partial t} + \nabla \boldsymbol{f}^\alpha \cdot \boldsymbol{v}^\alpha + \boldsymbol{f}^\alpha \nabla \cdot \boldsymbol{v}^\alpha\right) \mathrm{d}V \\ &= \int_V \left[\frac{\partial \boldsymbol{f}^\alpha}{\partial t} + \nabla \cdot (\boldsymbol{f}^\alpha \otimes \boldsymbol{v}^\alpha)\right] \mathrm{d}V.\end{aligned} \tag{2.15}$$

For a scalar physical property f^α per unit volume, we have

$$\frac{d}{dt}\int_V f^\alpha \mathrm{d}V = \int_V \left[\frac{\partial f^\alpha}{\partial t} + \nabla \cdot (f^\alpha \boldsymbol{v}^\alpha)\right] \mathrm{d}V. \tag{2.16}$$

Applying the divergence theorem, we get the expression

$$\frac{d}{dt}\int_V f^\alpha \mathrm{d}V = \int_V \frac{\partial f^\alpha}{\partial t} \mathrm{d}V + \int_{\partial V} f^\alpha \boldsymbol{v}^\alpha \cdot \boldsymbol{n} \mathrm{d}A \tag{2.17}$$

where ∂V is the boundary of the domain V and $\boldsymbol{n}$ is the outward unit normal to the surface $\mathrm{d}A$.

The spatial velocity gradient of phase α,

$$\boldsymbol{L}^\alpha = \nabla \boldsymbol{v}^\alpha, \tag{2.18}$$

can be decomposed into symmetric and skew-symmetric parts as

$$\boldsymbol{L}^\alpha = \boldsymbol{D}^\alpha + \boldsymbol{W}^\alpha, \tag{2.19}$$

where $\boldsymbol{D}^\alpha$ and $\boldsymbol{W}^\alpha$ are the rate of deformation and spin tensors, respectively, which may be expressed as

$$\boldsymbol{D}^\alpha = \frac{1}{2}(\boldsymbol{L}^\alpha + \boldsymbol{L}^{\alpha\intercal}) \quad \text{and} \quad \boldsymbol{W}^\alpha = \frac{1}{2}(\boldsymbol{L}^\alpha - \boldsymbol{L}^{\alpha\intercal}). \tag{2.20}$$

2.4 Conservation Laws

The various physical processes within a porous medium induced by external and internal factors are described mathematically using conservation laws, which describe the evolution of physical parameters relevant to the processes. The main conservation laws for a porous medium are mass, momentum and energy balance equations.

The kinematic equations described in the previous section are used to derive the balance equations for a given porous medium. The derivation of these balance equations considers internal and external factors affecting the state of the porous medium and the interactions between the phases in the medium. This is required

to ensure that the individual balance equations of the phases result in the balance equation of the whole mixture when superimposed; see Hassanizadeh and Gray (1980). In the following sections, the balance equations of mass, momentum and energy are derived for an individual phase in a porous medium and for the mixture as a whole. The presentation follows the works of de Boer (2006) and Lewis and Schrefler (1998).

2.4.1 Mass Balance

The law of conservation of mass for phase α requires that the rate of change of mass be equal to any other mass of that phase being added to or leaving from the system, internally from other constituents or externally from other sources. The rate of change of mass M^α of phase α over a domain V is described by

$$\frac{\mathrm{D}_\alpha M^\alpha}{\mathrm{D}t} = \frac{\mathrm{D}_\alpha}{\mathrm{D}t} \int_V \rho^\alpha \mathrm{d}V \tag{2.21}$$

and mass conservation requires this rate to be balanced with all mass exchanges among other phases, i.e.

$$\frac{\mathrm{D}_\alpha}{\mathrm{D}t} \int_V \rho^\alpha \mathrm{d}V + \sum_\beta M^{\beta\alpha} = 0 \tag{2.22}$$

where the second term in the above equation represents the sum of mass exchanges per unit volume from all phases β to phase α. Applying Reynold's transport theorem to the rate of change of M^α, a generalized mass balance equation for phase α can be written as

$$\frac{\mathrm{D}_\alpha \rho^\alpha}{\mathrm{D}t} + \rho^\alpha \nabla \cdot \boldsymbol{v}^\alpha + \sum_\beta M^{\beta\alpha} = 0. \tag{2.23}$$

The general mass balance equation for a porous medium with N constituents is then obtained by summation of the individual mass balance equations for each phase i.e.

$$\sum_{\alpha=1}^{N} \left[\frac{\mathrm{D}_\alpha \rho^\alpha}{\mathrm{D}t} + \rho^\alpha \nabla \cdot \boldsymbol{v}^\alpha + \sum_\beta M^{\beta\alpha} \right] = 0. \tag{2.24}$$

The mass exchange term between the phases has the constraint

$$\sum_{\alpha=1}^{N} \sum_\beta M^{\beta\alpha} = 0 \tag{2.25}$$

when summed over all the N constituents of the mixture, reducing the overall mass balance equation to

$$\sum_{\alpha=1}^{N} \left[\frac{\mathrm{D}_\alpha \rho^\alpha}{\mathrm{D}t} + \rho^\alpha \nabla \cdot \boldsymbol{v}^\alpha \right] = 0. \tag{2.26}$$

In (2.23), the motion of a particle of phase α is expressed relative to the same phase. In practice, it is more convenient to take one of the phases (usually the solid phase) as a reference to describe the motion of all other phases. The individual mass balance equations for these phases can then be modified by introducing their relative velocity with respect to the reference phase.

2.4.2 Linear Momentum Balance

The balance of linear momentum for a given phase α requires that the material time derivative its momentum $\boldsymbol{P}^\alpha$ be in equilibrium with the sum of all internal interaction forces and external forces. The rate of change of momentum over a domain V is described by

$$\frac{\mathrm{D}_\alpha \boldsymbol{P}^\alpha}{\mathrm{D}t} = \frac{\mathrm{D}_\alpha}{\mathrm{D}t} \int_V \rho^\alpha \boldsymbol{v}^\alpha \mathrm{d}V \tag{2.27}$$

and the balance of linear momentum requires

$$\frac{\mathrm{D}_\alpha}{\mathrm{D}t} \int_V \rho^\alpha \boldsymbol{v}^\alpha \mathrm{d}V + \sum_\beta \boldsymbol{P}^{\beta\alpha} = \boldsymbol{F}^\alpha \tag{2.28}$$

where the second term represents the sum internal momentum exchanges over time to phase α from all other phases β and $\boldsymbol{F}^\alpha$ represents external forces. The external forces involve body forces $\rho^\alpha \boldsymbol{b}^\alpha$ acting on the constituents over the volume V and surface forces $\boldsymbol{t}^\alpha$ acting on the boundary ∂V i.e.

$$\boldsymbol{F}^\alpha = \int_V \rho^\alpha \boldsymbol{b}^\alpha \mathrm{d}V + \int_{\partial V} \boldsymbol{t}^\alpha \mathrm{d}A \tag{2.29}$$

Cauchy's stress tensor $\boldsymbol{\sigma}^\alpha$ and the surface tractions $\boldsymbol{t}^\alpha$ of phase α are related by

$$\boldsymbol{t}^\alpha = \boldsymbol{\sigma}^\alpha \boldsymbol{n} \tag{2.30}$$

where $\boldsymbol{n}$ is an outward unit normal vector on the boundary. Using (2.15), applying the divergence theorem and considering the mass balance principle, the linear momentum balance equation for phase α becomes

$$\nabla \cdot \boldsymbol{\sigma}^\alpha + \rho^\alpha \boldsymbol{b}^\alpha + \sum_\beta \boldsymbol{P}^{\beta\alpha} = \rho^\alpha \boldsymbol{a}^\alpha. \tag{2.31}$$

The overall linear momentum balance equation for the mixture with N constituents is obtained by summation of the individual phase equations i.e.

$$\sum_{\alpha=1}^{N} \left[\nabla \cdot \boldsymbol{\sigma}^\alpha + \rho^\alpha \boldsymbol{b}^\alpha + \sum_\beta \boldsymbol{P}^{\beta\alpha} \right] = \sum_{\alpha=1}^{N} \rho^\alpha \boldsymbol{a}^\alpha. \tag{2.32}$$

The sums of the partial stresses, body forces and acceleration can be represented by their total equivalents:

$$\sum_{\alpha=1}^{N} \boldsymbol{\sigma}^\alpha = \boldsymbol{\sigma}, \quad \sum_{\alpha=1}^{N} \rho^\alpha \boldsymbol{b}^\alpha = \rho \boldsymbol{b} \quad \text{and} \quad \sum_{\alpha=1}^{N} \rho^\alpha \boldsymbol{a}^\alpha = \rho \boldsymbol{a}. \tag{2.33}$$

The internal exchange of momentum between the phases is required to satisfy the constraint

$$\sum_{\alpha=1}^{N}\sum_{\beta}\boldsymbol{P}^{\beta\alpha}=0. \tag{2.34}$$

Using (2.33) and (2.34) in (2.32), the linear momentum balance equation for the mixture becomes

$$\nabla\cdot\boldsymbol{\sigma}+\rho\boldsymbol{b}=\rho\boldsymbol{a}. \tag{2.35}$$

For a static condition ($\boldsymbol{a}=\boldsymbol{0}$), this reduces to

$$\nabla\cdot\boldsymbol{\sigma}+\rho\boldsymbol{b}=\boldsymbol{0}. \tag{2.36}$$

2.4.3 Angular Momentum Balance

The balance of angular momentum or moment of momentum states that the material time derivative of the angular momentum is equal to the moments of all external forces where the moments are referred to a certain fixed point. The angular momentum $\boldsymbol{H}^{\alpha}$ of phase α is given by

$$\boldsymbol{H}^{\alpha}=\int_{V}\boldsymbol{x}\times\rho^{\alpha}\boldsymbol{v}^{\alpha}\mathrm{d}V \tag{2.37}$$

where $\boldsymbol{x}$ is a position vector to the fixed point. The moment of the external forces using (2.29) is given by

$$\boldsymbol{M}^{\alpha}=\int_{V}\boldsymbol{x}\times\rho^{\alpha}\boldsymbol{b}^{\alpha}\mathrm{d}V+\int_{\partial V}\boldsymbol{x}\times\boldsymbol{t}^{\alpha}\mathrm{d}A. \tag{2.38}$$

Angular momentum balance requires

$$\frac{\mathrm{D}_{\alpha}}{\mathrm{D}t}\int_{V}\boldsymbol{x}\times\rho^{\alpha}\boldsymbol{v}^{\alpha}\mathrm{d}V=\int_{V}\boldsymbol{x}\times\rho^{\alpha}\boldsymbol{b}^{\alpha}\mathrm{d}V+\int_{\partial V}\boldsymbol{x}\times\boldsymbol{t}^{\alpha}\mathrm{d}A \tag{2.39}$$

where the moment of the exchanged momentum between the phases is omitted. Simplifying the above equation by applying the mass balance and momentum balance principles derived earlier gives

$$\int_{V}\boldsymbol{x}\times\rho^{\alpha}\boldsymbol{a}^{\alpha}\mathrm{d}V=\int_{V}\boldsymbol{x}\times\rho^{\alpha}\boldsymbol{a}^{\alpha}\mathrm{d}V+\int_{V}\boldsymbol{I}\times\boldsymbol{\sigma}^{\alpha}\mathrm{d}V \tag{2.40}$$

where $\boldsymbol{I}$ is the identity tensor. The above equation requires

$$\boldsymbol{I}\times\boldsymbol{\sigma}^{\alpha}=\boldsymbol{0} \tag{2.41}$$

and this is satisfied if

$$\boldsymbol{\sigma}^{\alpha}=(\boldsymbol{\sigma}^{\alpha})^{\mathsf{T}}. \tag{2.42}$$

The total stress as the sum of the partial stresses consequently must satisfy

$$\sum_{\alpha=1}^{N}\boldsymbol{\sigma}^{\alpha}=\sum_{\alpha=1}^{N}(\boldsymbol{\sigma}^{\alpha})^{\mathsf{T}}\;\Rightarrow\;\boldsymbol{\sigma}=\boldsymbol{\sigma}^{\mathsf{T}}. \tag{2.43}$$

Thus, the conservation of angular momentum proves that Cauchy's stress tensor is symmetric. Note that if the angular momentum exchange between the phases is assumed to be non-zero, the stress tensor would not be symmetric, requiring the introduction of additional rotational degrees of freedom.

2.4.4 Energy Balance

The law of conservation of energy, the first law of thermodynamics, requires that the rate of change of the internal and kinetic energies be balanced by the rate of mechanical work and heat. For phase α in a porous medium, this is written mathematically as

$$\frac{\mathrm{D}_\alpha E^\alpha}{\mathrm{D}t} + \frac{\mathrm{D}_\alpha K^\alpha}{\mathrm{D}t} + \sum_\beta E^{\beta\alpha} = W^\alpha + H^\alpha \tag{2.44}$$

where E^α is the internal energy, K^α is the kinetic energy, $E^{\beta\alpha}$ is the rate of internal energy exchange from all other phases β to phase α, W^α is the rate of mechanical energy or work and H^α is the rate of heat energy. For a given domain V, we have

$$\begin{aligned} E^\alpha &= \int_V \rho^\alpha e^\alpha \mathrm{d}V \\ K^\alpha &= \int_V \frac{1}{2}\rho^\alpha \boldsymbol{v}^\alpha \cdot \boldsymbol{v}^\alpha \mathrm{d}V \\ W^\alpha &= \int_V \boldsymbol{v}^\alpha \cdot \rho^\alpha \boldsymbol{b}^\alpha \mathrm{d}V + \int_{\partial V} \boldsymbol{v}^\alpha \cdot \boldsymbol{t}^\alpha \mathrm{d}A \\ H^\alpha &= \int_V \rho^\alpha h^\alpha \mathrm{d}V - \int_{\partial V} \boldsymbol{q}^\alpha \mathrm{d}A \end{aligned} \tag{2.45}$$

where $e^\alpha = e^\alpha(\boldsymbol{x}, t)$ is the specific internal energy $\alpha, h^\alpha = h^\alpha(\boldsymbol{x}, t)$ is the partial energy source and $\boldsymbol{q}^\alpha = \boldsymbol{q}^\alpha(\boldsymbol{x}, t)$ is the partial heat flux vector.

Using (2.45) in (2.44), simplifying the material time derivatives of the integrals and utilizing the mass and linear momentum balance equations in (2.23) and (2.31), the energy balance equation for phase α becomes

$$\begin{aligned} \rho^\alpha \frac{\mathrm{D}_\alpha e^\alpha}{\mathrm{D}t} - \sum_\beta M^{\beta\alpha}\left(e^\alpha - \frac{1}{2}\boldsymbol{v}^\alpha \cdot \boldsymbol{v}^\alpha\right) + \rho^\alpha \boldsymbol{v}^\alpha \cdot \boldsymbol{a}^\alpha - \boldsymbol{\sigma}^\alpha : \boldsymbol{L}^\alpha \\ -\boldsymbol{v}^\alpha \cdot (\nabla \cdot \boldsymbol{\sigma}^\alpha + \rho^\alpha \boldsymbol{b}^\alpha) + \nabla \cdot \boldsymbol{q}^\alpha + \sum_\beta E^{\beta\alpha} = Q^\alpha \end{aligned} \tag{2.46}$$

where $Q^\alpha = \rho^\alpha h^\alpha$ is the heat supply to phase α. The overall energy balance equation is obtained by summation of the individual energy balance equations of

the constituents of the porous medium i.e.

$$\sum_{\alpha=1}^{N}\left[\rho^{\alpha}\frac{\mathrm{D}_{\alpha}e^{\alpha}}{\mathrm{D}t}-\sum_{\beta}M^{\beta\alpha}\left(e^{\alpha}-\frac{1}{2}\boldsymbol{v}^{\alpha}\cdot\boldsymbol{v}^{\alpha}\right)+\rho^{\alpha}\boldsymbol{v}^{\alpha}\cdot\boldsymbol{a}^{\alpha}-\boldsymbol{\sigma}^{\alpha}:\boldsymbol{L}^{\alpha}\right.$$
$$\left.-\boldsymbol{v}^{\alpha}\cdot(\nabla\cdot\boldsymbol{\sigma}^{\alpha}+\rho^{\alpha}\boldsymbol{b}^{\alpha})+\nabla\cdot\boldsymbol{q}^{\alpha}+\sum_{\beta}E^{\beta\alpha}\right]=\sum_{\alpha=1}^{N}Q^{\alpha}. \tag{2.47}$$

If the momentum exchange between the phases is assumed to be zero, the energy balance equation reduces to

$$\sum_{\alpha=1}^{N}\left[\rho^{\alpha}\frac{\mathrm{D}_{\alpha}e^{\alpha}}{\mathrm{D}t}-\sum_{\beta}M^{\beta\alpha}\left(e^{\alpha}-\frac{1}{2}\boldsymbol{v}^{\alpha}\cdot\boldsymbol{v}^{\alpha}\right)-\boldsymbol{\sigma}^{\alpha}:\boldsymbol{L}^{\alpha}\right.$$
$$\left.+\nabla\cdot\boldsymbol{q}^{\alpha}+\sum_{\beta}E^{\beta\alpha}\right]=\sum_{\alpha=1}^{N}Q^{\alpha}. \tag{2.48}$$

The total heat supply and total heat flux can be expressed as

$$Q=\sum_{\alpha=1}^{N}Q^{\alpha}\quad\text{and}\quad\boldsymbol{q}=\sum_{\alpha=1}^{N}\boldsymbol{q}^{\alpha} \tag{2.49}$$

and a constraint on the energy exchange between the phases is introduced as

$$\sum_{\alpha=1}^{N}\sum_{\beta}E^{\beta\alpha}=0. \tag{2.50}$$

This reduces the energy balance equation to

$$\sum_{\alpha=1}^{N}\left[\rho^{\alpha}\frac{\mathrm{D}_{\alpha}e^{\alpha}}{\mathrm{D}t}-\sum_{\beta}M^{\beta\alpha}\left(e^{\alpha}-\frac{1}{2}\boldsymbol{v}^{\alpha}\cdot\boldsymbol{v}^{\alpha}\right)-\boldsymbol{\sigma}^{\alpha}:\boldsymbol{L}^{\alpha}\right]+\nabla\cdot\boldsymbol{q}=Q. \tag{2.51}$$

2.5 Thermodynamics and Phase Change

The second law of thermodynamics (entropy inequality) is used to state the restrictions on constitutive equations. It follows from the conservation of energy (first law of thermodynamics) with the introduction of the absolute temperature.

2.5.1 Entropy Inequality

The assumption of entropy inequality for each phase α is a sufficient but restrictive condition. For the existence of dissipation mechanisms within the porous medium, an entropy inequality for all the constituents is both a necessary and sufficient condition, de Boer (2006).

For phase α, let

$$S^\alpha = \int_V \rho^\alpha s^\alpha \mathrm{d}V \tag{2.52}$$

be its entropy where s^α is the specific entropy. With T^α as the absolute temperature of phase α, the entropy inequality for all the constituents of the porous medium is expressed as

$$\sum_{\alpha=1}^{N} \frac{\mathrm{D}_\alpha S^\alpha}{\mathrm{D}t} \geq \sum_{\alpha=1}^{N} \int_V \frac{1}{T^\alpha} \rho^\alpha h^\alpha \mathrm{d}V - \sum_{\alpha=1}^{N} \int_{\partial V} \frac{1}{T^\alpha} \boldsymbol{q}^\alpha \cdot \mathrm{d}A. \tag{2.53}$$

Performing the material time derivative in the above equation using the transport theorem, utilizing the mass balance equation and the divergence theorem, the local form of the entropy inequality becomes

$$\sum_{\alpha=1}^{N} \left[\rho^\alpha \frac{\mathrm{D}_\alpha s^\alpha}{\mathrm{D}t} - \sum_\beta M^{\beta\alpha} s^\alpha - \frac{1}{T^\alpha} \rho^\alpha h^\alpha + \nabla \cdot \left(\frac{1}{T^\alpha} \boldsymbol{q}^\alpha \right) \right] \geq 0. \tag{2.54}$$

The entropy inequality may also be written as a function of the Helmholtz free energy

$$\psi^\alpha = e^\alpha - T^\alpha s^\alpha \tag{2.55}$$

together with the energy balance in (2.48). The inequality in (2.54) considers a general case where the constituents have a different absolute temperature T^α. It may be simplified for the case when all the constituents have the same absolute temperature $T = T^\alpha$.

2.5.2 Phase Transitions

The physical processes in a porous medium sometimes involve the transition of one phase into another such as phase change from liquid to vapor, liquid to solid or solid to liquid. These types of phase changes are referred to as first-order transitions, see de Boer and Bluhm (1999), whereas other transitions such as from a super fluid to ordinary fluid (e.g. helium) are called second-order transitions. The discussion here focuses on first-order transitions. We take a closer look here at the effect of phase transitions in a porous medium.

The balance equations in Section 2.4 are presented in a general form such that the effect of phase transition(s) on the conserved quantities can be considered. Consider a two-phase porous medium where phase transition from one phase to another occurs, e.g. freezing/melting. The exchange of quantities during phase change remains constrained. For instance, the mass balance equations for the individual constituents, according to (2.23), are given by

$$\begin{aligned} \frac{\mathrm{D}_\alpha \rho^\alpha}{\mathrm{D}t} + \rho^\alpha \nabla \cdot \boldsymbol{v}^\alpha + M^{\beta\alpha} = 0 \\ \frac{\mathrm{D}_\beta \rho^\beta}{\mathrm{D}t} + \rho^\beta \nabla \cdot \boldsymbol{v}^\beta + M^{\alpha\beta} = 0 \end{aligned} \tag{2.56}$$

wherein the sum on the mass exchange term is omitted since we have only one phase contributing to the mass of another. The constraint in (2.25) implies

$$M^{\alpha\beta} + M^{\beta\alpha} = 0. \tag{2.57}$$

Phase transitions in porous media have been studied in the past with several simplifying assumptions. The need for a rigorous mathematical and thermodynamical treatment of such problems was clear. Phase change from liquid to gas was given a detailed thermodynamic treatment, for example, by de Boer and Kowalski (1995) and de Boer (1995), showing that the phase transition is governed by the difference of the chemical potentials of the constituents. A review of various phase change phenomena in porous media such as freezing/melting, boiling, drying/evaporation and condensation was presented by Yortsos and Stubos (2001). A detailed thermodynamic approach to various phase change problems can be found in Frémond (2012).

The thermodynamic equilibrium between the phases during phase change is described by the Clausius-Clapeyron equation. This equation can be derived based on the equilibrium requirement between the chemical potentials of the two phases; see Loch (1978) for the specific case of freezing and melting. For two phases α and β undergoing phase transition, their chemical potentials are required to be in equilibrium, i.e.

$$\mu^{\alpha} = \mu^{\beta}. \tag{2.58}$$

The chemical potentials are a function of the specific entropies, the specific volumes, the pressures and the temperatures of the phases. In terms of these quantities, we have

$$-(s^{\alpha} - s^{\beta})\mathrm{d}T + v^{\alpha}\mathrm{d}p^{\alpha} - v^{\beta}\mathrm{d}p^{\beta} = 0 \tag{2.59}$$

where s^{α} and s^{β} are the specific entropies of the phases, v^{α} and v^{β} their specific volumes, p^{α} and p^{β} the pressures and T is the temperature, assuming the same temperature for both phases. The equation above may be rearranged to give

$$\mathrm{d}p^{\beta} = \frac{v^{\alpha}}{v^{\beta}}\mathrm{d}p^{\alpha} - \frac{1}{v^{\beta}}(s^{\alpha} - s^{\beta})\mathrm{d}T. \tag{2.60}$$

In terms of the densities $\rho^{\alpha} = 1/v^{\alpha}$ and $\rho^{\beta} = 1/v^{\beta}$, we have

$$\mathrm{d}p^{\beta} = \frac{\rho^{\beta}}{\rho^{\alpha}}\mathrm{d}p^{\alpha} - \rho^{\beta}(s^{\alpha} - s^{\beta})\mathrm{d}T. \tag{2.61}$$

The change in entropy between the phases under constant pressure and temperature may be expressed as

$$s^{\alpha} - s^{\beta} = \frac{L}{T} \tag{2.62}$$

where L is the specific latent heat which depends on the type of phase change that occurs e.g. latent heat of fusion for melting. Using this in (2.61) gives

$$\mathrm{d}p^{\beta} = \frac{\rho^{\beta}}{\rho^{\alpha}}\mathrm{d}p^{\alpha} - \frac{\rho^{\beta}L}{T}\mathrm{d}T. \tag{2.63}$$

2.6 Conduction Laws

The equations governing the flow of fluid and heat in a porous medium are given by Darcy's law and Fourier's law, respectively. We refer to these laws here as conduction laws, as used in Coussy (2004).

2.6.1 Darcy's Law

The specific discharge of fluid in a porous medium was shown to be proportional to the head loss based on experiments by Henry Darcy in 1857, Verruijt (2013). Darcy's law may be derived for fully saturated porous media from the fluid momentum balance equation, see for instance Whitaker (1986).

Darcy's law relates the flow of fluid in a porous medium with respect to the solid phase as

$$\boldsymbol{w} = n^{\mathrm{f}}(\boldsymbol{v}^{\mathrm{f}} - \boldsymbol{v}^{\mathrm{s}}) \tag{2.64}$$

where n^{f} is the volume fraction of the fluid, $\boldsymbol{v}^{\mathrm{f}}$ is the fluid velocity and $\boldsymbol{v}^{\mathrm{s}}$ is the solid velocity. A more general form of Darcy's law, considering the relative permeability of a phase in a medium where the permeability varies, is given by

$$\boldsymbol{w} = \frac{k_{\mathrm{r}}}{\mu}\boldsymbol{\kappa} \cdot (\nabla p^{\mathrm{f}} - \rho_{\mathrm{f}}\boldsymbol{b} - \rho_{\mathrm{f}}\boldsymbol{a}^{\mathrm{s}} - \rho_{\mathrm{f}}\boldsymbol{a}^{\mathrm{fs}}) \tag{2.65}$$

where k_{r} is the relative permeability coefficient varying between 0 and 1, μ is the viscosity of the fluid, $\boldsymbol{\kappa}$ is the intrinsic permeability matrix of the material, p^{f} is the fluid pressure, $\boldsymbol{b}$ represents body forces, $\boldsymbol{a}^{s}$ is the acceleration of the solid phase and $\boldsymbol{a}^{\mathrm{fs}}$ is the relative acceleration between the fluid and solid phases. The tortuosity of the pores is sometimes considered in the Darcy equation. If the inertia terms are neglected, Darcy's law reduces to

$$\boldsymbol{w} = \frac{k_{\mathrm{r}}}{\mu}\boldsymbol{\kappa} \cdot (\nabla p^{\mathrm{f}} - \rho_{\mathrm{f}}\boldsymbol{b}). \tag{2.66}$$

It is common to express Darcy's law in terms of the hydraulic conductivity matrix $\boldsymbol{k}$ instead of the intrinsic permeability matrix $\boldsymbol{\kappa}$, where the two are related by

$$\boldsymbol{k} = \frac{\rho_{\mathrm{f}} g}{\mu}\boldsymbol{\kappa} \tag{2.67}$$

in which g is the acceleration due to gravity. This results in

$$\boldsymbol{w} = \frac{k_{\mathrm{r}}}{\rho_{\mathrm{f}} g}\boldsymbol{k} \cdot (\nabla p^{\mathrm{f}} - \rho_{\mathrm{f}}\boldsymbol{b}) \tag{2.68}$$

wherein we have kept the same relative coefficient k_{r} for hydraulic conductivity that varies with the porosity and degree of fluid saturation of the porous medium.

2.6.2 Fourier's Law

Thermal conduction in a porous medium is expressed using Fourier's law which states that the rate of heat flow is proportional to the negative gradient of the

temperature. Fourier's law for the heat flux $\boldsymbol{q}$ is given by

$$\boldsymbol{q} = -\boldsymbol{\lambda}\nabla T \tag{2.69}$$

where $\boldsymbol{\lambda}$ is the effective thermal conductivity matrix of the porous medium and T is the temperature. For isotropic thermal conductivity in a medium, the above equation becomes

$$\boldsymbol{q} = -\lambda\nabla T \tag{2.70}$$

where λ is the effective thermal conductivity coefficient which is a function of the individual thermal conductivities of the constituents of the porous medium and their volume fractions. Fourier's law has a similar form both at the microscopic and macroscopic levels, Coussy (2004).

2.7 Constitutive Laws

The balance equations presented in Section 2.4 are valid for any porous medium. To complete these balance equations for a specific material, a constitutive model needs to be introduced, de Souza Neto et al. (2011). We first introduce the effective stress concept before discussing the constitutive equations required to complete the description.

2.7.1 The Effective Stress Concept

The effective stress concept is widely used in porous media applications, especially in soil mechanics. The historical development of this concept is documented in de Boer and Ehlers (1990). The concept was already conceived and studied by scientists by the end of the 19th century. A significant development with a mathematical background came later in early 20th century from the significant contributions of Paul Fillunger and especially Karl von Terzaghi; see Skempton (1960).

The main idea behind effective stress in a porous medium is separating the stress that effectively causes solid deformation, hence the name, from all other stresses in the mixture. If we consider a porous medium composed of two phases, solid (s) and fluid (f), the total stress as the sum of the partial stresses is given according to $(2.33)_1$ by

$$\boldsymbol{\sigma} = \boldsymbol{\sigma}^{\mathrm{s}} + \boldsymbol{\sigma}^{\mathrm{f}}. \tag{2.71}$$

The partial stresses corresponding to the fluid phase, using the volume fraction concept, can be written us

$$\boldsymbol{\sigma}^{\mathrm{f}} = n^{\mathrm{f}}\boldsymbol{\sigma}_{\mathrm{f}} \tag{2.72}$$

where n^{f} is the volume fraction of the fluid and $\boldsymbol{\sigma}_{\mathrm{f}}$ is the pore fluid stress. However, a distinction should be made between the partial stress of the solid phase $\boldsymbol{\sigma}^{\mathrm{s}}$ and the effective stress $\boldsymbol{\sigma}'$; this has been discussed, for example, by Prévost (1980). The partial stress of the solid phase is given by

$$\boldsymbol{\sigma}^{\mathrm{s}} = \boldsymbol{\sigma}' + n^{\mathrm{s}}\boldsymbol{\sigma}_{\mathrm{f}} \tag{2.73}$$

where $n^{\mathrm{s}}\boldsymbol{\sigma}_{\mathrm{f}}$ takes into account the effect of the pore fluid stress on the individual solid grains of the porous medium. It is assumed, in the above equation, that

the contact areas between the solid grains are negligible such that the pore fluid surrounds each grain. Each solid grain is subjected to intergranular forces that are in excess of the pore fluid stress and this is characterized by the effective stress $\boldsymbol{\sigma}'$. The total stress for a fluid-saturated porous medium is then given by

$$\boldsymbol{\sigma} = \boldsymbol{\sigma}^{\mathrm{s}} + \boldsymbol{\sigma}^{\mathrm{f}} = \boldsymbol{\sigma}' + \boldsymbol{\sigma}_{\mathrm{f}}. \tag{2.74}$$

2.7.2 Stress-Strain Relations

A constitutive equation for the solid phase relates the effective stress and the strain. The constitutive stress-strain relation in a general form may be expressed as

$$\mathrm{d}\boldsymbol{\sigma}' = \boldsymbol{D}(\mathrm{d}\boldsymbol{\varepsilon} - \mathrm{d}\boldsymbol{\varepsilon}^{\mathrm{c}} - \mathrm{d}\boldsymbol{\varepsilon}^{\mathrm{s}}_{\mathrm{v}} - \mathrm{d}\boldsymbol{\varepsilon}^{\mathrm{o}}) \tag{2.75}$$

where $\boldsymbol{D} = \boldsymbol{D}(\boldsymbol{\sigma}', \boldsymbol{\varepsilon}, \dot{\boldsymbol{\varepsilon}})$ is the constitutive tangent tensor, $\mathrm{d}\boldsymbol{\varepsilon}$ is the total strain increment, $\mathrm{d}\boldsymbol{\varepsilon}^{\mathrm{c}}$ is the creep strain increment, $\mathrm{d}\boldsymbol{\varepsilon}^{\mathrm{s}}_{\mathrm{v}}$ is the volumetric strain increment and $\mathrm{d}\boldsymbol{\varepsilon}^{\mathrm{o}}$ considers all other strain increments not directly associated with the effective stress. Let p represent the average fluid pressure from all the fluid phases in the porous medium. This pressure induces a hydrostatic stress distribution in the solid phase, thus causing a purely volumetric strain given in incremental form by

$$\mathrm{d}\boldsymbol{\varepsilon}^{\mathrm{s}}_{\mathrm{v}} = -\boldsymbol{I}\frac{\mathrm{d}p}{3K_{\mathrm{s}}} \tag{2.76}$$

where K_{s} is the bulk modulus of the solid skeleton. The effective stress relation in (2.74) is usually modified by a corrective parameter known as Biot's coefficient, α, Lewis and Schrefler (1998). The modified effective stress equation (keeping the same notation for the modified effective stress) reads

$$\boldsymbol{\sigma} = \boldsymbol{\sigma}' + \alpha p \boldsymbol{I} \tag{2.77}$$

where $\boldsymbol{I}$ is the identity tensor. It can be shown that Biot's coefficient takes the value

$$\alpha = 1 - \frac{K_{\mathrm{o}}}{K_{\mathrm{s}}} \tag{2.78}$$

where K_{o} is the overall bulk modulus of the porous medium. We can now simply write

$$\mathrm{d}\boldsymbol{\sigma}' = \boldsymbol{D}(\mathrm{d}\boldsymbol{\varepsilon} - \mathrm{d}\boldsymbol{\varepsilon}^{\mathrm{c}} - \mathrm{d}\boldsymbol{\varepsilon}^{\mathrm{o}}). \tag{2.79}$$

The constitutive tangent tensor takes various forms depending on the type of stress-strain relation employed. Some examples of constitutive laws include linear elasticity, thermoelasticity, elastoplasticity and viscoplasticity. In this thesis, we focus on linearly elastic and thermoelastic constitutive laws.

The tangent stiffness for linear elasticity (for stresses and strains in Voigt notation) is given by

$$\boldsymbol{D} = \frac{E}{(1+\nu)(1-2\nu)}\begin{bmatrix} \boldsymbol{D}_{11} & \boldsymbol{0} \\ \boldsymbol{0} & \boldsymbol{D}_{22} \end{bmatrix} \tag{2.80}$$

where

$$\begin{aligned} \boldsymbol{D}_{11} &= (1-2\nu)\boldsymbol{I} + \nu \boldsymbol{1}, \\ \boldsymbol{D}_{22} &= \frac{1-2\nu}{2}\boldsymbol{I}, \end{aligned} \tag{2.81}$$

$\boldsymbol{1}$ is a matrix of ones, E is the Young's modulus of the soil and ν is the Poisson's ratio. For thermoelastic material models, these parameters are usually defined as a function of temperature and/or other temperature dependent parameters.

2.7.3 Compressibility of Phases

For compressible phases in a porous medium, the density of a phase may be a function of pressure, temperature and other factors. We look at the equations of state for water, the most common fluid in a porous medium, and solid skeleton. See Lewis and Schrefler (1998).

The equation of state for water is given by

$$\rho_{\mathrm{w}} = \rho_{\mathrm{wo}} \exp\left[-\alpha_{\mathrm{w}} T + \frac{1}{K_{\mathrm{w}}}(p^{\mathrm{w}} - p_{\mathrm{o}}^{\mathrm{w}})\right] \tag{2.82}$$

where ρ_{w} and ρ_{wo} are the current and initial densities, α_{w} is the thermal expansion coefficient, K_{w} is the bulk modulus and p^{w} and $p_{\mathrm{o}}^{\mathrm{w}}$ are the current and initial pore water pressures. Performing Taylor series expansion of (2.82) and retaining first order terms gives

$$\rho_{\mathrm{w}} = \rho_{\mathrm{wo}} \left[1 - \alpha_{\mathrm{w}} T + \frac{1}{K_{\mathrm{w}}}(p^{\mathrm{w}} - p_{\mathrm{o}}^{\mathrm{w}})\right] \tag{2.83}$$

which can then be used to derive

$$\frac{1}{\rho_{\mathrm{wo}}}\frac{\mathrm{D}_{\mathrm{w}}\rho_{\mathrm{w}}}{\mathrm{D}t} = \frac{1}{K_{\mathrm{w}}}\frac{\mathrm{D}_{\mathrm{w}}p^{\mathrm{w}}}{\mathrm{D}t} - \alpha_{\mathrm{w}}\frac{\mathrm{D}_{\mathrm{w}}T}{\mathrm{D}t}. \tag{2.84}$$

For a compressible solid phase, the material time derivative of the density may be derived from the mass balance of the solid:

$$\frac{\mathrm{D}_{\mathrm{s}}(\rho^{\mathrm{s}} V^{\mathrm{s}})}{\mathrm{D}t} = 0. \tag{2.85}$$

The solid density is a function of the average pressure on the solid from all other phases p^s, the temperature T and the first invariant of the effective stress tr $\boldsymbol{\sigma}'$. The variation of the solid density may then be written as

$$\frac{1}{\rho_{\mathrm{s}}}\frac{\mathrm{D}_{\mathrm{s}}\rho_{\mathrm{s}}}{\mathrm{D}t} = \frac{1}{K_{\mathrm{s}}}\frac{\mathrm{D}_{\mathrm{s}}p^{\mathrm{s}}}{\mathrm{D}t} - \alpha_{\mathrm{s}}\frac{\mathrm{D}_{\mathrm{s}}T}{\mathrm{D}t} - \frac{1}{3(n-1)K_{\mathrm{s}}}\frac{\mathrm{D}_{\mathrm{s}}(\mathrm{tr}\ \boldsymbol{\sigma}')}{\mathrm{D}t} \tag{2.86}$$

where α_{s} is the thermal expansion coefficient of the solid. The first term on the right hand side of the equation above represents the volumetric strain of the solid. This strain may be negligible for soils but significant for materials such as rock. Introducing a constitutive equation for the first invariant of the effective stress and

using Biot's coefficient from (2.78), an alternative form of the solid compressibility may be written as

$$\frac{1}{\rho_{\mathrm{s}}}\frac{\mathrm{D}_{\mathrm{s}}\rho_{\mathrm{s}}}{\mathrm{D}t} = \frac{1}{1-n}\left[\frac{\alpha-n}{K_{\mathrm{s}}}\frac{\mathrm{D}_{\mathrm{s}}p^{\mathrm{s}}}{\mathrm{D}t} - \alpha_{\mathrm{s}}(\alpha-n)\frac{\mathrm{D}_{\mathrm{s}}T}{\mathrm{D}t} - (1-\alpha)\nabla\cdot\boldsymbol{v}^{\mathrm{s}}\right]. \tag{2.87}$$

2.8 Coupled Problems

Different types of physical processes may occur in a porous medium depending on the type of the material and its application. Typical examples include hydraulic, mechanical, thermal and chemical processes. Two or more physical processes often occur in a porous medium leading to what we refer to as coupled processes. We focus on hydraulic, hydro-mechanical and thermo-hydro-mechanical phenomena in soils.

In the following sections, we discuss how the general conservation laws are used to derive the governing equations for the specific processes under consideration. To illustrate this, we assume a fluid-saturated biphasic porous medium with solid (s) and fluid (f) phases. Based on the volume fraction concept and (2.5), the partial densities for the solid and fluid phases, ρ^{s} and ρ^{f}, are given by

$$\rho^{\mathrm{s}} = n^{\mathrm{s}}\rho_{\mathrm{s}} \quad \text{and} \quad \rho^{\mathrm{f}} = n^{\mathrm{f}}\rho_{\mathrm{f}} \tag{2.88}$$

where n^{s} and n^{f} are the volume fractions of the solid and fluid, respectively, and ρ_{s} and ρ_{f} are their real densities at the microscopic level. For a fluid-saturated porous medium, we have

$$n^{\mathrm{s}} + n^{\mathrm{f}} = 1. \tag{2.89}$$

For simplicity in the following sections, we set $n^{\mathrm{f}} = n$ and $n^{\mathrm{s}} = 1-n$. We will refer to n as the porosity of the material.

2.8.1 Hydraulic Processes (p or p-v Formulation)

Hydraulic processes in a porous medium are mainly described by the law of conservation of mass. The mass balance equation for the fluid phase according to (2.23) is

$$\frac{\mathrm{D}_{\mathrm{f}}\rho^{\mathrm{f}}}{\mathrm{D}t} + \rho^{\mathrm{f}}\nabla\cdot\boldsymbol{v}^{\mathrm{f}} = 0 \tag{2.90}$$

in which we have ignored any mass exchange between the solid and fluid phases. Considering the flow of the fluid with respect to the solid phase, we write the material time derivative of ρ^{f} according to (2.13) as

$$\frac{\mathrm{D}_{\mathrm{s}}\rho^{\mathrm{f}}}{\mathrm{D}t} - \nabla\rho^{\mathrm{f}}\cdot\boldsymbol{v}^{\mathrm{sf}} + \rho^{\mathrm{f}}\nabla\cdot\boldsymbol{v}^{\mathrm{f}} = 0 \tag{2.91}$$

which, according to (2.12), becomes

$$\frac{\partial\rho^{\mathrm{f}}}{\partial t} + \nabla\rho^{\mathrm{f}}\cdot\boldsymbol{v}^{\mathrm{f}} + \rho^{\mathrm{f}}\nabla\cdot\boldsymbol{v}^{\mathrm{f}} = 0. \tag{2.92}$$

wherein we have used $\boldsymbol{v}^{\mathrm{sf}} = \boldsymbol{v}^{\mathrm{s}} - \boldsymbol{v}^{\mathrm{f}}$. From $(2.88)_2$, we have

$$\frac{\partial \rho^{\mathrm{f}}}{\partial t} = \frac{\partial (n\rho_{\mathrm{f}})}{\partial t} = \frac{\partial n}{\partial t}\rho_{\mathrm{f}} + n\frac{\partial \rho_{\mathrm{f}}}{\partial t}. \tag{2.93}$$

The porosity remains constant if there are no mechanical deformations i.e. $\frac{\partial n}{\partial t} = 0$. With this, and neglecting any spatial variations in the fluid density (i.e. $\nabla \rho^{\mathrm{f}} = 0$), (2.92) reduces to

$$\frac{\partial \rho_{\mathrm{f}}}{\partial t} + \rho_{\mathrm{f}} \nabla \cdot \boldsymbol{v}^{\mathrm{f}} = 0. \tag{2.94}$$

If the fluid is assumed to be incompressible, (2.94) further reduces to

$$\nabla \cdot \boldsymbol{v}^{\mathrm{f}} = 0. \tag{2.95}$$

The fluid velocity according to Darcy's law in this case is $\boldsymbol{w} = n(\boldsymbol{v}^{\mathrm{f}} - \boldsymbol{v}^{\mathrm{s}}) = n\boldsymbol{v}^{\mathrm{f}}$, with no mechanical deformations ($\boldsymbol{v}^{\mathrm{s}} = \boldsymbol{0}$). Using (2.67) and (2.68), the fluid mass balance equation for a constant hydraulic conductivity ($k_{\mathrm{r}} = 1$) can be written as

$$\nabla \cdot \left[-\frac{1}{\gamma_{\mathrm{f}}} \boldsymbol{k} \cdot (\nabla p^{\mathrm{f}} - \rho_{\mathrm{f}} \boldsymbol{b}) \right] = 0 \tag{2.96}$$

where γ_{f} is the unit weight of the fluid. The only flow driving forces considered here are the fluid pressure p^{f} and the body forces $\boldsymbol{b}$. The equation above governs the steady-state flow of fluid in a porous medium and may be solved for the pressure as the unknown, resulting in the so called p-formulation.

For a compressible fluid, the temporal variation of the fluid density needs to be taken into account. For instance, if our fluid is water, from the equation of state for water in (2.84) we may write

$$\frac{\partial \rho_{\mathrm{f}}}{\partial t} = \frac{\rho_{\mathrm{f}}}{K_{\mathrm{f}}} \frac{\partial p^{\mathrm{f}}}{\partial t} \tag{2.97}$$

where K_{f} is the bulk modulus of the fluid and isothermal conditions are assumed. Using (2.97) in (2.94), we get

$$\frac{n}{K_{\mathrm{f}}} \frac{\partial p^{\mathrm{f}}}{\partial t} + \nabla \cdot \boldsymbol{w} = 0 \tag{2.98}$$

wherein we have used $\boldsymbol{w} = n\boldsymbol{v}^{\mathrm{f}}$. Sometimes, the above equation is solved together with Darcy's law for the pressure p^{f} and Darcy's velocity $\boldsymbol{w}$ as the unknowns. The equations to be solved simultaneously in this case are

$$\begin{aligned} \frac{n}{K_{\mathrm{f}}} \frac{\partial p^{\mathrm{f}}}{\partial t} + \nabla \cdot \boldsymbol{w} &= 0 \\ \boldsymbol{w} + \frac{1}{\gamma_{\mathrm{f}}} \boldsymbol{k} \cdot (\nabla p^{\mathrm{f}} - \rho_{\mathrm{f}} \boldsymbol{b}) &= 0 \end{aligned} \tag{2.99}$$

which results in the so called p-v formulation.

2.8.2 Hydro-Mechanical Processes (u-p Formulation)

Hydro-mechanical processes couple the flow of fluid in a porous medium with solid deformation. The governing equations describing the coupling are derived by superposition of the individual linear momentum and mass balance equations of the solid and fluid phases.

From (2.92) and (2.93), with no spatial variations in fluid density, the mass balance equation for the fluid phase is given by

$$\rho_{\mathrm{f}} \frac{\partial n}{\partial t} + n \frac{\partial \rho_{\mathrm{f}}}{\partial t} + n \rho_{\mathrm{f}} \nabla \cdot \boldsymbol{v}^{\mathrm{f}} = 0. \tag{2.100}$$

The mass balance equation for the solid phase, based on (2.23), is given by

$$\frac{\mathrm{D}_{\mathrm{s}} \rho^{\mathrm{s}}}{\mathrm{D}t} + \rho^{\mathrm{s}} \nabla \cdot \boldsymbol{v}^{\mathrm{s}} = 0. \tag{2.101}$$

From $(2.88)_1$ we have $\rho^{\mathrm{s}} = (1-n)\rho_{\mathrm{s}}$. Using this in the above equation, and neglecting spatial variations in the porosity and the solid density, gives

$$-\rho_{\mathrm{s}} \frac{\partial n}{\partial t} + (1-n) \frac{\partial \rho_{\mathrm{s}}}{\partial t} + (1-n) \rho_{\mathrm{s}} \nabla \cdot \boldsymbol{v}^{\mathrm{s}} = 0. \tag{2.102}$$

Dividing (2.100) by ρ_{f} and (2.102) by ρ_{s} and adding the two equations gives the overall mass balance equation for the fluid-saturated porous medium as

$$\frac{(1-n)}{\rho_{\mathrm{s}}} \frac{\partial \rho_{\mathrm{s}}}{\partial t} + (1-n) \nabla \cdot \boldsymbol{v}^{\mathrm{s}} + \frac{n}{\rho_{\mathrm{f}}} \frac{\partial \rho_{\mathrm{f}}}{\partial t} + n \nabla \cdot \boldsymbol{v}^{\mathrm{f}} = 0. \tag{2.103}$$

Rearranging the above equation gives

$$\nabla \cdot \boldsymbol{v}^{\mathrm{s}} + \frac{(1-n)}{\rho_{\mathrm{s}}} \frac{\partial \rho_{\mathrm{s}}}{\partial t} + \frac{n}{\rho_{\mathrm{f}}} \frac{\partial \rho_{\mathrm{f}}}{\partial t} + \nabla \cdot \boldsymbol{w} = 0 \tag{2.104}$$

where $\boldsymbol{w} = n(\boldsymbol{v}^{\mathrm{f}} - \boldsymbol{v}^{\mathrm{s}})$ is Darcy's velocity. Assuming isothermal conditions and water as the fluid, the compressibility of the fluid is given by (2.97) and from (2.87) we get for the solid phase

$$\frac{1-n}{\rho_{\mathrm{s}}} \frac{\partial \rho_{\mathrm{s}}}{\partial t} = \frac{\alpha - n}{K_{\mathrm{s}}} \frac{\partial p^{\mathrm{f}}}{\partial t} - (1-\alpha) \nabla \cdot \boldsymbol{v}^{\mathrm{s}} \tag{2.105}$$

where for a single fluid phase we have set $p^{\mathrm{s}} = p^{\mathrm{f}}$. Equation (2.104), based on (2.97) and (2.105), can be rewritten as

$$\alpha \nabla \cdot \boldsymbol{v}^{\mathrm{s}} + \left(\frac{\alpha - n}{K_{\mathrm{s}}} + \frac{n}{K_{\mathrm{f}}} \right) \frac{\partial p^{\mathrm{f}}}{\partial t} + \nabla \cdot \boldsymbol{w} = 0. \tag{2.106}$$

For incompressible solid and fluid phases ($1/K_{\mathrm{s}} = 1/K_{\mathrm{f}} = 0$ and $\alpha = 1$), the mass balance equation reduces to

$$\nabla \cdot \boldsymbol{v}^{\mathrm{s}} + \nabla \cdot \boldsymbol{w} = 0. \tag{2.107}$$

The linear momentum balance equations for the solid and fluid phases, according to (2.31), assuming a static condition and no momentum exchange between the phases, are given by

$$\begin{aligned} \nabla \cdot \boldsymbol{\sigma}^{\mathrm{s}} + \rho^{\mathrm{s}} \boldsymbol{b}^{\mathrm{s}} &= \mathbf{0} \\ \nabla \cdot \boldsymbol{\sigma}^{\mathrm{f}} + \rho^{\mathrm{f}} \boldsymbol{b}^{\mathrm{f}} &= \mathbf{0}. \end{aligned} \tag{2.108}$$

Summation of the two equations above and use of $(2.33)_2$, (2.71) and (2.77), gives the momentum balance equation for the whole medium as

$$\nabla \cdot (\boldsymbol{\sigma}' + \alpha p^{\mathrm{f}} \boldsymbol{I}) + \rho \boldsymbol{b} = \mathbf{0} \tag{2.109}$$

wherein the total density of the porous medium is

$$\rho = \rho^{\mathrm{s}} + \rho^{\mathrm{f}} = (1-n)\rho_{\mathrm{s}} + n\rho_{\mathrm{f}}. \tag{2.110}$$

For coupled hydro-mechanical (HM) processes in a porous medium, the mass balance equation in (2.106) and the linear momentum balance equation in (2.109) can be solved simultaneously for the displacement and pressure field variables. This results in what is known as a u-p formulation. Sometimes these equations are solved simultaneously with Darcy's equation to obtain the displacement, pressure and Darcy's velocity, leading to the so-called u-p-v formulation.

2.8.3 Thermo-Hydro-Mechanical Processes (u-p-T Formulation)

Thermo-hydro-mechanical (THM) processes in a porous medium couple heat transfer and fluid flow with the deformation of solid. The governing equations describing the coupling are derived by superposition of the individual linear momentum, mass and energy balance equations of constituent phases.

We consider a fluid-saturated porous medium again. The linear momentum balance equation in this case is the same as in (2.109). The overall mass balance equation is derived from (2.104) by considering non-isothermal conditions for the compressibilities of the solid and fluid phases. Based on (2.84) and (2.87), we get

$$\begin{aligned} \frac{1-n}{\rho_{\mathrm{s}}} \frac{\partial \rho_{\mathrm{s}}}{\partial t} &= \frac{\alpha - n}{K_{\mathrm{s}}} \frac{\partial p^{\mathrm{f}}}{\partial t} - (\alpha - n)\alpha_{\mathrm{s}} \frac{\partial T}{\partial t} - (1-\alpha)\nabla \cdot \boldsymbol{v}^{\mathrm{s}} \\ \frac{n}{\rho_{\mathrm{f}}} \frac{\partial \rho_{\mathrm{f}}}{\partial t} &= \frac{n}{K_{\mathrm{f}}} \frac{\partial p^{\mathrm{f}}}{\partial t} - n\alpha_{\mathrm{w}} \frac{\partial T}{\partial t}. \end{aligned} \tag{2.111}$$

Using (2.111) in (2.104) and simplifying gives the overall mass balance equation for a fluid-saturated porous medium subjected to THM coupled processes as

$$\alpha \nabla \cdot \boldsymbol{v}^{\mathrm{s}} + \left(\frac{\alpha - n}{K_{\mathrm{s}}} + \frac{n}{K_{\mathrm{f}}} \right) \frac{\partial p^{\mathrm{f}}}{\partial t} - \alpha_{\mathrm{o}} \frac{\partial T}{\partial t} + \nabla \cdot \boldsymbol{w} = 0 \tag{2.112}$$

where $\alpha_{\mathrm{o}} = n\alpha_{\mathrm{w}} + (\alpha - n)\alpha_{\mathrm{s}}$ is the overall thermal expansion coefficient of the porous medium.

The energy balance equation for a single phase, neglecting any mass, momentum and energy exchanges between the solid and fluid phases, is obtained from (2.46) as

$$\rho^{\alpha}\frac{\mathrm{D}_{\alpha}e^{\alpha}}{\mathrm{D}t} - \boldsymbol{\sigma}^{\alpha} : \boldsymbol{L}^{\alpha} + \nabla \cdot \boldsymbol{q}^{\alpha} = Q^{\alpha} \tag{2.113}$$

The individual energy balance equations for the solid and fluid phases are then written as

$$\begin{aligned} \rho^{\mathrm{s}}\frac{\mathrm{D}_{\mathrm{s}}e^{\mathrm{s}}}{\mathrm{D}t} - \boldsymbol{\sigma}^{\mathrm{s}} : \boldsymbol{L}^{\mathrm{s}} + \nabla \cdot \boldsymbol{q}^{\mathrm{s}} &= Q^{\mathrm{s}} \\ \rho^{\mathrm{f}}\frac{\mathrm{D}_{\mathrm{f}}e^{\mathrm{f}}}{\mathrm{D}t} - \boldsymbol{\sigma}^{\mathrm{f}} : \boldsymbol{L}^{\mathrm{f}} + \nabla \cdot \boldsymbol{q}^{\mathrm{f}} &= Q^{\mathrm{f}}. \end{aligned} \tag{2.114}$$

Viscous dissipation may be significant in applications where the material flows at high rates e.g. due to injection or molding in polymer processing. For the applications of interest in this thesis, it may be neglected. With this assumption and taking all material time derivatives with respect to the solid phase, using (2.13), the individual balance equations become

$$\begin{aligned} \rho^{\mathrm{s}}\frac{\mathrm{D}_{\mathrm{s}}e^{\mathrm{s}}}{\mathrm{D}t} + \nabla \cdot \boldsymbol{q}^{\mathrm{s}} &= Q^{\mathrm{s}} \\ \rho^{\mathrm{f}}\frac{\mathrm{D}_{\mathrm{s}}e^{\mathrm{f}}}{\mathrm{D}t} + \rho^{\mathrm{f}}\nabla e^{\mathrm{f}} \cdot (\boldsymbol{v}^{\mathrm{f}} - \boldsymbol{v}^{\mathrm{s}}) + \nabla \cdot \boldsymbol{q}^{\mathrm{f}} &= Q^{\mathrm{f}} \end{aligned} \tag{2.115}$$

The specific internal energies for the solid and fluid phases as a function of temperature are given by

$$e^{\mathrm{s}} = c_{\mathrm{s}}T \quad \text{and} \quad e^{\mathrm{f}} = c_{\mathrm{f}}T \tag{2.116}$$

where c_{s} and c_{f} are their respective specific heat capacities. Applying these to (2.115) gives

$$\begin{aligned} \rho^{\mathrm{s}}c_{\mathrm{s}}\frac{\mathrm{D}_{\mathrm{s}}T}{\mathrm{D}t} + \nabla \cdot \boldsymbol{q}^{\mathrm{s}} &= Q^{\mathrm{s}} \\ \rho^{\mathrm{f}}c_{\mathrm{f}}\frac{\mathrm{D}_{\mathrm{s}}T}{\mathrm{D}t} + \rho^{\mathrm{f}}c_{\mathrm{f}}\nabla T \cdot (\boldsymbol{v}^{\mathrm{f}} - \boldsymbol{v}^{\mathrm{s}}) + \nabla \cdot \boldsymbol{q}^{\mathrm{f}} &= Q^{\mathrm{f}}. \end{aligned} \tag{2.117}$$

Summation of the individual balance equations gives the overall energy balance equation for the porous medium as

$$(\rho^{\mathrm{s}}c_{\mathrm{s}} + \rho^{\mathrm{f}}c_{\mathrm{f}})\frac{\mathrm{D}_{\mathrm{s}}T}{\mathrm{D}t} + \rho^{\mathrm{f}}c_{\mathrm{f}}\nabla T \cdot (\boldsymbol{v}^{\mathrm{f}} - \boldsymbol{v}^{\mathrm{s}}) + \nabla \cdot \boldsymbol{q} = Q \tag{2.118}$$

wherein we have implied

$$\begin{aligned} \boldsymbol{q} &= \boldsymbol{q}^{\mathrm{s}} + \boldsymbol{q}^{\mathrm{f}} \\ Q &= Q^{\mathrm{s}} + Q^{\mathrm{f}} \end{aligned} \tag{2.119}$$

for the total heat flux and heat supply, respectively.

Defining the effective heat capacity of the medium as

$$(\rho c)_{\mathrm{eff}} = \rho^{\mathrm{s}}c_{\mathrm{s}} + \rho^{\mathrm{f}}c_{\mathrm{f}} = (1-n)\rho_{\mathrm{s}}c_{\mathrm{s}} + n\rho_{\mathrm{f}}c_{\mathrm{f}} \tag{2.120}$$

and noting that $\boldsymbol{w} = n(\boldsymbol{v}^{\mathrm{f}} - \boldsymbol{v}^{\mathrm{s}})$ is Darcy's velocity, (2.118) is further simplified to obtain the energy balance equation for the medium as

$$(\rho c)_{\mathrm{eff}} \frac{\mathrm{D}_{\mathrm{s}} T}{\mathrm{D}t} + \rho_{\mathrm{f}} c_{\mathrm{f}} \boldsymbol{w} \cdot \nabla T + \nabla \cdot \boldsymbol{q} = Q. \tag{2.121}$$

The material time derivative of the temperature with respect to the solid phase is given by

$$\frac{\mathrm{D}_{\mathrm{s}} T}{\mathrm{D}t} = \frac{\partial T}{\partial t} + \nabla T \cdot \boldsymbol{v}^{\mathrm{s}}. \tag{2.122}$$

For the applications of interest in this thesis, the convective heat flux in the solid phase is usually negligible i.e. $\nabla T \cdot \boldsymbol{v}^{\mathrm{s}} \approx 0$. With this assumption and using Fourier's law, (2.69), in (2.121), the energy balance equation for the medium becomes

$$(\rho c)_{\mathrm{eff}} \frac{\partial T}{\partial t} + \rho_{\mathrm{f}} c_{\mathrm{f}} \boldsymbol{w} \cdot \nabla T - \nabla \cdot (\boldsymbol{\lambda} \nabla T) = Q. \tag{2.123}$$

For THM coupled processes in a porous medium, the linear momentum, mass and energy conservation laws in (2.109), (2.112) and (2.123), respectively, may be solved simultaneously for the displacement, pressure and temperature field variables. This results in what is usually referred to as a *u-p-T* formulation.

"*The purpose of computation is insight, not numbers.*"
– Richard Hamming

Chapter 3

Isogeometric Analysis

This chapter presents the fundamentals behind Isogeometric Analysis (IGA), the computational method applied in this thesis. This finite element like method uses spline basis functions similar to what is used in Computer Aided Design (CAD). Formulation of the basis functions and construction of geometries is briefly discussed. The refinement capabilities in IGA are discussed and a comparison is made with traditional Finite Element Analysis (FEA). The steps involved in the formulation of boundary value problems, which are similar to FEA, are then presented.

3.1 Background

IGA is a computational method that was initiated by the seminal research work of Hughes et al. (2005). The main motivation behind the introduction of IGA is the idea of bridging the existing gap between CAD and FEA. The main steps in the development of a product or a structure that relies on a finite element like method are creating the geometric design, generating an analysis suitable mesh, performing FEA and post-processing the results. The geometric design is continuously optimized until the desired result is achieved and each modification requires a new mesh generation. It has been estimated that, for certain industrial applications, about 80% of the time in the process is spent on geometric design and mesh generation, Cottrell et al. (2009). IGA aims to make the development process seamless by creating a direct link between CAD and FEA, by using the spline basis function in the geometry for analysis. The automatic geometry-to-mesh mapping in IGA significantly improves design optimization, verification and validation and uncertainty quantification.

The original work by Hughes et al. (2005) showed the potential of IGA through applications to linear elastic structural analysis and fluid flow simulations. It then inspired several other research works in the years that followed. Over the past ten years, computational research on IGA has been growing steadily. It has been

applied to several disciplines of science and engineering. Some of the studies include application to structural vibrations by Cottrell et al. (2006) and Reali (2006), fluid-structure interaction by Bazilevs et al. (2006), biomechanics by Zhang et al. (2007), phase-field modeling by Gómez et al. (2008), structural analysis of shells by Kiendl et al. (2009), electromagnetics by Buffa et al. (2010), free-surface flow by Akkerman et al. (2011), contact problems by De Lorenzis et al. (2011) and Temizer et al. (2011), damage problems by Verhoosel et al. (2011), topology optimization by Dedè et al. (2012) and poromechanics and hydraulic fracture by Irzal et al. (2014). IGA has shown commendable success in these different areas of application and has opened the door for further research. In the present work, it is applied to the simulation of coupled problems in porous media.

In the following sections, the fundamentals behind B-Splines and NURBS are presented. The refinement strategies available in IGA are discussed in comparison with their counterparts in FEA. LR B-Splines, which allow local refinement unlike B-Splines and NURBS, are then briefly discussed. A comparison between IGA and FEA is made and the similarities and differences are highlighted. Formulation of boundary value problems in IGA is then discussed and the main steps involved are pointed out.

3.2 Spline Fundamentals

The fundamentals behind B-Splines and Non-Uniform Rational B-Splines (NURBS) are presented in this section, based largely on Cottrell et al. (2009). Additional details may be referred from Piegl and Tiller (2012).

3.2.1 B-Splines

The starting point for the discussion of B-Splines in to define a *knot vector*. A knot vector is a sequence of non-decreasing coordinates where each member of the sequence is called a *knot*. For a knot vector represented by

$$\Xi = \{\xi_1, \xi_2, ..., \xi_{n+p+1}\}, \quad \xi_i \in \mathbb{R}, \tag{3.1}$$

ξ_i is the i^{th} knot, $i = 1, 2, ..., n+p+1$ is the knot index, p is the polynomial degree and n is the number of basis functions. If the knots of Ξ are equally spaced, it is called a *uniform* knot vector. The opposite of a uniform knot vector is a *non-uniform* knot vector where the knots are not equally spaced. A knot vector is called *open* if its first and last knots appear $p+1$ times. If a knot is repeated m times in the knot vector, m is called the *multiplicity* of that knot. Two knots with different values bound a *knot span*, which is analogous to an element in FEA.

We can now define B-Spline basis functions which are constructed from knot vectors. For $p = 0$, the basis functions are piecewise constants given by

$$N_{i,0}(\xi) = \begin{cases} 1 & \text{if } \xi_i \leq \xi < \xi_{i+1} \\ 0 & \text{otherwise.} \end{cases} \tag{3.2}$$

For $p \geq 1$, the basis functions are defined by the *Cox-de Boor recursion formula*:

$$N_{i,p}(\xi) = \frac{\xi - \xi_i}{\xi_{i+p} - \xi_i} N_{i,p-1}(\xi) + \frac{\xi_{i+p+1} - \xi}{\xi_{i+p+1} - \xi_{i+1}} N_{i+1,p-1}(\xi). \tag{3.3}$$

Let's consider examples of constructing basis functions based on uniform and non-uniform knot vectors. For a uniform knot vector given by $\Xi = \{0, 1, 2, 3, 4, 5, 6, 7, 8\}$, we have $n + p + 1 = 9$ and thus we get 8 basis functions for $p = 0$, 7 basis functions for $p = 1$, 6 basis functions for $p = 2$ and so on. The pattern of the number of basis functions for different polynomial degrees is shown in Figure 3.1. The basis functions for linear, quadratic, cubic and quartic orders of interpolation are shown in Figure 3.2. For a non-uniform knot vector given by $\Xi = \{0, 0, 0, 1, 2, 2, 3, 4, 4, 5, 5, 5\}$, the resulting 9 quadratic basis functions are shown in Figure 3.3.

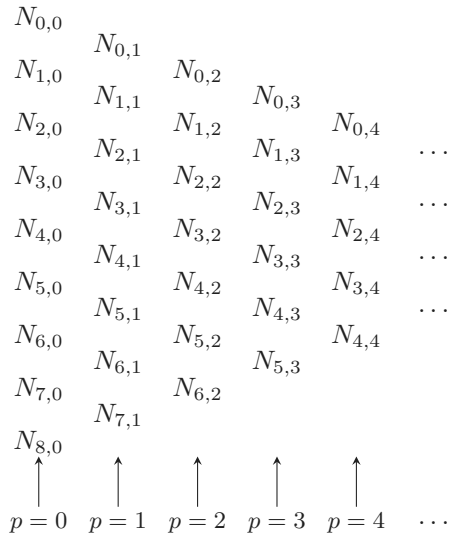

Figure 3.1: Number of basis functions for different polynomial degrees based on the uniform knot vector $\Xi = \{0, 1, 2, 3, 4, 5, 6, 7, 8\}$.

B-Spline basis functions have several important properties. Some of these properties are:

1. They have a homogeneous pattern for all polynomial degrees, which may not be the case for quadratic and higher degree finite element basis functions.

2. They constitute a partition of unity for a given value of ξ i.e.

$$\sum_{i=0}^{n} N_{i,p}(\xi) = 1, \quad \forall \xi. \tag{3.4}$$

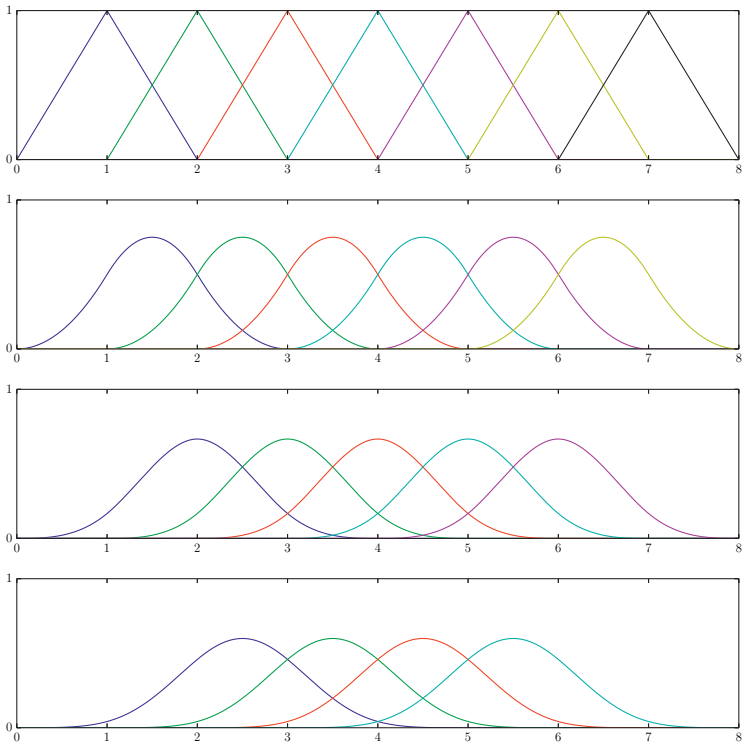

Figure 3.2: Linear , quadratic, cubic and quartic B-Spline basis functions based on the uniform knot vector $\Xi = \{0, 1, 2, 3, 4, 5, 6, 7, 8\}$.

3. All basis functions have pointwise non-negative values over the entire domain i.e.

$$N_{i,p}(\xi) \geq 0, \quad \forall \xi, \tag{3.5}$$

whereas finite element basis functions may take both positive and negative values. This property of B-Spline basis functions is advantageous in evaluating mass matrices for dynamic problems.

4. Since the basis functions are piecewise polynomials, all derivatives of $N_{i,p}(\xi)$ exist within a knot span. In other words, the functions are C^{∞} continuous in the interior of a knot span.

5. At knot locations, $N_{i,p}(\xi)$ is $p - m$ times continuously differentiable i.e. it is C^{p-m} continuous, where m is the multiplicity of the knot. This is one of the most distinctive features of IGA which has important implications for the applications in this thesis. For example, for the quadratic ($p = 2$) basis functions in Figure 3.3, the continuities at each knot are given by C^{2-m} and are shown in the plot.

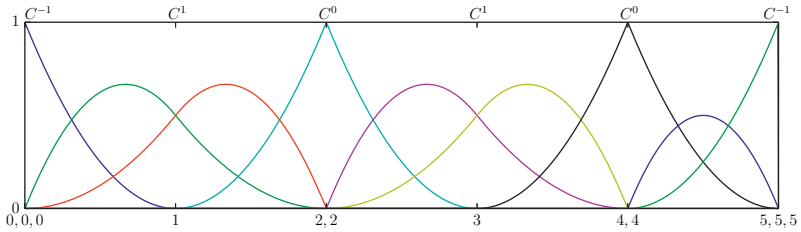

Figure 3.3: Quadratic B-Spline basis functions based on the non-uniform knot vector $\Xi = \{0, 0, 0, 1, 2, 2, 3, 4, 4, 5, 5, 5\}$.

6. The support of basis functions of degree p is always $p + 1$ knot spans i.e. $N_{i,p}(\xi) = 0$ if ξ is outside the interval $[\xi_i, \xi_{i+p+1})$.

The recursive definition of B-Spline basis functions in (3.3) implies that their derivatives can be represented in terms of lower order bases. The derivative of the i^{th} basis function is given by

$$\frac{\mathrm{d}}{\mathrm{d}\xi} N_{i,p}(\xi) = \frac{p}{\xi_{i+p} - \xi_i} N_{i,p-1}(\xi) - \frac{p}{\xi_{i+p+1} - \xi_{i+1}} N_{i+1,p-1}(\xi). \tag{3.6}$$

A generalization to higher-order derivatives gives

$$\frac{\mathrm{d}^k}{\mathrm{d}^k\xi} N_{i,p}(\xi) = \frac{p!}{(p-k)!} \sum_{j=0}^{k} \alpha_{k,j} N_{i+j,p-k}(\xi) \tag{3.7}$$

where

$$\begin{aligned}
\alpha_{0,0} &= 1, \\
\alpha_{k,0} &= \frac{\alpha_{k-1,0}}{\xi_{i+p-k+1} - \xi_i}, \\
\alpha_{k,j} &= \frac{\alpha_{k-1,j} - \alpha_{k-1,j-1}}{\xi_{i+p+j-k+1} - \xi_{i+j}} \quad j = 1, ..., k-1, \\
\alpha_{k,k} &= \frac{-\alpha_{k-1,k-1}}{\xi_{i+p+1} - \xi_{i+k}}.
\end{aligned}$$

The denominator of the coefficients may be zero if the knot vector contains repeated knots. In that case, the coefficients are defined to be zero in numerical implementations. The first derivatives of the basis functions in Figure 3.2 are shown in Figure 3.4.

3.2.2 Non-Uniform Rational B-Splines (NURBS)

NURBS are constructed from B-Splines and can represent a wide array of objects that cannot be exactly represented by polynomials. A NURBS entity in $\mathbb{R}^d$ is obtained by projective transformation of a B-Spline entity in $\mathbb{R}^{d+1}$. For a given

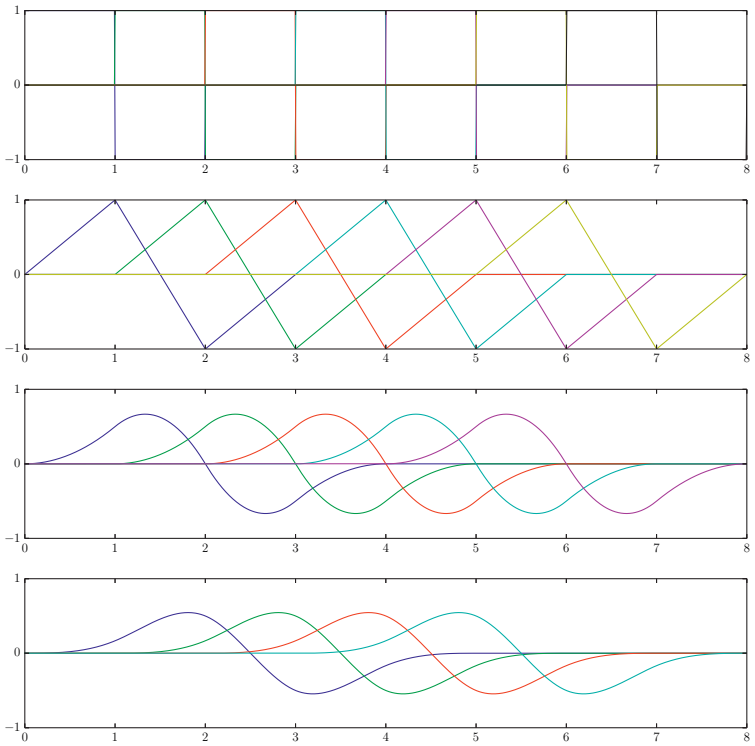

Figure 3.4: Derivatives of the linear , quadratic, cubic and quartic B-Spline basis functions based on the uniform knot vector $\Xi = \{0, 1, 2, 3, 4, 5, 6, 7, 8\}$.

set of B-Spline basis functions $N_{i,p}(\xi)$, we introduce a scalar, piecewise polynomial *weighting function*

$$W(\xi) = \sum_{\hat{i}=1}^{n} N_{\hat{i},p} w_{\hat{i}}, \tag{3.8}$$

where $w_{\hat{i}}$ is referred to as the $\hat{i}^{\text{th}}$ weight. The NURBS basis, which is a piecewise rational function, is now given by

$$R_i^p(\xi) = \frac{N_{i,p}(\xi) w_i}{W(\xi)}. \tag{3.9}$$

For univariate B-Spline basis functions $N_{i,p}(\xi)$ and $M_{j,q}(\eta)$, with polynomial degrees p and q and corresponding knot vectors $\Xi = \{\xi_1, \xi_2, ..., \xi_{n+p+1}\}$ and $\mathcal{H} = \{\eta_1, \eta_2, ..., \xi_{m+q+1}\}$, respectively, the NURBS basis functions used to construct geometries in $\mathbb{R}^2$ are defined by

$$R_{i,j}^{p,q}(\xi, \eta) = \frac{N_{i,p}(\xi) M_{j,q}(\eta) w_{i,j}}{\sum_{\hat{i}=1}^{n} \sum_{\hat{j}=1}^{m} N_{\hat{i},p}(\xi) M_{\hat{j},q}(\eta) w_{\hat{i},\hat{j}}} \tag{3.10}$$

where $w_{i,j}$ are the weights, $i = 1, 2, ...n$ and $j = 1, 2, ...m$. Similarly, the rational basis functions used to construct geometries in $\mathbb{R}^3$ are defined by

$$R^{p,q,r}_{i,j,k}(\xi, \eta, \zeta) = \frac{N_{i,p}(\xi) M_{j,q}(\eta) L_{k,r}(\zeta) w_{i,j,k}}{\sum_{\hat{i}=1}^{n} \sum_{\hat{j}=1}^{m} \sum_{\hat{k}=1}^{l} N_{\hat{i},p}(\xi) M_{\hat{j},q}(\eta) L_{\hat{k},r}(\zeta) w_{\hat{i},\hat{j},\hat{k}}} \tag{3.11}$$

where $L_{k,r}(\zeta)$ are B-Spline basis functions corresponding to the knot vector $\mathcal{Z} = \{\zeta_1, \zeta_2, ..., \zeta_{l+r+1}\}$, r is the polynomial degree and $k = 1, 2, ..., l$.

The derivatives of NURBS basis functions depend on the derivatives of non-rational B-Spline basis functions as they are constructed from them. Based on (3.9), we get

$$\frac{\mathrm{d}}{\mathrm{d}\xi} R^p_i(\xi) = w_i \frac{N'_{i,p}(\xi) W(\xi) - N_{i,p}(\xi) W'(\xi)}{(W(\xi))^2} \tag{3.12}$$

where

$$N'_{i,p}(\xi) = \frac{\mathrm{d}}{\mathrm{d}\xi} N_{i,p}(\xi) \quad \text{and} \quad W'(\xi) = \sum_{\hat{i}=1}^{n} N'_{\hat{i},p}.w_{\hat{i}} \tag{3.13}$$

Higher-order derivatives of NURBS basis functions may be written as a function of the lower-order derivatives, Cottrell et al. (2009). These are not included here.

3.2.3 B-Spline Geometries

B-Spline curves, surfaces or volumes are constructed based on the basis functions. We will first define important terminologies before we proceed to show how geometries in different spatial dimensions are constructed.

Control mesh: is a mesh defined by *control points* and is like a scaffolding that controls the actual geometry. It resembles a finite element mesh with quadrilateral elements in two dimensions and trilinear hexahedra in three dimensions. The degrees of freedom in IGA are located at the control points.

Physical mesh: is a decomposition of the actual geometry into *patches* and/or knot spans. Patches are subdomains of the geometry divided into knot spans, which are bounded by knots. Knots are points, lines and surfaces for 1D, 2D and 3D geometries, respectively.

Index space: is a space defined for each knot value, including repeated knots. The presence of repeated knots leads to zero parametric areas in the index space.

Parameter space: is a space defined by the non-zero intervals between the knots. The parameter space may be normalized to fall in the domain $\Omega = [0, 1]^d$, where d is the spatial dimension.

Parent element: is a space defined for each knot span for the purpose of numerical integration and is given over a domain $\Omega = [-1, 1]^d$.

The index space, parameter space and parent element for a selected knot span, based on the knot vectors $\Xi = \{0, 0, 1, 2, 2\}$ and $\mathcal{H} = \{0, 0, 1, 2, 3, 3\}$, are shown in Figure 3.5.

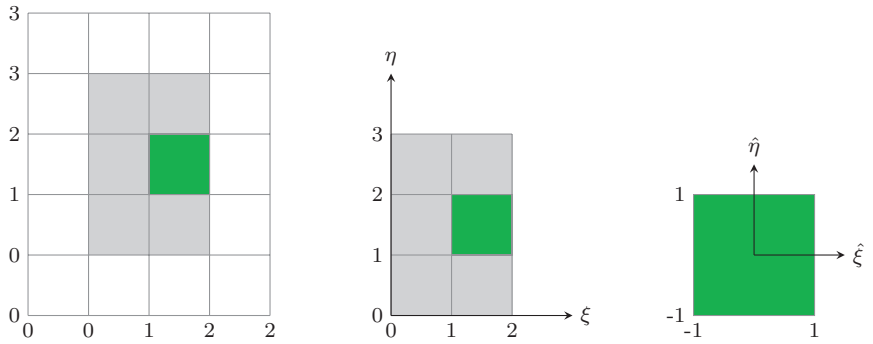

Figure 3.5: Representation of a knot span in different spaces based on the knot vectors $\Xi = \{0, 0, 1, 2, 2\}$ and $\mathcal{H} = \{0, 0, 1, 2, 3, 3\}$.

B-Spline geometries are formed as a linear combination of control points and basis functions. For a given set of control points $\boldsymbol{P}_i \in \mathbb{R}^d$ (the vector-valued coefficients of the basis functions) and n basis functions $N_{i,p}, i = 1, 2, ..., n$, a piecewise polynomial *B-Spline curve* is defined by

$$\boldsymbol{C}(\xi) = \sum_{i=1}^{n} N_{i,p}(\xi)\boldsymbol{P}_i. \tag{3.14}$$

Similarly, for basis functions $N_{i,p}(\xi)$ and $M_{j,q}(\eta)$, with polynomial degrees p and q, and knot vectors $\Xi = \{\xi_1, \xi_2, ..., \xi_{n+p+1}\}$ and $\mathcal{H} = \{\eta_1, \eta_2, ..., \xi_{m+q+1}\}$, respectively, a *B-Spline surface* is defined by

$$\boldsymbol{S}(\xi, \eta) = \sum_{i=1}^{n}\sum_{j=1}^{m} N_{i,p}(\xi)M_{j,q}(\eta)\boldsymbol{P}_{i,j} \tag{3.15}$$

where $\boldsymbol{P}_{i,j}, i = 1, 2, ..., n, j = 1, 2, ..., m$ is a control net. The tensor product structure of the surface implies that its basis is pointwise non-negative and constitutes a partitions of unity $\forall(\xi, \eta) \in [\xi_1, \xi_{n+p+1}] \times [\eta_1, \eta_{m+q+1}]$ i.e.

$$\sum_{i=1}^{n}\sum_{j=1}^{m} N_{i,p}(\xi)M_{j,q}(\eta) = \left(\sum_{i=1}^{n} N_{i,p}(\xi)\right)\left(\sum_{j=1}^{m} M_{j,q}(\eta)\right) = 1. \tag{3.16}$$

B-Spline volumes are built in a similar way as B-Spline surfaces. With an additional univariate basis function $L_{k,r}(\zeta)$, polynomial degree r, corresponding to the knot vector $\mathcal{Z} = \{\zeta_1, \zeta_2, ..., \zeta_{l+r+1}\}$, the volume is defined by

$$\boldsymbol{V}(\xi, \eta, \zeta) = \sum_{i=1}^{n}\sum_{j=1}^{m}\sum_{k=1}^{l} N_{i,p}(\xi)M_{j,q}(\eta)L_{k,r}(\zeta)\boldsymbol{P}_{i,j,k} \tag{3.17}$$

where $\boldsymbol{P}_{i,j,k}, i = 1, 2, ..., n, j = 1, 2, ..., m, k = 1, 2, ..., l$, is a control lattice.

3.2.4 NURBS Geometries

NURBS geometries are constructed based on the rational basis functions obtained by the weighting procedure described in Section 3.2.2. NURBS basis functions can represent more complex geometries and are the standard in many CAD software.

For univariate rational basis functions $R_i^p(\xi)$ and control points $\boldsymbol{P}_i$, a *NURBS curve* is given by

$$\boldsymbol{C}(\xi) = \sum_{i=1}^{n} R_i^p(\xi)\boldsymbol{P}_i. \tag{3.18}$$

Given a control net $\boldsymbol{P}_{i,j}$ and bivariate rational basis functions $R_{i,j}^{p,q}(\xi,\eta)$, a *NURBS surface* is defined by

$$\boldsymbol{S}(\xi,\eta) = \sum_{i=1}^{n}\sum_{j=1}^{m} R_{i,j}^{p,q}(\xi,\eta)\boldsymbol{P}_{i,j}. \tag{3.19}$$

Similarly, for a control lattice $\boldsymbol{P}_{i,j,k}$ and trivariate rational basis functions $R_{i,j,k}^{p,q,r}(\xi,\eta,\zeta)$, a *NURBS volume* is obtained from

$$\boldsymbol{V}(\xi,\eta,\zeta) = \sum_{i=1}^{n}\sum_{j=1}^{m}\sum_{k=1}^{l} R_{i,j,k}^{p,q,r}(\xi,\eta,\zeta)\boldsymbol{P}_{i,j,k}. \tag{3.20}$$

3.3 Refinement Methods

The basis functions representing a B-Spline or NURBS object can be refined in several ways without altering the geometry and leaving the parametrization intact. The properties of the basis functions mean that the element size, polynomial degree and continuity can be controlled during refinement. The refinement methods in IGA are briefly discussed in the following sections. For details on these, see Cottrell et al. (2009).

3.3.1 Knot Insertion (h-refinement)

Knot insertion is a refinement method where new knots are added to the existing object, thereby resulting in refined basis functions and control points. The FEA equivalent of knot insertion is mesh refinement, which is achieved by dividing larger original elements into smaller ones. Mesh refinement in FEA and knot insertion in IGA become identical if we insert new knots with multiplicities equal to the polynomial degree such that a C^0 continuity is maintained between elements. However, we can repeat existing knots to control the continuity of the basis functions, which makes knot insertion more flexible than mesh refinement.

Consider a B-Spline or NURBS object defined by the knot vector $\Xi = \{\xi_1, \xi_2, ..., \xi_{n+p+1}\}$, polynomial degree p, basis functions $N_{i,p}(\xi)$ and control points $\boldsymbol{P}_i$. Insertion of new m knots $\bar{\xi}$ into Ξ results in a new knot vector $\bar{\Xi}$ which has $n+m+p+1$ knots. For $\bar{\xi} \in [\xi_k, \xi_{k+1})$, a new set of control points $\bar{\boldsymbol{P}}_i$ can now be calculated based on the new knot vector from (see Piegl and Tiller (2012))

$$\bar{\boldsymbol{P}}_i = \alpha_i \boldsymbol{P}_i + (1-\alpha_i)\boldsymbol{P}_{i-1} \tag{3.21}$$

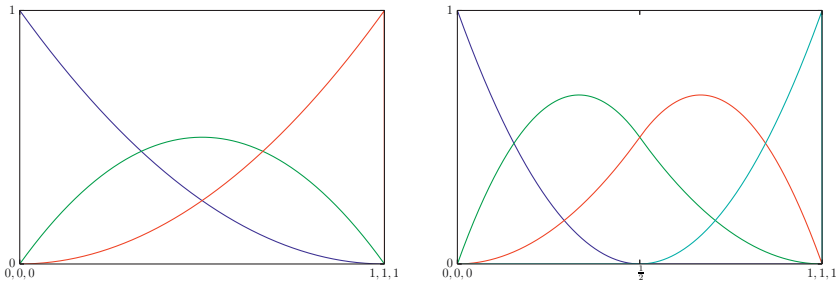

Figure 3.6: h-refinement: Original and refined basis functions.

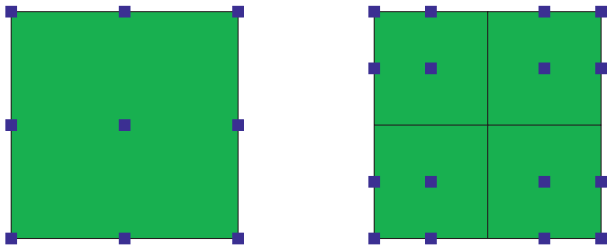

Figure 3.7: h-refinement: Control points and physical mesh before and after knot insertion. Original knot vectors: $\Xi = \mathcal{H} = \{0, 0, 0, 1, 1, 1\}$. Refined knot vectors: $\bar{\Xi} = \bar{\mathcal{H}} = \left\{0, 0, 0, \frac{1}{2}, 1, 1, 1\right\}$. The polynomial order in both cases is $p = 2$.

where

$$\alpha_i = \begin{cases} 1 & \text{if } i \leq k - p \\ \frac{\bar{\xi} - \xi_i}{\xi_{i+p} - \xi_i} & \text{if } k - p + 1 \leq i \leq k \\ 0 & \text{if } i \geq k + 1. \end{cases} \tag{3.22}$$

The equation above implies that only p new control points need to be computed. The new know vector $\bar{\Xi} = \left\{\xi_1, \xi_2, ..., \bar{\xi}, ..., \xi_{n+m+p+1}\right\}$ also results in new basis functions $\bar{N}_{i,p}(\xi)$. Illustration of knot insertion is performed on the knot vector $\Xi = \{0, 0, 0, 1, 1, 1\}$. Inserting the knot $\bar{\xi} = \frac{1}{2}$ gives a new knot vector $\bar{\Xi} = \left\{0, 0, 0, \frac{1}{2}, 1, 1, 1\right\}$. The original and refined quadratic basis functions are shown in Figure 3.6.

The effect of h-refinement for a simple two-dimensional case is illustrated by considering a geometry defined by the knot vectors $\Xi = \mathcal{H} = \{0, 0, 0, 1, 1, 1\}$, which has a single element. Insertion of knew knots $\bar{\xi} = \frac{1}{2}$ and $\bar{\eta} = \frac{1}{2}$ into both knot vectors, i.e. in both directions, results in the new knot vectors $\bar{\Xi} = \bar{\mathcal{H}} = \left\{0, 0, 0, \frac{1}{2}, 1, 1, 1\right\}$. This splits the original geometry into four elements. New control points are calculated based on the new knot vectors. The original and refined control points, together with the physical mesh, are shown in Figure 3.7.

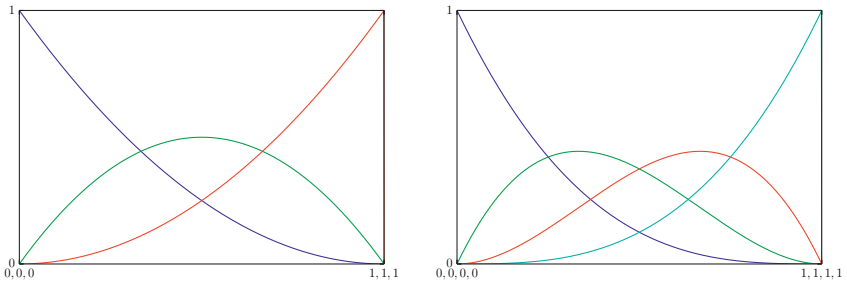

Figure 3.8: p-refinement: Original and refined basis functions.

3.3.2 Degree Elevation (p-refinement)

Raising the polynomial degree is another method of refining B-Spline or NURBS basis functions and the corresponding objects. In this method, the multiplicity of each knot is increased by the amount the polynomial degree is raised, but no new knots are added. This preserves the continuities of the original basis functions. Degree elevation in IGA has similarities with p-refinement in FEA in that the polynomial degree is raised in both cases. However, in FEA the continuity between all elements is C^0 whereas we may have varying continuities between knot spans in IGA.

To illustrate degree elevation, we consider the same original knot vector as in the previous section: $\Xi = \{0, 0, 0, 1, 1, 1\}$. Raising the polynomial degree by one gives the new knot vector $\bar{\Xi} = \{0, 0, 0, 0, 1, 1, 1, 1\}$. The original quadratic and refined cubic basis functions corresponding to these knot vectors are shown in Figure 3.8.

The result of p-refinement on a simple two-dimensional geometry is illustrated for the geometry defined by the knot vectors $\Xi = \mathcal{H} = \{0, 0, 0, 1, 1, 1\}$. Raising the polynomial degree in both directions gives the new knot vectors $\bar{\Xi} = \bar{\mathcal{H}} = \{0, 0, 0, 0, 1, 1, 1, 1\}$. The physical mesh before and after degree elevation has the same one element but the number of control elements increases after refinement. Note that the location of the control points in this case is different from what we get with knot insertion. The control points and physical mesh before and after degree elevation are shown in Figure 3.9.

3.3.3 k-refinement

Knot insertion and degree elevation are non-commutative and this results in a refinement method which is unique to IGA: k-refinement. Knot insertion followed by degree elevation results in basis functions with a new polynomial degree but does not change the continuity at the inserted knots. On the other hand, degree elevation followed by knot insertion gives a new polynomial degree with an increased continuity at the newly inserted knots. Consider the linear basis functions from $\Xi = \{0, 0, 1, 1\}$, shown in Figure 3.10(a). Insertion of two knew knots gives the new

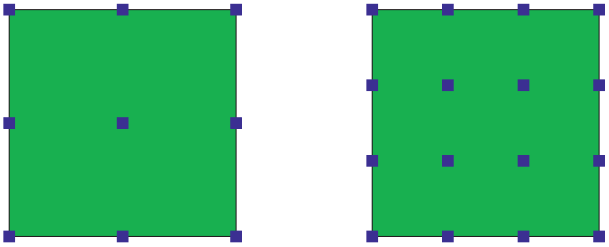

Figure 3.9: p-refinement: Control points and physical mesh before and after degree elevation. Original knot vectors: $\Xi = \mathcal{H} = \{0, 0, 0, 1, 1, 1\}$. Refined knot vectors: $\bar{\Xi} = \bar{\mathcal{H}} = \{0, 0, 0, 0, 1, 1, 1, 1\}$. The polynomial order is raised from $p = 2$ to $p = 3$.

knot vector $\bar{\Xi}_1 = \left\{0, 0, \frac{1}{3}, \frac{2}{3}, 1, 1\right\}$. This followed by degree elevation results in the knot vector $\bar{\Xi}_2 = \left\{0, 0, 0, \frac{1}{3}, \frac{1}{3}, \frac{2}{3}, \frac{2}{3}, 1, 1, 1\right\}$. The basis functions corresponding to $\bar{\Xi}_1$ and $\bar{\Xi}_2$ are shown in Figure 3.10(b). The reverse procedure results in a more interesting scenario. Performing degree elevation on the original knot vector gives $\bar{\Xi}_1 = \{0, 0, 0, 1, 1, 1\}$. When this is followed by insertion of the two new knots, we get $\bar{\Xi}_2 = \left\{0, 0, 0, \frac{1}{3}, \frac{2}{3}, 1, 1, 1\right\}$. The basis functions for the new knot vectors in this case are shown in Figure 3.10(c). For knot insertion followed by degree elevation, it can be seen that the basis functions maintain a C^0 continuity across knots. However, the continuity increases from C^0 to C^1 for k-refinement, i.e. degree elevation followed by knot insertion.

The growth of the number basis functions and control points is optimal in k-refinement. Illustration of this is performed by considering a simple two-dimensional geometry defined by the knot vectors $\Xi = \mathcal{H} = \{0, 0, 0, 1, 1, 1\}$. The control points and physical mesh corresponding to these original knot vectors is shown in Figure 3.11(a). Knot insertion followed by degree elevation results in the control points and physical mesh shown in Figure 3.11(b), where the new knot vectors are $\bar{\Xi} = \bar{\mathcal{H}} = \left\{0, 0, 0, 0, \frac{1}{2}, \frac{1}{2}, 1, 1, 1, 1\right\}$. The reverse procedure, k-refinement, gives the control points and physical mesh shown in Figure 3.11(c). The new knot vectors in this case are $\bar{\Xi} = \bar{\mathcal{H}} = \left\{0, 0, 0, 0, \frac{1}{2}, 1, 1, 1, 1\right\}$. It can bee see that we end up with fewer number of control points, and basis functions, in k-refinement compared to h-refinement followed by p-refinement. This results in a higher-continuity and higher-regularity mesh and there is no analogous refinement strategy in FEA. The savings from k-refinement in the number of control points and basis functions is even more significant for three-dimensional objects.

The three refinement methods discussed in this section, h-, $p-$ and k-refinement, can be combined in several ways resulting in a multitude of refinement options. The number of basis functions and control points can be controlled such that a physical mesh with the desired number of elements and continuities is obtained. The refinement capabilities in IGA make it a superior alternative to standard FEA.

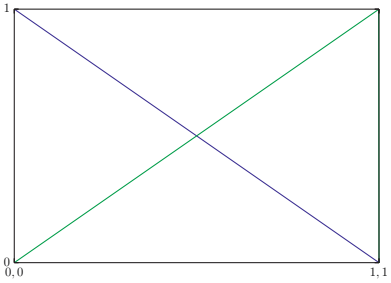

(a) Original linear basis functions

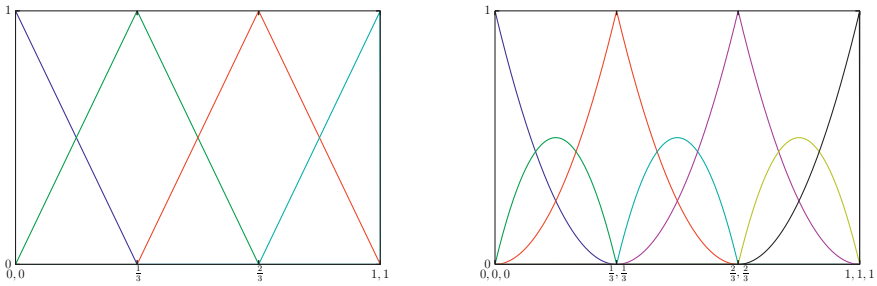

(b) Knot insertion → Degree elevation

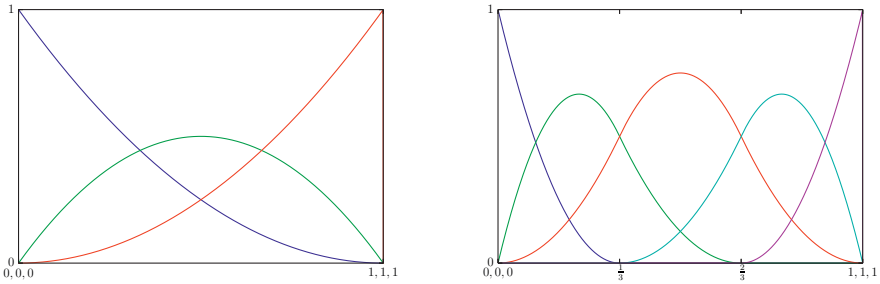

(c) Degree elevation → Knot insertion = k-refinement

Figure 3.10: k-refinement: Original and refined basis functions showing the non-commutativity of knot insertion and degree elevation.

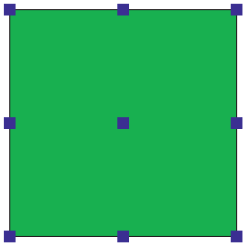

(a) Original: $\Xi = \mathcal{H} = \{0, 0, 0, 1, 1, 1\}$

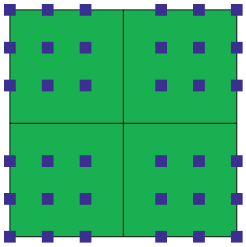

(b) h-refinement $\rightarrow$ p-refinement

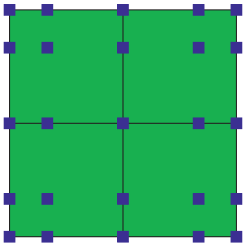

(c) k-refinement

Figure 3.11: k-refinement: Control points and physical mesh before and after refinement. Refined knot vectors: (b) $\bar{\Xi} = \bar{\mathcal{H}} = \left\{0, 0, 0, 0, \frac{1}{2}, \frac{1}{2}, 1, 1, 1, 1\right\}$ and (c) $\bar{\Xi} = \bar{\mathcal{H}} = \left\{0, 0, 0, 0, \frac{1}{2}, 1, 1, 1, 1\right\}$. We start with $p = 2$ in (a) and get $p = 3$ in (b) and (c).

3.4 Locally Refined (LR) B-Splines

B-Splines and NURBS geometries have a tensor product structure and this does not allow local refinement. Other spline technologies have been proposed to overcome this limitation. These include T-Splines proposed by Sederberg et al. (2003) and LR B-Splines by Dokken et al. (2013), which have been applied in IGA by Bazilevs et al. (2010) and Johannessen et al. (2014), respectively. LR B-Splines, which are used in this thesis, are briefly discussed.

The local refinement capability of LR B-Splines is achieved by introducing local knot vectors. A given knot vector Ξ can be used to construct i local knot vectors Ξ_i, from the components of the original knot vector. A single B-Spline of degree p may then be defined, using local knot vectors, as a separable function defined by n non-decreasing local knot vectors Ξ_i and the degrees p_i:

$$B_{\Xi}(\xi) = \prod_{i=1}^{n} B_{\Xi_i}(\xi_i). \tag{3.23}$$

To ensure that LR B-Splines maintain the partition of unity property, a scalar

weight $\gamma \in [0,1]$ is introduced to define a weighted B-Spline as

$$B_{\Xi}^{\gamma}(\xi) = \gamma \prod_{i=1}^{n} B_{\Xi_i}(\xi_i), \tag{3.24}$$

and thus we have

$$\sum_{i=1}^{n} \gamma_i B_i(\xi) = 1. \tag{3.25}$$

A given univariate B-Spline basis can be enriched by knot insertion without changing the geometric description. To insert a knot $\hat{\xi}$ into the knot vector Ξ between the knots ξ_{i-1} and ξ_i, we use the relation:

$$B_{\Xi}(\xi) = \alpha_1 B_{\Xi_1}(\xi) + \alpha_2 B_{\Xi_2}(\xi) \tag{3.26}$$

where

$$\begin{aligned} \alpha_1 &= \begin{cases} 1, & \xi_{p+1} \leq \hat{\xi} \leq \xi_{p+2} \\ \frac{\hat{\xi}-\xi_1}{\xi_{p+1}-\xi_1}, & \xi_1 \leq \hat{\xi} \leq \xi_{p+1} \end{cases} \\ \alpha_2 &= \begin{cases} \frac{\xi_{p+2}-\hat{\xi}}{\xi_{p+2}-\xi_2}, & \xi_2 \leq \hat{\xi} \leq \xi_{p+2} \\ 1, & \xi_1 \leq \hat{\xi} \leq \xi_2 \end{cases} \end{aligned} \tag{3.27}$$

and the knot vectors are

$$\begin{aligned} \Xi &= [\xi_1, \xi_2, ..., \xi_{i-1}, \quad \xi_i, ..., \xi_{p+1}, \xi_{p+2}] \\ \Xi_1 &= [\xi_1, \xi_2, ..., \xi_{i-1}, \hat{\boldsymbol{\xi}}, \xi_i, ..., \xi_{p+1} \quad\quad] \\ \Xi_2 &= [\quad \xi_2, ..., \xi_{i-1}, \hat{\boldsymbol{\xi}}, \xi_i, ..., \xi_{p+1}, \xi_{p+2}]. \end{aligned} \tag{3.28}$$

The insertion of the knot $\hat{\xi}$ into Ξ yields a knot vector of size $p+3$, generating two B-Splines described by the local knot vectors Ξ_1 and Ξ_2, both of size $p+2$.

Bivariate basis functions are refined in one parametric domain at a time. If we have a knot vector Ξ in the first parametric direction, and $\mathcal{H}$ in the second, we get a B-Spline

$$B_{\Xi,\mathcal{H}}(\xi,\eta) = B_{\Xi}(\xi) B_{\mathcal{H}}(\eta). \tag{3.29}$$

Local refinement is then performed first on $B_{\Xi}(\xi)$ according to (3.26), and then on $B_{\mathcal{H}}(\eta)$ following the same procedure.

A detailed presentation of LR B-Splines with examples and applications can be found in Johannessen et al. (2014), Johannessen et al. (2015a) and Johannessen et al. (2015b). Some of the properties of LR B-Splines are discussed by Bressan (2013).

3.5 Comparison with FEA

IGA and traditional FEA have several similarities as computational methods. Some of their shared properties include the partition of unity properties of the basis

Table 3.1: Comparison between IGA and traditional FEA.

	IGA	**FEA**
1	Control and physical meshes	Single mesh
2	Physical mesh composed of *knot spans*	Mesh composed of *elements*
3	Control points on control mesh	Nodal points on mesh
4	Degrees of freedom at control points	Degrees of freedom at nodes
5	Physical mesh on 'exact' geometry	Geometry only approximated
6	Isoparametric mapping on patch level	Isoparametric mapping on element level
7	Basis functions do not interpolate field variables at control points	Basis functions interpolate field variables at nodal points
8	Basis functions always take positive values	Basis functions may take positive and negative values
9	High and controllable continuity between knot spans, C^{p-m}	Continuity between elements always C^0
10	h-, p- and k-refinements available	h- and p-refinements available
11	Variation diminishing property when fitted to discontinuous data	Oscillatory when fitted to discontinuous data

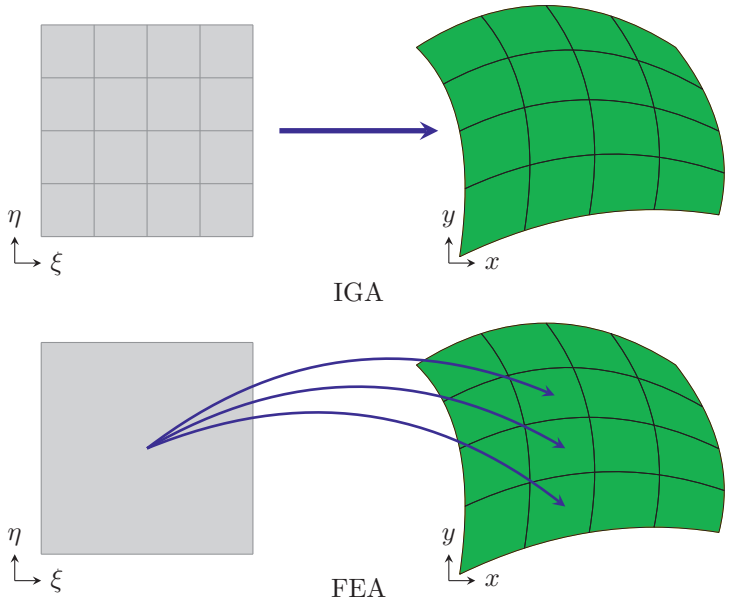

Figure 3.12: Isoparametric mapping in IGA and FEA.

functions, the fact that both make use of the isoparametric concept, their computer implementation architecture and satisfaction of patch tests. However, there are some fundamental differences that set IGA and traditional FEA apart. Some key differences are summarized in Table 3.1.

The isoparametric concept is utilized both in IGA and traditional FEA, but in a different way, as pointed out in Table 3.1. In IGA, mapping from the physical space to the parametric space (with isoparametric coordinates) is performed for each patch in the domain. However, in traditional FEA, the mapping is performed for each element in the finite element mesh. This difference is illustrated in Figure 3.12.

3.6 Boundary Value Problems (BVPs)

The general steps involved in the application of a computational method like IGA to the solution of BVPs are mostly similar to traditional FEA. The main steps are presented in the following sections. Formulations and procedures that are different in IGA are highlighted.

3.6.1 Mathematical Formulation

A physical problem in a domain Ω may be mathematically formulated in terms of partial differential equations (PDEs) which take the general form

$$\mathcal{L}(u) = f \quad \text{in } \Omega \tag{3.30}$$

where $\mathcal{L}$ is a differential operator and u is the unknown field variable. The domain Ω may be subjected to the boundary conditions (discussed in detail in the next section)

$$B(u) = \overline{g} \quad \text{on } \partial\Omega \tag{3.31}$$

where $\partial\Omega$ is the boundary of Ω; see Ames (2014). The resulting problem is referred to as a Boundary Value Problem (BVP) and an illustration of this is shown in Figure 3.13. Examples of such BVPs, in the context of this thesis, include groundwater flow, thermal consolidation of soils and ground freezing. The best way to solve such problems governed by PDEs is to derive analytical solutions. However, for many practical problems, analytical solutions are difficult to obtain. Some of the reasons for this include a domain with boundaries which are difficult to describe mathematically and a domain with multiple regions of complex material properties, Segerlind and Saunders (1987).

3.6.2 Boundary Conditions

The three main types of boundary conditions for the closure of a BVP are Dirichlet, Neumann and Robin boundary conditions.

Dirichlet Boundary Conditions

When known values of the field variables of a PDE are specified at the boundaries of the domain, they are referred to as Dirichlet boundary conditions, sometimes called essential boundary conditions. Examples of Dirichlet boundary conditions

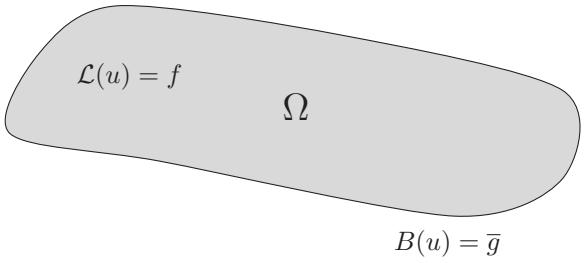

Figure 3.13: Illustration of a boundary value problem.

include prescribed displacements and temperature values on a boundary. They are mathematically expressed as

$$u = \overline{u}(\boldsymbol{x}, t) \quad \text{on } \Gamma_D \tag{3.32}$$

where $\overline{u}$ is the specified value of field variable u, as a function of space $\boldsymbol{x}$ and time t, on the Dirichlet boundary $\Gamma_D \subset \partial\Omega$. The special case when $\overline{u} = 0$ is known as a homogeneous Dirichlet boundary condition.

Neumann Boundary Conditions

When the normal derivatives, or some combination of derivatives (depending on the underlying PDE), of the field variables are specified on a boundary, they are referred to as Neumann boundary conditions. Examples of Neumann boundary conditions include specified fluid and heat fluxes. Neumann boundary conditions, when the differential operator $\mathcal{L}$ is a Laplacian, are mathematically expressed as

$$\frac{\partial u}{\partial n} := \boldsymbol{n} \cdot \nabla u = \overline{q}(\boldsymbol{x}, t) \quad \text{on } \Gamma_N \tag{3.33}$$

where $\boldsymbol{n}$ is the normal to the Neumann boundary $\Gamma_N \subset \partial\Omega$ and $\overline{q}$ is the specified normal derivative of u on Γ_N. The case when $\overline{q} = 0$ is referred to as a homogeneous Neumann or natural boundary condition.

Robin Boundary Conditions

When the value of a field variable on a boundary is given as a linear combination of its normal derivative (Neumann) and a specified value (Dirichlet), we get a Robin boundary condition, often called boundary conditions of the third kind. A typical example of a Robin boundary condition is the transfer of heat on a surface by convection. Mathematically, it is expressed as

$$\alpha(\boldsymbol{x}, t)u + \beta(\boldsymbol{x}, t)\frac{\partial u}{\partial n} = \overline{h}(\boldsymbol{x}, t) \quad \text{on } \Gamma_R \tag{3.34}$$

where α and β are non-zero functions or constants and $\overline{h}$ is the resulting value of u on the boundary $\Gamma_R \subset \partial\Omega$.

3.6.3 Strong and Weak Forms

With the PDEs describing a physical process and the corresponding boundary conditions in place, the strong form of the resulting BVP may be stated as: Given $f : \Omega \to \mathbb{R}$ and functions $\overline{u}(\boldsymbol{x}, t),\ \overline{q}(\boldsymbol{x}, t),\ \alpha(\boldsymbol{x}, t),\ \beta(\boldsymbol{x}, t)$ and $\overline{h}(\boldsymbol{x}, t)$, find $u : \Omega \to \mathbb{R}$ such that

$$\begin{cases} \mathcal{L}(u) = f & \text{in } \Omega \\ u = \overline{u} & \text{on } \Gamma_D \\ \mathcal{N}(u) = \overline{q} & \text{on } \Gamma_N \\ \alpha u + \beta \mathcal{N}(u) = \overline{h} & \text{on } \Gamma_R \end{cases} \tag{3.35}$$

where $\mathcal{N}$ is a differential operator corresponding to $\mathcal{L}$, $\Gamma_D \cup \Gamma_N \cup \Gamma_R = \partial\Omega$ and $\Gamma_D \cap \Gamma_N \cap \Gamma_R = \varnothing$. Such a strong form of a BVP requires strong continuity of the field variables. As pointed out earlier, it is often difficult to obtain an exact solution for the strong forms of many practical problems. A numerical approach is usually required and a weak form of the problem is used to find the solution in finite element like methods.

The weak form is an integral form of the problem and requires weaker continuity of the field variables and this results in a set of discretized system of equations. The weak form of the problem may be created using energy principles or weighted residual methods.

For the strong form in (3.35), one way of defining the weak form requires characterizing two classes of functions: *trial solutions* and *weighting functions*. The derivatives of the trial solutions are required to be square-integrable i.e. if $u : \Omega \to \mathbb{R}^d$ is a trial solution, we require

$$\int_\Omega \nabla u \cdot \nabla u \, \mathrm{d}\Omega < +\infty. \tag{3.36}$$

The solution space that contains such functions is called a Sobolev space $H^1(\Omega)$, which is characterized by

$$H^1(\Omega) = \left\{ u \in L^2(\Omega); \partial u / \partial x_i \in L^2(\Omega), 1 \leq i \leq d \right\} \tag{3.37}$$

where d is the spatial dimension and $L^2(\Omega)$ is the space of square-integrable functions characterized by $\int_\Omega u^2 \mathrm{d}\Omega < +\infty$.

The trial solution and weighting function spaces can now be defined as

$$\begin{aligned} V &= \left\{ u \in H^1(\Omega) : u = \overline{u} \quad \text{on } \Gamma_D \right\} \\ \hat{V} &= \left\{ w \in H^1(\Omega) : w = 0 \quad \text{on } \Gamma_D \right\} \end{aligned} \tag{3.38}$$

where $w \in \hat{V}$ is an arbitrary test function. The weak form of (3.35) can now be obtained by multiplying $(3.35)_1$ by w and then integrating over the domain Ω. It may be formally stated as: Given $f,\ \overline{u}\ , \overline{q}$ and $\overline{h}$, find $u \in V$ such that $\forall w \in \hat{V}$

$$\int_\Omega w \left[\mathcal{L}(u) - f \right] \mathrm{d}\Omega = 0. \tag{3.39}$$

3.6.4 Galerkin Formulation

In Galerkin's method, we construct finite dimensional approximations V_h and $\hat{V}_h$ of the trial and weighting function spaces V and $\hat{V}$, respectively, such that

$$V_h \subset V \quad \text{and} \quad \hat{V}_h \subset \hat{V}. \tag{3.40}$$

For $u_h \in V_h$ and $w_h \in \hat{V}_h$, the weak form in (3.39) may be written as

$$\int_\Omega w_h \left[\mathcal{L}(u_h) - f\right] \mathrm{d}\Omega = 0. \tag{3.41}$$

This equation defines an approximate solution u_h. Galerkin's method leads to a system of matrix equations. The unknown field variable may be approximated as a linear combination of B-Spline or NURBS basis functions $\boldsymbol{N}$ and control point values $\boldsymbol{u}^{\mathrm{c}}$ as

$$u_h = \boldsymbol{N}\boldsymbol{u}^{\mathrm{c}}. \tag{3.42}$$

Using this in (3.41) results in matrices in integral form that may be evaluated by numerical integration, which will be discussed in the next section.

3.6.5 Numerical Integration

Application of Galerkin's method results in element matrices and vectors of the form

$$\boldsymbol{K}_e = \int_\Omega \boldsymbol{G}\mathrm{d}\Omega \quad \text{or} \quad \boldsymbol{f}_e = \int_\Gamma \boldsymbol{G}\mathrm{d}\Gamma \tag{3.43}$$

where $\boldsymbol{G}$ is a matrix which depends on the basis functions and their derivatives with respect to coordinates in the physical space, Ω is an integration domain and Γ an integration boundary (see Zienkiewicz and Taylor (1989)). These element matrices are usually evaluated by using numerical integration methods as closed form expressions are impractical for most problems.

After spatial discretization using Galerkin's method, evaluation of the resulting integrals by numerical integration (for each element) requires transformation of elements in the physical space (Ω^e) to parent elements ($\tilde{\Omega}^e$). For B-Splines and NURBS, the transformation is first made from the physical space to the parametric space (to parametric elements $\hat{\Omega}^e$) and then to the parent element; see Cottrell et al. (2009) and Kadapa (2014). This is illustrated for a two-dimensional case in Figure 3.14. The coordinates in the physical space (x, y, z) as a function of the parametric coordinates (ξ, η, ζ) can be written as

$$\boldsymbol{x}(\xi, \eta, \zeta) = (x, y, z) = \sum_{i=0}^{n} N_i(\xi, \eta, \zeta)\boldsymbol{x}_i = \boldsymbol{N}\boldsymbol{x}. \tag{3.44}$$

The coordinates of the parametric space may be expressed as a function of the coordinates of the parent element $(\tilde{\xi}, \tilde{\eta}, \tilde{\zeta})$ i.e.

$$\xi = \xi(\tilde{\xi}), \quad \eta = \eta(\tilde{\eta}) \quad \text{and} \quad \zeta = \zeta(\tilde{\zeta}) \tag{3.45}$$

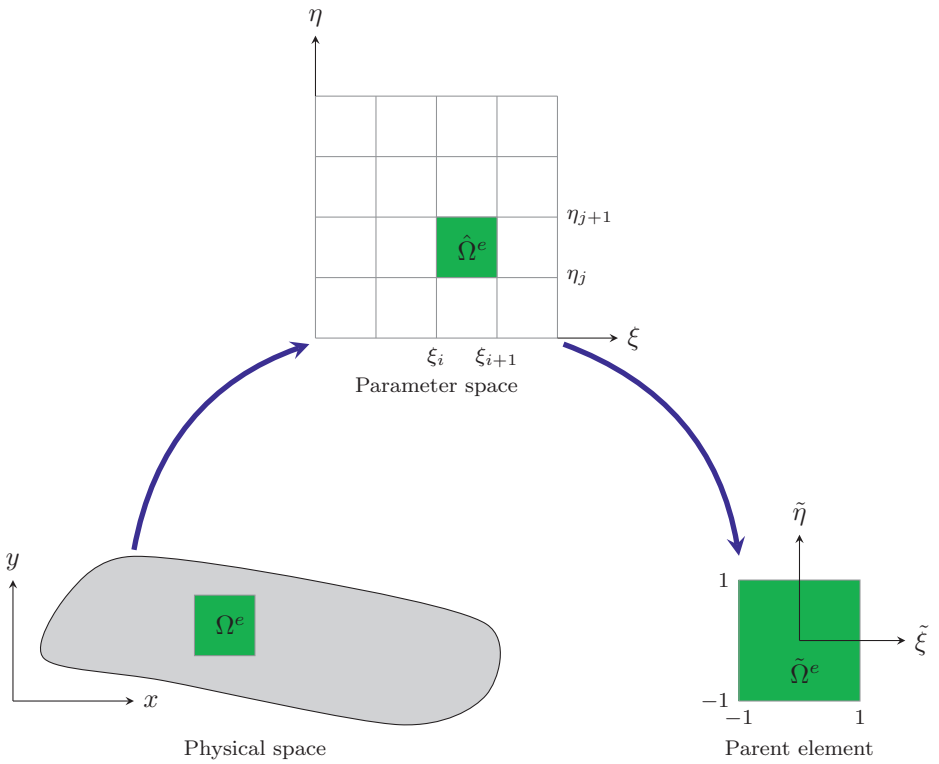

Figure 3.14: Geometrical mapping of an element in the physical space to the parametric space and then to the parent element for numerical integration.

For example, in two-dimensions, an element in the parametric space is a rectangle $[\xi_i, \xi_{i+1}] \times [\eta_j, \eta_{j+1}]$ and is mapped to a square $[-1, 1] \times [-1, 1]$ in the parent domain. Thus, there is no cross-coupling between (ξ, η, ζ) and $(\tilde{\xi}, \tilde{\eta}, \tilde{\zeta})$. The physical coordinates in terms of the coordinates of the parent domain become

$$\boldsymbol{x}(\xi, \eta, \zeta) = \sum_{i=0}^{n} N_i(\xi(\tilde{\xi}), \eta(\tilde{\eta}), \zeta(\tilde{\zeta}))\boldsymbol{x}_i = \boldsymbol{N}(\xi(\tilde{\xi}), \eta(\tilde{\eta}), \zeta(\tilde{\zeta}))\boldsymbol{x}. \tag{3.46}$$

The first derivatives of the basis functions with respect to the parent domain coordinates are obtained by the chain rule as

$$\begin{Bmatrix} \frac{\partial N_i}{\partial \tilde{\xi}} \\ \frac{\partial N_i}{\partial \tilde{\eta}} \\ \frac{\partial N_i}{\partial \tilde{\zeta}} \end{Bmatrix} = \underbrace{\begin{bmatrix} \frac{\partial x}{\partial \tilde{\xi}} & \frac{\partial y}{\partial \tilde{\xi}} & \frac{\partial z}{\partial \tilde{\xi}} \\ \frac{\partial x}{\partial \tilde{\eta}} & \frac{\partial y}{\partial \tilde{\eta}} & \frac{\partial z}{\partial \tilde{\eta}} \\ \frac{\partial x}{\partial \tilde{\zeta}} & \frac{\partial y}{\partial \tilde{\zeta}} & \frac{\partial z}{\partial \tilde{\zeta}} \end{bmatrix}}_{\boldsymbol{J}} \begin{Bmatrix} \frac{\partial N_i}{\partial x} \\ \frac{\partial N_i}{\partial y} \\ \frac{\partial N_i}{\partial z} \end{Bmatrix} = \boldsymbol{J} \begin{Bmatrix} \frac{\partial N_i}{\partial x} \\ \frac{\partial N_i}{\partial y} \\ \frac{\partial N_i}{\partial z} \end{Bmatrix} \tag{3.47}$$

where $\boldsymbol{J}$ is the Jacobian matrix of transformation. Inverse of the above equation

implies

$$\begin{Bmatrix} \frac{\partial N_i}{\partial x} \\ \frac{\partial N_i}{\partial y} \\ \frac{\partial N_i}{\partial z} \end{Bmatrix} = \boldsymbol{J}^{-1} \begin{Bmatrix} \frac{\partial N_i}{\partial \tilde{\xi}} \\ \frac{\partial N_i}{\partial \tilde{\eta}} \\ \frac{\partial N_i}{\partial \tilde{\zeta}} \end{Bmatrix} \tag{3.48}$$

which requires $\boldsymbol{J}$ to be invertible, i.e. non-singular. Applying the chain rule to $\boldsymbol{J}$ gives

$$\boldsymbol{J} = \underbrace{\begin{bmatrix} \frac{\partial \xi}{\partial \tilde{\xi}} & 0 & 0 \\ 0 & \frac{\partial \eta}{\partial \tilde{\eta}} & 0 \\ 0 & 0 & \frac{\partial \zeta}{\partial \tilde{\zeta}} \end{bmatrix}}_{\boldsymbol{A}} \underbrace{\begin{bmatrix} \frac{\partial x}{\partial \xi} & \frac{\partial y}{\partial \xi} & \frac{\partial z}{\partial \xi} \\ \frac{\partial x}{\partial \eta} & \frac{\partial y}{\partial \eta} & \frac{\partial z}{\partial \eta} \\ \frac{\partial x}{\partial \zeta} & \frac{\partial y}{\partial \zeta} & \frac{\partial z}{\partial \zeta} \end{bmatrix}}_{\boldsymbol{B}} = \boldsymbol{A}\boldsymbol{B}. \tag{3.49}$$

The determinant of the Jacobian matrix is then

$$\begin{aligned} \det \boldsymbol{J} &= \det \boldsymbol{A} \times \det \boldsymbol{B} \\ &= \frac{\partial \xi}{\partial \tilde{\xi}} \times \frac{\partial \eta}{\partial \tilde{\eta}} \times \frac{\partial \zeta}{\partial \tilde{\zeta}} \times \det \boldsymbol{B}. \end{aligned} \tag{3.50}$$

For the derivatives of the basis functions with respect to the parent domain coordinates, application of the chain rule gives

$$\begin{Bmatrix} \frac{\partial N_i}{\partial \tilde{\xi}} \\ \frac{\partial N_i}{\partial \tilde{\eta}} \\ \frac{\partial N_i}{\partial \tilde{\zeta}} \end{Bmatrix} = \begin{bmatrix} \frac{\partial \xi}{\partial \tilde{\xi}} & 0 & 0 \\ 0 & \frac{\partial \eta}{\partial \tilde{\eta}} & 0 \\ 0 & 0 & \frac{\partial \zeta}{\partial \tilde{\zeta}} \end{bmatrix} \begin{Bmatrix} \frac{\partial N_i}{\partial \xi} \\ \frac{\partial N_i}{\partial \eta} \\ \frac{\partial N_i}{\partial \zeta} \end{Bmatrix} = \boldsymbol{A} \begin{Bmatrix} \frac{\partial N_i}{\partial \xi} \\ \frac{\partial N_i}{\partial \eta} \\ \frac{\partial N_i}{\partial \zeta} \end{Bmatrix}. \tag{3.51}$$

Based on (3.49) and (3.51), (3.48) can now be written as

$$\begin{Bmatrix} \frac{\partial N_i}{\partial x} \\ \frac{\partial N_i}{\partial y} \\ \frac{\partial N_i}{\partial z} \end{Bmatrix} = \boldsymbol{B}^{-1} \begin{Bmatrix} \frac{\partial N_i}{\partial \xi} \\ \frac{\partial N_i}{\partial \eta} \\ \frac{\partial N_i}{\partial \zeta} \end{Bmatrix}. \tag{3.52}$$

The elements of matrix $\boldsymbol{B}$ are calculated from

$$\begin{aligned} \frac{\partial x}{\partial \xi} &= \sum_{i=0}^{n} \frac{\partial N_i}{\partial \xi} x_i, \quad \frac{\partial x}{\partial \eta} = \sum_{i=0}^{n} \frac{\partial N_i}{\partial \eta} x_i, \quad \frac{\partial x}{\partial \zeta} = \sum_{i=0}^{n} \frac{\partial N_i}{\partial \zeta} x_i \\ \frac{\partial y}{\partial \xi} &= \sum_{i=0}^{n} \frac{\partial N_i}{\partial \xi} y_i, \quad \frac{\partial x}{\partial \eta} = \sum_{i=0}^{n} \frac{\partial N_i}{\partial \eta} y_i, \quad \frac{\partial y}{\partial \zeta} = \sum_{i=0}^{n} \frac{\partial N_i}{\partial \zeta} y_i \\ \frac{\partial z}{\partial \xi} &= \sum_{i=0}^{n} \frac{\partial N_i}{\partial \xi} z_i, \quad \frac{\partial z}{\partial \eta} = \sum_{i=0}^{n} \frac{\partial N_i}{\partial \eta} z_i, \quad \frac{\partial z}{\partial \zeta} = \sum_{i=0}^{n} \frac{\partial N_i}{\partial \zeta} z_i. \end{aligned} \tag{3.53}$$

Transformation of the domain, and variables with respect to which the numerical integration is performed, is achieved by using the determinant of $\boldsymbol{J}$. For example,

for a volume element, we have

$$\mathrm{d}x\,\mathrm{d}y\,\mathrm{d}z = \det \boldsymbol{J}\,\mathrm{d}\tilde{\xi}\,\mathrm{d}\tilde{\eta}\,\mathrm{d}\tilde{\zeta}. \tag{3.54}$$

The evaluation of element matrices of the form in $(3.43)_1$ can now be written as

$$\boldsymbol{K}_e = \int_{-1}^{1}\int_{-1}^{1}\int_{-1}^{1} \boldsymbol{G}(\tilde{\xi},\tilde{\eta},\tilde{\zeta}) \det \boldsymbol{J}\,\mathrm{d}\tilde{\xi}\,\mathrm{d}\tilde{\eta}\,\mathrm{d}\tilde{\zeta}. \tag{3.55}$$

The limits of integration in the above equation are simple but algebraic integration cannot be performed because an explicit expression for $\boldsymbol{G}$ is difficult to obtain for most practical problems. The evaluation is thus performed by using numerical integration methods such as Newton-Cotes integration or Gaussian quadrature. We discuss Gaussian quadrature here, which is employed in this thesis.

Gaussian quadrature evaluates an integral as a weighted sum of the values of the function to be integrated at specified points in the integration domain. For a function $f(\xi)$ in one dimension, Gaussian quadrature rule is stated as

$$\int_{-1}^{1} f(\xi)\mathrm{d}\xi = \sum_{i=1}^{n} w_i f(\xi_i) \tag{3.56}$$

where $w_i \in \mathbb{R}$ are called the integration weights at the specified points ξ_i and $i = 1, 2, ..., n$. Application of this to evaluation of an element matrix of the form given in (3.55), starting from the inner integral and proceeding to the outer, gives

$$\begin{aligned} \boldsymbol{K}_e &= \int_{-1}^{1}\int_{-1}^{1}\int_{-1}^{1} \boldsymbol{G}(\tilde{\xi},\tilde{\eta},\tilde{\zeta}) \det \boldsymbol{J}\,\mathrm{d}\tilde{\xi}\,\mathrm{d}\tilde{\eta}\,\mathrm{d}\tilde{\zeta} \\ &= \sum_{k=1}^{n}\sum_{j=1}^{n}\sum_{i=1}^{n} \boldsymbol{G}(\tilde{\xi}_i,\tilde{\eta}_j,\tilde{\zeta}_k) w_i w_j w_k \det \boldsymbol{J} \end{aligned} \tag{3.57}$$

where w_i, w_j and w_k are the integration weights and the functions $\boldsymbol{G}$ are evaluated at the integration points $(\tilde{\xi}_i, \tilde{\eta}_j, \tilde{\zeta}_k)$.

Numerical integration in IGA using high continuity B-Spline or NURBS basis functions and solution of the resulting system of equations may result in high computational costs. Optimizing the efficiency of the numerical integration is studied by some researchers such as Hughes et al. (2010). A detailed study on the performance of IGA using direct and iterative solvers is presented by Collier et al. (2012) and Collier et al. (2013), respectively.

3.6.6 Assembly and Solution

The element matrices and vectors computed using numerical integration are assembled for all knot spans (elements) in the patch (for a single patch domain) or for all patches (for a multiple patch domain). The assembly process for element matrices $\boldsymbol{K}_e$ and vectors $\boldsymbol{f}_e$ can be mathematically described as

$$\boldsymbol{K} = \mathop{\mathsf{A}}_{e=1}^{n_e}(\boldsymbol{K}_e) \quad \text{and} \quad \boldsymbol{f} = \mathop{\mathsf{A}}_{e=1}^{n_e}(\boldsymbol{f}_e) \tag{3.58}$$

where A is an assembly operator, following the notation of Hughes (2012), and n_e is the total number of knot spans in the whole domain.

After assembling the element matrices and vectors over the whole domain, for all patches, we end up with a system of matrix equations to be solved for the unknown field variables. Depending on the type of the problem, the final system of matrix equations may be linear or nonlinear. A linear system of equations takes the form

$$\boldsymbol{K}\boldsymbol{u}^{\mathrm{c}} = \boldsymbol{f} \tag{3.59}$$

and may be solved for the unknown field variables using the appropriate solvers. A typical structure of a nonlinear system of matrix equations is given by

$$\boldsymbol{K}(\boldsymbol{u}^{\mathrm{c}})\boldsymbol{u}^{\mathrm{c}} = \boldsymbol{f} \tag{3.60}$$

where we have solution dependent coefficient matrices $\boldsymbol{K}(\boldsymbol{u}^{\mathrm{c}})$. These types of equations are solved in an iterative way using, for example, the Newton-Raphson method. This requires calculating the residual and requiring it to vanish i.e.

$$\boldsymbol{R}(\boldsymbol{u}^{\mathrm{c}}) = \boldsymbol{K}(\boldsymbol{u}^{\mathrm{c}})\boldsymbol{u}^{\mathrm{c}} - \boldsymbol{f} = \boldsymbol{0}. \tag{3.61}$$

Linearizing the residual using Taylor series expansion about $\boldsymbol{u}_i^{\mathrm{c}}$ and neglecting higher-order terms gives

$$\boldsymbol{R}(\boldsymbol{u}_{i+1}^{\mathrm{c}}) = \boldsymbol{R}(\boldsymbol{u}_i^{\mathrm{c}}) + \frac{\partial \boldsymbol{R}(\boldsymbol{u}_i^{\mathrm{c}})}{\partial \boldsymbol{u}_i^{\mathrm{c}}}\delta\boldsymbol{u}^{\mathrm{c}} = \boldsymbol{0} \tag{3.62}$$

where $\delta\boldsymbol{u}^{\mathrm{c}} = \boldsymbol{u}_{i+1}^{\mathrm{c}} - \boldsymbol{u}_i^{\mathrm{c}}$. The equation above can now be solved for $\delta\boldsymbol{u}^{\mathrm{c}}$ from

$$\boldsymbol{J}\delta\boldsymbol{u}^{\mathrm{c}} = -\boldsymbol{R}(\boldsymbol{u}_i^{\mathrm{c}}) \tag{3.63}$$

where $\boldsymbol{J} = \frac{\partial \boldsymbol{R}(\boldsymbol{u}_i^{\mathrm{c}})}{\partial \boldsymbol{u}_i^{\mathrm{c}}}$ is called the Jacobian matrix. The solution at each iteration is then updated using

$$\boldsymbol{u}_{i+1}^{\mathrm{c}} = \boldsymbol{u}_i^{\mathrm{c}} + \delta\boldsymbol{u}^{\mathrm{c}}. \tag{3.64}$$

We have herein overlooked temporal discretization for time-dependent problems. The structure of the final matrix equations, however, takes a similar form as in the above cases with the left and right hand sides of the equation being dependent on current and/or previous time step solutions. This depends on the type of temporal discretization method employed.

Part II

Papers

Paper I:

Adaptive Isogeometric Finite Element Analysis of Steady-state Groundwater Flow

International Journal for Numerical and Analytical Methods in Geomechanics

40(5):738-765, 2016. DOI: 10.1002/nag.2425

INTERNATIONAL JOURNAL FOR NUMERICAL AND ANALYTICAL METHODS IN GEOMECHANICS
Int. J. Numer. Anal. Meth. Geomech. 2016; **40**:738–765
Published online 5 September 2015 in Wiley Online Library (wileyonlinelibrary.com). DOI: 10.1002/nag.2425

Adaptive isogeometric finite element analysis of steady-state groundwater flow

Yared W. Bekele[1,*,†], Trond Kvamsdal[2], Arne M. Kvarving[3] and Steinar Nordal[1]

[1]*Department of Civil and Transport Engineering, Norwegian University of Science and Technology, Trondheim, Norway*
[2]*Department of Mathematical Sciences, Norwegian University of Science and Technology, Trondheim, Norway*
[3]*Department of Applied Mathematics, SINTEF ICT, Trondheim, Norway*

SUMMARY

Numerical challenges occur in the simulation of groundwater flow problems because of complex boundary conditions, varying material properties, presence of sources or sinks in the flow domain, or a combination of these. In this paper, we apply adaptive isogeometric finite element analysis using locally refined (LR) B-splines to address these types of problems. The fundamentals behind isogeometric analysis and LR B-splines are briefly presented. Galerkin's method is applied to the standard weak formulation of the governing equation to derive the linear system of equations. A posteriori error estimates are calculated to identify which B-splines should be locally refined. The error estimates are calculated based on recovery of the L_2-projected solution. The adaptive analysis method is first illustrated by performing simulation of benchmark problems with analytical solutions. Numerical applications to two-dimensional groundwater flow problems are then presented. The problems studied are flow around an impervious corner, flow around a cutoff wall, and flow in a heterogeneous medium. The convergence rates obtained with adaptive analysis using local refinement were, in general, observed to be of optimal order in contrast to simulations with uniform refinement.

Received 22 February 2015; Revised 24 July 2015; Accepted 3 August 2015

KEY WORDS: adaptive refinement; isogeometric analysis; a posteriori error estimates; groundwater flow

1. INTRODUCTION

Finite element (FE) modeling of groundwater flow problems has been a subject extensively studied by several researchers over the past decades. The earliest studies which addressed this problem include the finite element analysis (FEA) of seepage through dams by Finn [1], Galerkin's method in aquifer analysis by Pinder and Frind [2], FE modeling of flow in saturated–unsaturated porous media by Reeves and Duguid [3], and a three-dimensional FE model for a multi-aquifer system by Gupta *et al.* [4]. Some studies proposed improvements to the FE modeling of groundwater flow based on the numerical challenges observed in previous studies. Yeh [5] proposed an approach to eliminate problems of discontinuity in the Darcy velocity field, which results when taking the derivatives of the FE computed pressure field. Botha and Bakkes [6] studied the convergence of the Galerkin FE method when applied to groundwater flow problems, with special reference to quadrature effects and the accuracy of the solution. Tharp [7] presented an enriched FE simulation of groundwater flow by introducing a new quadrilateral element to enable accurate modeling with coarse meshes. Dogrul and Kadir [8] presented an FE post-processing technique to compute mass conserving flow rates at element faces.

*Correspondence to: Yared Worku Bekele, Department of Civil and Transport Engineering, Norwegian University of Science and Technology, NO-7491, Trondheim, Norway.
†E-mail: yared.bekele@ntnu.no

The numerical challenges that occur in the simulation of groundwater flow problems may be induced by the complexity of the boundary conditions in the flow domain, the varying hydraulic conductivity properties of the porous material, and the presence of sources or sinks, such as an infiltration well, or a combination of these. One of the approaches used to treat such numerical difficulties is to superpose an analytical solution in the vicinity of the problem area with a numerical model in the rest of the domain. Analytical solutions are, however, difficult to obtain for most physical problems involving groundwater flow. The other approach is to use special numerical techniques to address the singularity or discontinuity problems. We briefly look at some of the techniques proposed by some researchers for different types of problems.

Some of the singularities that arise in the numerical simulation of groundwater flow were studied and discussed by Lafe *et al.* [9]. The singularities considered are flow around a sharp corner where the velocity goes to infinity, flow between zones of different hydraulic conductivity, flow around a cutoff wall and the presence of sources or sinks in the flow domain. The effects of the different singularities were studied and discussed. Weak singularities as in the case of flow between zones of varying hydraulic conductivity were treated by concentrating integration points at the area of the singularity. The use of special elements is recommended for stronger singularities such as flow around a cutoff wall.

Groundwater flow with a free seepage surface is one of the problems that requires a special treatment due to the complex boundary conditions. The derivative of the hydraulic potential goes to infinity at the point of intersection between the free surface and the downstream face of the dam. Even though we are not dealing with a free surface problem in the present work, we review the numerical techniques proposed by various researchers as it is a related problem to our scope. Liang and Zhang [10] presented a mathematical study of the FE method for a unidimensional single-phase nonlinear free boundary problem in groundwater flow. Neuman and Witherspoon [11] proposed an iterative approach to steady seepage of groundwater with a free surface. Larabi and De Smedt [12] studied the numerical solution of groundwater flow involving free boundaries by a fixed FE method by iteratively adjusting the moving boundaries. An adaptive FE approach for the free surface seepage problem was presented by Rank and Werner [13]. They used a posteriori error estimates and adaptive mesh refinement such that the influence of singularities on the convergence rate disappears. Sharif and Wiberg [14] used an interface-capturing technique to solve seepage flow problems with free surface in porous media and studied two and three-dimensional seepage through dams. The performance of an FE adaptive mesh algorithm for seepage flow with a free surface was analyzed by Borieu and Bruch [15]. The algorithm was especially tested in order to enable parallel computations. A slightly different approach to the free surface problem was presented by Jie *et al.* [16] where they apply the natural element method by constructing shape functions based on Voroni diagrams. They argue that the method is more suitable for the analysis of seepage problems with a free surface than the FE method. Adaptive error analysis for seepage problems was presented by Burkley and Bruch [17] based on the Zienkiewicz–Zhu error estimator.

The other source of numerical challenges in the computation of groundwater flow problems is the complexity of the material properties in the flow domain. Flow between zones of different hydraulic conductivity represents a less severe discontinuity which may be treated by a finer mesh at the intersection of the different zones. Heterogeneous aquifers, on the other hand, represent a more complex case. Smaoui *et al.* [18] studied the modeling of groundwater flow in heterogeneous porous media by the FE method. Cao and Kitanidis [19] presented a methodology for the computation of flow in a heterogeneous isotropic formation using adaptive mesh refinement. Dual equations with hydraulic head and stream function were solved numerically. They claim that the application of a standard FE method requires a large number of nodes to model flow in high-contrast formations. However, the number of unknowns to achieve a certain accuracy may be reduced by adaptive mesh refinement procedures that rely on a posteriori error estimates to identify areas where refinements are most needed.

The presence of sources or sinks in the flow domain creates areas of large changes in the hydraulic gradient. Such a problem for unconfined aquifers with an infiltration well was studied using adaptive mesh refinement by George and Thomas [20]. They performed simulation on flow domains with isotropic as well as heterogeneous hydraulic conductivity fields. The simulations were performed

DOI: 10.1002/nag

starting with a coarse mesh, and refinement or coarsening steps were applied depending on the computed errors.

In this paper, we address some of the numerical challenges observed in computational models for groundwater flow problems using adaptive isogeometric FEA. We use LR B-splines, first proposed by Dokken *et al.* [21], and later applied to adaptive isogeometric analysis (IGA) by Johannessen *et al.* [22]. First, the governing equations of steady-state groundwater flow are presented. The fundamentals of IGA are then briefly discussed by introducing B-splines and non-uniform rational B-splines (NURBS). LR B-splines, which allow local refinement unlike B-splines and NURBS, are then presented. In the numerical examples section, the method is first applied to benchmark problems with analytical solutions and then to flow problems around an impervious corner, around a cutoff wall and in a heterogeneous formation.

2. GOVERNING EQUATIONS

The governing equation for groundwater flow can be obtained by deriving the fluid mass conservation equation for a given porous medium. The general form of the governing equation for groundwater flow is given by

$$S\frac{\partial h}{\partial t} = \frac{\partial}{\partial x}\left(k_x(h)\frac{\partial h}{\partial x}\right) + \frac{\partial}{\partial y}\left(k_y(h)\frac{\partial h}{\partial y}\right) + \frac{\partial}{\partial z}\left(k_z(h)\frac{\partial h}{\partial z}\right) + f \tag{1}$$

where S is the so-called specific storativity, h is the unknown hydraulic head, k_x, k_y, and k_z are the components of the hydraulic conductivity matrix along the principal axes, and f represents a source or sink term for the flow. The aforementioned equation generally represents transient groundwater flow, that is, the hydraulic head varies with time, and the flow may be saturated or unsaturated. Unsaturated flow is characterized by a condition where the hydraulic conductivity is a function of the unknown hydraulic head. In this paper, we are interested in saturated flow under steady-state conditions. For such a case, the governing equation reduces to

$$\frac{\partial}{\partial x}\left(k_x\frac{\partial h}{\partial x}\right) + \frac{\partial}{\partial y}\left(k_y\frac{\partial h}{\partial y}\right) + \frac{\partial}{\partial z}\left(k_z\frac{\partial h}{\partial z}\right) + f = 0 \tag{2}$$

which may be written in a more compact form as

$$\nabla \cdot (\mathbf{k}\nabla h) + f = 0 \tag{3}$$

where $\mathbf{k}$ is the hydraulic conductivity matrix for general three-dimensional condition given by

$$\mathbf{k} = \begin{bmatrix} k_x & 0 & 0 \\ 0 & k_y & 0 \\ 0 & 0 & k_z \end{bmatrix} \tag{4}$$

The hydraulic head represents the total energy driving the flow and is expressed per unit weight at any point in the flow domain as

$$h = \frac{p^w}{\gamma^w} + z + \frac{v^2}{2g} \tag{5}$$

where p^w/γ^w is the pressure head, γ^w is the unit weight of water, z is the elevation head, and $v^2/2g$ is the velocity head, with g being the acceleration due to gravity. The velocity head is usually neglected because steady-state groundwater flow velocities are usually very small. It can be shown that the first term in Eq. (3) represents the divergence of Darcy's velocity, which is given by

$$\mathbf{v} = -\frac{1}{\gamma^w}\mathbf{k}\left(\nabla p^w - \rho^w \mathbf{g}\right) \tag{6}$$

DOI: 10.1002/nag

for a flow driven by pressure gradients and gravity $\mathbf{g} = -g\nabla z$. We can now introduce the proper boundary conditions and write the strong form of the problem as

$$\begin{aligned} \nabla \cdot \mathbf{v} &= f \quad \text{in } \Omega \\ p^w &= \hat{p}^w \quad \text{on } \Gamma_D \\ \mathbf{v} \cdot \mathbf{n} &= q^w \quad \text{on } \Gamma_N \end{aligned} \tag{7}$$

where Ω represents the groundwater flow domain, $\hat{p}^w$ is the imposed pressure on the Dirichlet boundary Γ_D, q^w is the water flux on the Neumann boundary Γ_N, and $\mathbf{n}$ is the normal to the boundary. Here, we have the overall boundary to Ω as $\Gamma = \Gamma_N \cup \Gamma_D$. The pressure $p^w : \Omega \to \mathbb{R}$ is our primary unknown, and the Darcy velocity $\mathbf{v} : \Omega \to \mathbb{R}$ can be determined as a secondary solution.

3. ISOGEOMETRIC ANALYSIS

3.1. Fundamentals

Since its first introduction by Hughes *et al.* [23], IGA has been successfully applied to several areas of engineering mechanics problems. The fundamental aim for the introduction of IGA was the idea of bridging the gap between computer-aided design (CAD) and FEA. The main concept behind the method is the application of the same basis functions used in CAD for performing FEA. In the process of its application to various engineering problems, IGA has shown advantages over the conventional FE method, for instance, the ease of performing simulations using elements with higher-order continuity.

The current standard basis functions in CAD are B-splines and NURBS. To overcome the limitations of B-splines and NURBS, such as water tightness in CAD and local refinement in analysis, other spline technologies have been proposed. These include T-Splines introduced by Sederberg *et al.* [24] and LR B-splines by Dokken *et al.* [21]. In this paper, LR B-splines are used for the simulation of steady-state seepage problems. Prior to that, the fundamental concepts behind IGA are briefly presented here for reference.

3.1.1. B-splines and NURBS. We start the discussion on B-splines and NURBS by first defining a *knot vector*. A knot vector in one dimension is a non-decreasing set of coordinates in the parameter space, written as $\Xi = \{\xi_1, \xi_2, \ldots, \xi_{n+p+1}\}$, where $\xi_i \in \mathbb{R}$ is the i^{th} knot, i is the knot index, $i = 1, 2, \ldots, n + p + 1$, p is the polynomial order, and n is the number of basis functions. Knot vectors may be uniform or non-uniform depending on whether the knots are equally spaced in the parameter space or not.

A univariate B-spline curve is parameterized by a linear combination of n B-spline basis functions, $\{N_{i,p}\}_{i=1}^{n}$. The coefficients corresponding to these functions, $\{\mathbf{B}_i\}_{i=1}^{n}$, are referred to as control points. The B-spline basis functions are recursively defined starting with piecewise constants ($p = 0$)

$$N_{i,0}(\xi) = \begin{cases} 1 \text{ if } \xi_i \le \xi < \xi_{i+1} \\ 0 \text{ otherwise} \end{cases} \tag{8}$$

For higher-order polynomial degrees ($p \ge 1$), the basis functions are defined by the Cox–de Boor recursion formula

$$N_{i,p}(\xi) = \frac{\xi - \xi_i}{\xi_{i+p} - \xi_i} N_{i,p-1}(\xi) + \frac{\xi_{i+p+1} - \xi}{\xi_{i+p+1} - \xi_{i+1}} N_{i+1,p-1}(\xi) \tag{9}$$

B-spline geometries, curves, surfaces, and solids are constructed from a linear combination of B-spline basis functions. Given n basis functions $N_{i,p}$ and corresponding control points $\mathbf{B}_i \in \mathbb{R}^d, i = 1, 2, \ldots, n$, a piecewise polynomial B-spline curve is given by

$$\mathbf{C}(\xi) = \sum_{i=1}^{n} N_{i,p}(\xi)\mathbf{B}_i \tag{10}$$

DOI: 10.1002/nag

Similarly, for a given control net $\mathbf{B}_{i,j}, i = 1, 2, \ldots, n, j = 1, 2, \ldots, m$, polynomial orders p and q, and knot vectors $\Xi = \{\xi_1, \xi_2, \ldots, \xi_{n+p+1}\}$ and $\mathcal{H} = \{\eta_1, \eta_2, \ldots, \eta_{m+q+1}\}$, a tensor product B-spline surface is defined by

$$\mathbf{S}(\xi, \eta) = \sum_{i=1}^{n} \sum_{j=1}^{m} N_{i,p}(\xi) M_{j,q}(\eta) \mathbf{B}_{i,j} \tag{11}$$

B-spline solids are constructed in a similar way as B-spline surfaces from tensor products over a control lattice.

Non-uniform rational B-splines are built from B-splines to represent a wide array of objects that cannot be exactly represented by polynomials. An NURBS entity in $\mathbb{R}^d$ is obtained by projective transformation of a B-spline entity in $\mathbb{R}^{d+1}$. The control points for the NURBS geometry are found by performing exactly the same projective transformation to the control points of the B-spline curve.

More about B-splines and NURBS in an IGA setting can be found in [25].

3.1.2. LR B-splines. LR B-splines were proposed to overcome the limitation of B-splines and NURBS with respect to local refinement. B-splines and NURBS are formulated as tensor products of univariate B-splines, and thus, refinement in one of the univariate B-splines will cause the insertion of an entire new row or column of knots in the bivariate spline space. LR B-splines were first used in (adaptive) IGA by Johannessen *et al.* [22].

For a short description of LR B-splines, local knot vectors are defined first. A given knot vector Ξ can be used to construct i local knot vectors Ξ_i, from the components of the original knot vector. A single B-spline of degree p may then be defined, using local knot vectors, as a separable function defined by n non-decreasing local knot vectors Ξ_i and the degrees p_i

$$B_{\Xi}(\xi) = \prod_{i=1}^{n} B_{\Xi_i}(\xi_i) \tag{12}$$

To ensure that LR B-splines maintain the partition of unity property, a scalar weight $\gamma \in [0, 1]$ is introduced to define a weighted B-spline as

$$B_{\Xi}^{\gamma}(\xi) = \gamma \prod_{i=1}^{n} B_{\Xi_i}(\xi_i) \tag{13}$$

Next, we define box mesh, tensor mesh and LR mesh. A box mesh is a partitioning of a two-dimensional rectangular domain into smaller rectangles by horizontal and vertical lines. A tensor mesh is a box mesh where there are no T-joints, that is, all horizontal and vertical lines span the entire length. An LR mesh $\mathcal{M}_n$ is a box mesh, which results from a series of single line insertions from an initial tensor mesh $\mathcal{M}_0$, and each intermediate mesh is also a box mesh. A box mesh, tensor mesh, or LR mesh with *multiplicities* is a mesh where each line segment has a corresponding integer value n, called the line multiplicity. Each multiplicity must satisfy $0 < n \leq p$, where p is the polynomial degree. These mesh types are illustrated in Figure 1(a)–(c).

The *support* of a (weighted) B-spline $B(\xi, \eta) = \gamma B_{\Xi}(\xi) B_{\mathcal{H}}(\eta)$ is the closure of all points where it takes nonzero value, where $\Xi = \{\xi_0, \xi_1, \ldots, \xi_{p_1+1}\}$ and $\mathcal{H} = \{\eta_0, \eta_1, \ldots, \eta_{p_1+1}\}$. A weighted

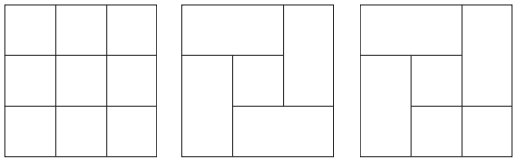

(a) Tensor mesh (b) Box mesh (c) LR mesh

Figure 1. Mesh types, after [22].

DOI: 10.1002/nag

B-spline has *minimal support* on an LR Mesh $\mathcal{M}$ if for every horizontal and vertical line of multiplicity n in the mesh $\mathcal{M}$ that traverses the support of the B-spline, there exist unique knot(s) corresponding to the lines depending on whether the lines traverse the interior or the edge of the B-spline.

We can now define LR B-splines based on the terminologies presented earlier. For a given LR Mesh $\mathcal{M}$, a function B is called an *LR B-spline* on $\mathcal{M}$ if $B_{\Xi}^{\gamma}(\xi) = \gamma B_{\Xi}(\xi) B_{\mathcal{H}}(\eta)$ is a weighted B-spline where all knot lines (and the knot line multiplicities) in Ξ and $\mathcal{H}$ are also in $\mathcal{M}$, and B has a minimal support on $\mathcal{M}$.

A given B-spline basis can be enriched by knot insertion without changing the geometric description. To insert a knot $\hat{\xi}$ into the knot vector Ξ between the knots ξ_{i-1} and ξ_i, we use the relation

$$B_{\Xi}(\xi) = \alpha_1 B_{\Xi_1}(\xi) + \alpha_2 B_{\Xi_2}(\xi) \tag{14}$$

where

$$\begin{aligned} \alpha_1 &= \begin{cases} 1, & \xi_{p+1} \le \hat{\xi} \le \xi_{p+2} \\ \frac{\hat{\xi}-\xi_1}{\xi_{p+1}-\xi_1}, & \xi_1 \le \hat{\xi} \le \xi_{p+1} \end{cases} \\ \alpha_2 &= \begin{cases} \frac{\xi_{p+2}-\hat{\xi}}{\xi_{p+2}-\xi_2}, & \xi_2 \le \hat{\xi} \le \xi_{p+2} \\ 1, & \xi_1 \le \hat{\xi} \le \xi_2 \end{cases} \end{aligned} \tag{15}$$

and the knot vectors are

$$\begin{aligned} \Xi &= \left[\xi_1, \xi_2, \ldots, \xi_{i-1}, \quad \xi_i, \ldots, \xi_{p+1}, \xi_{p+2}\right] \\ \Xi_1 &= [\xi_1, \xi_2, \ldots, \xi_{i-1}, \hat{\boldsymbol{\xi}}, \xi_i, \ldots, \xi_{p+1}] \\ \Xi_2 &= [\quad \xi_2, \ldots, \xi_{i-1}, \hat{\boldsymbol{\xi}}, \xi_i, \ldots, \xi_{p+1}, \xi_{p+2}] \end{aligned} \tag{16}$$

The insertion of the knot $\hat{\xi}$ into Ξ yields a knot vector of size $p+3$, generating two B-splines described by the local knot vectors Ξ_1 and Ξ_2, both of size $p+2$.

Refinement by knot insertion using the aforementioned technique is illustrated on the B-splines given by the local knot vectors $\Xi_2 = [0,0,1,2]$, $\Xi_3 = [0,1,2,3]$ and $\Xi_4 = [1,2,3,3]$, all derived from the knot vector $\Xi = [0,0,0,1,2,3,3,4,4,4]$. For example, if we want to insert $\hat{\xi} = 3/2$ into the knot vector Ξ_3 between knots $\xi_2 = 1$ and $\xi_3 = 2$, this implies values of $\alpha_1 = \alpha_2 = 3/4$, and the resulting split is shown in Figure 2(b). Similarly, the resulting B-spline splits when inserting $\hat{\xi} = 3/2$ in Ξ_2 and Ξ_4 are shown in Figure 2(a) and (c).

Bivariate functions are refined in one parametric domain at a time. If we have a knot vector Ξ in the first parametric direction, and $\mathcal{H}$ in the second, we obtain a B-spline $B_{\Xi,\mathcal{H}}(\xi,\eta) = B_{\Xi}(\xi) B_{\mathcal{H}}(\eta)$. Splitting in one direction is achieved by

$$\begin{aligned} B_{\Xi}(\xi,\eta) &= B_{\Xi}(\xi) B_{\mathcal{H}}(\eta) \\ &= \left(\alpha_1 B_{\Xi_1}(\xi) + \alpha_2 B_{\Xi_2}(\xi)\right) B_{\mathcal{H}}(\eta) \\ &= \alpha_1 B_{\Xi_1}(\xi,\eta) + \alpha_2 B_{\Xi_2}(\xi,\eta) \end{aligned} \tag{17}$$

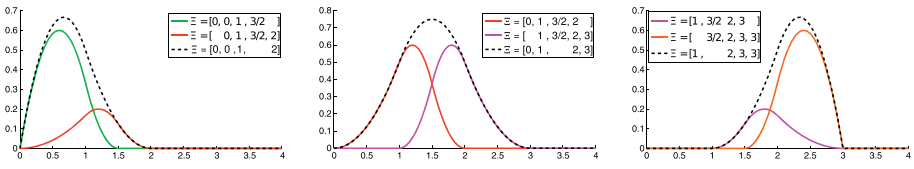

(a) Split of Ξ_2 (b) Split of Ξ_3 (c) Split of Ξ_4

Figure 2. Knot insertion example for LR B-splines, after [22].

DOI: 10.1002/nag

For a weighted B-spline, we have

$$\begin{aligned} B^{\gamma}_{\Xi}(\xi,\eta) &= \gamma B_{\Xi}(\xi) B_{\mathcal{H}}(\eta) \\ &= \gamma \left(\alpha_1 B_{\Xi_1}(\xi) + \alpha_2 B_{\Xi_2}(\xi)\right) B_{\mathcal{H}}(\eta) \\ &= B^{\gamma_1}_{\Xi_1}(\xi,\eta) + B^{\gamma_2}_{\Xi_2}(\xi,\eta) \end{aligned} \tag{18}$$

where $\gamma_1 = \alpha_1\gamma$ and $\gamma_2 = \alpha_2\gamma$.

LR B-splines form a partition of unity, that is,

$$\sum_{i=1}^{n} \gamma_i B_i(\xi) = 1 \tag{19}$$

To control adaptive refinement in IGA with LR B-splines, we introduce a refinement parameter β. The refinement parameter β is defined such that two LR B-splines $\mathcal{L}_{i-1}$ and $\mathcal{L}_i$ satisfy

$$\mathcal{L}_{i-1} \subset \mathcal{L}_i \qquad \text{and} \qquad (1+\beta)|\mathcal{L}_{i-1}| \leq |\mathcal{L}_i| \tag{20}$$

which states that $\mathcal{L}_i$ should be a refinement of $\mathcal{L}_{i-1}$, and the number of B-splines should grow by at least β percent during each iteration. Thus, β in this case represents the growth rate of the number of basis functions in the solution space, that is, if we have n degrees of freedom at refinement step i, we will have, at least, $n \times (1 + \beta/100)$ degrees of freedom at refinement step $i + 1$. We could also choose β to represent the percentage of elements with the largest error contribution to be refined. For the numerical examples in this paper, β refers to the growth rate of the basis functions. The value of β in a simulation is selected such that the adaptive simulation is as efficient and as accurate as possible. Smaller values for β result in a more accurate adaptive refinement, while larger values reduce the number of refinement steps, and thereby the computation time. Typical values are in the range $5\% \leq \beta \leq 20\%$, [22].

3.2. Variational formulation

In this section, we present the weak formulation of the governing equation. Our aim is to solve the following equation:

$$\nabla \cdot \left[-\frac{1}{\gamma^w} \mathbf{k} \left(\nabla p^w - \rho^w \mathbf{g} \right) \right] = f$$

for the pressure p^w with the boundary conditions given in Eq. (7). The standard weak formulation is derived by applying a differentiable test function v to the previous equation, integrating over the domain Ω and applying Green's theorem to the integrand with the divergence operator. We can write a proper statement of the weak form as follows:

Find $p^w \in V$ such that

$$a(p^w, v) = L(v) \qquad \forall v \in \hat{V} \tag{21}$$

where

$$\begin{aligned} a(p^w, v) &= \int_{\Omega} \nabla v \cdot \frac{1}{\gamma^w} \mathbf{k} \cdot \nabla p^w \, \mathrm{d}\Omega \\ L(v) &= \int_{\Omega} f v \, \mathrm{d}\Omega + \int_{\Omega} \nabla v \cdot \frac{1}{\gamma^w} \mathbf{k} \cdot \rho^w \mathbf{g} \, \mathrm{d}\Omega - \int_{\Gamma_N} q^w v \, \mathrm{d}\Gamma \end{aligned} \tag{22}$$

The trial and test spaces V and $\hat{V}$ are defined as

$$\begin{aligned} V &= \left\{ v \in H^1(\Omega) : v = \hat{p}^w \quad \text{on} \quad \Gamma_D \right\} \\ \hat{V} &= \left\{ v \in H^1(\Omega) : v = 0 \quad \text{on} \quad \Gamma_D \right\} \end{aligned} \tag{23}$$

DOI: 10.1002/nag

3.3. Galerkin finite element formulation

The FE approximation corresponding to the variational formulation given in Eq. (21) reads: Find $p_h^w \in V_h$ such that

$$a(p_h^w, v_h) = L(v_h) \qquad \forall v_h \in \hat{V}_h \tag{24}$$

where p_h^w is the FE approximation to the pressure field, v_h is the FE test function, and for compatible FE trial and test spaces, we have $V_h \subset V$ and $\hat{V}_h \subset \hat{V}$, respectively. Notice that the dimensions for $\hat{V}$ and V are infinite, whereas the dimensions for $\hat{V}_h$ and V_h are finite (i.e., equal to the number of FE basis functions).

The FE pressure may be written as a linear combination of the FE basis functions $\mathbf{N}$ and the nodal values (control point values in IGA) $\bar{\mathbf{p}}^w$ as

$$p_h^w = \mathbf{N}\bar{\mathbf{p}}^w \tag{25}$$

Applying Galerkin's method, the test functions in the weak form are chosen to be the same as the shape functions (after the non-homogeneous Dirichlet boundary conditions are taken care of, that is, their effect is moved to the right hand side). Thus, when applied to the weak form in Eq. (21), this results in the following linear matrix equation:

$$\mathbf{A}\bar{\mathbf{p}}^w = \mathbf{b} \tag{26}$$

where

$$\begin{aligned} \mathbf{A} &= \int_\Omega (\nabla \mathbf{N})^T \frac{1}{\gamma^w} \mathbf{k} \, (\nabla \mathbf{N}) \mathrm{d}\Omega \\ \mathbf{b} &= \int_\Omega \mathbf{N} f \, \mathrm{d}\Omega + \int_\Omega (\nabla \mathbf{N})^T \frac{1}{\gamma^w} \mathbf{k} \, \rho^w \mathbf{g} \mathrm{d}\Omega - \int_{\Gamma_N} \mathbf{N} q^w \mathrm{d}\Gamma \end{aligned} \tag{27}$$

4. ERROR ESTIMATES AND ADAPTIVITY

4.1. Introduction

In this section, we discuss the procedures for calculating a posteriori error estimates based on recovery of the computed solution. The adaptive mesh refinement strategies based on the error criteria are also discussed.

Since the 1970s, several strategies have been developed to estimate the discretization error of an FE solution. Babuska and Rheinboldt presented the pioneering effort in this regard back in 1978 [26, 27]. Since then, many different estimation procedures have been introduced (see [28] for an overview). A popular class of error estimators denoted as *recovery-based estimators* consist of deriving a simple smoothing technique that yields a solution field or, more commonly, the gradient of the solution, that converges faster than the FE solution or its gradient, respectively. A very popular prototype for such approaches is the Zienkiewicz–Zhu error estimate (so-called ZZ estimate). Initial reference to such estimates can be found in [29], and further development with *superconvergent patch recovery* (SPR) in [30, 31]. The success of this approach in the engineering community relies on an intuitive mechanical definition and a certain ease of implementation compared with other class of available error estimates, without sacrificing the numerical effectivity.

The second author of this paper has more than two decades of experience in developing and implementing a posteriori error estimators. First, in [32] and [33], we extended the SPR procedure by recovering statically admissible stress fields for plane stress and Reissner–Mindlin plates, respectively. Then, goal-oriented recovery of stresses in elasticity and surface forces (drag and lift) for Stokes problems were developed and presented in the papers [34, 35], and [36], respectively. Object-oriented implementation of the SPR recovery procedures is described in [37] and [38]. Recently, we have developed a posteriori error estimates for IGA (see [39] and [40]). The first paper gives an extensive study of different recovery-based error estimators. Furthermore, it presents, for the first time, a true *superconvergent* patch recovery method for adaptive IGA using LR B-splines.

DOI: 10.1002/nag

Our main aim with the present paper is to show the possibilities that open up with adaptive IGA using LR B-splines. An open-source package for using LR B-splines may be downloaded at http://lrbsplines.com/. However, anyone who wants to perform adaptive IGA using LR B-splines will have to implement an algorithm for a posteriori error estimation. Based on the experiences mentioned previously, we have chosen herein to use a simple a posteriori error estimator, the continuous global L_2 (CGL2) projection, as first presented in [29] for FE and in [40] for IGA, as it gives reasonably good results and is easy to implement.

4.2. A priori error estimates

Let p^w and p_h^w represent the exact and isogeometric FE solutions, respectively. The discretization error in the pressure, e, and the error in the pressure gradient, e_σ, are defined as

$$\begin{aligned} e &:= p^w - p_h^w \\ e_\sigma &:= \nabla p^w - \nabla p_h^w \end{aligned} \tag{28}$$

Introducing the error norms in L_2 corresponding to e and e_σ

$$\begin{aligned} \|e\|_{L^2(\Omega)} &:= \|p^w - p_h^w\|_{L^2(\Omega)} = \left(\int_\Omega \left(p^w - p_h^w\right)^2 \mathrm{d}\Omega \right)^{1/2} \\ \|e_\sigma\|_{L^2(\Omega)} &:= \|\nabla p^w - \nabla p_h^w\|_{L^2(\Omega)} = \left(\int_\Omega \left(\nabla p^w - \nabla p_h^w\right)^T \left(\nabla p^w - \nabla p_h^w\right) \mathrm{d}\Omega \right)^{1/2} \end{aligned} \tag{29}$$

Steady-state groundwater flow is a self-adjoint problem, and it follows that the computed FE solution is optimal in energy norm. The energy norm using the bilinear form from Section 3.2 is given by (which is equivalent to seminorm of error e on $H_0^1(\Omega)$)

$$\|e\|_E = \sqrt{a(e,e)} = |e|_{H_0^1(\Omega)} \tag{30}$$

which is the same as

$$\|e\|_E = \left(\int_\Omega \left(\nabla p^w - \nabla p_h^w\right)^T \frac{1}{\gamma^w} \mathbf{k} \left(\nabla p^w - \nabla p_h^w\right) \mathrm{d}\Omega \right)^{1/2} \tag{31}$$

If the analytical solution of a variational problem involving first-order differentiation (as is the case herein) is sufficiently smooth, that is, $p^w \in H^{p+1}$, and the FE mesh $\mathcal{M}_0$ is regular and quasi-uniform, the error in the approximate FE solution on a family of uniformly refined meshes $\{\mathcal{M}_k\}$ is bounded by

$$\|p^w - p_h^w\|_E = C h^p \|p^w\|_{H^{p+1}} \tag{32}$$

where C is some problem-dependent constant, h is the characteristic size of the finite elements, p is the degree of the largest complete polynomial in the FE basis functions, and $||p^w||_{H^{p+1}}$ denotes the Sobolev norm of order $p+1$.

For problems where the solution is not sufficiently smooth, $p^w \notin H^{p+1}$, for example, problems with singular points within the solution domain or on its boundary, we have the error bound

$$\|p^w - p_h^w\|_E = C h^\alpha \|p^w\|_{H^{\alpha+1}} \tag{33}$$

where the value of the non-negative real parameter α depends on how the family of meshes $\{\mathcal{M}_k\}$ are created.[‡] Assume that λ is a real number characterizing the strength of the singularity. For a sequence of uniformly, or nearly uniformly, refined meshes we then have

$$\alpha = \min\{p, \lambda\}. \tag{34}$$

[‡]As α is not necessarily an integer, $\|p^w\|_{H^{\alpha+1}}$ is a *a Sloboditskii* norm.

DOI: 10.1002/nag

Thus, when $\lambda < p$, the rate of convergence is limited by the strength of the singularity and not the polynomial order.

4.3. A posteriori error estimates

The a priori error estimates do not give any quantification of the error for a simulation with a given mesh and a spline space; we only obtain information about the expected convergence rate. However, in order to perform an adaptive refinement, we need to quantify the error distribution throughout the mesh, that is, on each element. For this, we use *a posteriori error estimates* that in one way or another are based on the computed FE solution p_h^w. A popular approach for a posteriori error estimation is based on post-processing the gradients of the FE computed pressure solution, as the FE computed pressure gradient, ∇p_h^w, can be improved by global projection or local smoothing.

As mentioned previously, we use herein CGL2 projection to obtain the improved gradients ∇p_r^w. The improved convergence rate for ∇p_r^w is due to *superconvergent* that has been proven under certain conditions of the regularity of the solution and the mesh topology by Wahlbin [41], both for C^0 finite elements and C^{p-1} splines. We aim to obtain an improved pressure gradient field

$$\nabla p_r^w = \mathbf{N}\mathbf{a}_r \tag{35}$$

where $\mathbf{N}$ are the shape functions for the pressure (Eq. (25)) and $\mathbf{a}_r$ is the unknown vector of new control variables determining the recovered pressure gradient ∇p_r^w. Notice that the computed pressure gradient reads

$$\nabla p_h^w = \nabla \mathbf{N}\mathbf{p}^w \tag{36}$$

that is, we are aiming to recover a pressure gradient ∇p_r^w in a one polynomial order higher spline space than the computed pressure gradient ∇p_h^w. The vector of control variables $\mathbf{a}_r$ are determined by forcing a least square fit (i.e., global L_2 projection) of ∇p_r^w to the computed FE pressure gradient ∇p_h^w, that is,

$$\mathcal{J}(\mathbf{a}_r) = \int_\Omega \left(\nabla p_r^w - \nabla p_h^w\right)^T \cdot \left(\nabla p_r^w - \nabla p_h^w\right) \mathrm{d}\Omega \tag{37}$$

is minimized with respect to $\mathbf{a}_r$. The minimization

$$\frac{\partial \mathcal{J}}{\partial \mathbf{a}_r} = 2\int_\Omega \left(\frac{\partial \nabla p_r^w}{\partial \mathbf{a}_r}\right)^T \cdot \left(\nabla p_r^w - \nabla p_h^w\right) \mathrm{d}\Omega \tag{38}$$

yields a linear system of equations given by

$$\mathbf{A}\mathbf{a}_r = \mathbf{b}_r \tag{39}$$

where

$$\mathbf{A} = \int_\Omega \mathbf{N}^T\mathbf{N}\mathrm{d}\Omega \qquad \text{and} \qquad \mathbf{b}_r = \int_\Omega \mathbf{N}^T \nabla p_h^w \mathrm{d}\Omega \tag{40}$$

We now use the improved gradients to obtain an indication of the error in the computed pressure

$$e_{\sigma_r} := \nabla p_r^w - \nabla p_h^w \tag{41}$$

The corresponding energy norm associated with the bilinear form is

$$\|e_r\|_E = \left(\int_\Omega \left(\nabla p_r^w - \nabla p_h^w\right) \cdot \frac{1}{\gamma^w}\mathbf{k} \cdot \left(\nabla p_r^w - \nabla p_h^w\right) \mathrm{d}\Omega\right)^{1/2} \tag{42}$$

DOI: 10.1002/nag

The quality of the error estimate based on improved gradients is measured by its effectivity index, which is defined as the ratio of the estimated error to the actual error

$$\theta = \frac{\|e_r\|_{E(\Omega)}}{\|e\|_{E(\Omega)}} \tag{43}$$

The relative global error (in percentage) is a dimensionless error quantity defined for exact and recovered error estimates, respectively, as

$$\rho = \frac{\|e\|_E}{\|p^w\|_E} \times 100\% \quad \text{and} \quad \rho_r = \frac{\|e_r\|_E}{\|p_r^w\|_E} \times 100\% \tag{44}$$

where $\|p^w\|_E = \sqrt{a(p^w, p^w)}$ and $\|p_r^w\|_E = \sqrt{a(p_r^w, p_r^w)}$ are the energy norms of the exact and L_2-projected solutions, respectively.

4.4. Adaptive refinement

Once a posteriori error estimates are established, the elements that require refinements are identified based on a tolerance criteria. The next step is to locally refine the elements. For a linear two-dimensional element or knotspan that requires refinements, knot insertion splits that element into four new elements. However, for B-splines of higher polynomial order, $p > 1$, the splitting cross cannot be limited to only the element in question. Thus, local refinement strategies must be selected to have the desired refinement for a given element and its neighbors. We have three local refinement strategies for LR B-splines, namely, *full span*, *minimum span*, and *structured mesh* refinement. The ideas behind these strategies are briefly discussed here, and for the details we refer to [22].

The full span refinement strategy refines every B-spline with support on the element identified for refinement. The mesh line inserted in one direction will span from the minimum to the maximum knot of all functions with support on the identified element. This strategy ensures that all B-splines with support on the identified element are split by the refinement. This approach is illustrated in Figure 3(a).

In the minimum span refinement strategy, a cross is inserted in the identified element where the refinement footprint is limited, unlike the full span approach. The inserted mesh lines will be as short as possible but will split at least one B-spline. The B-spline to be split may be identified based on which of the available B-splines has the smallest parametric support. But, in general, there is lack of such uniqueness. Thus, a random B-spline is selected and refined. This approach is shown in Figure 3(b).

Identifying which B-splines need refinement instead of which elements is another way to refine B-splines. In [22], the error for a B-spline is defined as the sum of the errors in all the knotspans in the support of the given B-spline. A fraction of the B-splines with the highest error are then refined as illustrated in Figure 3(c) resulting in a structured mesh refinement.

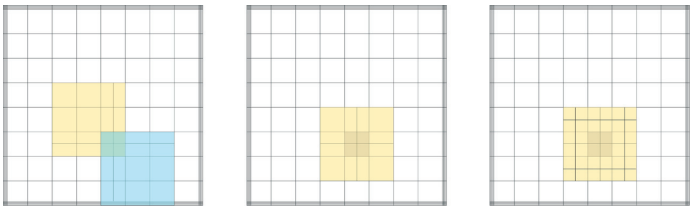

(a) Fullspan: Split all functions on one element (b) Min Span: Split one random function on one element (c) Structured Mesh: Split all knot spans on one B-spline

Figure 3. Local refinement strategies for LR B-splines, after [22].

DOI: 10.1002/nag

5. NUMERICAL EXAMPLES

5.1. Aims of the numerical examples

The aim of the numerical experiments herein is to investigate whether adaptive refinement using LR B-splines achieves optimal convergence rates for groundwater flow problems that may involve highly varying material properties, singularities, and/or rough right hand sides such that it gives better accuracy per number of degrees of freedom compared with uniform refinement. The adaptive strategy is based on controlling the growth rate of the basis functions in the solution space, according to the parameter β and a specified error tolerance or maximum number of degrees of freedom. Furthermore, we want to investigate the sensitivity in accuracy and convergence rates towards polynomial order p. We start the numerical examples with two verification problems with known analytical solutions:

- the wavefront well problem and
- the L-shape problem.

These problems are used to verify the numerical implementation and study the effectivity of the error estimates and the adaptive simulation in handling certain challenging effects. In the wavefront well problem, we study the effects of a rough right hand side and the effect of isotropy or anisotropy in material properties, whereas the analytical solution for the L-shape problem is characterized by having a singularity of the gradient in the re-entrant corner on the boundary. The availability of an analytical solution allows us to calculate exact a posteriori error estimates to drive the adaptive mesh refinement, as well as study and report the effectivity index for the presented recovery-based error estimator.

To demonstrate the potential offered by adaptive IGA, we address the following groundwater flow problems:

- flow around an impervious corner;
- flow around a cutoff wall; and
- flow in a heterogeneous medium.

Analytical solutions are not available for these problems, and we use the a posteriori error estimator to drive the adaptive refinement. Here we compare the achieved accuracy per number of degrees of freedom, $ndof$, obtained with adaptive and uniform refinement.

5.2. Verification problems with analytical solutions

5.2.1. The wavefront well problem. The first illustrative example we consider is the so-called wavefront well problem, [42], defined over a square domain.

Problem definition. The strong form of the problem in Eq. (7), assuming the flow is solely driven by pressure gradients, reduces to

$$\begin{cases} \nabla \cdot [-\boldsymbol{\kappa} \nabla p^w(x,y)] = f(x,y) & (x,y) \in \Omega \\ p^w(x,y) = \hat{p}^w(x,y) & (x,y) \in \partial\Omega \end{cases} \tag{45}$$

The numerical simulation domain is defined by a square area $\Omega = [0,1]\times[0,1]$ where the boundaries are $\Gamma_D = \partial\Omega$ and $\Gamma_N = \varnothing$, shown in Figure 4(a). The exact analytical solution for the pressure field is given by

$$p^w(x,y) = \arctan(50(-0.25 + \sqrt{(x-0.5)^2 + (y-0.5)^2})) \tag{46}$$

Note that the right hand side $f(x,y)$ is generated by taking the Laplacian (∇^2) of the analytical solution stated in Equation 46, and is given in Appendix A for a variable degree of anisotropy. The analytical solution depicted in Figure 4(b) displays a 'front'-type of behavior where the solution is rapidly changing across a circular band inside the domain. This problem is mathematically smooth, that is, $p^w \in H^{p+1}(\Omega)$ for any finite p. However, because of the highly varying right hand side, we

DOI: 10.1002/nag

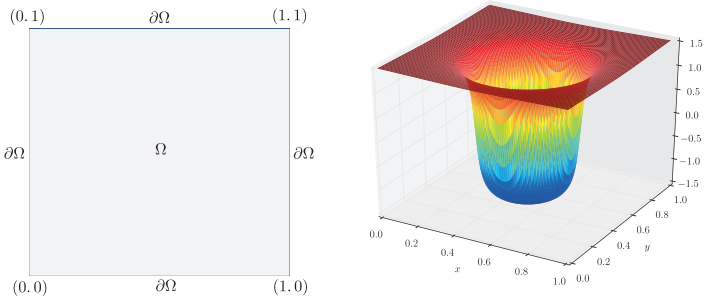

(a) The domain Ω and its boundary (b) 3D plot of analytical solution

Figure 4. The wavefront problem: numerical simulation domain and analytical solution plot.

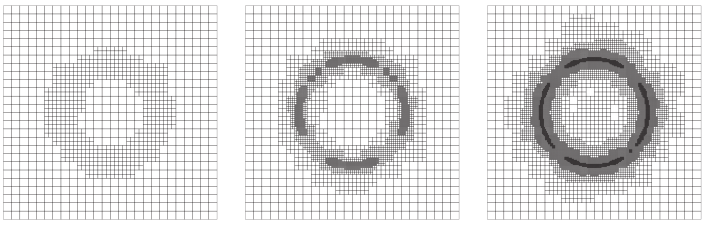

(a) $p = 2, ndof = 1138$ (b) $p = 2, ndof = 3443$ (c) $p = 2, ndof = 10339$

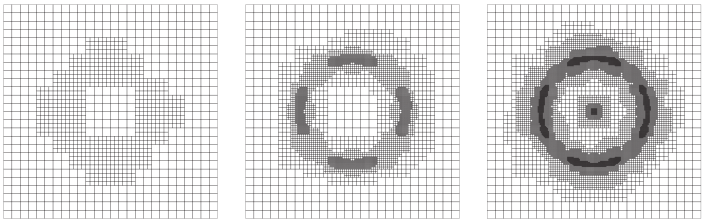

(d) $p = 3, ndof = 1234$ (e) $p = 3, ndof = 3775$ (f) $p = 3, ndof = 11320$

Figure 5. The wavefront problem: adaptive meshes for $\beta = 20\%$ at different refinement steps for the isotropic case. Each column represents the same refinement step for varying polynomial degrees.

may only expect an optimal convergence rate when the element size h is less than a given threshold that depends on the sharpness or bandwidth of the interior layer. Hence, we may expect suboptimal convergence rate for uniform mesh refinement when the mesh is not fine enough.

Two cases are considered for the conductivity matrix $\boldsymbol{\kappa}$ – isotropic and anisotropic. For simplicity in deriving the source function, the conductivity equivalent coefficients are set equal to

$$\boldsymbol{\kappa} = \begin{bmatrix} 1 & 0 \\ 0 & 1 \end{bmatrix} \quad \text{and} \quad \boldsymbol{\kappa} = \begin{bmatrix} 10 & 0 \\ 0 & 1 \end{bmatrix} \tag{47}$$

Results – isotropic case. The adaptive simulation is performed for polynomial degrees of $p = 2$ and $p = 3$. The refinement parameter is selected as $\beta = 20\%$. Adaptive refinement is performed up to a specified maximum number of iterations or maximum number of degrees of freedom.

The physical meshes for selected refinement steps are shown in Figure 5(a)–(c) for $p = 2$ and in Figure 5(d)–(f) for $p = 3$. The structured mesh refinement strategy is used for this problem. Note that the adaptive meshes are not perfectly symmetric, even though the solution and error distribution are symmetric, because our refinement parameter β only controls the growth rate of the number of

DOI: 10.1002/nag

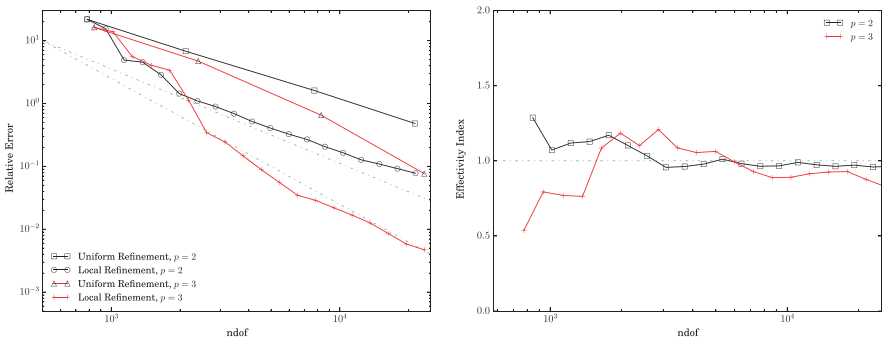

(a) (b)

Figure 6. The wavefront problem: convergence and effectivity index plots for the isotropic case. The dotted lines in (a) correspond to slopes of $-3/2$ and -2.

basis functions, as explained in Section 3.1.2. We observe, however, that the physical meshes especially at higher refinement steps are nearly symmetric because the error is symmetrically distributed because of its dependence on the hydraulic conductivity matrix.

The convergence plots for this case are shown in Figure 6(a) in terms of relative error versus number of degrees of freedom. The effectivity index plot is shown in Figure 6(b) for the polynomial degrees considered. It can be seen from the curves that an optimal convergence rate is obtained after a sufficient number of refinements for this problem. A similar problem has been studied in [40] using different a posteriori error estimators, of which CGL2 (used here) is one. Error recovery based on CGL2 projection was observed to perform well for this problem.

Results - anisotropic case. The problem is simulated with the same setup as in the isotropic case with the only difference being in the anisotropy of the $\boldsymbol{\kappa}$ matrix. The errors are no longer symmetrically distributed in the domain, and this is reflected in the physical meshes obtained at different refinements steps, shown in Figure 7(a)–(c) for $p = 2$ and Figure 7(d)–(f) for $p = 3$. The convergence plots obtained for the anisotropic case, Figure 8(a), are similar to the isotropic case. The effectivity index plot for this case is shown in Figure 8(b).

5.2.2. The L-shape problem. The second example with analytical solution is the L-shape problem with domain and boundary conditions shown in Figure 9(a).

Problem definition. The boundary conditions are summarized as

$$\begin{cases} \nabla \cdot (-\boldsymbol{\kappa} \nabla p^w) = 0 & \text{in} \quad \Omega \\ p^w(r, \theta) = 0 & \text{on} \quad \Gamma_D \\ \frac{\partial p^w}{\partial \boldsymbol{n}} = q^w & \text{on} \quad \Gamma_N \end{cases} \tag{48}$$

We choose $\kappa_x = \kappa_y = 1$ for simplicity. The exact analytical solution is given by

$$p^w = r^{2/3} \sin\left(\frac{2\theta - \pi}{3}\right) \tag{49}$$

where $r^2 = x^2 + y^2$ and $\theta = \arctan(y/x)$. The analytical solution plot is shown in Figure 9(b). The expression for the Neumann boundary condition, q^w, is derived based on the analytical solution and is not included here.

For the given elliptic problem, the re-entrant corner at $(0, 0)$ in the domain causes a singularity in the solution. It is known that the convergence for uniform mesh refinement is limited by the strength of the singularity $\lambda = 2/3$, as $p^w \in H^{5/3}(\Omega)$, that is, the convergence rate (versus degrees of freedom) is equal to $-1/3$. For problems where the solution is not sufficiently smooth,

DOI: 10.1002/nag

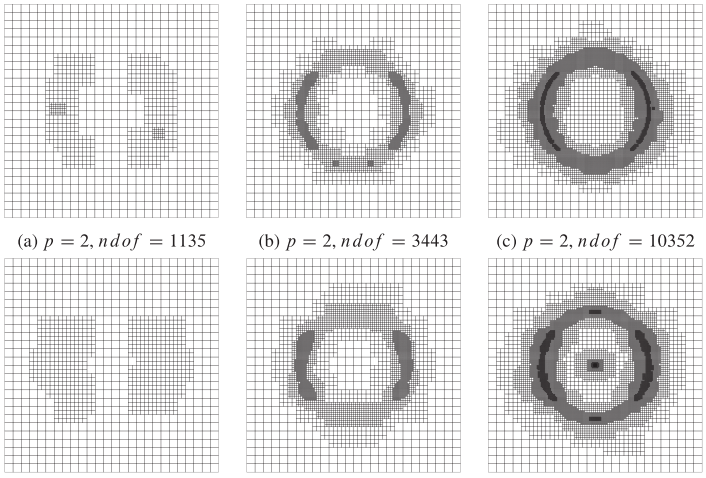

(a) $p = 2, ndof = 1135$ (b) $p = 2, ndof = 3443$ (c) $p = 2, ndof = 10352$

(d) $p = 3, ndof = 1222$ (e) $p = 3, ndof = 3751$ (f) $p = 3, ndof = 11230$

Figure 7. The wavefront problem: adaptive meshes for $\beta = 20\%$ at different refinement steps for the anisotropic case. Each column represents the same refinement step for varying polynomial degrees.

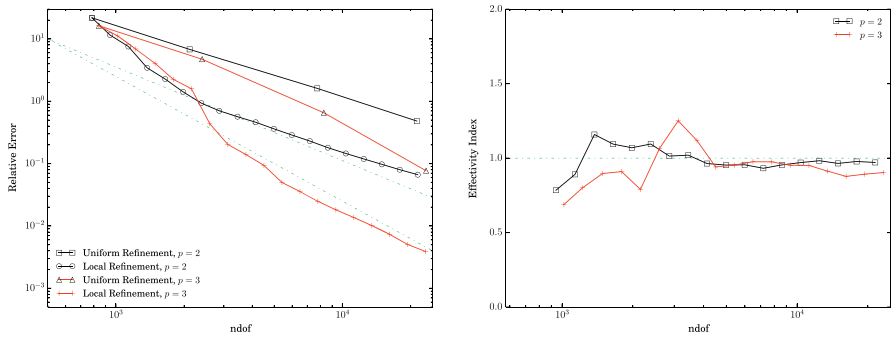

(a) (b)

Figure 8. The wavefront problem: convergence and effectivity index plots for the anisotropic case. The dotted lines in (a) correspond to slopes of $-3/2$ and -2.

$p^w \notin H^{p+1}(\Omega)$, we do not obtain an optimal convergence rate when we perform uniform mesh refinement. In particular, the use of higher-order polynomials is then inefficient.

Results. The L-shape problem is analyzed for polynomial degrees of $p = 2$ and $p = 3$. The refinement parameter is selected as $\beta = 20\%$. In Figure 10(a), we see that we achieve optimal convergence rates when we perform adaptive refinement, whereas for uniform refinement, the convergence rate is the same for both $p = 2$ and $p = 3$ and limited by the strength of the singularity. The effectivity index plots obtained are shown in Figure 10(b), and we see that we have $0.9 < \theta < 1.1$. We want to underline that the obtained effectivity indices are very good (i.e., close to 1.0) compared with what we typically achieve for regular finite elements [32].

5.3. Flow around an impervious corner

The next numerical example we consider is flow of water around an impervious corner, for example, groundwater flow under the base of a concrete dam (Figure 11). The presence of a sharp corner introduces singularity in the numerical solution leading to infinite velocities.

DOI: 10.1002/nag

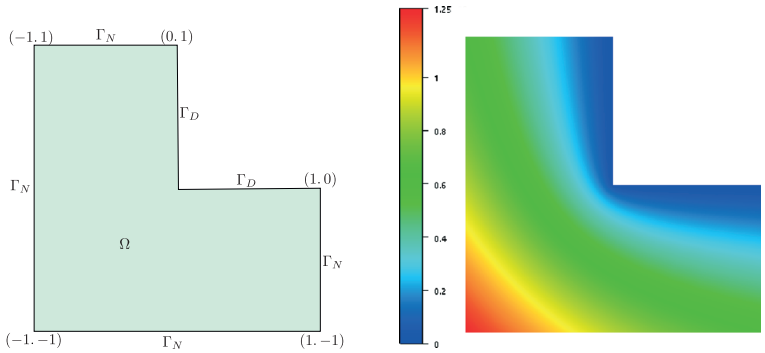

(a) Domain (b) Analytical solution

Figure 9. The L-shape problem: domain with boundary conditions and analytical solution plot.

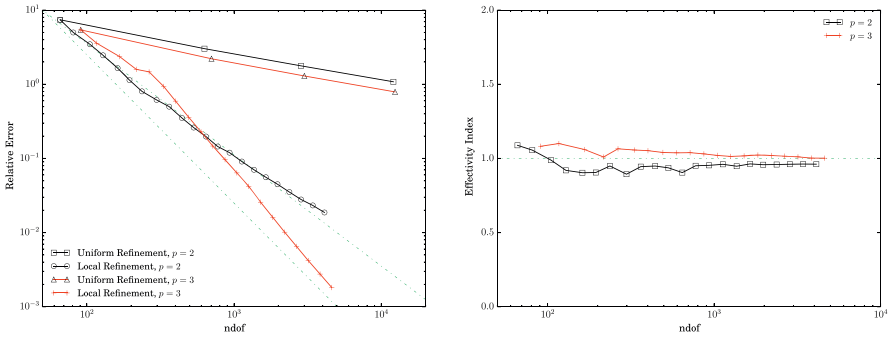

(a) (b)

Figure 10. The L-shape problem: convergence and effectivity index plots.

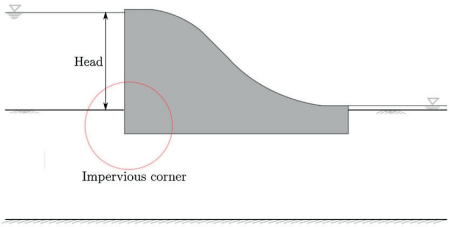

Figure 11. One example of seepage around an impervious corner.

5.3.1. Problem definition. We study a selected area of this problem with adaptive mesh refinement by considering the appropriate boundary conditions. The problem is idealized as an L-shape problem where the boundary conditions are applied such that they reflect the physical problem, shown in Figure 12(a). Dirichlet boundary conditions are applied at the top horizontal and the right vertical edges of the idealized numerical simulation domain. For simplicity, a homogeneous Dirichlet boundary condition is applied at the right vertical edge, which may be slightly different in the physical problem depending on the boundary conditions at the downstream area. The impervious boundary Γ_{N1} represents a homogeneous Neumann boundary condition. We assume the fluxes to be negligible on Γ_{N2}. The boundary conditions are summarized as

DOI: 10.1002/nag

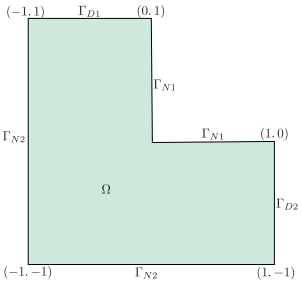

(a) Domain

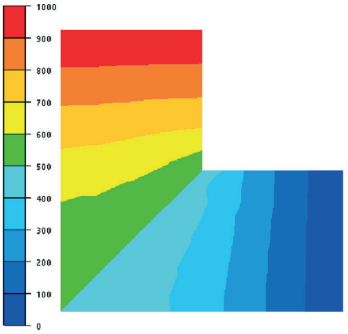

(b) Equipotential lines, $ndof = 66$

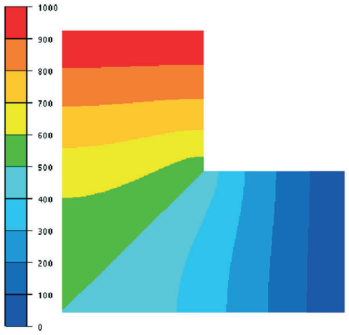

(c) Equipotential lines, $ndof = 3571$

Figure 12. The impervious corner problem: idealized numerical simulation domain and equipotential lines for coarse and fine meshes.

$$\begin{cases} p^w = 1000 & \text{on} \quad \Gamma_{D1} \\ p^w = 0 & \text{on} \quad \Gamma_{D2} \\ \frac{\partial p^w}{\partial n} = 0 & \text{on} \quad \Gamma_{N1} \cup \Gamma_{N2} \end{cases} \tag{50}$$

The equipotential lines obtained from simulations with uniform refinement using coarse and fine meshes are shown in Figure 12(b) and (c), respectively.

5.3.2. Results. The mesh refinement parameter for this problem is selected as $\beta = 20\%$, and the adaptive simulations are performed in combination with polynomial degrees of $p = 2$, $p = 3$, and $p = 4$. The full-span refinement strategy is used in this case.

The convergence plots in Figure 13 compare the relative errors from simulations with local and uniform refinement for the different polynomial degrees analyzed. Observe the significant increase of convergence order, that is, optimal convergence rate, achieved by the adaptive procedure. The convergence rate with local refinement in this case appears to improve with increasing polynomial order.

The resulting physical meshes at selected refinement steps are shown in Figure 14. The meshes and the resulting number of degrees of freedom for $p = 2$ at the 5th, 10th, and 15th refinement steps are shown in Figure 14(a)–(c). Similar results for $p = 3$ and $p = 4$ are shown in Figure 14(d)–(f) and Figure 14(g)–(i), respectively.

5.4. Flow around a cutoff wall

Seepage cutoff walls are used in geotechnical engineering to protect structure foundations from the damaging effects of groundwater flow or to exclude groundwater from an excavation and thereby

DOI: 10.1002/nag

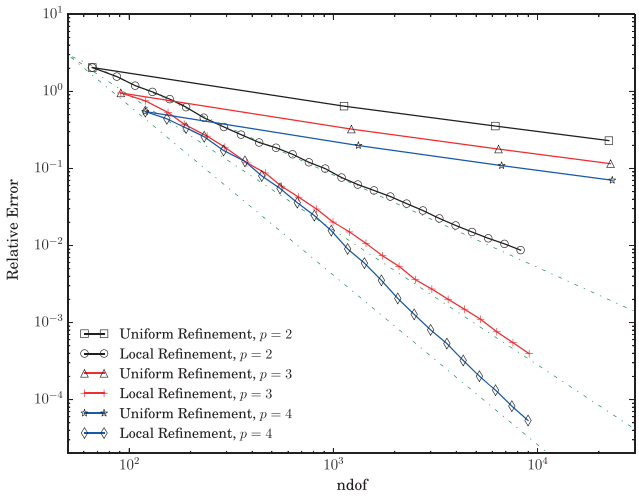

Figure 13. The impervious corner problem: convergence plots.

minimize the requirement of dewatering pumping. The cutoff walls are usually made of an impervious or very low permeability material, such as a steel sheet-pile wall, and extend up to a zone of low permeability. In the computational modeling of groundwater flow, the tips of such cutoff walls represent points of singularity [9], making the numerical solution difficult or erroneous.

5.4.1. Problem definition. We consider the flow of water around a 10m long cutoff wall installed under the base of a dam with a cross-sectional width of 50 m (Figure 15). The soil medium is considered to be homogeneous with an isotropic hydraulic conductivity of 15 m/day.

The simulation domain chosen for the described dam with a cutoff wall is shown in Figure 16(a). The cutoff wall is included in the geometry by inserting a C^{-1} discontinuous knot. The base of the dam, the cutoff wall, and the boundary to the impervious layer represent homogeneous Neumann boundaries and are respectively designated as Γ_{N1}, Γ_{N2}, and Γ_{N3}. Non-homogeneous Dirichlet boundary conditions are applied at the left and right boundaries of the domain, Γ_{D1} and Γ_{D2}. The magnitudes for these values are chosen based on the anticipated flow field that will result from the hydraulic head differences at the upstream and downstream faces of the dam. Pressure head values that vary linearly with height z are assumed, and the boundary conditions can be summarized as

$$\begin{cases} p^w = z + 100 & \text{on} \quad \Gamma_{D1} \\ p^w = 30 - z & \text{on} \quad \Gamma_{D2} \\ \frac{\partial p^w}{\partial n} = 0 & \text{on} \quad \Gamma_{N1} \cup \Gamma_{N2} \cup \Gamma_{N3} \end{cases} \tag{51}$$

The equipotential lines obtained from simulations with refinements using coarse and fine meshes are shown in Figure 16(b) and (c), respectively. The pressure heads vary between 120 kPa, at the left boundary, and 10 kPa, at the right boundary. These correspond to hydraulic heads of approximately 12 and 1 m at the upstream and downstream faces of the dam, respectively.

5.4.2. Results. We start the adaptive simulation for the cutoff problem with a relatively coarse mesh of around 300 degrees of freedom. The polynomial degrees are varied between $p = 2$, $p = 3$ and $p = 4$. The problem is also simulated using standard linear finite elements, $p = 1$, for comparison with FEA. The refinement parameter β in this case is selected as 10%, and a structured mesh adaptive refinement strategy is used.

The pressure profiles obtained using a coarse mesh could show significant discretization errors. This is illustrated by plotting horizontal and vertical pressure profile plots for coarse and locally

DOI: 10.1002/nag

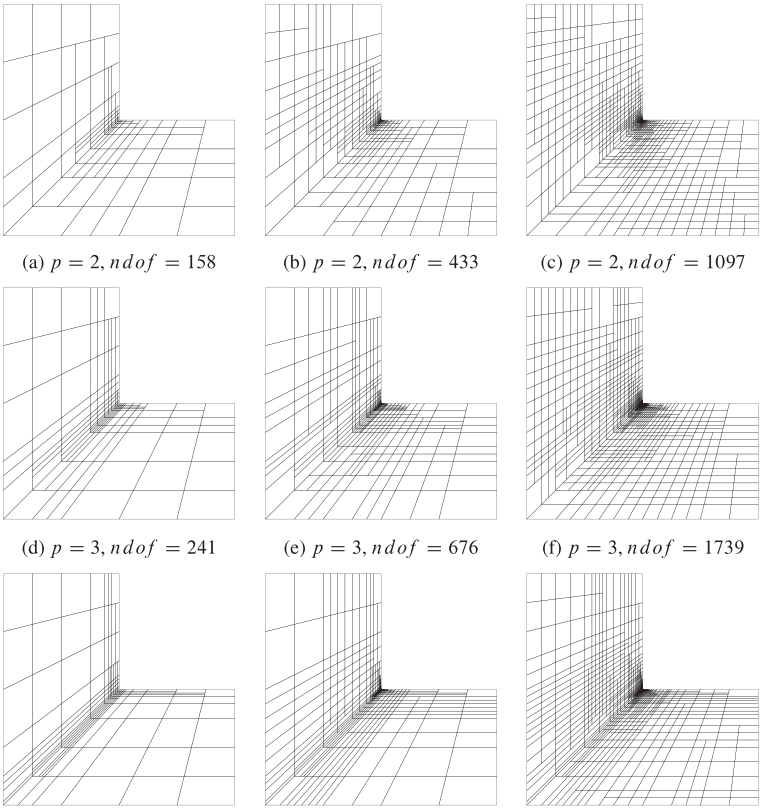

(a) $p = 2, ndof = 158$ (b) $p = 2, ndof = 433$ (c) $p = 2, ndof = 1097$

(d) $p = 3, ndof = 241$ (e) $p = 3, ndof = 676$ (f) $p = 3, ndof = 1739$

(g) $p = 4, ndof = 290$ (h) $p = 4, ndof = 807$ (i) $p = 4, ndof = 2068$

Figure 14. The impervious corner problem: adaptive meshes at different refinement steps for the selected $\beta = 20\%$. Each column represents the same refinement step for varying polynomial degrees.

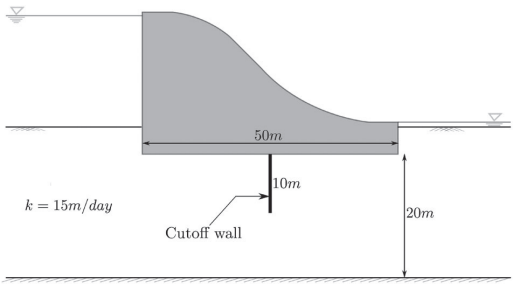

Figure 15. The cutoff wall problem: physical setup of dam with a cutoff wall.

refined meshes around the cutoff wall. Figure 17(a) shows horizontal pressure profiles 2 m above the tip of the cutoff wall, plotted over a horizontal distance of 25 and 12.5 m on both sides of the cutoff wall. Notice the significant difference in pressure drop over the cutoff wall, that is, $71.1 - 58.9 = 12.2$ kPa and $75.5 - 54.5 = 21.0$ kPa for the coarse mesh and fine mesh, respectively. This corresponds to more than 40% underestimation of the pressure drop calculated by the coarse mesh,

DOI: 10.1002/nag

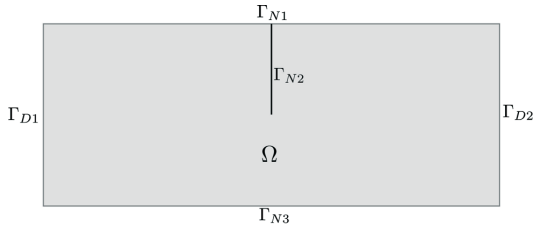

(a) Domain

(b) Equipotential lines, $ndof = 315$

(c) Equipotential lines, $ndof = 5715$

Figure 16. The cutoff wall problem: domain with boundary conditions and equipotential lines for coarse and fine meshes. The maximum and minimum pressure head values are 120 and 10 kPa.

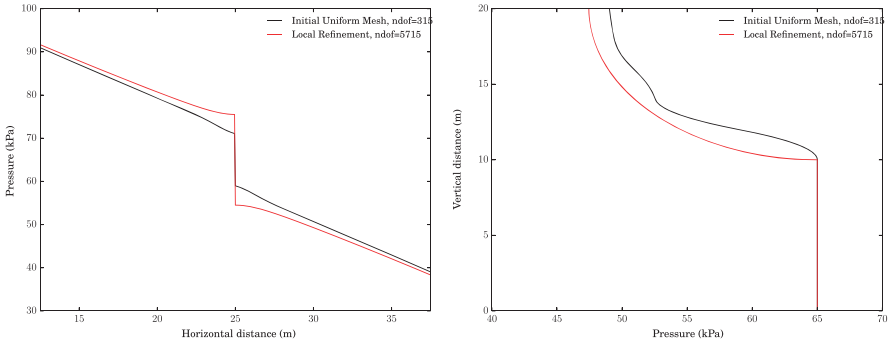

(a) (b)

Figure 17. The cutoff wall problem: horizontal and vertical pressure profile plots.

which affects the expected effect of water flow at the downstream base of the dam. Vertical pressure profiles at the location of the cutoff wall, and spanning over the entire height of the domain, are shown in Figure 17(b). Again, we observe significant differences in the obtained solutions.

The physical meshes obtained at selected refinement steps are shown in Figure 18(a). The meshes and the resulting number of degrees of freedom for $p = 2$ at the 4th and 12th refinement steps

DOI: 10.1002/nag

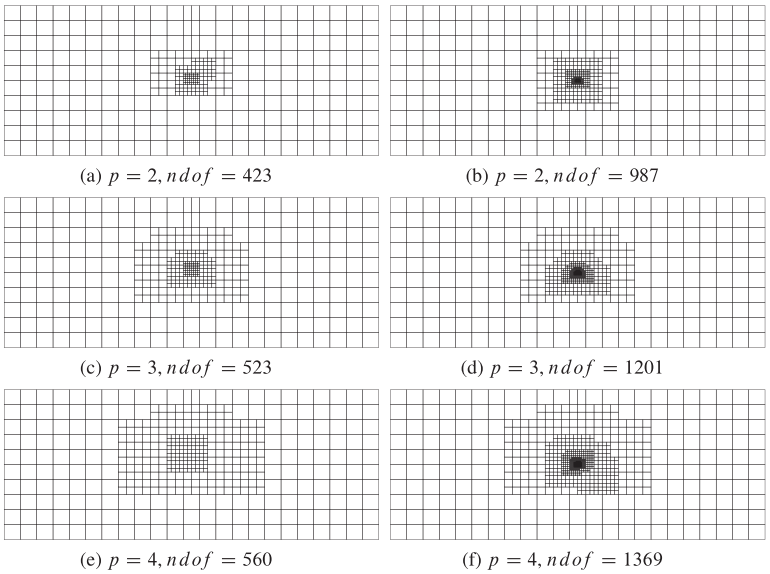

(a) $p = 2, ndof = 423$ (b) $p = 2, ndof = 987$

(c) $p = 3, ndof = 523$ (d) $p = 3, ndof = 1201$

(e) $p = 4, ndof = 560$ (f) $p = 4, ndof = 1369$

Figure 18. The cutoff wall problem: adaptive meshes at different refinement steps for the selected $\beta = 10\%$. Each column represents the same refinement step for varying polynomial degrees.

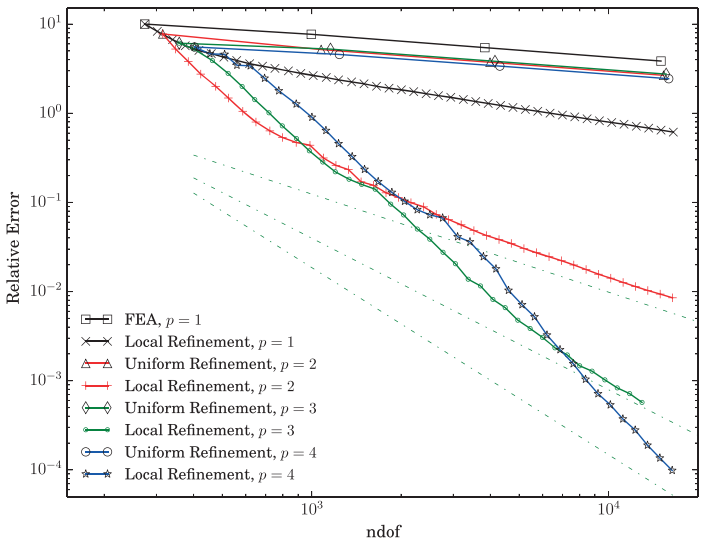

Figure 19. The cutoff wall problem: convergence plots.

are shown in Figure 18(a) and (b). The corresponding results for $p = 3$ are shown in Figure 18(c) and (d), whereas Figure 18(e) and (f) shows those for $p = 4$. At large refinement numbers, extra refinements are observed at the boundaries where non-homogeneous Dirichlet boundary conditions are applied because these are only approximated.

DOI: 10.1002/nag

The convergence plots comparing the relative errors from uniform and local refinement are shown in Figure 19. The results from an FEA using standard linear finite elements, $p = 1$, are included for comparison. For linear elements, FEA and IGA result in similar basis functions, and we use this fact to compare the FEA results with local refinement using linear LR B-splines. We observe that local refinement performs slightly better in this case. The uniform refinement simulations with higher order polynomials show that the results are only marginally better in recovering errors compared to the FEA results. Local refinement simulation using higher order polynomials, however, show good convergence properties. Optimal convergence rates are obtained for $p = 2$ and $p = 3$ for the maximum number of degrees of freedom specified in the adaptive simulation. The convergence rate appears to improve for $p = 4$ but requires more refinement steps to reach an optimal order, thereby increasing the total number of degrees of freedom.

5.5. *Flow in a heterogeneous medium*

The errors observed in the numerical simulation of groundwater flow in heterogeneous formations using coarse meshes could be very significant, [19]. Using a very fine mesh for such cases helps in reducing these errors, but a uniform refinement throughout the domain implies unnecessarily fine meshes at locations where the errors are smaller. In such cases, adaptive simulation with local refinement could be more effective.

5.5.1. Problem definition. We consider a square domain of size 1×1 m. The heterogeneous hydraulic conductivity k on the flow domain is assumed to follow a lognormal distribution. The probability density function for the lognormal distribution of k is

$$f(k) = \frac{1}{\sigma k \sqrt{2\pi}} e^{-\frac{(\ln(k)-\mu)^2}{2\sigma^2}} \tag{52}$$

where μ is the mean and σ is the standard deviation of the normally distributed logarithm of the hydraulic conductivity. A random field with $\mu = -15$ and $\sigma = 7$ was generated.

For smoothing out the randomly generated data, a Gaussian filter of the form

$$g(x, y) = e^{-\frac{1}{3}\left(\frac{x^2}{l_x} + \frac{y^2}{l_y}\right)} \tag{53}$$

is applied. The filter dimensions in the x and y directions are chosen to be the same with values of $l_x = l_y = 20$. The smoothed data were truncated such that the hydraulic conductivity values vary between 10^{-3} and 10^{-7} m/s. The realization of the stationary random field generated is shown in Figure 20 in terms of color field and 3D plots.

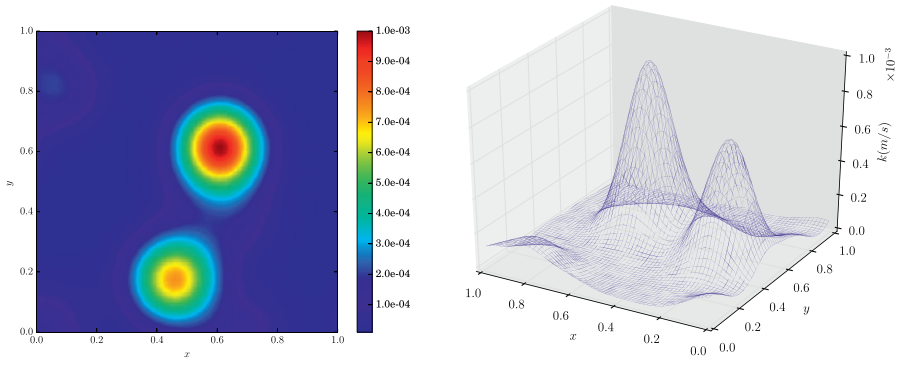

(a) Field plot (b) 3D plot

Figure 20. The heterogeneous problem: realization of the randomly generated hydraulic conductivity field.

DOI: 10.1002/nag

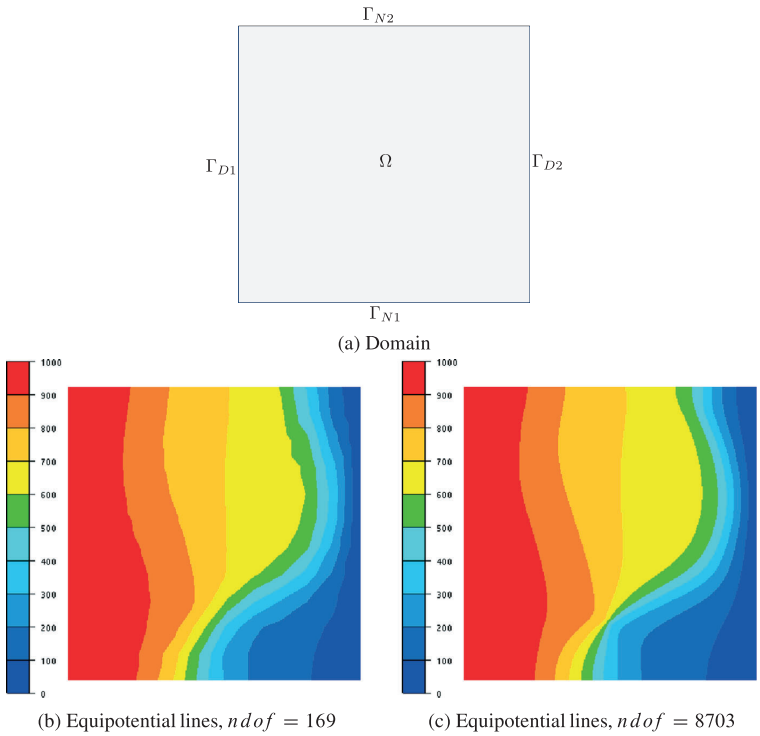

(a) Domain

(b) Equipotential lines, $ndof = 169$ (c) Equipotential lines, $ndof = 8703$

Figure 21. The heterogeneous problem: simulation domain with boundary conditions and equipotential lines for coarse and fine meshes.

Dirichlet boundary conditions are applied on the left and right boundaries of the heterogeneous square domain to create a pressure gradient. The top and bottom boundaries of the domain are represented by homogeneous Neumann (no-flux) boundary conditions. An illustration of the applied boundary conditions is shown in Figure 21(a). These boundary conditions are

$$\begin{cases} p^w = 1000 & \text{on} \quad \Gamma_{D1} \\ p^w = 0 & \text{on} \quad \Gamma_{D2} \\ \frac{\partial p^w}{\partial n} = 0 & \text{on} \quad \Gamma_{N1} \cup \Gamma_{N2} \end{cases} \tag{54}$$

The equipotential lines obtained from simulation with uniform refinement using coarse and fine meshes are shown in Figure 21(b) and (c), respectively. The difference in the hydraulic conductivity within the domain creates preferential flow paths, and this results in very large changes in the pressure gradient at some locations of the domain.

5.5.2. Results. The heterogeneous problem is simulated starting from a relatively coarse mesh with number of degrees of freedom being around 170. Polynomial degrees of $p = 2$ and $p = 3$ are considered and the refinement parameter β in this case is selected as 10%. The resulting physical meshes for selected refinement steps are shown in Figure 22. In particular, Figure 22(a)–(c) shows the locally refined meshes for $p = 2$, whereas Figure 22(d)–(f) shows those for $p = 3$.

The convergence plots comparing local and uniform refinements for $p = 2$ and $p = 3$ are shown in Figure 23. The plots indicate that the convergence rate gained by using local refinement is not very significant. The reason for this is that unlike complex boundary conditions which could imply

DOI: 10.1002/nag

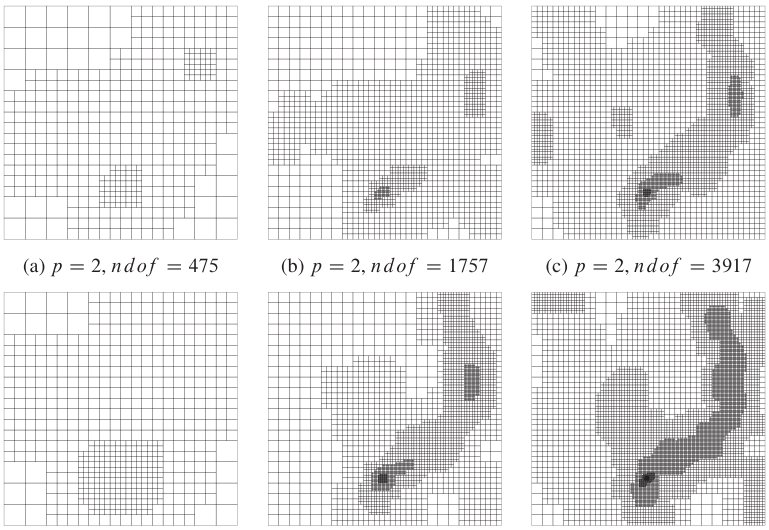

(a) $p = 2, ndof = 475$ (b) $p = 2, ndof = 1757$ (c) $p = 2, ndof = 3917$

(d) $p = 3, ndof = 631$ (e) $p = 3, ndof = 2977$ (f) $p = 3, ndof = 7429$

Figure 22. The heterogeneous problem: adaptive meshes at different refinement steps for the selected $\beta = 10\%$. Each column represents the same refinement step for varying polynomial degrees.

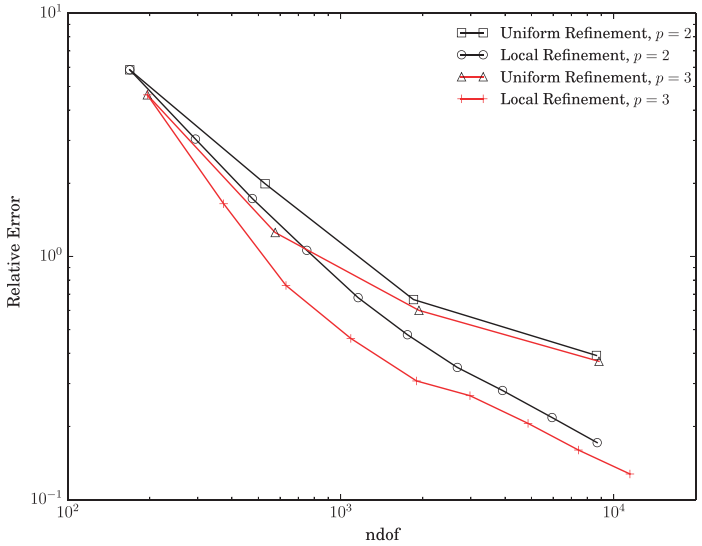

Figure 23. The heterogeneous problem: convergence plots.

strong singularities, varying material behavior is a weak discontinuity. The error recovery using local refinement, however, could be more significant compared with uniform refinement for simulations over large heterogeneous domains.

The random hydraulic conductivity field considered in Figure 20 shows a very large variability in the conductivity values. In some cases, the hydraulic conductivity fields in heterogeneous aquifers could show variability of a lesser magnitude within the domain. One such lognormal random field is

DOI: 10.1002/nag

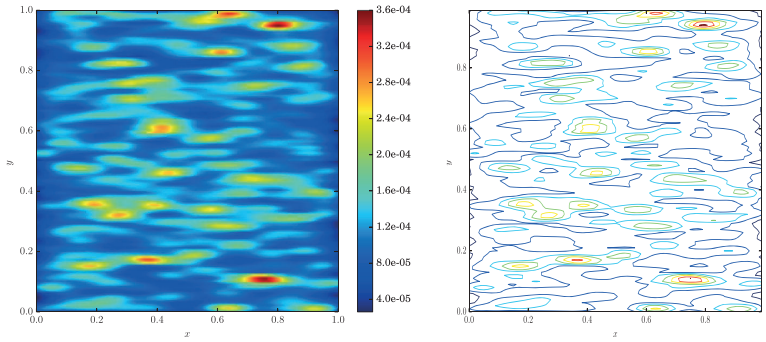

(a) Field plot (b) Contour plot

Figure 24. The heterogeneous problem: realization of the randomly generated hydraulic conductivity field.

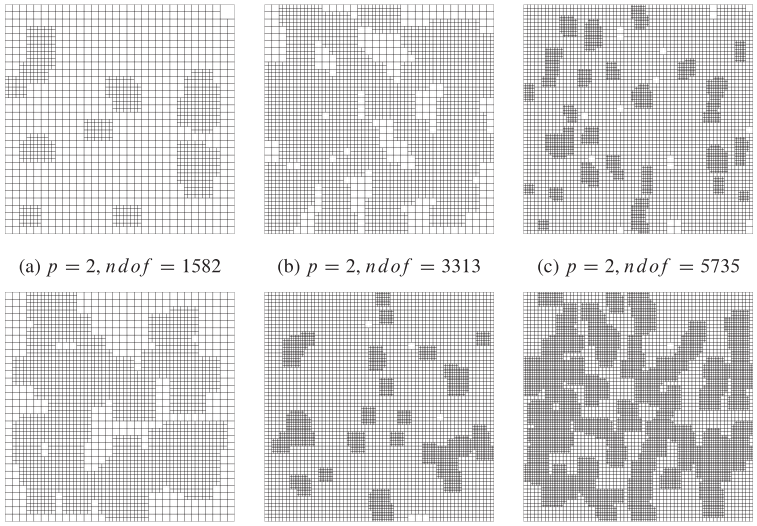

(a) $p = 2, ndof = 1582$ (b) $p = 2, ndof = 3313$ (c) $p = 2, ndof = 5735$

(d) $p = 3, ndof = 2791$ (e) $p = 3, ndof = 5860$ (f) $p = 3, ndof = 10156$

Figure 25. The heterogeneous problem: adaptive meshes at different refinement steps for the selected $\beta = 20\%$. Each column represents the same refinement step for varying polynomial degrees.

generated and shown in Figure 24. The random field is generated by assuming a mean $\mu = -10$ and a variance $\sigma^2 = 2$. The filter dimensions in this case are taken as $l_x = 1$ and $l_y = 15$. The hydraulic conductivity values vary by an order of magnitude of 10. Adaptive simulations were performed with $p = 2$ and $p = 3$, using $\beta = 20\%$. The resulting adaptive meshes at selected refinement steps are shown in 25. The difference in convergence rates between uniform and local refinement for this case is small and is not shown here.

Material property variation in other cases may be of a non-homogeneous type, and such a problem may be handled depending on the strength of the discontinuity introduced by the non-homogeneity. Weak discontinuities, such as material interfaces in a domain with layered materials, can be simulated accurately by ensuring C^0 continuity at the interfaces, without requiring adaptive refinement. This is achieved in IGA by making the multiplicity of the knots, m, at the interfaces equal to the

DOI: 10.1002/nag

polynomial degree, p, used, that is, C^{p-m} continuity. Strong discontinuities, such as cracks and impervious interfaces, result in jumps in the computed solution and introduce singularities depending on their location in the flow domain. These features can be simulated by introducing C^{-1} discontinuities, which is one of the powerful features of IGA. The cutoff wall example in Section 5.4 represents a special case of such strong discontinuities.

6. CONCLUDING REMARKS

Steady-state groundwater flow problems with varying numerical challenges were studied using adaptive IGA with locally refined (LR) B-splines. In particular, the problems studied were flow around an impervious corner, flow around a cutoff wall and flow in a heterogeneous medium. The simulations were performed using both local and uniform refinement. The adaptive simulations with local refinement rely on a posteriori error estimates as a refinement criteria where the error estimates are based on CGL2 projection of the computed solution. The effectivity of the error estimator was verified with benchmark problems which have analytical solutions, before being used in the application examples. In general, adaptive simulations with local refinement were observed to outperform simulations with uniform refinement in terms of error recovery. Optimal convergence rates were obtained for problems with strong singularities where the rates were observed to improve with increasing polynomial orders. Application to problems with weak discontinuities, because of material property variation, shows that optimal convergence rates may not be achieved, but adaptive refinement still performed better than uniform refinement in error recovery. Local refinement could especially be more useful for large-scale groundwater flow problems, with singularities and/or discontinuities, where simulations with uniform refinement could be computationally expensive.

In the present study, only two-dimensional groundwater flow problems were presented. Application to three-dimensional problems, however, is straightforward where the mathematical procedures are a simple extension of the formulations presented in Section 3.1.2. In particular, we will have trivariate functions for three-dimensional problems based on three knot vectors in each direction. As in the bivariate case, the refinements are performed in one parametric domain at a time as illustrated in Eq. (17).

APPENDIX A: SOURCE FUNCTION AND SECONDARY SOLUTION FOR THE WAVEFRONT PROBLEM

The source function f corresponding to the assumed analytical solution of the wavefront problem numerical example in Section 5.2.1 is given by

$$f = \left[\frac{250000(a-0.25)}{a^2b^2} + \frac{50}{a^3b}\right]\left[c(x-0.5)^2 + (y-0.5)^2\right] - \frac{50(c+1)}{ab}$$

where

$$\begin{aligned} a &= \sqrt{(x-0.5)^2 + (y-0.5)^2} \\ b &= 2500\,[a-0.25]^2 + 1 \\ c &= \frac{\kappa_x}{\kappa_y} \quad \Rightarrow \text{Degree of anisotropy} \end{aligned}$$

The secondary solution, that is, the velocity, for the wavefront problem is derived from the Darcy equation as

$$\mathbf{v} = -\frac{50}{ab}\begin{Bmatrix} c(x-0.5) \\ (y-0.5) \end{Bmatrix} \tag{A.1}$$

DOI: 10.1002/nag

ACKNOWLEDGEMENTS

This work is financially supported by the Research Council of Norway and industrial partners through the research project SAMCoT, Sustainable Arctic Marine and Coastal Technology. The authors gratefully acknowledge the support. Special thanks to all in the IFEM software team at SINTEF Applied Mathematics and Dr. Kjetil A. Johannessen for his work on LR B-splines.

REFERENCES

1. Finn WDL. Finite-element analysis of seepage through dams. *Journal of Soil Mechanics & Foundations Div, ASCE SM6* 1967; **92**:41–48.
2. Pinder GF, Frind EO. Application of Galerkin's procedure to aquifer analysis. *Water Resources Research* 1972; **8**(1):108–120.
3. Reeves M, Duguid JO. Water movement through saturated–unsaturated porous media: a finite-element Galerkin model. *Technical report*, Oak Ridge National Lab.: Tenn.(USA, 1975.
4. Gupta SK, Cole CR, Pinder GF. A finite-element three-dimensional groundwater (FE3DGW) model for a multi-aquifer system. *Water resources research* 1984; **20**(5):553–563.
5. Yeh GT. On the computation of Darcian velocity and mass balance in the finite-element modeling of groundwater-flow. *Water Resources Research* 1981; **17**(5):1529–1534.
6. Botha JF, Bakkes GN. Galerkin finite element method and the groundwater flow equation: 1. Convergence of the method. *Advances in Water Resources* 1982; **5**(2):121–126.
7. Tharp TM. An enriched finite-element for simulation of groundwater-flow to a well or drain. *Journal of Hydrology* 1982; **55**(1-4):237–245.
8. Dogrul EC, Kadir TN. Flow computation and mass balance in Galerkin finite-element groundwater models. *Journal of Hydraulic Engineering-Asce* 2006; **132**(11):1206–1214.
9. Lafe OE, Liu PLF, Liggett JA, Cheng AHD, Montes JS. Singularities in Darcy flow through porous media. *Journal of the Hydraulics Division* 1980; **106**(6):977–997.
10. Liang D, Zhang B. A finite element method for a unidimensional single-phase nonlinear free boundary problem in groundwater flow. *IMA Journal of Numerical Analysis* 1999; **19**(4):563–581.
11. Neuman SP, Witherspoon PA. Finite element method of analyzing steady seepage with a free surface. *Water Resources Research* 1970; **6**(3):889–897.
12. Larabi A, De Smedt F. Numerical solution of 3-D groundwater flow involving free boundaries by a fixed finite element method. *Journal of Hydrology* 1997; **201**(1-4):161–182.
13. Rank E, Werner H. An adaptive finite-element approach for the free-surface seepage problem. *International Journal for Numerical Methods in Engineering* 1986; **23**(7):1217–1228.
14. Sharif NH, Wiberg NE. Adaptive ICT procedure for non-linear seepage flows with free surface in porous media. *Communications in Numerical Methods in Engineering* 2002; **18**(3):161–176.
15. Boeriu S, Bruch JC. Performance analysis tools applied to a finite element adaptive mesh free boundary seepage parallel algorithm. *Computer Methods in Applied Mechanics and Engineering* 2005; **194**(2-5):297–312.
16. Jie YX, Liu LZ, Xu WJ, Li GX. Application of NEM in seepage analysis with a free surface. *Mathematics and Computers in Simulation* 2013; **89**:23–37.
17. Burkley VJ, Bruch JC. Adaptive error analysis in seepage problems. *International Journal for Numerical Methods in Engineering* 1991; **31**(7):1333–1356.
18. Smaoui H, Zouhri L, Ouahsine A, Carlier E. Modelling of groundwater flow in heterogeneous porous media by finite element method. *Hydrological Processes* 2012; **26**(4):558–569.
19. Cao J, Kitanidis PK. Adaptive-grid simulation of groundwater flow in heterogeneous aquifers. *Advances in Water Resources* 1999; **22**(7):681–696.
20. George K, Thomas H. Simulation of groundwater flow based on adaptive mesh refinement. In *Proceedings of the 7th International Congress on Environmental Modeling and Software*, Vol. 3, Ames DP, Quinn NWT, Rizzoli AE (eds). iEMSs: San Diego, CA, USA, 2014; 1236–1243.
21. Dokken T, Lyche T, Pettersen KF. Polynomial splines over locally refined box-partitions. *Computer Aided Geometric Design* 2013; **30**(3):331–356.
22. Johannessen KA, Kvamsdal T, Dokken T. Isogeometric analysis using LR B-splines. *Computer Methods in Applied Mechanics and Engineering* 2014; **269**(0):471–514.
23. Hughes TJR, Cottrell JA, Bazilevs Y. Isogeometric analysis: CAD, finite elements, NURBS, exact geometry and mesh refinement. *Computer Methods in Applied Mechanics and Engineering* 2005; **194**(39-41):4135–4195.
24. Sederberg TW, Zheng J, Bakenov A, Nasri A. T-splines and T-NURCCs. *ACM Transactions on Graphics* 2003; **22**(3):477–484.
25. Cottrell JA, Hughes TJR, Bazilevs Y. *Isogeometric Analysis: Toward Integration of CAD and FEA*. John Wiley & Sons: Chichester, West Sussex, U.K., Hoboken, NJ, 2009.
26. Babuška I, Rheinboldt WC. Error estimates for adaptive finite element computations. *SIAM Journal on Numerical Analysis* 1978; **15**(4):736–754.
27. Babuška I, Rheinboldt WC. A posteriori error estimates for the finite element method. *International Journal of Numerical Methods and Engineering* 1978; **12**:1597–1615.

DOI: 10.1002/nag

28. Ainsworth M, Oden JT. *A Posteriori Error Estimation in Finite Element Analysis. Pure and Applied Mathematics (New York)*. Wiley-Interscience [John Wiley & Sons]: New York, 2000.
29. Zienkiewicz OC, Zhu JZ. A simple error estimator and adaptive procedure for practical engineering analysis. *Internat. J. Numer. Methods Engrg.* 1987; **24**(2):337–357.
30. Zienkiewicz OC, Zhu JZ. The superconvergent patch recovery and a posteriori error estimates. I. The recovery technique. *International Journal for Numerical Methods in Engineering* 1992; **33**(7):1331–1364.
31. Zienkiewicz OC, Zhu JZ. The superconvergent patch recovery and a posteriori error estimates. II. Error estimates and adaptivity. *International Journal for Numerical Methods in Engineering* 1992; **33**(7):1365–1382.
32. Kvamsdal T, Okstad KM. Error estimation based on superconvergent patch recovery using statically admissible stress fields. *International Journal for Numerical Methods in Engineering* 1998; **42**(3):443–472.
33. Okstad KM, Kvamsdal T, Mathisen KM. Superconvergent patch recovery for plate problems using statically admissible stress resultant fields. *International Journal for Numerical Methods in Engineering* 1999; **44**(5):697–727.
34. Kvamsdal T, Okstad KM, Herfjord K. Error estimator for recovered surface forces in incompressible Navier–Stokes flow. *Proceedings for The 17th International Conference on Offshore Mechanics and Arctic Engineering*, Lisbon, Portugal, 1998.
35. Kvamsdal T. Variationally consistent postprocessing for adaptive recovery of stresses. *Proceedings for European Conference on Computational Mechanics*, Munich, Germany, 1999.
36. Melbø H, Kvamsdal T. Goal oriented error estimators for Stokes equations based on variationally consistent postprocessing. *Computer Methods in Applied Mechanics and Engineering* 2003; **192**(5–6):613–633.
37. Okstad KM, Kvamsdal T. Object-oriented programming in field recovery and error estimation. *Engineering with Computers* 1999; **15**(1):90–104.
38. Okstad KM, Kvamsdal T. Object-oriented field recovery and error estimation in finite element methods. In *Advances in Software Tools for Scientific Computing*, vol. 10, Langtangen HP, Bruaset AM, Quak E (eds)., Lecture Notes in Computational Science and Engineering, 2000; 283–317.
39. Kumar M, Kvamsdal T, Johannessen KA. Simple posteriori error estimators in adaptive isogeometric analysis. *Computers and Mathematics with Applications*. DOI: 10.1016/j.camwa.2015.05.031.
40. Kumar M, Kvamsdal T, Johannessen KA. Superconvergent patch recovery and a posteriori error estimation technique in adaptive isogeometric analysis. *Computer Methods in Applied Mechanics and Engineering* 2015. Submitted.
41. Wahlbin LB. *Superconvergence in Galerkin finite element methods*, Lecture Notes in Mathematics, vol. 1605. Springer-Verlag: Berlin, 1995.
42. Mitchell WF. A collection of 2D elliptic problems for testing adaptive algorithms. *Technical Report NISTIR 7668*, U.S. Department of Commerce, Technology Administration, National Institute of Standards and Technology: Gaithersburg, MD, USA, 2010.

Paper II:

On Mixed Isogeometric Analysis of Poroelasticity

Submitted to *Computers and Structures*

On Mixed Isogeometric Analysis of Poroelasticity

Yared W. Bekele[a,*], Eivind Fonn[b], Trond Kvamsdal[b,c], Arne M. Kvarving[b], Steinar Nordal[a]

[a] *Department of Civil and Transport Engineering, NTNU, Trondheim, Norway*
[b] *Department of Applied Mathematics, SINTEF ICT, Trondheim, Norway*
[c] *Department of Mathematical Sciences, NTNU, Trondheim, Norway*

Abstract

Pressure oscillations at small time steps have been known to be an issue in poroelasticity simulations. A review of proposed approaches to overcome this problem is presented. Critical time steps are specified to alleviate this in finite element analyses. We present a mixed isogeometric formulation here with a view to assessing the results at very small time steps. Numerical studies are performed on Terzaghi's problem and consolidation of a layered porous medium with a very low permeability layer for varying polynomial degrees, continuities across knot spans and spatial discretizations. Comparisons are made with equal order simulations.

Keywords: poroelasticity, isogeometric analysis, mixed formulation, pressure oscillations

1. Introduction

The study of porous materials, where the flow of fluid and solid deformation are coupled, is essential in several areas of science and engineering. The theory of poroelasticity is a mathematical formulation developed to describe these coupled processes and predict the response of fluid saturated/unsaturated porous media to external loading. There are different types of porous materials that are studied under this theory such as soil, rock, concrete and other man-made materials. Poroelasticity has a wide range of applications in different disciplines of engineering mechanics and natural sciences. Some of the application areas include geomechanics, biomechanics, reservoir engineering and earthquake engineering. In addition to these diverse areas of application, it is gaining popularity in the study of modern man-made porous media in material science.

The mathematical formulations describing the fluid-solid coupled processes are developed based on porous media theory where the multiphase medium is approximated as a continuum, [2]. The volume fraction concept is used for averaging the properties of the multiphase medium in a continuum formulation.

*Corresponding author

Email addresses: yared.bekele@ntnu.no (Yared W. Bekele), eivind.fonn@sintef.no (Eivind Fonn), trond.kvamsdal@math.ntnu.no (Trond Kvamsdal), arne.morten.kvarving@sintef.no (Arne M. Kvarving), steinar.nordal@ntnu.no (Steinar Nordal)

Preprint submitted to Computers and Structures

The governing partial differential equations of poroelasticity were first developed for a one-dimensional case by Terzaghi [3, 4]. The formulations were later generalized for a three-dimensional case and extended by Biot [5, 6, 7]. The mathematical formulations have been studied extensively by several researchers since then. Various analytical and numerical studies have been proposed in the literature. Analytical solutions were obtained for problems with simplified material domains and boundary conditions. Application to boundary value problems with complex material domains and boundary conditions required the use of numerical methods. The emergence of the finite element method opened the door for a detailed numerical study of poroelasticity and for application to arbitrary geometries and boundary conditions.

The finite element method was first applied to the governing equations of poroelasticity to solve the initial boundary value problem of flow in a saturated porous elastic medium by Sandhu and Wilson [8]. Hwang *et al.* [9] also used the finite element method for plane strain consolidation problems and verified the results against closed form solutions. The application of the finite element method started gaining momentum afterwards and several researchers engaged themselves not only on application problems but also in the investigation of the numerical properties of the method within the context of poroelasticity. Ghaboussi and Wilson [10] applied the finite element method to partially saturated elastic porous media and first noticed the ill-conditioning of the matrix equations that may result when an incompressible fluid is assumed to occupy the pore spaces. Booker and Small [11] investigated the stability of the numerical solution when the finite element method is applied to Biot's consolidation equations. The stability was studied for different numerical integration schemes and time-step sizes. The numerical performance of some finite element schemes for analysis of seepage in porous elastic media was studied by Sandhu *et al.* [12]. They studied various spatial and temporal discretization schemes and evaluated the numerical performances against the analytical solution of Terzaghi's one-dimensional consolidation problem. Triangular and quadrilateral elements with equal and mixed orders of interpolation for the displacement and pressure were considered. It was shown that the elements with equal orders of interpolation showed oscillatory behavior in the solution. Vermeer and Verruijt [13] derived a lower bound for the time-step size in the analysis of consolidation by finite elements in terms of the mesh size and the coefficient of consolidation. They showed that there is an accuracy condition in the finite element analysis of consolidation by using a critical time-step, below which oscillatory solutions are observed. The derived critical time-step is strictly valid for a one-dimensional case and a uniform finite element mesh. Reed [14] analyzed the numerical errors in the analysis of consolidation by finite elements. It was shown that the use of a mixed formulation for the field variables helps in reducing the pore pressure oscillations but may not remove them entirely. They instead used Gauss point smoothing to eliminate the pore pressure oscillations. Special finite elements for the analysis of consolidation were proposed by Sandhu *et al.* [15]. They presented "singularity" elements to model pore pressures in the vicinity of free-draining loaded surfaces immediately after application of loads. The elements were special in that they use special interpolation schemes which reflect the actual variation of the field variables.

The finite element method became a well-established method for the analysis of poroelas-

ticity problems and the mathematical properties of the governing equations and the numerical solution were studied in a further great detail. Murad and Loula [16] presented numerical analysis and error estimates of finite element approximations of Biot's consolidation problem. They used a mixed formulation and improved the rates of convergence by using a sequential Galerkin Petrov-Galerkin post-processing technique. In a further study, [17], they investigated the stability and convergence of finite elements approximations of poroelasticity. They derived decay functions showing that the pore pressure oscillations, arising from an unstable approximation of the incompressibility constraint on the initial conditions, decay in time. Finite element analysis of consolidation with automatic time-stepping and error control was presented by Sloan and Abbo [18, 19]. Automatic time increments were selected such that the temporal discretization error in the displacements is close to a specified tolerance. Ferronato *et al.* [20] studied the ill-conditioning of finite element poroelasticity equations with a focus on the instabilities that may affect the pore pressure solution. They claim that the origin of most instabilities is due to the assumption that, for initial conditions, the porous medium behaves as an incompressible medium if the pore fluid is incompressible. They also argue that oscillatory pore pressure solutions may not always be observed for very stiff and low permeable materials depending on the critical time step. Gambolati *et al.* [21] studied the numerical performance of projection methods in finite element consolidation models. Dureisseix *et al.* [22] proposed a large time increment (LATIN) computational strategy for problems of poroelasticity to improve the efficiency of the finite element analysis. A finite element formulation to overcome spatial pore pressure oscillations caused by small time increments was proposed by Zhu *et al.* [23]. Korsawe *et al.* [24] compared standard and mixed finite element methods for poroelasticity. In particular, Galerkin and least-squares mixed finite element methods were compared. They claim that Galerkin's method is able to preserve steep pressure gradients but overestimates the effective stresses. On the other hand, a least-squares mixed method was noticed to have the advantage of direct approximation of the primary variables and explicit approximation of Neumann type boundary conditions but to be computationally more expensive. A mixed least-squares finite element method for poroelasticity was also proposed by Tchonkova *et al.* [25], claiming that pore pressure oscillations are eliminated for different temporal discretizations. A coupling of mixed and continuous Galerkin finite element methods for poroelasticity was investigated for continuous and discrete in time cases by Phillips and Wheeler [26, 27]. They also studied a coupling of mixed and discontinuous Galerkin finite-element methods, [28]. Haga *et al.* [29] studied the causes of pressure oscillations in low-permeable and low-compressible media by presenting two, three and four field mixed formulations in terms of the field variables displacement, pore fluid pressure, fluid velocity and solid skeleton stress.

A posteriori error estimation and adaptive refinement in poroelasticity has been studied by very few researchers. Larsson and Runesson [30] presented a novel approach for space-time adaptive finite element analysis for the coupled consolidation problem in geomechanics. El-Hamalawi and Bolton [31] proposed an a posteriori error estimator for plane-strain geotechnical analyses based on superconvergent patch recovery with application to Biot's consolidation problem. They later extended the application of the a posteriori estimator for axisymmetric geotechnical analyses in [32]. Adaptive isogeometric finite element analysis,

with LR B-Splines, for steady-state groundwater flow problems was presented by Bekele *et al.* [33] but application to poroelasticity still remains as a task to study.

Isogeometric finite element analysis of poroelasticity was first presented by Irzal *et al.* [1]. The advantages of the smoothness of the basis functions in isogeometric analysis were highlighted in their application. One of the advantages of higher continuity is that the numerical implementation results in a locally mass conserving flow between knotspans, analogous to elements in finite element analysis. But the formulation presented relied on equal orders of interpolation for the field variables in poroelasticity, namely displacement and pore fluid pressure. Such a formulation, while still useful for several applications without significant numerical challenges, has limitations when it comes to problems where the material properties or boundary conditions are problematic.

In this paper, we present a mixed isogeometric formulation for poroelasticity. To our best knowledge, this is the first time that a mixed isogeometric formulation for poroelasticity is presented. The paper is structured as follows. In Section 2, the governing equations of poroelasticity are presented. The fundamentals of isogeometric analysis and its particular features of interest within the current context are discussed in Section 3. Numerical examples are given in Section 4 and the observations are summarized with concluding remarks in Section 5.

2. Governing Equations

Biot's poroelasticity theory [5, 6] couples elastic solid deformation with fluid flow in the porous medium where the fluid flow is assumed to be governed by Darcy's law. The governing equations of the theory, the necessary boundary conditions, weak formulation and Galerkin finite element discretization are presented in the following sections.

2.1. Linear Momentum Balance Equation

The linear momentum balance equation for a fluid-saturated porous medium is given by:

$$\nabla \cdot \underbrace{\left(\boldsymbol{\sigma}' + \alpha p^{\mathrm{f}} \boldsymbol{I}\right)}_{=\boldsymbol{\sigma}} + \rho \boldsymbol{b} = \mathbf{0} \tag{1}$$

where $\boldsymbol{\sigma}$ is the total stress, $\boldsymbol{\sigma}'$ is the effective stress, α is Biot's coefficient, p^{f} is the fluid pressure, $\boldsymbol{I}$ is an identity matrix, ρ is the overall density of the porous medium and $\boldsymbol{b}$ represents body forces. The Biot coefficient α can be calculated from:

$$\alpha = 1 - \frac{K_{\mathrm{t}}}{K_{\mathrm{s}}} \tag{2}$$

where K_{t} and K_{s} are the bulk moduli of the porous medium and solid particles, respectively.

The constitutive equation for poroelasticity relates stress and strain linearly as:

$$\boldsymbol{\sigma}' = \boldsymbol{D} : \boldsymbol{\varepsilon} \tag{3}$$

where $\boldsymbol{D}$ is a fourth-order stiffness tensor. Small deformations are also assumed, so the strain $\boldsymbol{\varepsilon}$ satisfies a linear first-order equation with respect to the displacement $\boldsymbol{u}$,

$$\boldsymbol{\varepsilon} = \frac{1}{2}\left(\nabla \boldsymbol{u} + \nabla^{\intercal} \boldsymbol{u}\right) \tag{4}$$

where $1/2(\nabla + \nabla^{\intercal})$ is the symmetrized gradient operator i.e.

$$\varepsilon_{ij} = \frac{1}{2}\left(\frac{\partial u_i}{\partial x_j} + \frac{\partial u_j}{\partial x_i}\right). \tag{5}$$

In the following, it will be convenient to lower tensors and higher differential operators to Voigt notation, which represents the symmetric $d \times d$ tensor $\boldsymbol{\sigma'}$ as a $d(d+1)/2$-vector, which we will denote with a tilde:

$$\underbrace{\begin{bmatrix} \sigma'_{xx} & \sigma'_{xy} & \sigma'_{xz} \\ \sigma'_{xy} & \sigma'_{yy} & \sigma'_{yz} \\ \sigma'_{xz} & \sigma'_{yz} & \sigma'_{zz} \end{bmatrix}}_{\boldsymbol{\sigma'}} \Longleftrightarrow \underbrace{\begin{Bmatrix} \sigma'_{xx} & \sigma'_{yy} & \sigma'_{zz} & \sigma'_{yz} & \sigma'_{xz} & \sigma'_{xy} \end{Bmatrix}^{\intercal}}_{\tilde{\boldsymbol{\sigma}}'}$$

A similar conversion takes place for the strains, where the shear strains are replaced by the *engineering* shear strains:

$$\underbrace{\begin{bmatrix} \varepsilon_{xx} & \varepsilon_{xy} & \varepsilon_{xz} \\ \varepsilon_{xy} & \varepsilon_{yy} & \varepsilon_{yz} \\ \varepsilon_{xz} & \varepsilon_{yz} & \varepsilon_{zz} \end{bmatrix}}_{\boldsymbol{\varepsilon}} \Longleftrightarrow \underbrace{\begin{Bmatrix} \varepsilon_{xx} & \varepsilon_{yy} & \varepsilon_{zz} & 2\varepsilon_{yz} & 2\varepsilon_{xz} & 2\varepsilon_{xy} \end{Bmatrix}^{\intercal}}_{\tilde{\boldsymbol{\varepsilon}}}$$

Voigt notation allows us to express the equilibrium equation and the stress-strain equation using the same differential operator $\boldsymbol{L}$,

$$\boldsymbol{L}^{\intercal} = \begin{bmatrix} \frac{\partial}{\partial x} & 0 & 0 & \frac{\partial}{\partial y} & 0 & \frac{\partial}{\partial z} \\ 0 & \frac{\partial}{\partial y} & 0 & \frac{\partial}{\partial x} & \frac{\partial}{\partial z} & 0 \\ 0 & 0 & \frac{\partial}{\partial z} & 0 & \frac{\partial}{\partial y} & \frac{\partial}{\partial x} \end{bmatrix} \tag{6}$$

Using $\boldsymbol{L}$ yields the following equilibrium equation in terms of the two primary unknowns $\boldsymbol{u}$ and p^{f},

$$\boldsymbol{L}^{\intercal}\tilde{\boldsymbol{D}}\boldsymbol{L}\boldsymbol{u} - \alpha\nabla p^{\mathrm{f}} + \rho\boldsymbol{b} = \boldsymbol{0}, \tag{7}$$

where $\tilde{\boldsymbol{D}}$ is the Voigt notation equivalent of $\boldsymbol{D}$, taking into account the aforementioned engineering shear strains. We will generally assume isotropic materials, where $\tilde{\boldsymbol{D}}$ takes the block form (in terms of Young's modulus E and Poisson's ratio ν)

$$\tilde{\boldsymbol{D}} = \frac{E}{(1+\nu)(1-2\nu)}\begin{bmatrix} \tilde{\boldsymbol{D}}_{11} & \boldsymbol{0} \\ \boldsymbol{0} & \tilde{\boldsymbol{D}}_{22} \end{bmatrix} \tag{8}$$

where the two blocks are given as

$$\begin{aligned} \tilde{\boldsymbol{D}}_{11} &= (1-2\nu)\boldsymbol{I} + \nu\boldsymbol{1} \\ \tilde{\boldsymbol{D}}_{22} &= \frac{1-2\nu}{2}\boldsymbol{I} \end{aligned} \tag{9}$$

and $\boldsymbol{1}$ is a matrix of ones.

2.2. Mass Balance Equation

A mass conservation equation together with the equilibrium equation in (7) completes the governing equations of poroelasticity. The *fluid content* ζ is given by

$$\zeta = \alpha \nabla \cdot \boldsymbol{u} + c p^{\mathrm{f}} \tag{10}$$

where c is the *storativity* or *specific storage coefficient* at constant strain. It is given by

$$c = \frac{\alpha - n}{K_{\mathrm{s}}} + \frac{n}{K_{\mathrm{f}}} \tag{11}$$

where K_{f} is the bulk modulus of the fluid and n is the porosity of the material. The change in the fluid content ζ satisfies the equation

$$\frac{\partial \zeta}{\partial t} + \nabla \cdot \boldsymbol{w} = 0 \tag{12}$$

where $\boldsymbol{w}$ is the fluid flux, which is given by Darcy's law as:

$$\boldsymbol{w} = -\frac{1}{\gamma_{\mathrm{f}}} \boldsymbol{k} \cdot \left(\nabla p^{\mathrm{f}} - \rho_{\mathrm{f}} \boldsymbol{b} \right) \tag{13}$$

where γ_{f} is the unit weight of the fluid, ρ_{f} its density and $\boldsymbol{k}$ is the hydraulic conductivity matrix.

The final equation of mass balance is then

$$\alpha \nabla \cdot \dot{\boldsymbol{u}} + c \frac{\partial p^{\mathrm{f}}}{\partial t} + \nabla \cdot \left[-\frac{1}{\gamma_{\mathrm{f}}} \boldsymbol{k} \cdot \left(\nabla p^{\mathrm{f}} - \rho_{\mathrm{f}} \boldsymbol{b} \right) \right] = 0. \tag{14}$$

2.3. Boundary Conditions

The governing linear momentum and mass balance equations in (7) and (14), respectively, are accompanied by the usual boundary conditions in the formulation of bounary value problems. Let $(\Gamma_D^{\mathrm{u}}, \Gamma_D^{\mathrm{p}})$ and $(\Gamma_N^{\mathrm{u}}, \Gamma_N^{\mathrm{p}})$ be two partitions of the boundary $\partial\Omega$ of domain Ω, for representing Dirichlet and Neumann boundary conditions, respectively.

The Dirichlet boundary conditions for the equilibrium (7) and mass balance (14) equations are

$$\begin{cases} \boldsymbol{u} = \overline{\boldsymbol{u}} & \text{on } \Gamma_D^{\mathrm{u}}, \\ p^{\mathrm{f}} = \overline{p}^{\mathrm{f}} & \text{on } \Gamma_D^{\mathrm{p}}, \end{cases} \tag{15}$$

where $\overline{\boldsymbol{u}}$ and $\overline{p}_{\mathrm{f}}$ are the prescribed displacement and pressure, respectively.

The Neumann boundary conditions are

$$\begin{cases} \boldsymbol{\sigma} \cdot \boldsymbol{n} = \overline{\boldsymbol{t}} & \text{on } \Gamma_N^{\mathrm{u}}, \\ \boldsymbol{w} \cdot \boldsymbol{n} = \overline{q} & \text{on } \Gamma_N^{\mathrm{p}}, \end{cases} \tag{16}$$

where $\boldsymbol{n}$ is the outward pointing normal vector, $\overline{\boldsymbol{t}}$ is the surface traction and $\overline{q}$ is the fluid flux on the boundary.

2.4. Variational Formulation

To derive the variational formulations of equations (7) and (14), we introduce a vector-valued test function $\delta\boldsymbol{u}$, which vanishes on Γ_D^{u}, and a scalar test function δp, which vanishes on Γ_D^{p}.

We start with the total stress formulation of the linear momentum balance equation, which from equation (7) is given by

$$\nabla \cdot \boldsymbol{\sigma} + \rho \boldsymbol{b} = 0. \tag{17}$$

Multiplying by the test function $\delta\boldsymbol{u}$ and integrating over the domain Ω gives

$$\int_\Omega \delta\boldsymbol{u}^\intercal \nabla \cdot \boldsymbol{\sigma} \mathrm{d}\Omega + \int_\Omega \delta\boldsymbol{u}^\intercal \rho \boldsymbol{b} \mathrm{d}\Omega = \boldsymbol{0}. \tag{18}$$

The first term in the above equation contains a double derivative of the unknown displacement, and is relaxed using a form of Green's theorem,

$$\begin{aligned} \int_\Omega \delta\boldsymbol{u}^\intercal \nabla \cdot \boldsymbol{\sigma} \mathrm{d}\Omega &= \sum_i \int_\Omega \delta u_i \nabla \cdot \boldsymbol{\sigma}_i \mathrm{d}\Omega \\ &= \sum_i \int_{\partial\Omega} \delta u_i \boldsymbol{\sigma}_i \cdot \boldsymbol{n} \mathrm{d}\Gamma - \sum_i \int_\Omega \boldsymbol{\nabla} \delta u_i \cdot \sigma_i \mathrm{d}\Omega \\ &= \int_{\Gamma_N^{\mathrm{u}}} \delta\boldsymbol{u}^\intercal \bar{\boldsymbol{t}} \mathrm{d}\Gamma - \int_\Omega \nabla\delta\boldsymbol{u} : \boldsymbol{\sigma} \mathrm{d}\Omega. \end{aligned} \tag{19}$$

Due to the symmetry of the stress tensor, the last term is expressible in Voigt notation,

$$\nabla\delta\boldsymbol{u} : \boldsymbol{\sigma} = (\boldsymbol{L}\delta\boldsymbol{u})^\intercal \boldsymbol{\sigma}, \tag{20}$$

yielding the weak form of (7) as

$$\int_\Omega (\boldsymbol{L}\delta\boldsymbol{u})^\intercal \tilde{\boldsymbol{D}} (\boldsymbol{L}\boldsymbol{u}) \mathrm{d}\Omega - \alpha \int_\Omega (\boldsymbol{L}\delta\boldsymbol{u})^\intercal \tilde{\boldsymbol{I}} p^{\mathrm{f}} \mathrm{d}\Omega = \int_\Omega \delta\boldsymbol{u}^\intercal \rho \boldsymbol{b} \mathrm{d}\Omega + \int_{\Gamma_N^{\mathrm{u}}} \delta\boldsymbol{u}^\intercal \bar{\boldsymbol{t}} \mathrm{d}\Gamma \tag{21}$$

where we have used $\tilde{\boldsymbol{I}}$ as the Voigt notation identity operator, which for a general three-dimensional case is given by:

$$\tilde{\boldsymbol{I}} = \{1, 1, 1, 0, 0, 0\}^\intercal \tag{22}$$

For the mass balance equation, multiplying (14) by the scalar test function δp and integrating over the domain Ω, we get

$$\alpha \int_\Omega \delta p \nabla \cdot \dot{\boldsymbol{u}} \mathrm{d}\Omega + c \int_\Omega \delta p \frac{\partial p^{\mathrm{f}}}{\partial t} \mathrm{d}\Omega + \int_\Omega \delta p \nabla \cdot \left[-\frac{1}{\gamma_{\mathrm{f}}} \boldsymbol{k} \cdot \left(\nabla p^{\mathrm{f}} - \rho_{\mathrm{f}} \boldsymbol{b} \right) \right] \mathrm{d}\Omega = 0. \tag{23}$$

Again, by applying Green's theorem to the last term, we obtain

$$\int_\Omega \delta p \nabla \cdot \left[-\frac{1}{\gamma_{\mathrm{f}}} \boldsymbol{k} \cdot \left(\nabla p^{\mathrm{f}} - \rho_{\mathrm{f}} \boldsymbol{b} \right) \right] \mathrm{d}\Omega = \int_{\Gamma_N^{\mathrm{p}}} \delta p \bar{q} \mathrm{d}\Gamma - \int_\Omega \nabla\delta p \cdot \left[-\frac{1}{\gamma_{\mathrm{f}}} \boldsymbol{k} \cdot \left(\nabla p^{\mathrm{f}} - \rho_{\mathrm{f}} \boldsymbol{b} \right) \right] \mathrm{d}\Omega. \tag{24}$$

Thus, the weak form of the mass balance equation, (14), is

$$\alpha \int_\Omega \delta p \nabla \cdot \dot{\boldsymbol{u}} \mathrm{d}\Omega + c \int_\Omega \delta p \frac{\partial p^{\mathrm{f}}}{\partial t} \mathrm{d}\Omega + \int_\Omega \nabla\delta p^\intercal \frac{1}{\gamma_{\mathrm{f}}} \boldsymbol{k} \nabla p^{\mathrm{f}} \mathrm{d}\Omega = \int_\Omega \nabla\delta p^\intercal \frac{1}{\gamma_{\mathrm{f}}} \boldsymbol{k} \rho_{\mathrm{f}} \boldsymbol{b} \mathrm{d}\Omega - \int_{\Gamma_N^{\mathrm{p}}} \delta p \bar{q} \mathrm{d}\Gamma. \tag{25}$$

2.5. Galerkin Finite Element Formulation

With a suitable number N of basis functions defined, let $\boldsymbol{N}_\mathrm{p} : \Omega \to \mathbb{R}^{1\times N}$ and $\boldsymbol{N}_\mathrm{u} : \Omega \to \mathbb{R}^{d\times dN}$ be the basis interpolation matrices for the pressure and displacement respectively. The unknowns and the test functions can then be represented using coefficient vectors:

$$\begin{aligned} \boldsymbol{u} &= \boldsymbol{N}_\mathrm{u}\boldsymbol{u}^\mathrm{c}, \quad \delta\boldsymbol{u} = \boldsymbol{N}_\mathrm{u}\delta\boldsymbol{u}^\mathrm{c}, \\ p^\mathrm{f} &= \boldsymbol{N}_\mathrm{p}\boldsymbol{p}^\mathrm{c}, \quad \delta p = \boldsymbol{N}_\mathrm{p}\delta\boldsymbol{p}^\mathrm{c} \end{aligned} \tag{26}$$

where $\boldsymbol{u}^\mathrm{c}$ and $\boldsymbol{p}^\mathrm{c}$ are the control point values of the displacement and pressure field variables. Application of (26) to the weak form of the linear momentum balance equation in (21) results in the matrix the discrete system of equations (after canceling $\delta\boldsymbol{u}^\mathrm{c}$ and $\boldsymbol{\delta}p^\mathrm{c}$, as equations (7) and (14) are supposed to be valid for any choice of these)

$$\boldsymbol{K}\boldsymbol{u}^\mathrm{c} - \boldsymbol{Q}\boldsymbol{p}^\mathrm{c} = \boldsymbol{f}_\mathrm{u} \tag{27}$$

where the stiffness matrix $\boldsymbol{K}$, the coupling matrix $\boldsymbol{Q}$ and the vector of body forces and surface tractions $\boldsymbol{f}_u$ are given by

$$\begin{aligned} \boldsymbol{K} &= \int_\Omega \boldsymbol{B}^\intercal \tilde{\boldsymbol{D}}\boldsymbol{B}\mathrm{d}\Omega \\ \boldsymbol{Q} &= \int_\Omega \boldsymbol{B}^\intercal \alpha\tilde{\boldsymbol{I}}\boldsymbol{N}_\mathrm{p}\mathrm{d}\Omega \\ \boldsymbol{f}_\mathrm{u} &= \int_\Omega \boldsymbol{N}_\mathrm{u}^\intercal \rho\boldsymbol{b}\mathrm{d}\Omega + \int_{\Gamma_N^\mathrm{u}} \boldsymbol{N}_\mathrm{u}^\intercal \bar{\boldsymbol{t}}\mathrm{d}\Gamma \end{aligned} \tag{28}$$

Here $\boldsymbol{B} = \boldsymbol{L}\boldsymbol{N}_\mathrm{u}$ is the strain-displacement matrix. Similarly, using (26) in the weak form of the mass balance equation in (25) results in the discrete system of equations

$$\boldsymbol{Q}^\intercal \frac{\partial \boldsymbol{u}^\mathrm{c}}{\partial t} + \boldsymbol{S}\frac{\partial \boldsymbol{p}^\mathrm{c}}{\partial t} + \boldsymbol{P}\boldsymbol{p}^\mathrm{c} = \boldsymbol{f}_\mathrm{p} \tag{29}$$

where the storage matrix $\boldsymbol{S}$, the permeability matrix $\boldsymbol{P}$ and the vector of fluid body forces and fluxes $\boldsymbol{f}_\mathrm{p}$ are given by

$$\begin{aligned} \boldsymbol{S} &= \int_\Omega \boldsymbol{N}_\mathrm{p}^\intercal c\boldsymbol{N}_\mathrm{p}\mathrm{d}\Omega \\ \boldsymbol{P} &= \int_\Omega \nabla\boldsymbol{N}_\mathrm{p}^\intercal \frac{1}{\gamma_\mathrm{f}}\boldsymbol{k}\nabla\boldsymbol{N}_\mathrm{p}\mathrm{d}\Omega \\ \boldsymbol{f}_\mathrm{p} &= \int_\Omega \nabla\boldsymbol{N}_\mathrm{p}^\intercal \frac{1}{\gamma_\mathrm{f}}\boldsymbol{k}\rho_\mathrm{f}\boldsymbol{b}\mathrm{d}\Omega - \int_{\Gamma_N^\mathrm{p}} \boldsymbol{N}_\mathrm{p}^\intercal \bar{q}\mathrm{d}\Gamma. \end{aligned} \tag{30}$$

Combining equations (27) and (29) results in the coupled system of equations for poroelasticity

$$\begin{bmatrix} \boldsymbol{0} & \boldsymbol{0} \\ \boldsymbol{Q}^\intercal & \boldsymbol{S} \end{bmatrix} \begin{Bmatrix} \dot{\boldsymbol{u}}^\mathrm{c} \\ \dot{\boldsymbol{p}}^\mathrm{c} \end{Bmatrix} + \begin{bmatrix} \boldsymbol{K} & -\boldsymbol{Q} \\ \boldsymbol{0} & \boldsymbol{P} \end{bmatrix} \begin{Bmatrix} \boldsymbol{u}^\mathrm{c} \\ \boldsymbol{p}^\mathrm{c} \end{Bmatrix} = \begin{Bmatrix} \boldsymbol{f}_\mathrm{u} \\ \boldsymbol{f}_\mathrm{p} \end{Bmatrix}. \tag{31}$$

A symmetric system of equations can be obtained by time-differentiating the first equation and multiplying one of the equations by -1, [34]:

$$\begin{bmatrix} -\boldsymbol{K} & \boldsymbol{Q} \\ \boldsymbol{Q}^{\intercal} & \boldsymbol{S} \end{bmatrix} \begin{Bmatrix} \dot{\boldsymbol{u}}^{\mathrm{c}} \\ \dot{\boldsymbol{p}}^{\mathrm{c}} \end{Bmatrix} + \begin{bmatrix} \boldsymbol{0} & \boldsymbol{0} \\ \boldsymbol{0} & \boldsymbol{P} \end{bmatrix} \begin{Bmatrix} \boldsymbol{u}^{\mathrm{c}} \\ \boldsymbol{p}^{\mathrm{c}} \end{Bmatrix} = \begin{Bmatrix} -\dot{\boldsymbol{f}}_{\mathrm{u}} \\ \boldsymbol{f}_{\mathrm{p}} \end{Bmatrix} \tag{32}$$

In this formulation, it is important that time-dependent quantities involved in $\boldsymbol{f}_u$, such as traction and body forces, are "ramped up" from an initial equilibrium instead of being applied immediately. This can be done in the first time step.

2.6. Temporal Discretization

The generalized trapezoidal rule (GTR) is applied for the temporal discretization of the coupled system of matrix equations in (32). Representing the vector of unknowns by $\boldsymbol{X} = \{\boldsymbol{u}^c, \boldsymbol{p}^c\}^{\intercal}$, we have the GTR approximation

$$\begin{aligned} \left.\frac{\partial \boldsymbol{X}}{\partial t}\right|_{n+\theta} &= \frac{\boldsymbol{X}_{n+1} - \boldsymbol{X}_n}{\Delta t} \\ \boldsymbol{X}_{n+\theta} &= (1-\theta)\boldsymbol{X}_n + \theta \boldsymbol{X}_{n+1} \end{aligned} \tag{33}$$

where θ is a time integration parameter which has limits $0 \leq \theta \leq 1$ and n is a time step identifier. Adopting backward Euler time stepping ($\theta = 1$) with time step Δt and applying (33) to (32) we obtain the system of equations

$$\begin{bmatrix} -\boldsymbol{K} & \boldsymbol{Q} \\ \boldsymbol{Q}^{\intercal} & \boldsymbol{S} + \Delta t \boldsymbol{P} \end{bmatrix} \begin{Bmatrix} \boldsymbol{u}^{\mathrm{c}} \\ \boldsymbol{p}^{\mathrm{c}} \end{Bmatrix}_{n+1} = \begin{bmatrix} -\boldsymbol{K} & \boldsymbol{Q} \\ \boldsymbol{Q}^{\intercal} & \boldsymbol{S} \end{bmatrix} \begin{Bmatrix} \boldsymbol{u}^{\mathrm{c}} \\ \boldsymbol{p}^{\mathrm{c}} \end{Bmatrix}_{n} + \Delta t \begin{Bmatrix} -\dot{\boldsymbol{f}}_u \\ \boldsymbol{f}_p \end{Bmatrix}_{n+1} \tag{34}$$

which is a linear system in this case, for poroelasticity, as the coefficient matrices are independent of the unknowns.

3. Isogeometric Analysis

3.1. Introduction

Since its first introduction by Hughes *et al.* [35], isogeometric analysis (IGA) has been successfully applied to several areas of engineering mechanics problems. The fundamental aim for the introduction of IGA was the idea of bridging the gap between finite element analysis (FEA) and computer-aided design (CAD). The main concept behind the method is the application of the same basis functions used in CAD for performing finite element analysis. In the process of its application to various engineering problems, IGA has shown advantages over the conventional finite element method, for instance the ease of performing finite element analysis using higher order polynomials.

We briefly present the fundamentals behind B-Splines and Non-Uniform Rational B-Splines (NURBS) in the next section and highlight the features of IGA that are important in our context.

3.2. Fundamentals on B-Splines and NURBS

We start the discussion on B-Splines and NURBS by first defining a *knot vector*. A knot vector in one dimension is a non-decreasing set of coordinates in the parameter space, written $\Xi = \{\xi_1, \xi_2, ..., \xi_{n+p+1}\}$, where $\xi_i \in \mathbb{R}$ is the i^{th} knot, i is the knot index, $i = 1, 2, ..., n+p+1$, p is the polynomial order, and n is the number of basis functions. Knot vectors may be uniform or non-uniform depending on whether the knots are equally spaced in the parameter space or not.

A univariate B-Spline curve is parametrized by a linear combination of n B-Spline basis functions, $\{N_{i,p}\}_{i=1}^{n}$. The coefficients corresponding to these functions, $\{\boldsymbol{X}_i\}_{i=1}^{n}$, are referred to as control points. The B-Spline basis functions are recursively defined starting with piecewise constants ($p = 0$):

$$N_{i,0}(\xi) = \begin{cases} 1 & \text{if } \xi_i \leq \xi < \xi_{i+1} \\ 0 & \text{otherwise} \end{cases} \tag{35}$$

For higher-order polynomial degrees ($p \geq 1$), the basis functions are defined by the Cox-de Boor recursion formula:

$$N_{i,p}(\xi) = \frac{\xi - \xi_i}{\xi_{i+p} - \xi_i} N_{i,p-1}(\xi) + \frac{\xi_{i+p+1} - \xi}{\xi_{i+p+1} - \xi_{i+1}} N_{i+1,p-1}(\xi) \tag{36}$$

B-Spline geometries, curves, surfaces and solids, are constructed from a linear combination of B-Spline basis functions. Given n basis functions $N_{i,p}$ and corresponding control points $\boldsymbol{P}_i \in \mathbb{R}^d, i = 1, 2, ..., n$, a piecewise polynomial B-Spline curve is given by:

$$\boldsymbol{C}(\xi) = \sum_{i=1}^{n} N_{i,p}(\xi) \boldsymbol{P}_i \tag{37}$$

Similarly, for a given control net $\boldsymbol{P}_{i,j}, i = 1, 2, ..., n, j = 1, 2, ..., m$, polynomial orders p and q, and knot vectors $\Xi = \{\xi_1, \xi_2, ..., \xi_{n+p+1}\}$, and $\mathcal{H} = \{\eta_1, \eta_2, ..., \eta_{m+q+1}\}$, a tensor product B-Spline surface is defined by:

$$\boldsymbol{S}(\xi, \eta) = \sum_{i=1}^{n} \sum_{j=1}^{m} N_{i,p}(\xi) M_{j,q}(\eta) \boldsymbol{P}_{i,j} \tag{38}$$

B-Spline solids are defined in a similar way as B-Spline surfaces from tensor products over a control lattice.

NURBS are built from B-Splines to represent a wide array of objects that cannot be exactly represented by polynomials. A NURBS entity in $\mathbb{R}^d$ is obtained by projective transformation of a B-Spline entity in $\mathbb{R}^{d+1}$. The control points for the NURBS geometry are found by performing exactly the same projective transformation to the control points of the B-Spline curve. A detailed treatment of B-Splines and NURBS can be referred from Cottrell *et al.* [36].

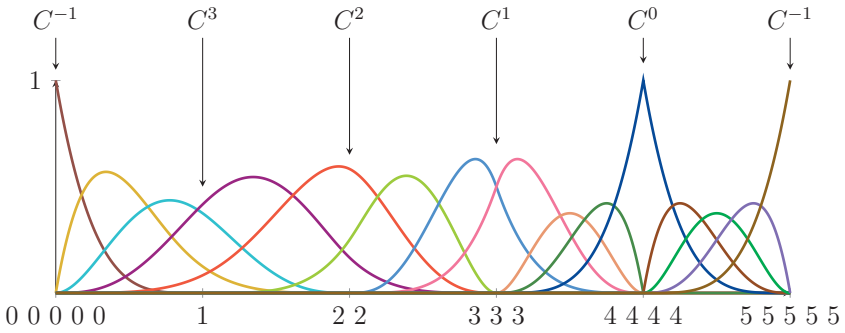

Figure 1: Different continuities across knotspans, after [36].

3.3. Important Features in Current Context

IGA has a number of advantages over FEA such as the ability to represent exact geometries of structures or domains, non-negative basis functions and isoparametric mapping at patch level. In the context of the current work, we focus on the features of IGA that are especially important. These features are improved continuity because of the smoothness of the basis functions and the ability to perform simulations with high continuity and high regularity meshes. We look closely into each here.

3.3.1. Continuity

One of the most distinctive and powerful features of IGA is that the basis functions will be C^{p-m} continuous across knotspans (analogous to elements in FEA), where p is the polynomial degree and m is the multiplicity of the knot. This means that the continuity across knotspans can be controlled by the proper choice of p and m. The continuity can be decreased by repeating a knot - important to model non-smooth geometry features or to facilitate the application of boundary conditions. For instance, quadratic ($p = 2$) splines are C^1 continuous over non-repeated knots while quadratic Lagrange finite element bases are only C^0 continuous. If we consider the quartic ($p = 4$) basis functions constructed from the open, non-uniform knot vector $\Xi = \{0, 0, 0, 0, 0, 1, 2, 2, 3, 3, 3, 4, 4, 4, 4, 5, 5, 5, 5, 5\}$, we get different continuities across knotspans as shown in Figure 1.

3.3.2. k-refinement

IGA and FEA both allow h- and p-refinements i.e. increasing the number of knotspans by knot insertion (increasing the number of elements in FEA) and raising the polynomial order. The non-commutativity of knot insertion and polynomial order elevation results in a type of refinement that is unique to IGA, called k-refinement. This is achieved by performing polynomial order elevation followed by knot insertion. This results in a high continuity mesh with the least number of degrees of freedom i.e. high regularity.

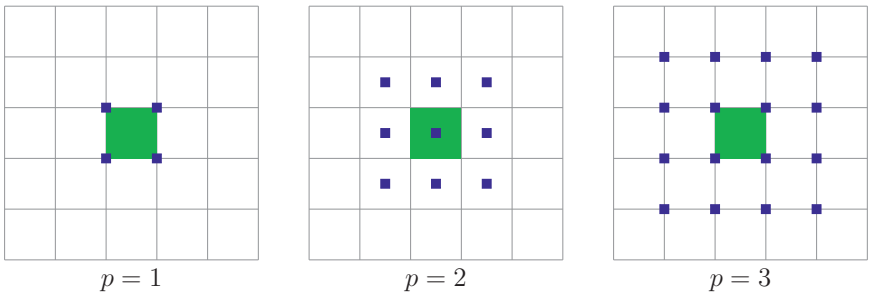

Figure 2: Number of control points for a given element on a simple B-Spline surface with different polynomial degrees. The element is highlighted and the blue squares represent control points.

3.4. Mixed Isogeometric Formulation

A mixed formulation is constructed by first defining the knot vectors and basis functions defining the geometry of the domain. The polynomial order defining the geometry is used as the polynomial degree for one of the field variables and is raised by the desired degree for the other field variable. In our context, the polynomial order for the pressure, p_{p}, is defined by the geometry construction and the polynomial order for the displacement, p_{u}, is raised by one. Both p_{p} and p_{u} can then be raised to the desired degree starting from the initial definition. For example, a simple two-dimensional geometry defined by the knot vectors $\Xi = \{0, 0, 1, 1\}$ and $\mathcal{H} = \{0, 0, 1, 1\}$ implies $p_{\mathrm{p}} = 1$ and $p_{\mathrm{u}} = 2$ with 4 and 9 control points, respectively. The number of control points, location of degrees of freedom in IGA, on a B-Spline surface for different polynomial degrees is shown in Figure 2.

4. Numerical Examples

In this section, the performance of a mixed isogeometric formulation is investigated for some numerical examples. We first consider Terzaghi's classical one-dimensional consolidation problem for verification and mesh convergence studies. Consolidation of a layered medium with a low permeability layer sandwiched between two high permeability layers is studied. The mixed formulation results are compared with equal order simulation.

4.1. Terzaghi's Problem

Terzaghi's problem is a classical one-dimensional consolidation problem with an analytical solution, which makes it suitable for code validation. A saturated porous medium subjected an external loading under plane-strain condition is considered where the fluid is allowed to dissipate only at the top boundary, hence resulting in a one-dimensional consolidation. A no flux boundary condition is assumed for the lateral and bottom boundaries. The displacement boundary conditions are such that the lateral sides are constrained from horizontal deformation and the bottom boundary is fixed in both the horizontal and vertical

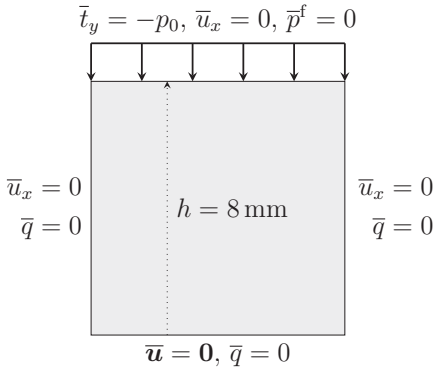

Figure 3: Terzaghi's problem: Domain and boundary conditions.

directions. The external load is applied as a Neumann traction p_0 at the top boundary. The domain and boundary conditions considered are shown in Figure 3.

The analytical solution for the pressure field as a function of time and space is given by:

$$\frac{p^{\mathrm{f}}(t,y)}{p_0} = \frac{4}{\pi}\sum_{i=1}^{\infty}\frac{(-1)^{i-1}}{2i-1}\exp\left[-(2i-1)^2\frac{\pi^2 t_{\mathrm{s}}}{4}\right]\cos\left[(2i-1)\frac{\pi y}{2h}\right]$$

where the dimensionless time t_{s} is given as a function of the consolidation coefficient c_{v} and drainage path h (total height for one-way drainage) by:

$$t_{\mathrm{s}} = \frac{c_{\mathrm{v}}}{h^2}t. \tag{39}$$

The consolidation coefficient c_{v} is given by:

$$c_{\mathrm{v}} = \frac{(1-\nu)E\kappa}{(1+\nu)(1-2\nu)} \tag{40}$$

The material parameters used for this problem are given in Table 1, as used in [1]. The choice of the storativity value $c = 0$ effectively corresponds to assuming incompressible solid grains and an incompressible fluid.

The Terzaghi verification problem is simulated in a mixed and equal order formulation for comparison. The polynomial degrees considered for the pressure are $p_{\mathrm{p}} = 1, 2, 3$. The corresponding values for the displacement in a mixed formulation are $p_{\mathrm{u}} = 2, 3, 4$. The number of elements used in the simulation is $N_{\mathrm{e}} = 72$. Critical and sub-critical time step sizes are considered to study the sensitivity of the simulations to temporal discretization and to evaluate accuracy of the solution for small time step sizes. The critical time step is calculated according to the relation derived in [13].

104

Table 1: Terzaghi's problem: Load and material parameters.

Parameter	**Value**	**Unit**
External load, p_0	1.0×10^6	Pa
Hydraulic conductivity, k	1.962×10^{-14}	m^2
Biot's coefficient, α	1.0	–
Young's modulus, E	6.0×10^6	Pa
Poisson's ratio, ν	0.4	–
Storativity, c	0	Pa^{-1}
Body forces, $\boldsymbol{b}$	$\mathbf{0}$	N

The results from a simulation using the critical time step are shown in Figure 4. A linear solution space is used for the pressure and a quadratic space for the displacement. The results from simulations with a sub-critical time step are shown in Figure 5 for mixed and equal order cases. The results with the time step size equal to the critical time step show no oscillations in the pressure values. On the other hand, slight oscillations are visible for the sub-critical time step case. These oscillations at very small time steps appear worse for the equal order simulations compared to the mixed simulation. In both cases, the results are observed to improve with increasing polynomial degrees.

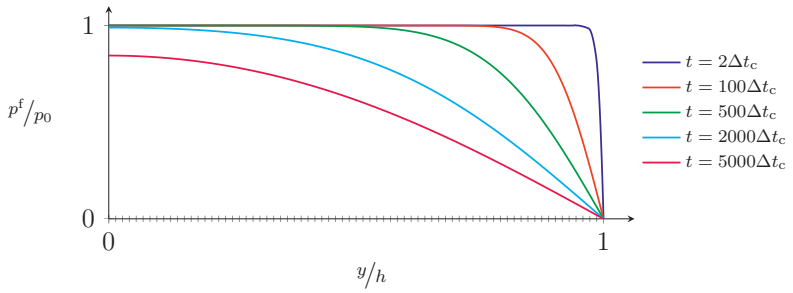

Figure 4: Numerical solution to the Terzhagi problem with $p_{\mathrm{p}} = 1$, $p_{\mathrm{u}} = 2$ and and $N_e = 72$ using critical time step.

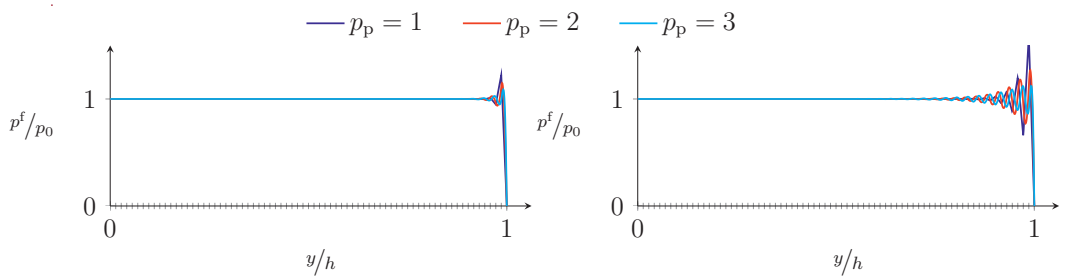

(a) Mixed (b) Equal order

Figure 5: Numerical solution to the Terzaghi problem with $N_{\mathrm{e}} = 72$ using a sub-critical time step of $\Delta t = 0.1\Delta t_{\mathrm{c}}$ for different polynomial degrees. All plots are shown for the first time step.

4.2. Terzaghi's Problem: Convergence Study

Next, a simplified version of the Terzaghi problem is used as a convergence study. We consider a domain with dimensions of $w \times h = 1 \times 1$ with the same boundary conditions as in the previous case. For simplicity we choose the following material parameters: $\alpha = 1$, $c = 0$, $E = 2/3$, $\nu = 0.25$ and $\kappa = 1$. The external load applied is $p_0 = 1$ and we assume no body forces i.e. $\boldsymbol{b} = \mathbf{0}$.

This case was run with an increasing number of degrees of freedom using polynomial degrees $p_{\mathrm{p}} = 1, 2, 3$ for the pressure and correspondingly $p_{\mathrm{u}} = 2, 3, 4$ for the displacement. In all cases, the time step was kept sufficiently small for the spatial discretization error to dominate and we look at the results at the end of the first time step.

The convergence study is performed by calculating the relative L^2 error of the pressure field. The relative error based on the computed pressure values, ρ_h, is calculated from

$$\rho_h = \frac{\|p_h^{\mathrm{f}} - p^{\mathrm{f}}\|_{L^2}}{\|p^{\mathrm{f}}\|_{L^2}} \tag{41}$$

where p_h^{f} and p^{f} are the computed and analytical solution pressures, respectively. The results

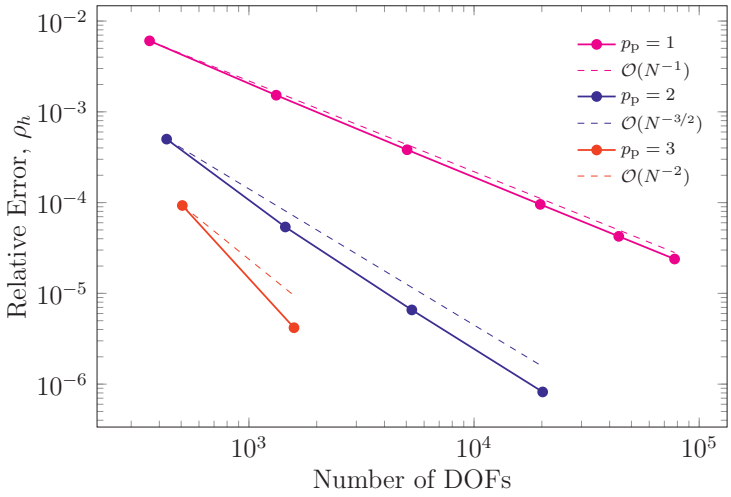

Figure 6: Convergence rates in the relative L^2 norm of pressure, for three different polynomial degrees.

from the mesh convergence study are shown in Figure 6 in terms of plots of the relative error versus the total number of degrees of freedom. The expected convergence rate based on the analytical solution is also shown. We observe from the results that optimal convergence rates are obtained for all polynomial degrees considered.

4.3. Low Permeability Layer

The next example we consider is the consolidation of a very low permeability layer sandwiched between two high permeability layers, as presented in [29]. A one-dimensional consolidation is assumed by applying the appropriate boundary conditions. The fluid is allowed to dissipate at the top boundary and a no flux condition is defined at the lateral and bottom boundaries. The bottom boundary is fixed from vertical and horizontal displacement and the domain is allowed to deform only in the vertical direction. An external load p_0 is applied at the top boundary. The problem setup with the boundary conditions is shown in Figure 7.

The material parameters for this problem are given in Table 2. Simplified material properties are assumed to focus on the permeability differences of the middle and the bounding layers.

The low permeability layer problem is studied using mixed and equal order simulations. The polynomial degrees for the pressure are increased continuously from linear to quartic i.e. $p_\mathrm{p} = 1, 2, 3, 4$. The corresponding polynomial degrees for the displacement in a mixed formulation are $p_\mathrm{u} = 2, 3, 4, 5$. The continuities at the boundaries between the layers are also varied. We consider C^0 and $C^{p_\mathrm{p}-1}$ continuities at these interfaces. In addition, simulations are performed for uniform and graded meshes. The results are presented for these different combinations.

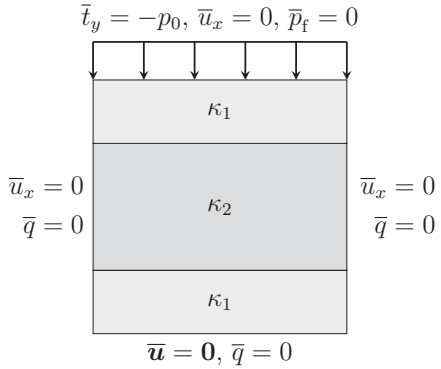

Figure 7: The Haga problem: Domain and boundary conditions.

Table 2: The Haga problem: Load and material parameters.

Parameter	**Value**	**Unit**
External load, p_0	1.0	Pa
Darcy coefficient, k_1/γ_f	1.0	m^2/Pa s
Darcy coefficient, k_2/γ_f	1.0×10^{-8}	m^2/Pa s
Biot's coefficient, α	1.0	–
Young's modulus, E	0.67	Pa
Poisson's ratio, ν	0.25	–
Storativity, c	0	Pa^{-1}
Body forces, $\boldsymbol{b}$	$\mathbf{0}$	N

The results from simulations with a uniformly refined mesh are shown in Figure 8 for the mixed and equal order cases. Severe pressure oscillations are observed within the low permeability layer for the equal order simulations. Due to its high permeability, the fluid in the top layer dissipates very quickly for the time step size considered here i.e. $\Delta t = 1s$. The pressure oscillations start as soon as the fluid in the low permeability layer starts dissipating. The results improve with increasing polynomial degrees but some oscillations are still seen for a quartic solution space for the pressure, $p_\mathrm{p} = 4$. The results with C^0 continuities at the material interfaces improve slightly better than with $C^{p_\mathrm{p}-1}$ continuity since a C^0 continuity is a more accurate representation of material interfaces. The pressure oscillations in the mixed simulations are less severe and are localized at the boundary between the low permeability and bottom layers. These again decrease with increasing polynomial degrees and a C^0 continuity at the material interfaces.

Simulations with a graded mesh are also performed for the different combination of polynomial degrees and interface continuities. The graded mesh is generated such that

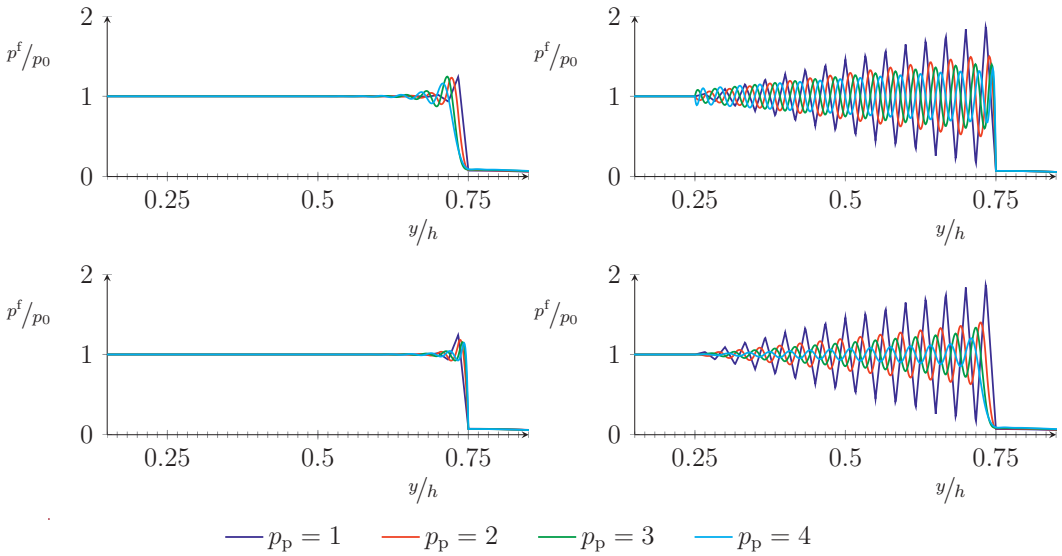

Figure 8: Numerical solution to the Haga problem using $N_{\mathrm{e}} = 60$ uniform elements and $\Delta t = 1\,\mathrm{s}$. All figures are shown after two time steps. On the left the mixed order method, and on the right the equal order method. The continuity in the boundary layer is $C^{p_{\mathrm{p}}-1}$ in the top row, and C^0 in the bottom row.

more elements are concentrated at the material interfaces. The results from this case are shown in Figure 9. The pressure oscillations in the equal order case improve significantly in this case compared to the results from uniform mesh refinement. However, the oscillations still occur throughout the low permeability layer. The equal order results for linear basis functions show a slightly strange behavior in that the oscillations are lesser within the low permeability layer than for higher order elements, but show slightly higher oscillations at the top material interface. The results are again better with a C^0 continuity at the material interfaces. The mixed simulation results also improve with a graded mesh. Almost no oscillations are noticed for combinations of higher polynomial degrees and C^0 continuities at the material interfaces.

5. Conclusions

Mixed isogeometric analysis of poroelasticity is presented where different order of polynomials are used for the displacement and pore pressure field variables. Numerical studies on Terzaghi's classical one-dimensional consolidation problem and consolidation of a layered soil with a middle low permeability layer are presented. The results from mixed polynomial order simulations are compared with equal order analyses. For Terzaghi's one-dimensional consolidation problem, the pore pressure oscillations are investigated when a time step size less than the critical value is used. The oscillations were observed to be higher in the equal

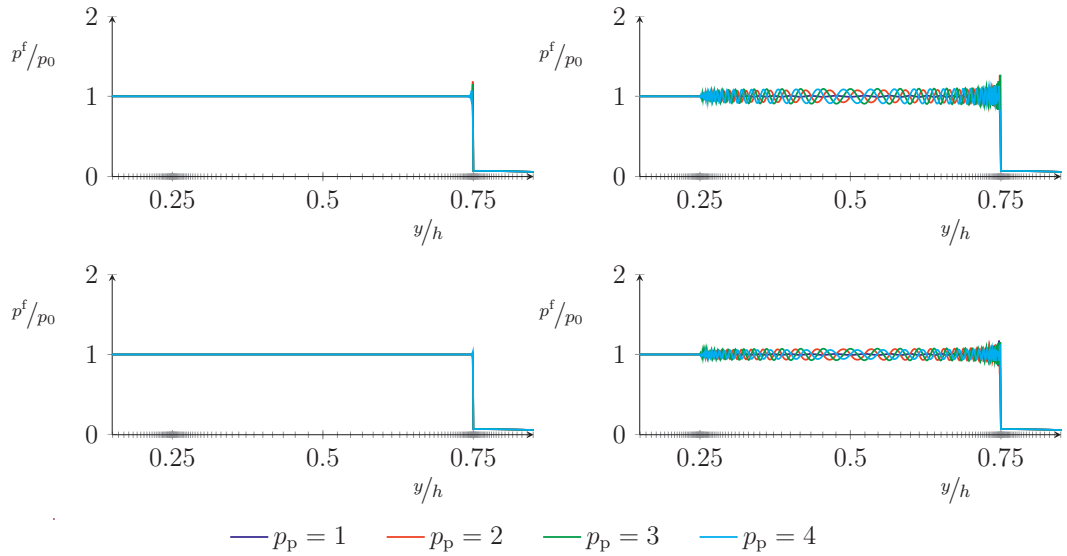

Figure 9: Numerical solution to the Haga problem using a graded mesh with small elements near the boundary layer and $\Delta t = 1\,\mathrm{s}$. All figures are shown after two time steps. On the left the mixed order method, and on the right the equal order method. The continuity in the boundary layer is $C^{p_{\mathrm{p}}-1}$ in the top row, and C^0 in the bottom row.

order simulations compared to the mixed order results. The oscillations are not completely removed in the mixed isogeometric simulations but it is observed that the they tend to decrease with increasing polynomial orders for the pore pressure. This is illustrated by the convergence of the relative L^2 norm of the pore pressure error for varying polynomial orders. The low permeability layer problem showed similar trends in the pore pressure oscillations i.e. the equal order simulations resulted in worse pore pressure oscillations compared to the mixed results. Again, in both cases, the oscillations decreased with increasing polynomial orders. The use of a graded mesh, where the knot spans are concentrated at the interfaces between the low permeability and other layers, resulted in much lower oscillations both in the equal order and mixed cases. This indicates the potential of adaptive refinement for such class of problems.

Acknowledgement

This work is financially supported by the Research Council of Norway and industrial partners through the research project SAMCoT, Sustainable Arctic Marine and Coastal Technology. The authors gratefully acknowledge the support.

References

[1] F. Irzal, J. J. Remmers, C. V. Verhoosel, R. de Borst, Isogeometric finite element analysis of poroelasticity, International Journal for Numerical and Analytical Methods in Geomechanics 37 (12) (2013) 1891–1907.

[2] R. de Boer, W. Ehlers, A historical review of the formulation of porous media theories, Acta Mechanica 74 (1-4) (1988) 1–8.

[3] K. v. Terzaghi, Die berechnung der durchlassigkeitsziffer des tones aus dem verlauf der hydrodynamischen spannungserscheinungen, Sitzungsberichte der Akademie der Wissenschaften in Wien, Mathematisch-Naturwissenschaftliche Klasse, Abteilung IIa 132 (1923) 125–138.

[4] K. Terzaghi, et al., Erdbaumechanik auf bodenphysikalischer grundlage.

[5] M. A. Biot, General theory of three-dimensional consolidation, Journal of applied physics 12 (2) (1941) 155–164.

[6] M. A. Biot, Theory of elasticity and consolidation for a porous anisotropic solid, Journal of Applied Physics 26 (2) (1955) 182–185.

[7] M. Biot, General solutions of the equations of elasticity and consolidation for a porous material, J. appl. Mech 23 (1) (1956) 91–96.

[8] R. S. Sandhu, E. L. Wilson, Finite-element analysis of seepage in elastic media, Journal of the Engineering Mechanics Division 95 (3) (1969) 641–652.

[9] C. Hwang, N. Morgenstern, D. Murray, On solutions of plane strain consolidation problems by finite element methods, Canadian Geotechnical Journal 8 (1) (1971) 109–118.

[10] J. Ghaboussi, E. L. Wilson, Flow of compressible fluid in porous elastic media, International Journal for Numerical Methods in Engineering 5 (3) (1973) 419–442.

[11] J. R. Booker, J. Small, An investigation of the stability of numerical solutions of Biot's equations of consolidation, International Journal of Solids and Structures 11 (7) (1975) 907–917.

[12] R. S. Sandhu, H. Liu, K. J. Singh, Numerical performance of some finite element schemes for analysis of seepage in porous elastic media, International Journal for Numerical and Analytical Methods in Geomechanics 1 (2) (1977) 177–194.

[13] P. Vermeer, A. Verruijt, An accuracy condition for consolidation by finite elements, International Journal for numerical and analytical methods in geomechanics 5 (1) (1981) 1–14.

[14] M. Reed, An investigation of numerical errors in the analysis of consolidation by finite elements, International journal for numerical and analytical methods in geomechanics 8 (3) (1984) 243–257.

[15] R. S. Sandhu, S. C. Lee, H.-I. The, Special finite elements for analysis of soil consolidation, International journal for numerical and analytical methods in geomechanics 9 (2) (1985) 125–147.

[16] M. A. Murad, A. F. Loula, Improved accuracy in finite element analysis of Biot's consolidation problem, Computer Methods in Applied Mechanics and Engineering 95 (3) (1992) 359–382.

[17] M. A. Murad, A. F. Loula, On stability and convergence of finite element approximations of Biot's consolidation problem, International Journal for Numerical Methods in Engineering 37 (4) (1994) 645–667.

[18] S. W. Sloan, A. J. Abbo, Biot consolidation analysis with automatic time stepping and error control part 1: theory and implementation, International Journal for Numerical and Analytical Methods in Geomechanics 23 (6) (1999) 467–492.

[19] S. W. Sloan, A. J. Abbo, Biot consolidation analysis with automatic time stepping and error control: Part 2: Applications, International Journal for Numerical and Analytical Methods in Geomechanics 23 (6) (1999) 493–529.

[20] M. Ferronato, G. Gambolati, P. Teatini, Ill-conditioning of finite element poroelasticity equations, International Journal of Solids and Structures 38 (34) (2001) 5995–6014.

[21] G. Gambolati, G. Pini, M. Ferronato, Numerical performance of projection methods in finite element consolidation models, International Journal for Numerical and Analytical Methods in Geomechanics 25 (14) (2001) 1429–1447.

[22] D. Dureisseix, P. Ladevèze, B. A. Schrefler, A LATIN computational strategy for multiphysics problems:

application to poroelasticity, International Journal for Numerical Methods in Engineering 56 (10) (2003) 1489–1510.

[23] G. Zhu, J.-H. Yin, S.-t. Luk, Numerical characteristics of a simple finite element formulation for consolidation analysis, Communications in Numerical Methods in Engineering 20 (10) (2004) 767–775.

[24] J. Korsawe, G. Starke, W. Wang, O. Kolditz, Finite element analysis of poro-elastic consolidation in porous media: Standard and mixed approaches, Computer Methods in Applied Mechanics and Engineering 195 (9) (2006) 1096–1115.

[25] M. Tchonkova, J. Peters, S. Sture, A new mixed finite element method for poro-elasticity, International journal for numerical and analytical methods in geomechanics 32 (6) (2008) 579–606.

[26] P. J. Phillips, M. F. Wheeler, A coupling of mixed and continuous Galerkin finite element methods for poroelasticity I: the continuous-in-time case, Computational Geosciences 11 (2) (2007) 131–144.

[27] P. J. Phillips, M. F. Wheeler, A coupling of mixed and continuous Galerkin finite element methods for poroelasticity II: the discrete-in-time case, Computational Geosciences 11 (2) (2007) 145–158.

[28] P. J. Phillips, M. F. Wheeler, A coupling of mixed and discontinuous Galerkin finite-element methods for poroelasticity, Computational Geosciences 12 (4) (2008) 417–435.

[29] J. B. Haga, H. Osnes, H. P. Langtangen, On the causes of pressure oscillations in low-permeable and low-compressible porous media, International Journal for Numerical and Analytical Methods in Geomechanics 36 (12) (2012) 1507–1522.

[30] F. Larsson, K. Runesson, A sequential-adaptive strategy in space-time with application to consolidation of porous media, Computer Methods in Applied Mechanics and Engineering 288 (2015) 146–171.

[31] A. El-Hamalawi, M. Bolton, An a posteriori error estimator for plane-strain geotechnical analyses, Finite elements in analysis and design 33 (4) (1999) 335–354.

[32] A. El-Hamalawi, M. Bolton, A-posteriori error estimation in axisymmetric geotechnical analyses, Computers and Geotechnics 29 (8) (2002) 587–607.

[33] Y. W. Bekele, T. Kvamsdal, A. M. Kvarving, S. Nordal, Adaptive isogeometric finite element analysis of steady-state groundwater flow, International Journal for Numerical and Analytical Methods in Geomechanics.

[34] R. Lewis, B. Schrefler, The finite element method in the static and dynamic deformation and consolidation of porous media, Numerical methods in engineering, John Wiley, 1998.

[35] T. J. R. Hughes, J. A. Cottrell, Y. Bazilevs, Isogeometric analysis: CAD, finite elements, NURBS, exact geometry and mesh refinement, Computer Methods in Applied Mechanics and Engineering 194 (3941) (2005) 4135–4195.

[36] J. A. Cottrell, T. J. R. Hughes, Y. Bazilevs, Isogeometric Analysis : Toward Integration of CAD and FEA, Wiley, Chichester, West Sussex, U.K., Hoboken, NJ, 2009.

Paper III:

Isogeometric Analysis of THM Coupled Processes in Ground Freezing

Submitted to *Computers and Geotechnics*

Isogeometric Analysis of THM Coupled Processes in Ground Freezing

Yared W. Bekele[a,*], Hiroyuki Kyokawa[b], Arne M. Kvarving[c], Trond Kvamsdal[c,d], Steinar Nordal[a]

[a]*Department of Civil and Transport Engineering, NTNU, Trondheim, Norway*
[b]*Advanced Analysis Department, Civil Engineering Design Division, Kajima Corporation, Japan*
[c]*Department of Applied Mathematics, SINTEF ICT, Trondheim, Norway*
[d]*Department of Mathematical Sciences, NTNU, Trondheim, Norway*

Abstract

An isogeometric analysis (IGA) based numerical model is presented for simulation of thermo-hydro-mechanically (THM) coupled processes in ground freezing. The momentum, mass and energy conservation equations are derived based on porous media theory. The governing equations are supplemented by a saturation curve, a hydraulic conductivity model and constitutive equations. Variational and Galerkin formulation results in a highly nonlinear system of equations, which are solved using Newton-Raphson iteration. Numerical examples on one-dimensional freezing and frost heave are presented. Good agreements were observed between the IGA based simulation and experimental results. The advantages of IGA for THM coupled problems are discussed qualitatively.

Keywords: isogeometric analysis, THM coupling, porous media, ground freezing

1. Introduction

THM coupled numerical modeling is essential in several areas of geo/poromechanics to understand the multi-physical properties and responses of materials. The thermal, hydraulic and mechanical properties of such materials interact with each other resulting in a more complex overall behavior. A schematic representation of such interactions is shown in Figure 1. For instance hydraulic processes alter the thermal regime through convection, mechanical processes affect the hydraulic regime by changing the porosity and so on.

THM coupled numerical modeling has been widely applied in the geomechanics of the high temperature regime environment. Examples of such application areas include geothermal energy extraction, safety assessment of nuclear waste repositories, oil and gas reservoir

*Corresponding author
Email addresses: yared.bekele@ntnu.no (Yared W. Bekele), kyokawa@kajima.com (Hiroyuki Kyokawa), arne.morten.kvarving@sintef.no (Arne M. Kvarving), trond.kvamsdal@math.ntnu.no (Trond Kvamsdal), steinar.nordal@ntnu.no (Steinar Nordal)

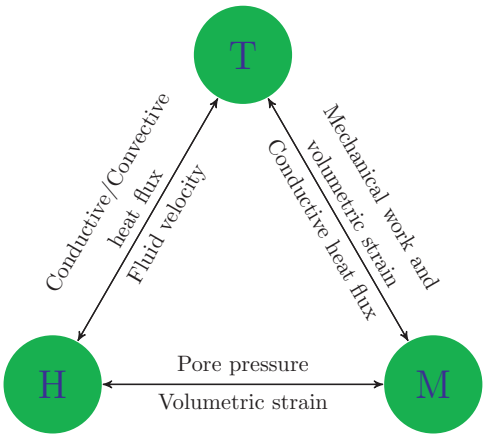

Figure 1: Schematic representation of Thermo-Hydro-Mechanical (THM) interactions, after [1]

engineering, underground energy storage and CO_2 sequestration; see for example Nowak *et al.* [2], Hudson *et al.* [3], Wang and Kolditz [4], Rutqvist *et al.* [5], Rutqvist *et al.* [6], Sanavia *et al.* [7], Wang *et al.* [8] and Tong *et al.* [9]. On the other hand, fully coupled THM modeling in frozen ground engineering is not as extensive. It is known that the freezing and thawing phenomena of ground can occur naturally, in cold regions, or artificially, as a construction technique in civil engineering. Some application areas in natural ground freezing and thawing include frost heave prediction, analysis and design of structures and foundations in cold regions and study of seasonal variation of temperature on the ground thermal properties. Artificial ground freezing on the other hand is a technology that has been successfully applied, over a long period of time, in the construction of structures on weak and/or unstable water-bearing grounds. Specific applications include the construction of tunnels of various purposes, the engineering of mines and pits, construction of underground storage facilities and the construction of foundations for industrial buildings on unstable ground. Artificial ground freezing is also used even in cold regions to control the seasonal thawing of frozen ground. The numerical proposed model in this paper will be applicable, within reason, to both natural and artificial ground freezing processes.

One of the earliest studies in the fully coupled THM modeling of frozen soils was presented by Mu and Ladanyi [10]. They made simplifying assumptions such as: the volume of soil particles remains constant in the freezing process, both unfrozen and frozen soil are isotropic, unfrozen soil is an elastic body with a constant Young's modulus where the Young's modulus and yield point are independent of the strain rate and confining pressure. The finite difference and finite element based simulation of unidirectional freezing was verified against experimental data. Selvadurai *et al.* [11] presented a computational model for frost heave with focus on soil-pipeline interaction and calibrated the proposed framework using one-dimensional frost heave tests. Another fully coupled THM model for frozen soil was proposed

by Li *et al.* [12]. The effective stress equation for frozen soil was presented as a function of thermal stress, ice swelling and pore pressure. A simple thermo-elastic consolidation and numerical modeling of a pile foundation were studied by the proposed model. Nishimura *et al.* [13] presented the formulation and application of the THM coupled finite element analysis of frozen soil. The proposed fully coupled model was applied to the analysis of frost heave prediction and reasonably good agreements were obtained when compared with experimental data. Liu and Yu [14] proposed a fully coupled THM model under frost action where analogy of the soil water characteristic curve from unsaturated soils was applied to describe the freezing and drying processes. In the stress-strain field, the total strain was defined as the sum of elastic, thermal, phase change of water, change of matric potential and initial strains. Neaupane and Yamabe [15] also proposed a fully coupled THM model for a frozen medium and successfully applied it to simulate a freeze-thaw experiment. Dall'Amico *et al.* [16] proposed a robust and energy-conserving model for a freezing variably saturated soil. Based on the claim that the energy balance equation shows a strongly nonlinear behavior, they propose a globally-convergent Newton scheme where the energy equation is expressed based on internal energy. Wang *et al.* [17] discussed the numerical simulation of water-heat coupled movements in a seasonally frozen soil. Neaupane *et al.* [1] presented the simulation of a fully coupled THM system in freezing and thawing rock. Peng *et al.* [18] proposed a model for coupled heat, moisture and stress-field of saturated soil during freezing. Recent studies on the subject include consolidation of thawing permafrost by Qi *et al.* [19], a three-phase THM finite element model for freezing soils by Zhou and Meschke [20] and a fully coupled thermo-hydro-mechanical model for rock mass under freezing and thawing condition by Kang *et al.* [21]. Other related studies include those by Hansson *et al.* [22], Thomas *et al.* [23], Coussy [24], Newman and Wilson [25] and Micholawski and Zhu [26].

In this paper, a fully coupled thermo-hydro-mechanical (THM) finite element model for ground freezing and thawing is proposed. The governing equations of the THM model are derived based on porous media theory where the multiphase medium is approximated as a continuum. The governing equations of the model are supplemented by other state equations for temperature dependent variables such as degree of saturation and hydraulic conductivity. Isogeometric analysis using B-Splines is applied to solve the final system of equations numerically. The higher continuities of B-Splines result in a locally mass and energy conserving numerical implementation, unlike the standard finite element method. In addition, we are able to represent CAD (computer aided design) geometries in an "exact" manner by applying isogeometric analysis; geometries are only approximated through mesh generation when using the standard finite element method.

The paper is structured as follows. The modeling approach used for deriving the governing equations is briefly presented in Section 2. The derivation of the governing momentum, mass and energy balance equations for each phase and for the mixture is discussed in Section 3. The supplementary equations that complete the governing equations, such as the soil-water characteristic curve and the hydraulic conductivity model, are presented in Section 4. The fundamentals behind isogeometric analysis and its important features in our current context are discussed in Section 5.1. Variational formulation of the governing equations, spatial discretization using Galerkin's method and the numerical implementation are

presented in Sections 5.2, 5.3 and 5.4, respectively. Numerical examples on one-dimensional freezing and a frost heave problem are presented in Section 6 and the theoretical and numerical highlights of the proposed model are summarized in Section 7.

2. Modeling Approach

The three phase porous medium composed of solid grains, water and ice is approximated as a homogeneous continuum as shown in Figure 2.

According to porous media theory, the partial density of phase α is defined in terms of its volume fraction n_α and material density ρ^α as:

$$\rho^\alpha := n_\alpha \rho_\alpha \tag{1}$$

For a saturated frozen soil, the partial densities for the solid, water and ice phases are, according to equation (1), given by:

$$\begin{aligned} \rho^{\mathrm{s}} &= n_{\mathrm{s}}\rho_{\mathrm{s}} = (1-n)\,\rho_{\mathrm{s}} \\ \rho^{\mathrm{w}} &= n_{\mathrm{w}}\rho_{\mathrm{w}} = nS_{\mathrm{w}}\rho_{\mathrm{w}} = n\,(1-S_{\mathrm{i}})\,\rho_{\mathrm{w}} \\ \rho^{\mathrm{i}} &= n_{\mathrm{i}}\rho_{\mathrm{i}} = nS_{\mathrm{i}}\rho_{\mathrm{i}} \end{aligned} \tag{2}$$

where n_{s}, n_{w} and n_{i} (with $n_{\mathrm{s}} + n_{\mathrm{w}} + n_{\mathrm{i}} = 1$) are the volume fractions of the solid, water and ice phases, respectively, n is the porosity, and S_{w} and S_{i} are the degrees of water and ice saturation respectively. For a fully saturated frozen soil, $S_{\mathrm{w}} + S_{\mathrm{i}} = 1$.

The total density of the porous medium is given as the sum of the partial densities of the component phases:

$$\rho = \rho^{\mathrm{s}} + \rho^{\mathrm{i}} + \rho^{\mathrm{w}} = (1-n)\,\rho_{\mathrm{s}} + nS_{\mathrm{i}}\rho_{\mathrm{i}} + nS_{\mathrm{w}}\rho_{\mathrm{w}} \tag{3}$$

The derivation of the governing equations is performed with respect to the solid phase and thus material time derivatives are extensively used in the derivations. The material time derivative of any differentiable function $f^\alpha(\boldsymbol{x}, t)$, varying in space $\boldsymbol{x}$ and in time t, referring to a moving particle of the α phase is given by:

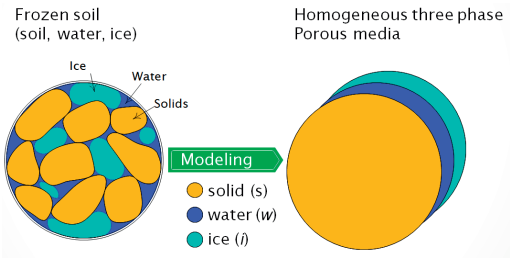

Figure 2: Multiphase porous medium modeled as a homogeneous continuum

$$\frac{\mathrm{D}_\alpha f^\alpha}{\mathrm{D}t} := \frac{\partial f^\alpha}{\partial t} + \nabla f^\alpha \cdot \boldsymbol{v}^\alpha. \tag{4}$$

In this case, material time derivatives of properties $f^\alpha(\boldsymbol{x}, t)$ relating to the water and ice phases are performed with respect to the solid phase. It can be shown that the material time derivative of $f^\alpha(\boldsymbol{x}, t)$ of phase $\alpha \in (\mathrm{w}, \mathrm{i})$ with respect to the solid phase is given by:

$$\frac{\mathrm{D}_\mathrm{s} f^\alpha}{\mathrm{D}t} = \frac{\mathrm{D}_\alpha f^\alpha}{\mathrm{D}t} + \nabla f^\alpha \cdot (\boldsymbol{v}^\mathrm{s} - \boldsymbol{v}^\alpha) \tag{5}$$

where $\boldsymbol{v}^\mathrm{s} - \boldsymbol{v}^\alpha$ is the relative velocity of phase α with respect to the solid phase.

3. Governing Equations

In this section, the governing partial differential equations of the proposed THM coupled model are presented. The three main governing equations for the saturated frozen soil are the linear momentum balance equation, the mass balance equation and the energy balance equation. These governing equations are supplemented by the modified Clausius-Clapeyron equation for thermodynamic equilibrium, the soil-water characteristic curve for the degree of water saturation as a function of pressure and temperature and a constitutive law for the stress-strain behavior of the solid skeleton.

3.1. Linear Momentum Balance Equation

The linear momentum balance equation is the equation of motion or equilibrium equation for the mixture. For a phase α of the mixture, it is given by:

$$\nabla \cdot \boldsymbol{\sigma}^\alpha + \rho^\alpha \boldsymbol{b}^\alpha + \sum_\beta \boldsymbol{P}^{\beta\alpha} = \rho_\alpha \frac{\mathrm{D}_\alpha \boldsymbol{v}^\alpha}{\mathrm{D}t} \tag{6}$$

where $\boldsymbol{\sigma}^\alpha$ is the partial stress of phase α, $\boldsymbol{P}^{\beta\alpha}$ are the interphase interactive forces between phase α and phase β and $\boldsymbol{b}^\alpha$ are the body forces for phase α. The equilibrium equation for the whole mixture is obtained as a summation of the individual equilibrium equation of each phase. Assuming a static problem, this results in:

$$\nabla \cdot \boldsymbol{\sigma} + \rho \boldsymbol{b} = \boldsymbol{0} \tag{7}$$

where $\boldsymbol{\sigma}$ are the total stresses and $\boldsymbol{b}$ are the body forces. The Bishop type effective stress in terms of the pore water and ice pressures p^w and p^i is given by:

$$\boldsymbol{\sigma}' = \boldsymbol{\sigma} + p^\mathrm{w} \boldsymbol{I} + S_\mathrm{i}(p^\mathrm{i} - p^\mathrm{w}) \boldsymbol{I} \tag{8}$$

where $\boldsymbol{I}$ is an identity matrix. The mechanical equilibrium equation in terms of the effective stresses can thus be written as:

$$\nabla \cdot \boldsymbol{\sigma}' - \nabla p^\mathrm{w} - \nabla(S_\mathrm{i}(p^\mathrm{i} - p^\mathrm{w})) + \rho \boldsymbol{b} = \boldsymbol{0}. \tag{9}$$

The effective stress is further linked to strain via a constitutive model. A simple constitutive model is presented in Section 4.4.

3.2. Mass Balance Equation

The general form of the mass balance equation for a phase α, considering phase change from phases β to phase α (with a mass exchange per unit volume of $M^{\beta\alpha}$), is given by:

$$\frac{\mathrm{D}_\alpha \rho^\alpha}{\mathrm{D}t} + \rho^\alpha \nabla \cdot \boldsymbol{v}^\alpha + \sum_\beta M^{\beta\alpha} = 0. \tag{10}$$

The mass balance equation for each phase is then derived and the equations for water and ice are derived with respect to the solid phase. The mass balance equation for the solid phase with the assumption of incompressible solid grains gives the time change of porosity as a function of solid displacement as:

$$\frac{\mathrm{D}_\mathrm{s} \rho^\mathrm{s}}{\mathrm{D}t} = 0 \Rightarrow \frac{\mathrm{D}_\mathrm{s} n}{\mathrm{D}t} = (1-n)\nabla \cdot \boldsymbol{v}^\mathrm{s}. \tag{11}$$

Summation of the individual mass balance equations for water and ice, together with the use of equation (11), gives the mass balance equation for the pores as:

$$(\rho_\mathrm{w} S_\mathrm{w} + \rho_\mathrm{i} S_\mathrm{i})\nabla \cdot \boldsymbol{v}^\mathrm{s} + n(\rho_\mathrm{w} - \rho_\mathrm{i})\frac{\mathrm{D}_\mathrm{s} S_\mathrm{w}}{\mathrm{D}t} + \rho_\mathrm{w} \nabla \cdot \boldsymbol{w} + \rho_\mathrm{i} \nabla \cdot \boldsymbol{w}' = 0 \tag{12}$$

where we have used the fact that the mass exchanges between water and ice cancel each other out i.e. $\Delta M_{iw} + \Delta M_{wi} = 0$. We have assumed herein that all phases are incompressible (no volume change under isotropic compression) and that the spatial variation of density (density gradient) is negligible for all phases. In Eq. (12), $\boldsymbol{w}$ and $\boldsymbol{w}'$ represent the water and ice fluxes relative to the solid phase. The water flux, for flow driven by pressure gradient and gravity, can be expressed using Darcy's law as:

$$\boldsymbol{w} = -\frac{1}{\gamma^\mathrm{w}} \boldsymbol{k} \left(\nabla p^\mathrm{w} - \rho_\mathrm{w} \boldsymbol{b}\right) \tag{13}$$

where $\boldsymbol{k}$ is the hydraulic conductivity matrix, which is a function of both pressure and temperature, and γ^w is the unit weight of water. A relative hydraulic conductivity model is required to control the evolution of $\boldsymbol{k}$ and this is presented in Section 4.3.

The ice flux relative to the solid phase is usually neglected but a relationship between $\boldsymbol{w}'$ and $\boldsymbol{w}$ can be derived such that:

$$\boldsymbol{w}' = \frac{S_\mathrm{i}}{S_\mathrm{w}} \boldsymbol{w} = \theta \boldsymbol{w}. \tag{14}$$

The above equation implies that some water flux is used for phase change between water and ice according to the current degree of ice saturation.

3.3. Energy Balance Equation

The general energy balance equation for a phase α, considering energy change due to phase change from phase β to phase α, is given by:

$$\rho_\alpha \frac{\mathrm{D}_\alpha e^\alpha}{\mathrm{D}t} + e^\alpha \left(- \sum_\beta M^{\beta\alpha} \right) + \Delta Q_\alpha^{\mathrm{ph}} = -\nabla \cdot \boldsymbol{q}^\alpha + Q^\alpha \tag{15}$$

where e^α is the specific internal energy of phase α, Q_α^{ph} is the additional energy causing phase change, $\boldsymbol{q}^\alpha$ is the conductive heat flux for phase α and Q_α is the sink or source term of energy for the same phase, which can be assumed to be equal to zero for a closed system. The internal energy of phase α, in terms of its heat capacity c_α and the temperature T is defined as:

$$e^\alpha := c_\alpha T. \tag{16}$$

Accordingly, the specific internal energies for the solid, water and ice phases can thus be expressed as:

$$e^{\mathrm{s}} = c_{\mathrm{s}} T, \qquad e^{\mathrm{w}} = c_{\mathrm{w}} T, \qquad e^{\mathrm{i}} = c_{\mathrm{i}} T \tag{17}$$

where c_{s}, c_{w} and c_{i} are the respective specific heat capacities for each phase. After formulating the specific energy balance equations for the solid, water and ice phases and making the same assumptions as in the mass balance equation, summation of the individual equations gives the energy balance equation for the three-phase medium as:

$$(\rho c)_{\mathrm{eff}} \frac{\mathrm{D}_{\mathrm{s}} T}{\mathrm{D}t} + \boldsymbol{a} \cdot \nabla T + L_{\mathrm{f}} \xi \frac{\mathrm{D}_{\mathrm{s}} S_{\mathrm{w}}}{\mathrm{D}t} = -\nabla \cdot \boldsymbol{q} + Q \tag{18}$$

where $\boldsymbol{a} = (\rho c)_{\mathrm{adv}} \boldsymbol{w}$ is an advective heat transfer vector, L_{f} is the latent heat of fusion and we have the volumetric parameter ξ as:

$$\xi = \frac{n \rho_{\mathrm{i}}}{S_{\mathrm{w}} + \frac{\rho_{\mathrm{i}}}{\rho_{\mathrm{w}}} S_{\mathrm{i}}}. \tag{19}$$

The effective heat capacity for the mixture and the advective heat transfer coefficient are given by:

$$\begin{aligned} (\rho c)_{\mathrm{eff}} &= \rho^{\mathrm{s}} c_{\mathrm{s}} + \rho^{\mathrm{w}} c_{\mathrm{w}} + \rho^{\mathrm{i}} c_{\mathrm{i}} \\ &= (1-n) \rho_{\mathrm{s}} c_{\mathrm{s}} + n S_{\mathrm{w}} \rho_{\mathrm{w}} c_{\mathrm{s}} + n S_{\mathrm{i}} \rho_{\mathrm{i}} c_{\mathrm{i}} \\ (\rho c)_{\mathrm{adv}} &= \rho_{\mathrm{w}} c_{\mathrm{w}} + \theta \rho_{\mathrm{i}} c_{\mathrm{i}} \end{aligned} \tag{20}$$

The total conductive heat flux, assuming isotropic thermal conductivity, can be expressed using Fourier's law as:

$$\boldsymbol{q} = -\lambda \nabla T. \tag{21}$$

The overall thermal conductivity λ for the multiphase porous medium can be obtained as the geometric mean of the individual thermal conductivities using, [27]:

$$\lambda = \lambda_{\mathrm{s}}^{1-n} \cdot \lambda_{\mathrm{w}}^{n S_{\mathrm{w}}} \cdot \lambda_{\mathrm{i}}^{n(1-S_{\mathrm{w}})} \tag{22}$$

where λ_{s}, λ_{w} and λ_{i} are the thermal conductivities of solid, water and ice respectively.

4. Supplementary Equations

4.1. Modified Clausius-Clapeyron Equation

The thermodynamic equilibrium between ice and soil in a freezing soil is described by the modified Clausius-Clapeyron equation, see [28]. The ice and water pressures in this equation are related by:

$$p^{\mathrm{i}} = \frac{\rho_{\mathrm{i}}}{\rho_{\mathrm{w}}} p^{\mathrm{w}} - \rho_{\mathrm{i}} L_{\mathrm{f}} \ln\left(\frac{T}{T_0}\right) \tag{23}$$

where T_{o}=273.15 K is the reference temperature and the relation is derived considering atmospheric pressure conditions. The equation is valid for practical temperature and pressure ranges of interest, [29].

4.2. Soil-Water Characteristic Curve

The other most important relation required to supplement the governing equations is the degree of water saturation as a function of pressure and temperature, i.e. $S_{\mathrm{w}} = f(p^{\mathrm{w}}, T)$, also known as the soil-water characteristic curve in unsaturated soil mechanics terminology. Based on van Genuchten's [30] model for unsaturated soils, and as modified in Nishimura *et al.* [13] and Zhou and Meschke [20], the soil-water characteristic curve for freezing and thawing porous media may be written as:

$$S_{\mathrm{w}} = 1 - S_{\mathrm{i}}^{max}\left[1 - \left\{1 + \left(\alpha(p^{\mathrm{i}} - p^{\mathrm{w}})\right)^{\beta}\right\}^{-\gamma}\right] \tag{24}$$

where S_{i}^{max} is the maximum degree of ice saturation for numerical reasons and α, β and γ are model parameters. Using the Clausius-Clapeyron equation, Eq. (23), which expresses p^{i} in terms of p^{w}, into Eq. (24) results in:

$$S_{\mathrm{w}} = 1 - S_{\mathrm{i}}^{max}\left[1 - \left\{1 + \left[\alpha\left((\frac{\rho_{\mathrm{i}}}{\rho_{\mathrm{w}}} - 1)p^{\mathrm{w}} - \rho_{\mathrm{i}} L_{\mathrm{f}} \ln(\frac{T}{T_{\mathrm{o}}})\right)\right]^{\beta}\right\}^{-\gamma}\right]. \tag{25}$$

The rate of change of S_{w} can thus be expressed as:

$$\frac{\partial S_{\mathrm{w}}}{\partial t} = \frac{\partial S_{\mathrm{w}}}{\partial p^{\mathrm{w}}}\frac{\partial p^{\mathrm{w}}}{\partial t} + \frac{\partial S_{\mathrm{w}}}{\partial T}\frac{\partial T}{\partial t} = S_{\mathrm{p}}\frac{\partial p^{\mathrm{w}}}{\partial t} + S_{\mathrm{T}}\frac{\partial T}{\partial t} \tag{26}$$

where S_{p} and S_{T} may, respectively, be referred to as isothermal and non-isothermal water capacities.

The model parameters α, β and γ can be selected for a given material based on experimental data. The effects of these model parameters on the degree of saturation are illustrated in the plots in Figure 3 as a function of temperature. A fixed value is used for the pore water pressure p^{w} and it can be shown that the effect of p^{w} on the degree of water saturation S_{w} is very limited compared to temperature.

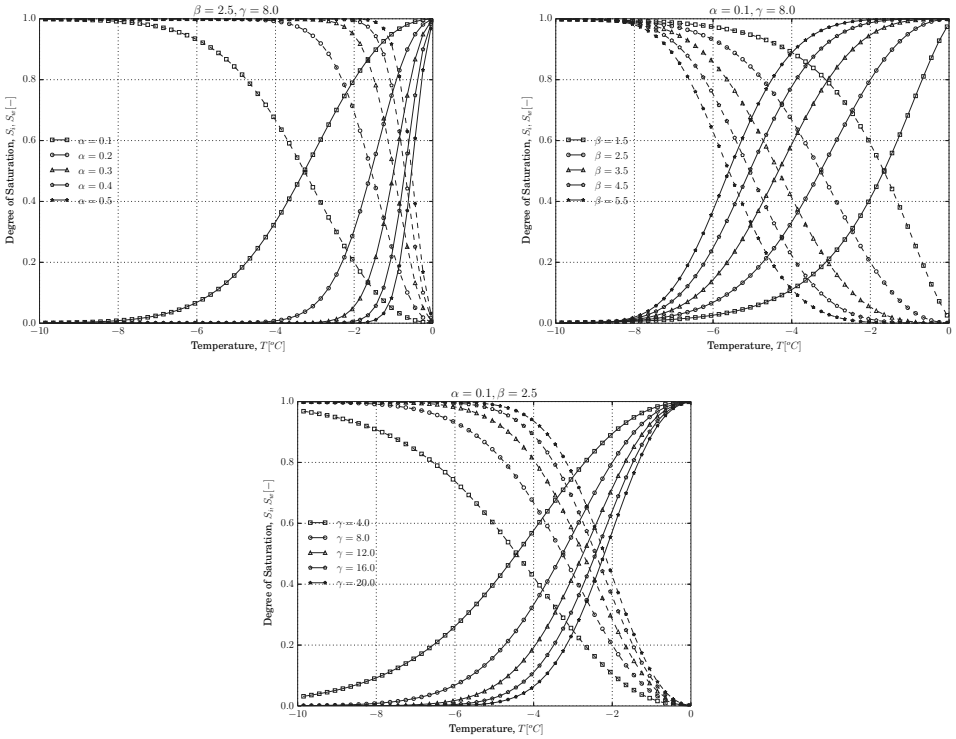

Figure 3: Effects of the saturation model parameters α, β and γ: Degree of water and ice saturation versus temperature for different combinations of the model parameters. The solid lines represent S_{w} and the dashed lines are for S_{i}. The parameter α has a unit of MPa^{-1} while β and γ are dimensionless.

4.3. Hydraulic Conductivity Model

The hydraulic conductivity of the porous medium changes continuously during the freezing/thawing process depending on the degree of water saturation i.e. as a function of temperature. To calculate the hydraulic conductivity at a given temperature, a relative hydraulic conductivity parameter is introduced to into Darcy's law, [13]. The modified Darcy's law and the corresponding relative hydraulic conductivity parameter are given by:

$$\begin{aligned} \boldsymbol{w} &= -\frac{k_{\mathrm{r}}}{\gamma^{\mathrm{w}}}\boldsymbol{k}\left(\nabla p^{\mathrm{w}} - \rho_{\mathrm{w}}\boldsymbol{b}\right) \\ k_r &= \sqrt{S_{\mathrm{w}}}\left[1 - \left(1 - S_{\mathrm{w}}^{1/m}\right)^m\right]^2 \end{aligned} \tag{27}$$

where m is a model parameter. The variation of k_{r} with degree of water saturation for selected values of m is plotted and shown in Figure 4.

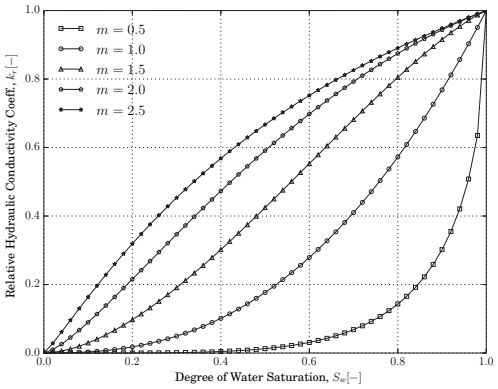

Figure 4: Relative hydraulic conductivity versus degree of water saturation.

4.4. Constitutive Equations

The general stress-strain relation in incremental form can be written as:

$$\mathrm{d}\boldsymbol{\sigma'} = \boldsymbol{D}(\mathrm{d}\varepsilon - \mathrm{d}\varepsilon^{\mathrm{ph}} - \mathrm{d}\varepsilon^{\mathrm{T}} - \mathrm{d}\varepsilon^{\mathrm{o}}) \tag{28}$$

where $d\boldsymbol{\sigma'}$ is the effective stress increment, $\boldsymbol{D}$ is the constitutive tangent stiffness tensor, $\mathrm{d}\boldsymbol{\varepsilon}$ is the total strain increment, $\mathrm{d}\boldsymbol{\varepsilon}^{\mathrm{ph}}$ is the strain increment due to phase change, $\mathrm{d}\boldsymbol{\varepsilon}^{\mathrm{T}}$ is the thermal strain increment and $\mathrm{d}\boldsymbol{\varepsilon}^{\mathrm{o}}$ represents a strain increment not directly associated with stress changes. The thermal strain is usually very small when compared to the strain due to phase change and may be neglected.

The constitutive equation proposed for the soil skeleton here is a simple nonlinear elastic relation with temperature dependent parameters. The tangent stiffness for linear elasticity (for stresses and strains in Voigt notation) is given by

$$\boldsymbol{D} = \frac{E}{(1+\nu)(1-2\nu)} \begin{bmatrix} \boldsymbol{D}_{11} & \boldsymbol{0} \\ \boldsymbol{0} & \boldsymbol{D}_{22} \end{bmatrix} \tag{29}$$

where

$$\begin{aligned} \boldsymbol{D}_{11} &= (1-2\nu)\boldsymbol{I} + \nu\boldsymbol{1}\,, \\ \boldsymbol{D}_{22} &= \frac{1-2\nu}{2}\boldsymbol{I}, \end{aligned} \tag{30}$$

where E is the Young's modulus, ν is the Poisson's ratio and $\boldsymbol{1}$ is a matrix of ones. These strength parameters are temperature dependent and simple nonlinear relations are derived as a function of degree of saturation, which is a function of temperature according to the soil-water characteristic curve. The Young's modulus E of the porous medium at a given temperature may be expressed as:

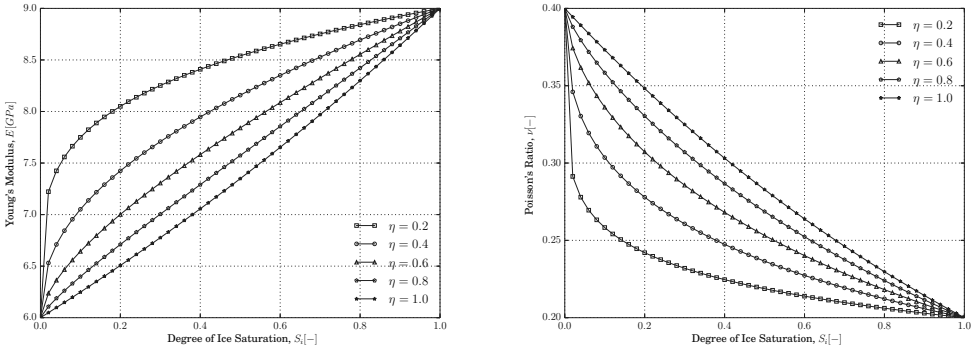

Figure 5: Strength parameters E and ν as a function of degree of ice saturation.

$$E = \left(\frac{E_\mathrm{i}}{E_\mathrm{s}}\right)^{S_\mathrm{i}^\eta} E_\mathrm{s} \tag{31}$$

where E_i and E_s are the Young's moduli of ice and solid skeleton respectively, S_i is the degree of ice saturation and η is a model parameter. A similar expression for the Poisson's ratio ν of the porous medium as a function of the Poisson's ratios of ice, ν_i, and solid skeleton, ν_s, is given by:

$$\nu = \left(\frac{\nu_\mathrm{i}}{\nu_\mathrm{s}}\right)^{S_\mathrm{i}^\eta} \nu_\mathrm{s}. \tag{32}$$

The strength parameter η may be chosen for a given material based on experimental data. If we assume for example that $E_\mathrm{s} = 6$ GPa, $E_\mathrm{i} = 9$ GPa, $\upsilon_\mathrm{s} = 0.4$ and $\nu_\mathrm{i} = 0.2$, the overall Young's modulus E and Poisson's ratio ν may be plotted as a function of degree of ice saturation for different values of η, as shown in Figure 5.

The thermal strain increment as a function of the thermal expansion coefficient of the solid skeleton and temperature increment is given by:

$$\mathrm{d}\boldsymbol{\varepsilon}^T = \frac{\alpha_\mathrm{s}}{3}\mathrm{d}T\boldsymbol{I}. \tag{33}$$

The volume expansion of the soil due to phase change is accounted for by the strain due to phase change, $\boldsymbol{\varepsilon}^\mathrm{ph}$, and is a function of the porosity and the degree of ice saturation. An expression for $\boldsymbol{\varepsilon}_\mathrm{ph}$ can be derived by formulating the volumetric strains $\varepsilon_\mathrm{v}^\mathrm{ph}$ as a function of n and S_i. Assuming isotropic expansion, the rate of volumetric expansion may be derived from the mass balance of ice and water during phase change, i.e. $\frac{\partial}{\partial t}\left\{(\rho_\mathrm{w}V_\mathrm{w}) + (\rho_\mathrm{i}V_\mathrm{i})\right\} = 0$, to give:

$$\dot{\varepsilon}_{\mathrm{v}}^{\mathrm{ph}} = \frac{n(\rho_{\mathrm{w}} - \rho_{\mathrm{i}})}{\rho_{\mathrm{w}} S_{\mathrm{w}} + \rho_{\mathrm{i}} S_{\mathrm{i}}} \frac{\mathrm{D}_{\mathrm{s}} S_{\mathrm{i}}}{\mathrm{D}t}. \tag{34}$$

The incremental strain due to phase change may then be written as:

$$d\boldsymbol{\varepsilon}^{\mathrm{ph}} = \frac{1}{3} \left(\frac{\partial \varepsilon_{\mathrm{v}}^{\mathrm{ph}}}{\partial S_{\mathrm{i}}} dS_{\mathrm{i}} \right) \boldsymbol{I}. \tag{35}$$

5. Isogeometric Analysis

5.1. Introduction

Since its first introduction by Hughes *et al.* [31], isogeometric analysis (IGA) has been successfully applied to several areas of engineering mechanics problems. The fundamental aim for the introduction of IGA was the idea of bridging the gap between finite element analysis (FEA) and computer-aided design (CAD). The main concept behind the method is the application of the same basis functions used in CAD for performing finite element analysis. In the process of its application to various engineering problems, IGA has shown advantages over the conventional finite element method, for instance the ease of performing finite element analysis using higher order polynomials.

We briefly present the fundamentals behind B-Splines and NURBS in the next section and highlight the features of IGA that are important in our context.

5.1.1. Fundamentals on B-Splines and NURBS

We start the discussion on B-Splines and NURBS by first defining a *knot vector*. A knot vector in one dimension is a non-decreasing set of coordinates in the parameter space, written $\Xi = \{\xi_1, \xi_2, ..., \xi_{n+p+1}\}$, where $\xi_i \in \mathbb{R}$ is the i^{th} knot, i is the knot index, $i = 1, 2, ..., n+p+1$, p is the polynomial order, and n is the number of basis functions. Knot vectors may be uniform or non-uniform depending on whether the knots are equally spaced in the parameter space or not.

A univariate B-Spline curve is parametrized by a linear combination of n B-Spline basis functions, $\{N_{i,p}\}_{i=1}^{n}$. The B-Spline basis functions are recursively defined starting with piecewise constants ($p = 0$):

$$N_{i,0}(\xi) = \begin{cases} 1 & \text{if } \xi_i \leq \xi < \xi_{i+1} \\ 0 & \text{otherwise.} \end{cases} \tag{36}$$

For higher-order polynomial degrees ($p \geq 1$), the basis functions are defined by the Cox-de Boor recursion formula:

$$N_{i,p}(\xi) = \frac{\xi - \xi_i}{\xi_{i+p} - \xi_i} N_{i,p-1}(\xi) + \frac{\xi_{i+p+1} - \xi}{\xi_{i+p+1} - \xi_{i+1}} N_{i+1,p-1}(\xi). \tag{37}$$

B-Spline geometries, curves, surfaces and solids, are constructed from a linear combination of B-Spline basis functions. Given n basis functions $N_{i,p}$ and corresponding control points

$\boldsymbol{P}_i \in \mathbb{R}^d, i = 1, 2, ..., n$, a piecewise polynomial B-Spline curve is given by:

$$\boldsymbol{C}(\xi) = \sum_{i=1}^{n} N_{i,p}(\xi)\boldsymbol{P}_i. \tag{38}$$

Similarly, for a given control net $\boldsymbol{P}_{i,j}, i = 1, 2, ..., n, j = 1, 2, ..., m$, polynomial orders p and q, and knot vectors $\Xi = \{\xi_1, \xi_2, ..., \xi_{n+p+1}\}$, and $\mathcal{H} = \{\eta_1, \eta_2, ..., \eta_{m+q+1}\}$, a tensor product B-Spline surface is defined by:

$$\boldsymbol{S}(\xi, \eta) = \sum_{i=1}^{n}\sum_{j=1}^{m} N_{i,p}(\xi)M_{j,q}(\eta)\boldsymbol{P}_{i,j}. \tag{39}$$

B-Spline solids are defined in a similar way as B-Spline surfaces from tensor products over a control lattice.

NURBS are built from B-Splines to represent a wide array of objects that cannot be exactly represented by polynomials. A NURBS entity in $\mathbb{R}^d$ is obtained by the projective transformation of a B-Spline entity in $\mathbb{R}^{d+1}$. The control points for the NURBS geometry are found by performing exactly the same projective transformation to the control points of the B-Spline geometry.

A detailed treatment of B-Splines and NURBS can be referred from Cottrell *et al.* [32].

5.1.2. Important Features in Current Context

IGA has a number of advantages over FEA such as the ability to represent exact CAD geometries of structures or domains during analysis, non-negative basis functions and isoparametric mapping at patch level. In the context of the current work, we focus on the features of IGA that are especially important. These features are the improved continuity of filed variables because of the smoothness of the basis functions and the ability to perform simulations with high continuity and high regularity meshes. Next, we will look into these features closely.

Continuity: One of the most distinctive and powerful features of IGA is that the basis functions will be C^{p-m} continuous across knot spans (analogous to elements in FEA), where p is the polynomial degree and m is the multiplicity of the knot. This means that the continuity across knot spans can be controlled by the proper choice of p and m. The continuity can be decreased by repeating a knot - important to model non-smooth geometry features or to facilitate the application of boundary conditions. For instance, quadratic ($p = 2$) splines are C^1 continuous over non-repeated knots while quadratic Lagrange finite element bases are only C^0 continuous. If we consider the quartic ($p = 4$) basis functions constructed from the open, non-uniform knot vector $\Xi = \{0, 0, 0, 0, 0, 1, 2, 2, 3, 3, 3, 4, 4, 4, 4, 5, 5, 5, 5, 5\}$, we get different continuities across knot spans as shown in Figure 6.

k-refinement: IGA and FEA both allow h- and p-refinements i.e. increasing the number of knot spans by knot insertion (increasing the number of elements in FEA) and raising the polynomial order. The non-commutativity of knot insertion and polynomial order elevation results in a type of refinement that is unique to IGA, called k-refinement. This is achieved by performing polynomial order elevation followed by knot insertion. This results in a high continuity mesh with the least number of degrees of freedom i.e. high regularity.

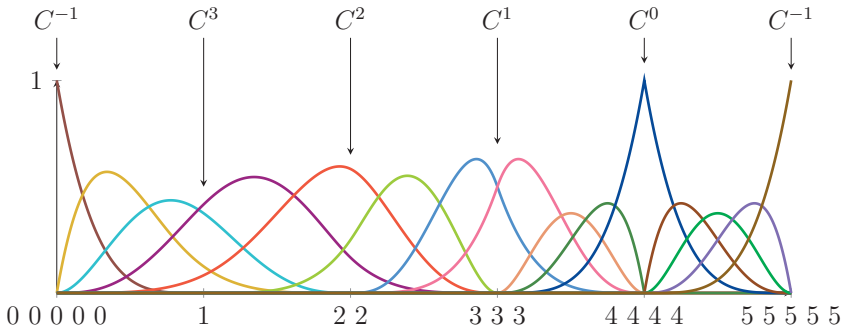

Figure 6: Different continuities across knot spans, after [32].

5.1.3. Mixed isogeometric formulation

A mixed formulation is constructed by first defining the knot vectors and basis functions defining the geometry of the domain. The polynomial order defining the geometry is used as the polynomial degree for one of the field variables and is raised by the desired degree for the other field variable. In our context, the polynomial orders for the pressure and temperature, p_{p} and p_{T}, are defined by the geometry construction and the polynomial order for the displacement, p_{u}, is raised by one. All polynomial orders can then be raised to the desired degree starting from the initial definition. For example, a simple two-dimensional geometry defined by the knot vectors $\Xi = \{0, 0, 1, 1\}$ and $\mathcal{H} = \{0, 0, 1, 1\}$ implies $p_{\mathrm{p}} = p_{\mathrm{T}} = 1$ and $p_{\mathrm{u}} = 2$ with 4 and 9 control points, respectively. The number of control points, location of degrees of freedom in IGA, on a B-Spline surface for different polynomial degrees is shown in Figure 7.

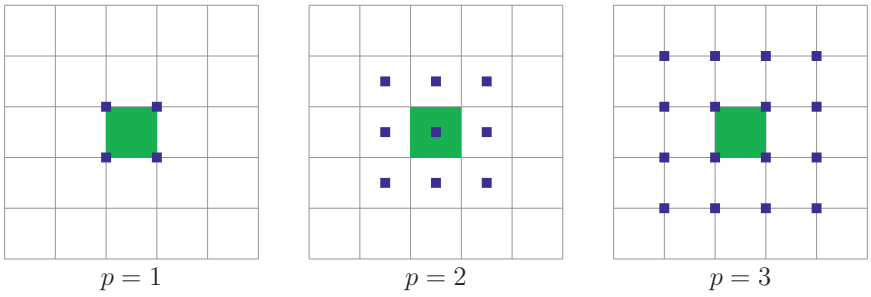

Figure 7: Number of control points for a given element on a simple B-Spline surface with different polynomial degrees. The element is highlighted and the blue squares represent control points.

5.2. Variational Formulation

We first define the initial and boundary conditions before presenting the variational formulation of the governing equations. The initial conditions for the displacement, pore water pressure and temperature at time $t = 0$ are:

$$\boldsymbol{u} = \boldsymbol{u}_{\mathrm{o}} \qquad p^{\mathrm{w}} = p_{\mathrm{o}}^{\mathrm{w}} \qquad T = T_{\mathrm{o}} \qquad \text{in } \Omega \text{ and on } \Gamma \tag{40}$$

where Ω and Γ are the domain and its boundary, respectively. The boundary conditions could be of Dirichlet type on Γ_D or Neumann type (fluxes and tractions) on Γ_N, where $\Gamma_D \cup \Gamma_N = \Gamma$. The Dirichlet boundary conditions may be defined as:

$$\begin{cases} \boldsymbol{u} = \overline{\boldsymbol{u}} & \text{on } \Gamma_D^{\mathrm{u}} \\ p^{\mathrm{w}} = \overline{p}^{\mathrm{f}} & \text{on } \Gamma_D^{\mathrm{p}} \\ T = \overline{T} & \text{on } \Gamma_D^{\mathrm{T}}. \end{cases} \tag{41}$$

The Neumann boundary conditions are defined as:

$$\begin{cases} \boldsymbol{\sigma} \cdot \boldsymbol{n} = \overline{\boldsymbol{t}} & \text{on } \Gamma_N^{\mathrm{u}} \\ \boldsymbol{w} \cdot \boldsymbol{n} = \overline{q}^{\mathrm{w}} & \text{on } \Gamma_N^{\mathrm{p}} \\ \boldsymbol{q} \cdot \boldsymbol{n} = \overline{q}^{\mathrm{T}} + \lambda_{\mathrm{e}}(T - T_{\mathrm{e}}) & \text{on } \Gamma_N^{\mathrm{T}} \end{cases} \tag{42}$$

where $\overline{\boldsymbol{t}}$ is the traction boundary condition and $\boldsymbol{n}$ is the outward unit normal vector to the boundary. The water and heat fluxes at the boundary are represented by $\overline{q}^{\mathrm{w}}$ and $\overline{q}^{\mathrm{T}}$, respectively. The thermal conductivity and temperature of the surrounding environment are denoted by λ_{e} and T_{e}, respectively.

We can now derive the weak formulations of the three main governing balance equations, Eq. (7), 12 and 18. Multiplying the rate form of the linear momentum balance equation arbitrary velocities $\delta\boldsymbol{v}$, integrating over the domain Ω and applying the divergence theorem gives the weak form as:

$$\int_{\Omega} \dot{\boldsymbol{\sigma}} \cdot \nabla \cdot \delta\boldsymbol{v} \mathrm{d}\Omega = \int_{\Gamma_N^{\mathrm{u}}} \dot{\overline{\boldsymbol{t}}} \delta\boldsymbol{v} \mathrm{d}\Gamma \tag{43}$$

where $\overline{\boldsymbol{t}}$ is the Neumann traction on the boundary Γ_{u}, $\dot{\boldsymbol{\sigma}} = \frac{\partial \boldsymbol{\sigma}}{\partial t}$ and $\dot{\overline{\boldsymbol{t}}} = \frac{\partial \overline{\boldsymbol{t}}}{\partial t}$. The rate of change of the total stress is derived from the effective stress relationship. Using the constitutive relation given in Eq. (28) into the effective stress formulation in Eq. (8), a generic form of the rate of change of total stress can be derived as:

$$\dot{\boldsymbol{\sigma}} = \boldsymbol{D}\dot{\boldsymbol{\varepsilon}} + \left(\frac{\partial \boldsymbol{\sigma}}{\partial p^{\mathrm{w}}} - \boldsymbol{D} \frac{\partial \boldsymbol{\varepsilon}^{\mathrm{ph}}}{\partial p^{\mathrm{w}}} \right) \frac{\partial p^{\mathrm{w}}}{\partial t} + \left(\frac{\partial \boldsymbol{\sigma}}{\partial T} - \boldsymbol{D} \frac{\partial \boldsymbol{\varepsilon}^{\mathrm{ph}}}{\partial T} \right) \frac{\partial T}{\partial t} \tag{44}$$

wherein we have neglected thermal and other strains. The weak form of the equilibrium equation can now be written as:

$$\int_\Omega \left[\boldsymbol{D}\dot{\boldsymbol{\varepsilon}} + \left(\frac{\partial \boldsymbol{\sigma}}{\partial p^{\mathrm{w}}} - \boldsymbol{D}\frac{\partial \boldsymbol{\varepsilon}^{\mathrm{ph}}}{\partial p^{\mathrm{w}}} \right) \frac{\partial p^{\mathrm{w}}}{\partial t} + \left(\frac{\partial \boldsymbol{\sigma}}{\partial T} - \boldsymbol{D}\frac{\partial \boldsymbol{\varepsilon}^{\mathrm{ph}}}{\partial T} \right) \frac{\partial T}{\partial t} \right] \nabla \cdot \delta \boldsymbol{v} \mathrm{d}\Omega = \int_{\Gamma_N^{\mathrm{u}}} \dot{\bar{\boldsymbol{t}}} \delta \boldsymbol{v} \mathrm{d}\Gamma. \quad (45)$$

The weak form of the mass balance equation is derived by multiplying Eq. (12) by an arbitrary pressure δp and integrating over the domain Ω to give:

$$\int_\Omega \left[(\rho_{\mathrm{w}} S_{\mathrm{w}} + \rho_{\mathrm{i}} S_{\mathrm{i}}) \nabla \cdot \boldsymbol{v}^{\mathrm{s}} + n(\rho_{\mathrm{w}} - \rho_{\mathrm{i}}) \frac{\mathrm{D}_{\mathrm{s}} S_{\mathrm{w}}}{\mathrm{D}t} + (\rho_{\mathrm{w}} + \theta \rho_{\mathrm{i}}) \nabla \cdot \boldsymbol{w} \right] \delta p \mathrm{d}\Omega = 0. \quad (46)$$

Applying the divergence theorem, using Eq. (26) and rearranging gives the weak form of the mass balance equation as:

$$\begin{aligned} &\int_\Omega \frac{\rho_{\mathrm{w}} S_{\mathrm{w}} + \rho_{\mathrm{i}} S_{\mathrm{i}}}{\rho_{\mathrm{w}} + \theta \rho_{\mathrm{i}}} \nabla \cdot \boldsymbol{v}^{\mathrm{s}} \delta p \mathrm{d}\Omega + \int_\Omega \frac{n(\rho_{\mathrm{w}} - \rho_{\mathrm{i}})}{\rho_{\mathrm{w}} + \theta \rho_{\mathrm{i}}} S_{\mathrm{p}} \frac{\partial p^{\mathrm{w}}}{\partial t} \delta p \mathrm{d}\Omega \\ &+ \int_\Omega \frac{n(\rho_{\mathrm{w}} - \rho_{\mathrm{i}})}{\rho_{\mathrm{w}} + \theta \rho_{\mathrm{i}}} S_{\mathrm{T}} \frac{\partial T}{\partial t} \delta p \mathrm{d}\Omega + \int_\Omega \nabla \delta p \cdot \frac{k_{\mathrm{r}}}{\gamma^{\mathrm{w}}} \boldsymbol{k} \cdot \nabla p^{\mathrm{w}} \mathrm{d}\Omega \\ &- \int_\Omega \nabla \delta p \cdot \frac{k_{\mathrm{r}}}{\gamma^{\mathrm{w}}} \boldsymbol{k} \cdot \rho_{\mathrm{w}} \boldsymbol{b} \mathrm{d}\Omega = - \int_{\Gamma_N^{\mathrm{p}}} \bar{q}^{\mathrm{w}} \delta p \mathrm{d}\Gamma \end{aligned} \quad (47)$$

where $\bar{q}^{\mathrm{w}}$ is the water flux on the Neumann boundary Γ_{p}.

The energy balance equation, Eq. (18), is a form of an unsteady advection-diffusion equation and may require stabilization during numerical implementation. The SUPG (Streamline Upwind/Petrov Galerkin) stabilization method is used here to choose appropriate test functions. Multiplying the energy balance equation by an arbitrary weighing function $\delta \tilde{T}$ and integrating over the domain Ω gives:

$$\int_\Omega \left[(\rho c)_{\mathrm{eff}} \frac{\mathrm{D}_{\mathrm{s}} T}{\mathrm{D}t} + \boldsymbol{a} \cdot \nabla T + L_{\mathrm{f}} \xi \frac{\mathrm{D}_{\mathrm{s}} S_{\mathrm{w}}}{\mathrm{D}t} + \nabla \cdot \boldsymbol{q} \right] \delta \tilde{T} \mathrm{d}\Omega = 0. \quad (48)$$

The weighting function in the SUPG method considering the advective term is:

$$\delta \tilde{T} = \delta T + \tau_{\mathrm{e}} \boldsymbol{a} \cdot \nabla \delta T \quad (49)$$

with

$$\tau_{\mathrm{e}} = \frac{h_{\mathrm{e}}}{2|\boldsymbol{a}|} \left(\coth \alpha - \frac{1}{\alpha} \right) \qquad \text{and} \qquad \alpha = \frac{|\boldsymbol{a}| h_{\mathrm{e}}}{2\lambda} \quad (50)$$

where h_{e} is the characteristic element length (maximum length) of the mesh and λ is the overall thermal conductivity of the porous medium. The weak form of the energy balance

equation, after applying the divergence theorem, can be written as:

$$\begin{aligned}
&\int_\Omega (\rho c)_{\text{eff}} \frac{\partial T}{\partial t} \delta T \mathrm{d}\Omega + \int_\Omega \boldsymbol{a} \cdot \nabla T \delta T \mathrm{d}\Omega + \int_\Omega L_\mathrm{f} \xi S_\mathrm{p} \frac{\partial p^\mathrm{w}}{\partial t} \delta T \mathrm{d}\Omega \\
&+ \int_\Omega L_\mathrm{f} \xi S_\mathrm{T} \frac{\partial T}{\partial t} \delta T \mathrm{d}\Omega + \int_\Omega \nabla \delta T \lambda \nabla T \mathrm{d}\Omega \\
&+ \sum_e \left[\int_\Omega \tau_\mathrm{e} \boldsymbol{a} \cdot \nabla \delta T \left\{ (\rho c)_{\text{eff}} \frac{\partial T}{\partial t} + \boldsymbol{a} \cdot \nabla T + L_\mathrm{f} \xi S_\mathrm{p} \frac{\partial p^\mathrm{w}}{\partial t} \right. \right. \\
&\left. \left. + L_\mathrm{f} \xi S_\mathrm{T} \frac{\partial T}{\partial t} + \nabla \cdot \lambda \nabla T \right\} \mathrm{d}\Omega \right] = - \int_{\Gamma_N^\mathrm{T}} \overline{q}^\mathrm{T} \delta T \mathrm{d}\Gamma
\end{aligned} \tag{51}$$

where $\overline{q}^\mathrm{T}$ is the heat flux on the Neumann boundary Γ_T. The stabilizing term to be summed over the number of elements is not continuous in the global space.

5.3. Galerkin Formulation

The governing equations are to be solved for three field variables: displacement, pore water pressure and temperature. This forms the so called $u - p - T$ formulation. We use a mixed formulation to express the field variables in terms of the basis functions and the control point values (nodal values in FEA). Choosing the basis functions $\boldsymbol{N}_\mathrm{u}$,$\boldsymbol{N}_\mathrm{p}$ and $\boldsymbol{N}_\mathrm{T}$ for the displacement, pore water pressure and temperature, respectively, we write:

$$\begin{aligned}
\boldsymbol{u} &= \boldsymbol{N}_\mathrm{u} \boldsymbol{u}^\mathrm{c}, & \frac{\partial \boldsymbol{u}}{\partial t} &= \boldsymbol{N}_\mathrm{u} \frac{\partial \boldsymbol{u}^\mathrm{c}}{\partial t} \\
p^\mathrm{w} &= \boldsymbol{N}_\mathrm{p} \boldsymbol{p}^\mathrm{c}, & \frac{\partial p^\mathrm{w}}{\partial t} &= \boldsymbol{N}_\mathrm{p} \frac{\partial \boldsymbol{p}^\mathrm{c}}{\partial t} \\
T &= \boldsymbol{N}_\mathrm{T} \boldsymbol{T}^\mathrm{c}, & \frac{\partial T}{\partial t} &= \boldsymbol{N}_\mathrm{T} \frac{\partial \boldsymbol{T}^\mathrm{c}}{\partial t}
\end{aligned} \tag{52}$$

where $\boldsymbol{u}^\mathrm{c}$, $\boldsymbol{p}^\mathrm{c}$ and $\boldsymbol{T}^\mathrm{c}$ are the control point displacement, pore water pressure and temperature values. In a Galerkin formulation, we choose the arbitrary test functions to be the same as the basis functions. Application to the weak form of the equilibrium equation, Eq. (45), results in the system of equations:

$$\boldsymbol{C}_\mathrm{uu} \frac{\partial \boldsymbol{u}^\mathrm{c}}{\partial t} + \boldsymbol{C}_\mathrm{up} \frac{\partial \boldsymbol{p}^\mathrm{c}}{\partial t} + \boldsymbol{C}_\mathrm{uT} \frac{\partial \boldsymbol{T}^\mathrm{c}}{\partial t} = \boldsymbol{f}_\mathrm{u} \tag{53}$$

where

$$\begin{aligned}
\boldsymbol{C}_\mathrm{uu} &= \int_\Omega \nabla \boldsymbol{N}_\mathrm{u}^\intercal \boldsymbol{D} \nabla \boldsymbol{N}_\mathrm{u} \mathrm{d}\Omega \\
\boldsymbol{C}_\mathrm{up} &= \int_\Omega \nabla \boldsymbol{N}_\mathrm{u}^\intercal \left(\frac{\partial \boldsymbol{\sigma}}{\partial p^\mathrm{w}} - \boldsymbol{D} \frac{\partial \boldsymbol{\varepsilon}^\mathrm{ph}}{\partial p^\mathrm{w}} \right) \boldsymbol{N}_\mathrm{p} \mathrm{d}\Omega \\
\boldsymbol{C}_\mathrm{uT} &= \int_\Omega \nabla \boldsymbol{N}_\mathrm{u}^\intercal \left(\frac{\partial \boldsymbol{\sigma}}{\partial T} - \boldsymbol{D} \frac{\partial \boldsymbol{\varepsilon}^\mathrm{ph}}{\partial T} \right) \boldsymbol{N}_\mathrm{T} \mathrm{d}\Omega
\end{aligned}$$

$$\boldsymbol{f}_{\mathrm{u}} = \int_{\Gamma_N^{\mathrm{u}}} \boldsymbol{N}_{\mathrm{u}}^{\intercal} \dot{\bar{\boldsymbol{t}}} \mathrm{d}\Gamma.$$

Galerkin formulation to the weak form of the mass balance equation, Eq. (47), results in:

$$\boldsymbol{K}_{\mathrm{pp}} \boldsymbol{p}^{\mathrm{c}} + \boldsymbol{C}_{\mathrm{pu}} \frac{\partial \boldsymbol{u}^{\mathrm{c}}}{\partial t} + \boldsymbol{C}_{\mathrm{pp}} \frac{\partial \boldsymbol{p}^{\mathrm{c}}}{\partial t} + \boldsymbol{C}_{\mathrm{pT}} \frac{\partial \boldsymbol{T}^{\mathrm{c}}}{\partial t} = \boldsymbol{f}_{\mathrm{p}} \tag{54}$$

where

$$\begin{aligned}
\boldsymbol{K}_{\mathrm{pp}} &= \int_{\Omega} \nabla \boldsymbol{N}_{\mathrm{p}}^{\intercal} \frac{k_{\mathrm{r}}}{\gamma^{\mathrm{w}}} \boldsymbol{k} \nabla \boldsymbol{N}_{\mathrm{p}} \mathrm{d}\Omega \\
\boldsymbol{C}_{\mathrm{pu}} &= \int_{\Omega} \boldsymbol{N}_{\mathrm{p}}^{\intercal} \frac{\rho_{\mathrm{w}} S_{\mathrm{w}} + \rho_{\mathrm{i}} S_{\mathrm{i}}}{\rho_{\mathrm{w}} + \theta \rho_{\mathrm{i}}} \nabla \boldsymbol{N}_{\mathrm{u}} \mathrm{d}\Omega \\
\boldsymbol{C}_{\mathrm{pp}} &= \int_{\Omega} \boldsymbol{N}_{\mathrm{p}}^{\intercal} \frac{n(\rho_{\mathrm{w}} - \rho_{\mathrm{i}})}{\rho_{\mathrm{w}} + \theta \rho_{\mathrm{i}}} S_{\mathrm{p}} \boldsymbol{N}_{\mathrm{p}} \mathrm{d}\Omega \\
\boldsymbol{C}_{\mathrm{pT}} &= \int_{\Omega} \boldsymbol{N}_{\mathrm{p}}^{\intercal} \frac{n(\rho_{\mathrm{w}} - \rho_{\mathrm{i}})}{\rho_{\mathrm{w}} + \theta \rho_{\mathrm{i}}} S_{\mathrm{T}} \boldsymbol{N}_{\mathrm{T}} \mathrm{d}\Omega \\
\boldsymbol{f}_{\mathrm{p}} &= \int_{\Omega} \nabla \boldsymbol{N}_{\mathrm{p}}^{\intercal} \frac{k_{\mathrm{r}}}{\gamma^{\mathrm{w}}} \boldsymbol{k} \rho_{\mathrm{w}} \boldsymbol{b} \mathrm{d}\Omega - \int_{\Gamma_N^{\mathrm{p}}} \boldsymbol{N}_{\mathrm{p}}^{\intercal} \bar{q}^{\mathrm{w}} \mathrm{d}\Gamma.
\end{aligned}$$

Similarly, application to the weak form of the energy balance equation, Eq. (51), gives the system of equations:

$$(\boldsymbol{K}_{\mathrm{TT}} + \boldsymbol{K}_{\mathrm{TT}}^{\mathrm{s}}) \boldsymbol{T}^{\mathrm{c}} + (\boldsymbol{C}_{\mathrm{Tp}} + \boldsymbol{C}_{\mathrm{Tp}}^{\mathrm{s}}) \frac{\partial \boldsymbol{p}^{\mathrm{c}}}{\partial t} + (\boldsymbol{C}_{\mathrm{TT}} + \boldsymbol{C}_{\mathrm{TT}}^{\mathrm{s}}) \frac{\partial \boldsymbol{T}^{\mathrm{c}}}{\partial t} = \boldsymbol{f}_{\mathrm{T}} \tag{55}$$

where

$$\begin{aligned}
\boldsymbol{K}_{\mathrm{TT}} &= \int_{\Omega} \nabla \boldsymbol{N}_{\mathrm{T}}^{\intercal} \boldsymbol{a} \boldsymbol{N}_{\mathrm{T}} \mathrm{d}\Omega + \int_{\Omega} \nabla \boldsymbol{N}_{\mathrm{T}}^{\intercal} \boldsymbol{\lambda} \nabla \boldsymbol{N}_{\mathrm{T}} \mathrm{d}\Omega + \int_{\Gamma_N^{\mathrm{T}}} \boldsymbol{N}_{\mathrm{T}}^{\intercal} \lambda_{\mathrm{e}} \boldsymbol{N}_{\mathrm{T}} \mathrm{d}\Omega \\
\boldsymbol{K}_{\mathrm{TT}}^{\mathrm{s}} &= \int_{\Omega} \nabla \boldsymbol{N}_{\mathrm{T}}^{\intercal} \tau_{\mathrm{e}} \boldsymbol{a} \cdot \boldsymbol{a} \nabla \boldsymbol{N}_{\mathrm{T}} \mathrm{d}\Omega + \int_{\Omega} \nabla \boldsymbol{N}_{\mathrm{T}}^{\intercal} \tau_{\mathrm{e}} \boldsymbol{a} \cdot \boldsymbol{\lambda} \nabla (\nabla \boldsymbol{N}_{\mathrm{T}}) \mathrm{d}\Omega \\
\boldsymbol{C}_{\mathrm{Tp}} &= \int_{\Omega} \boldsymbol{N}_{\mathrm{T}}^{\intercal} L_{\mathrm{f}} \xi S_{\mathrm{p}} \boldsymbol{N}_{\mathrm{p}} \mathrm{d}\Omega \\
\boldsymbol{C}_{\mathrm{Tp}}^{\mathrm{s}} &= \int_{\Omega} \boldsymbol{N}_{\mathrm{T}}^{\intercal} L_{\mathrm{f}} \xi S_{\mathrm{p}} \tau_{\mathrm{e}} \boldsymbol{a} \nabla \boldsymbol{N}_{\mathrm{p}} \mathrm{d}\Omega \\
\boldsymbol{C}_{\mathrm{TT}} &= \int_{\Omega} \boldsymbol{N}_{\mathrm{T}}^{\intercal} (\rho c)_{\mathrm{eff}} \boldsymbol{N}_{\mathrm{T}} \mathrm{d}\Omega + \int_{\Omega} \boldsymbol{N}_{\mathrm{T}}^{\intercal} L_{\mathrm{f}} \xi S_{\mathrm{T}} \boldsymbol{N}_{\mathrm{T}} \mathrm{d}\Omega \\
\boldsymbol{C}_{\mathrm{TT}}^{\mathrm{s}} &= \int_{\Omega} \nabla \boldsymbol{N}_{\mathrm{T}}^{\intercal} (\rho c)_{\mathrm{eff}} \tau_{\mathrm{e}} \boldsymbol{a} \boldsymbol{N}_{\mathrm{T}} \mathrm{d}\Omega + \int_{\Omega} \boldsymbol{N}_{\mathrm{T}}^{\intercal} L_{\mathrm{f}} \xi S_{\mathrm{T}} \tau_{\mathrm{e}} \boldsymbol{a} \nabla \boldsymbol{N}_{\mathrm{T}} \mathrm{d}\Omega \\
\boldsymbol{f}_{\mathrm{T}} &= - \int_{\Gamma_N^{\mathrm{T}}} \boldsymbol{N}_{\mathrm{T}}^{\intercal} \bar{q}^{\mathrm{T}} \mathrm{d}\Gamma + \int_{\Gamma_N^{\mathrm{T}}} \boldsymbol{N}_{\mathrm{T}}^{\intercal} \lambda_{\mathrm{e}} T_{\mathrm{e}} \mathrm{d}\Gamma
\end{aligned}$$

Letting $\boldsymbol{K}^{*}_{\mathrm{TT}} = \boldsymbol{K}_{\mathrm{TT}} + \boldsymbol{K}^{\mathrm{s}}_{\mathrm{TT}}$, $\boldsymbol{C}^{*}_{\mathrm{Tp}} = \boldsymbol{C}_{\mathrm{Tp}} + \boldsymbol{C}^{\mathrm{s}}_{\mathrm{Tp}}$ and $\boldsymbol{C}^{*}_{\mathrm{TT}} = \boldsymbol{C}_{\mathrm{TT}} + \boldsymbol{C}^{\mathrm{s}}_{\mathrm{TT}}$, the system of matrix equations, Eq. (53), (54) and (55), are summarized in to a fully coupled system as:

$$\begin{bmatrix} \boldsymbol{0} & \boldsymbol{0} & \boldsymbol{0} \\ \boldsymbol{0} & \boldsymbol{K}_{\mathrm{pp}} & \boldsymbol{0} \\ \boldsymbol{0} & \boldsymbol{0} & \boldsymbol{K}^{*}_{\mathrm{TT}} \end{bmatrix} \begin{Bmatrix} \boldsymbol{u}^{\mathrm{c}} \\ \boldsymbol{p}^{\mathrm{c}} \\ \boldsymbol{T}^{\mathrm{c}} \end{Bmatrix} + \begin{bmatrix} \boldsymbol{C}_{\mathrm{uu}} & \boldsymbol{C}_{\mathrm{up}} & \boldsymbol{C}_{\mathrm{uT}} \\ \boldsymbol{C}_{\mathrm{pu}} & \boldsymbol{C}_{\mathrm{pp}} & \boldsymbol{C}_{\mathrm{pT}} \\ \boldsymbol{0} & \boldsymbol{C}^{*}_{\mathrm{Tp}} & \boldsymbol{C}^{*}_{\mathrm{TT}} \end{bmatrix} \frac{\partial}{\partial t} \begin{Bmatrix} \boldsymbol{u}^{\mathrm{c}} \\ \boldsymbol{p}^{\mathrm{c}} \\ \boldsymbol{T}^{\mathrm{c}} \end{Bmatrix} = \begin{Bmatrix} \boldsymbol{f}_{\mathrm{u}} \\ \boldsymbol{f}_{\mathrm{p}} \\ \boldsymbol{f}_{\mathrm{T}} \end{Bmatrix} \tag{56}$$

which can be written in a more compact form as:

$$\boldsymbol{K}\boldsymbol{X} + \boldsymbol{C}\frac{\partial \boldsymbol{X}}{\partial t} = \boldsymbol{F} \tag{57}$$

where the coefficient matrices $\boldsymbol{K}$ and $\boldsymbol{C}$, the external load vector $\boldsymbol{F}$ and the vector of unknowns $\boldsymbol{X}$ are evident from Eq. (56). The matrices $\boldsymbol{K}$ and $\boldsymbol{C}$ are generally functions of $\boldsymbol{X}$, making the coupled system of equations highly nonlinear.

5.4. Numerical Implementation

We aim to solve the fully coupled system in Eq. (57) in a monolithic way since the equations are strongly coupled and highly nonlinear. Temporal discretization of the system of matrix equations is performed using the Generalized Trapezoidal Rule (GTR). For the rate of change of the unknown vector $\boldsymbol{X}$, we have the approximation:

$$\begin{aligned} \left.\frac{\partial \boldsymbol{X}}{\partial t}\right|_{n+\theta} &= \frac{\boldsymbol{X}_{n+1} - \boldsymbol{X}_{n}}{\Delta t} \\ \boldsymbol{X}_{n+\theta} &= (1-\theta)\boldsymbol{X}_{n} + \theta \boldsymbol{X}_{n+1} \end{aligned} \tag{58}$$

where θ is a time integration parameter which has limits $0 \leq \theta \leq 1$. The system of matrix equations at time $t_{n+\theta}$ is then:

$$\boldsymbol{K}\boldsymbol{X}_{n+\theta} + \boldsymbol{C}\left.\frac{\partial \boldsymbol{X}}{\partial t}\right|_{n+\theta} = \boldsymbol{F}_{n+\theta}. \tag{59}$$

Using the approximation in Eq. (58) into Eq. (59) and adopting a fully implicit time integration scheme with $\theta = 1$, we get:

$$\left[\Delta t \boldsymbol{K} + \boldsymbol{C}\right]_{n+1} \boldsymbol{X}_{n+1} = \boldsymbol{C}_{n+1}\boldsymbol{X}_{n} + \Delta t \boldsymbol{F}_{n+1}. \tag{60}$$

The residual at time step t_{n+1} is then:

$$\boldsymbol{R}_{n+1} = \left[\Delta t \boldsymbol{K} + \boldsymbol{C}\right]_{n+1} \boldsymbol{X}_{n+1} - \boldsymbol{C}_{n+1}\boldsymbol{X}_{n} - \Delta t \boldsymbol{F}_{n+1}. \tag{61}$$

After first-order Taylor series expansion of the residual, we solve for the increment of the unknown vector $\Delta \boldsymbol{X}^{i+1}_{n+1}$ using a Newton-Raphson iteration scheme:

$$\left.\frac{\partial \boldsymbol{R}}{\partial \boldsymbol{X}}\right|^{i}_{n+1} \Delta \boldsymbol{X}^{i+1}_{n+1} \cong -\boldsymbol{R}^{i}_{n+1} \tag{62}$$

where i is the iteration number and we have the Jacobian matrix in the above equation as:

$$\boldsymbol{J} = \frac{\partial \boldsymbol{R}}{\partial \boldsymbol{X}}. \tag{63}$$

The vector of unknowns at time step t_{n+1} is updated after each iteration using:

$$\boldsymbol{X}_{n+1}^{i+1} = \boldsymbol{X}_{n+1}^{i} + \Delta \boldsymbol{X}_{n+1}^{i+1}. \tag{64}$$

6. Numerical Examples

In this section, numerical examples are presented to verify and validate the proposed THM model. In particular, we first look at a one-dimensional freezing problem with drained and undrained boundary conditions. We then present simulation of frost heave due to a chilled gas pipeline buried in a silty soil.

6.1. One-dimensional Freezing

The first numerical example we consider is the freezing of a soil column in a plane strain condition, which is studied in [33] using FEA.

6.1.1. Problem Definition

The simulation domain is a 2m long soil column with an initial homogeneous temperature of $T_\mathrm{o} = 1\,^\circ\mathrm{C}$, shown in Figure 8.

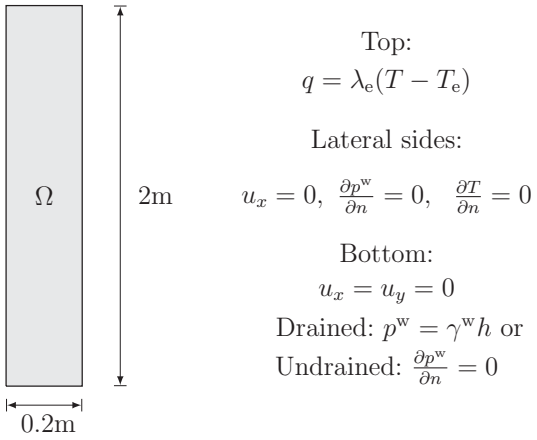

Figure 8: One-dimensional freezing: Computational domain and boundary conditions.

The soil column is subjected to cooling at the top boundary where the environment temperature is $T_\mathrm{e} = -10\,^\circ\mathrm{C}$. An initial hydrostatic condition is assumed for the pore water pressure throughout the soil column. The thermal conductivity of the external environment

Table 1: One-dimensional freezing: Material and model parameters.

Parameter	**Value**	**Unit**
Thermal properties:		
Thermal conductivity of soil, λ_s	1.5	W/m/K
Thermal conductivity of water, λ_w	0.6	W/m/K
Thermal conductivity of ice, λ_i	2.2	W/m/K
Specific heat capacity of soil, c_s	800	J/kg/K
Specific heat capacity of water, c_w	4190	J/kg/K
Specific heat capacity of ice, c_i	2095	J/kg/K
Latent heat of fusion, L_f	334	kJ/kg
Hydraulic properties:		
Hydraulic conductivity, k	1.0×10^{-5}	m/s
Saturation model parameter 1, α	0.1	MPa^{-1}
Saturation model parameter 2, β	2.5	–
Saturation model parameter 3, γ	8.0	–
Hydraulic conductivity model parameter, m	0.87	–
Mechanical properties:		
Young's modulus of soil, E_s	3.0	MPa
Young's modulus of ice, E_i	9100	MPa
Poisson's ratio of soil, ν_s	0.2	–
Poisson's ratio of ice, ν_i	0.4	–
Strength model parameter, η	1.0	–
Mass and volume properties:		
Initial porosity, n	0.44	–
Density of soil, ρ_s	2650	$\mathrm{kg/m}^3$
Density of water, ρ_w	1000	$\mathrm{kg/m}^3$
Density of ice, ρ_i	910	$\mathrm{kg/m}^3$

is assumed to be $\lambda_\mathrm{e} = 0.01$ kW/m^2/K, which simulates air and other surface covering material such as snow. The freezing process is assumed to obey Newton's law of cooling such that the heat transferred in to the soil column is $q = \lambda_\mathrm{e}(T - T_\mathrm{e})$. The vertical and horizontal displacements are fixed at the bottom boundary and the horizontal displacements are fixed at the lateral boundaries. The top and lateral boundaries are allowed to move freely in the vertical direction. The lateral boundaries are sealed and insulated i.e. the water and the heat fluxes are set to zero. The top boundary is allowed to transfer heat from the environment into the soil column. Two drainage boundary conditions are considered at the bottom: drained ($p^\mathrm{w} = 0$) and undrained ($\frac{\partial p^\mathrm{w}}{\partial n} = 0$). The top boundary is assumed to be permeable ($p^w = 0$) in the simulation here. This may be considered permeable at the beginning of the simulation and changed to an impermeable boundary when freezing

starts, thus changing the pressure boundary condition from a Dirichlet to a Neumann type. This assumption is expected to result in slight differences in the displacement and pore pressure results but the effect is negligible on the temperature and ice saturation profiles. The material and model parameters used for the simulation are given in Table 1.

6.1.2. Results

Results of the simulation for a drained bottom boundary are shown in Figure 9 in terms of vertical displacement, pore water pressure temperature and ice saturation profiles versus depth at selected time steps. The corresponding results for an undrained bottom boundary are shown in Figure 10. A comparison of the drained and undrained results shows that the temperature and ice saturation profiles of the two cases are more or less the same. This indicates that advective heat transfer has little effect on the thermal state in this particular example. On the other hand, significant differences are observed in the vertical displacement and pore water pressure profiles for the two bottom drainage cases. The final vertical heave in the drained case is larger than the heave in the undrained case by a significant margin. The evolution of the total vertical heave with time, at the top boundary, for the two cases is shown in Figure 11. This highlights the influence of water migration in frost heave, which is a well-known phenomenon. A closer look at the vertical displacement profiles in the two cases reveals that the soil continuously expands in the drained case due to a continuous supply of water from the drained boundary. However, in the undrained case, as the soil column expands at the top due to freezing, contraction is observed at the bottom since there is no continuous water supply. Negative pore water pressures are observed as water is sucked into the freezing front.

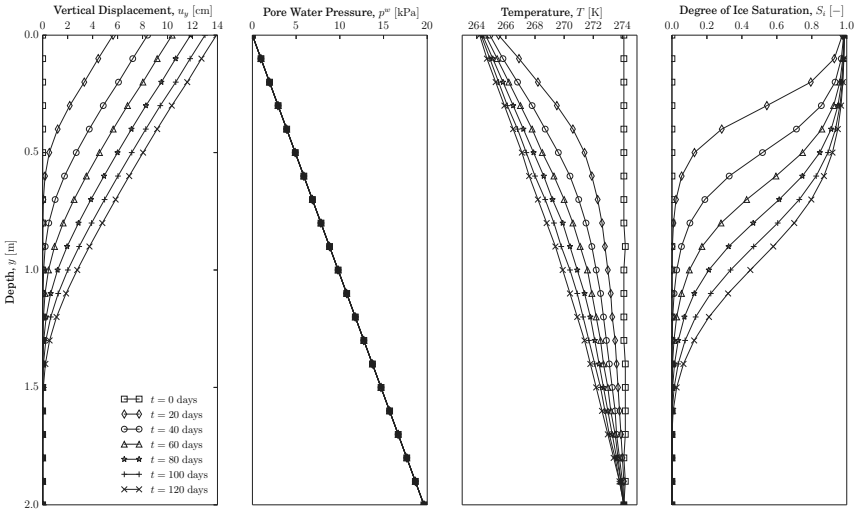

Figure 9: One-dimensional freezing: Results for a drained bottom boundary.

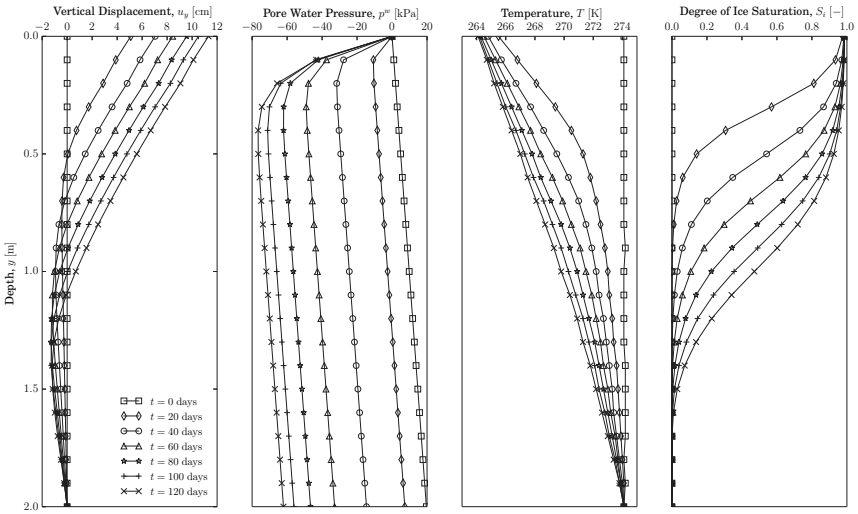

Figure 10: One-dimensional freezing: Results for an undrained bottom boundary.

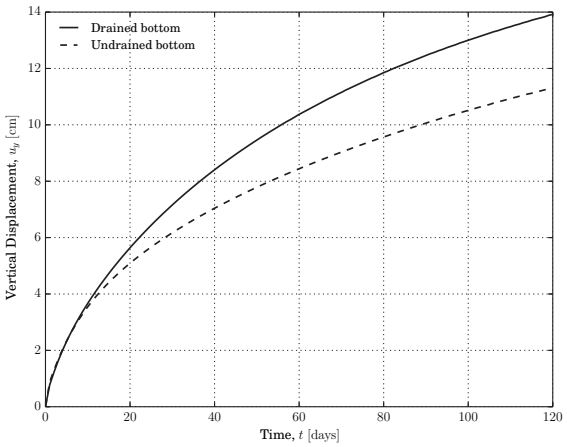

Figure 11: One-dimensional freezing: Vertical displacement of the top boundary versus time for drained and undrained bottom boundaries.

6.2. Frost Heave

Prediction of frost heave is important in the design and safety analysis of structures in or on frost susceptible soils. Frost heave can cause structural damages such as displacement of retaining walls, lifting of pavements and lifting of foundations and distortion of unheated buildings, [29]. An accurate prediction and modeling of the thermal properties of such soils under sub-zero temperatures is essential. We here present a numerical example based on field-scale experimental observations on the nature of frost heaving; see Smith and Patterson [34]. The field scale test performed considers a chilled pipeline buried in soil and an outer environment with sub-zero temperature. The heave displacements from the test are documented and the results are used for comparison against simulations. Other relevant information is referred from the numerical studies by Selvadurai *et al.* [35] and Mikkola and Hartikainen [36].

6.2.1. Problem Definition

The gas pipeline in the full-scale experiment has a diameter of 273 mm and is buried in silt. The length of the pipeline is 16 m and the 8 m wide test trench is filled with silt up to a depth of 1.75 m. The backfill on top of the pipeline has a height of 0.33 m. The numerical model is setup in two dimensions and we take advantage of symmetry and model only half of the cross-sectional domain. The computational domain is shown in Figure 12. The water table is located at 90 cm below the top surface but the whole domain is assumed to be saturated due to capillarity.

The following boundary conditions are defined: both the horizontal and vertical displacements are fixed at the bottom boundary and the lateral boundaries are constrained from

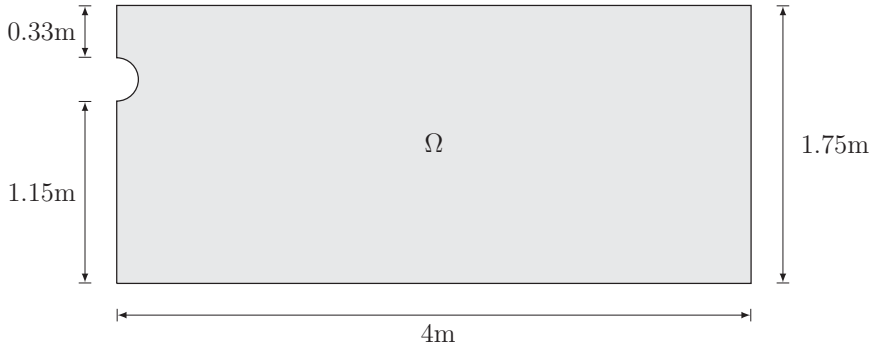

Figure 12: Frost heave: Computational domain.

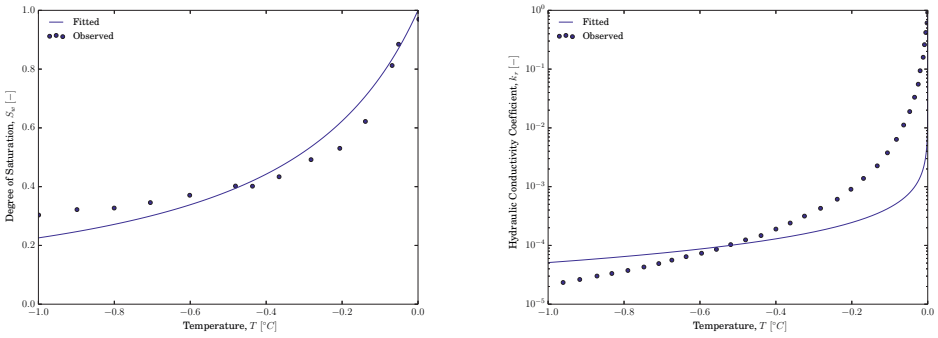

Figure 13: Frost heave: Estimation of saturation model parameters and hydraulic conductivity model parameter based on experimental data.

horizontal displacement. The bottom boundary is drained and adiabatic. The top boundary is undrained and its temperature is $-0.75\,°\mathrm{C}$ from the hall temperature. The lateral boundaries are impermeable and adiabatic. The temperature in the pipeline is maintained at a constant value of $-5\,°\mathrm{C}$ throughout the experiment. The initial temperature of the silt is $4\,°\mathrm{C}$.

The material properties for the silt are given in Table 2. The saturation model parameters are estimated based on curve fitting to experimental data of unfrozen water content versus temperature. The hydraulic conductivity model parameter is similarly estimated by fitting a curve to an experimental hydraulic conductivity versus temperature data. The experimental data and the fitted curves are shown in Figure 13. The strength parameter is selected such that the frozen strength of the silt is comparable to empirical estimates such as in [37].

Table 2: Frost heave: Material and model parameters.

Parameter	**Value**	**Unit**
Thermal properties:		
Thermal conductivity of soil, λ_s	0.65	W/m/K
Thermal conductivity of water, λ_w	0.6	W/m/K
Thermal conductivity of ice, λ_i	2.2	W/m/K
Specific heat capacity of soil, c_s	800	J/kg/K
Specific heat capacity of water, c_w	4190	J/kg/K
Specific heat capacity of ice, c_i	2095	J/kg/K
Latent heat of fusion, L_f	334	kJ/kg
Hydraulic properties:		
Hydraulic conductivity, k	5.0×10^{-9}	m/s
Saturation model parameter 1, α	0.5	MPa^{-1}
Saturation model parameter 2, β	1.82	–
Saturation model parameter 3, γ	0.45	–
Hydraulic conductivity model parameter, m	0.28	–
Mechanical properties:		
Young's modulus of soil, E_s	1.0	MPa
Young's modulus of ice, E_i	9100	MPa
Poisson's ratio of soil, ν_s	0.3	–
Poisson's ratio of ice, ν_i	0.4	–
Strength model parameter, η	5.0	–
Mass and volume properties:		
Initial porosity, n	0.4	–
Density of soil, ρ_s	2650	$\mathrm{kg/m}^3$
Density of water, ρ_w	1000	$\mathrm{kg/m}^3$
Density of ice, ρ_i	910	$\mathrm{kg/m}^3$

6.2.2. Results

The mesh used for the simulation is shown in Figure 14. Quadratic polynomial degrees are used for the pressure and the temperature ($p_p = p_T = 2$) and cubic polynomial degrees for the displacement ($p_u = 3$). The simulation is run for a time period of 358 days, as in the experiment.

The degree of ice saturation in the simulation domain after 358 days is shown in Figure 15. We observe from the result that freezing is initiated from two fronts; the subzero temperatures in the pipeline and the top boundary. Frost penetration occurs slowly and we see that we still have an unfrozen area in the domain after 358 days. This is due to the hydraulic and thermal properties of the silt in the experiment. Some unfrozen water still remains in areas of the frozen part, as expected from the unfrozen water content data from

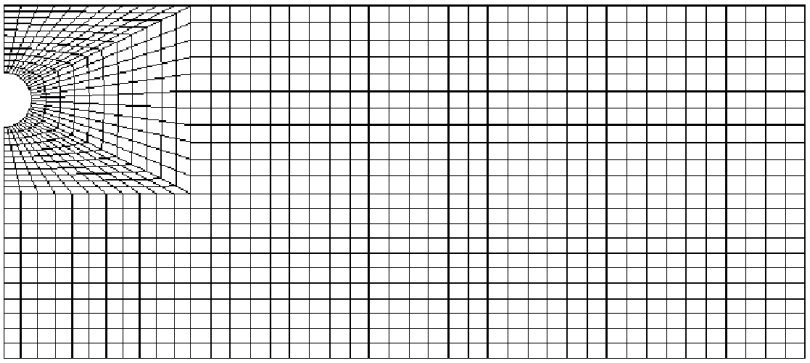

Figure 14: Frost heave: Spatial discretization.

Figure 15: Frost heave: Ice saturation at the final step i.e. after 358 days.

experiments.

The temperature profiles showing the evolution of the freezing front are presented in Figure 16 for time periods after 100, 200 and 300 days. At the end of the simulation, and the experiment, some portion of the silt still has a temperature above the freezing temperature. The evolution of the 0 °C isotherm from the simulation shows a good agreement with the experimental results reported by Smith and Patterson [34]. A total heave of about 20 cm is observed at the centerline of the pipe. The heave displacement was monitored in the experiment at locations denoted Site 2, Site 3 and Site 4, which are located at the top and 25 cm, 65 cm and 100 cm from the centerline of the pipe, respectively. The heave displacements from the simulation at these locations are plotted against the observed data and the results are shown in Figure 17. As can be seen, the results from the simulation show a reasonably good agreement with the observed data.

(a) $t = 100$ days

(b) $t = 200$ days

(c) $t = 300$ days

Figure 16: Frost heave: Temperature profiles at selected time steps.

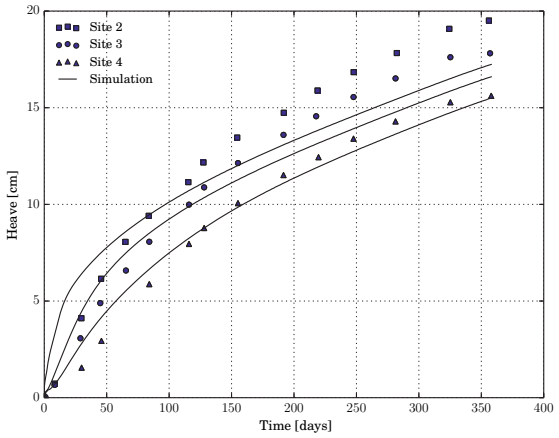

Figure 17: Frost heave: Heave displacements from experiment and simulation. The solid lines for simulation from top to bottom correspond to Site 2, Site 3 and Site 4.

7. Conclusions

An isogeometric analysis based fully coupled thermo-hydro-mechanical (THM) numerical model for ground freezing is presented. A saturated frozen soil, with solid, water and ice phases, is assumed. The governing equations of the model are derived based on porous media theory. Volume expansion and contraction strains, due to phase change from water to ice and ice to water, are incorporated into the governing equations. The governing equations are supplemented by other temperature dependent state parameters such as the soil-water characteristic curve and the hydraulic conductivity model.

The proposed numerical model is first qualitatively validated by asserting that the standard governing equations of poroelasticity are derived for the specific case where the degree of ice saturation is zero. This is further discussed in Appendix A. The model is then used to simulate freezing problems. In particular, numerical examples on one-dimensional freezing of a soil column and a two-dimensional frost heave simulation, with a pipeline transporting chilled gas, are presented. The two-dimensional frost heave problem is based on field-scale experimental data and the numerical simulation results were observed to be in a good agreement with the experimental results.

The numerical implementation of the model is based on isogeometric analysis using B-Splines for numerical integration. The continuity of the B-Splines basis functions across knot spans, analogous to elements in the standard finite element method, can be controlled to a deisred degree. This is unlike in the finite element method, where the basis function are only C^0 continuous across element boundaries. This improves the accuracy of derived quantities such as stresses, strains and fluxes. Further numerical studies are required to quantify

this. The use of isogeometric analysis also has the advantage that CAD geometries can be represented in an 'exact' manner, which are only approximated through mesh generation in the traditional finite element method.

Acknowledgement

This work is financially supported by the Research Council of Norway and industrial partners through the research project SAMCoT, Sustainable Arctic Marine and Coastal Technology. The authors gratefully acknowledge the support.

Appendix A. Validation of THM Model

The governing equations and the final discretized system of equations can be validated for a specific case. The approach used here is to check if the system of equations reduce to the well-know equations of poroelasticity when no freezing is considered. This means that we assume the degree of ice saturation to be zero, i.e. $S_\mathrm{i} = 0$, which for a saturated porous medium implies $S_\mathrm{w} = 1$. A constant degree of water saturation further implies that the isothermal and non-isothermal water capacities become zero i.e. $S_\mathrm{p} = S_\mathrm{T} = 0$. With these conditions, the governing equations in Eq. (9), (12) and (18) reduce to:

$$\nabla \cdot \boldsymbol{\sigma}' - \nabla p^\mathrm{w} + \rho \boldsymbol{b} = 0 \tag{A.1}$$

$$\nabla \cdot \boldsymbol{v}^\mathrm{s} + \nabla \cdot \boldsymbol{w} = 0 \tag{A.2}$$

$$(\rho c)_\mathrm{eff} \frac{\mathrm{D}_\mathrm{s} T}{\mathrm{D}t} + \boldsymbol{a} \cdot \nabla T = -\nabla \cdot \boldsymbol{q} + Q \tag{A.3}$$

If we further assume isothermal conditions such that there are no spatial and temporal changes in temperature i.e. $\nabla T = 0$ and $\frac{\partial T}{\partial t} = 0$, the equations effectively reduce to the governing equations of a consolidation problem with incompressible solid grains and water. The THM numerical implementation is verified by simulating a consolidation problem. The thermal material properties are supplied in the input such that the coefficient matrices related to temperature are non-zero. A positive initial temperature is assumed and all the boundaries of the consolidation model are set to be adiabatic. The results are not included here.

References

[1] K. M. Neaupane, T. Yamabe, R. Yoshinaka, Simulation of a fully coupled thermo-hydro-mechanical system in freezing and thawing rock, International Journal of Rock Mechanics and Mining Sciences 36 (5) (1999) 563–580.

[2] T. Nowak, H. Kunz, D. Dixon, W. Wang, U.-J. Görke, O. Kolditz, Coupled 3-D thermo-hydro-mechanical analysis of geotechnological in situ tests, International Journal of Rock Mechanics and Mining Sciences 48 (1) (2011) 1–15.

[3] J. A. Hudson, O. Stephansson, J. Andersson, Guidance on numerical modelling of thermo-hydro-mechanical coupled processes for performance assessment of radioactive waste repositories, International Journal of Rock Mechanics and Mining Sciences 42 (5) (2005) 850–870.

[4] W. Wang, O. Kolditz, Object-oriented finite element analysis of thermo-hydro-mechanical (THM) problems in porous media, International Journal for Numerical Methods in Engineering 69 (1) (2007) 162–201.
[5] J. Rutqvist, L. Börgesson, M. Chijimatsu, A. Kobayashi, L. Jing, T. Nguyen, J. Noorishad, C.-F. Tsang, Thermohydromechanics of partially saturated geological media: governing equations and formulation of four finite element models, International Journal of Rock Mechanics and Mining Sciences 38 (1) (2001) 105–127.
[6] J. Rutqvist, L. Börgesson, M. Chijimatsu, T. Nguyen, L. Jing, J. Noorishad, C.-F. Tsang, Coupled thermo-hydro-mechanical analysis of a heater test in fractured rock and bentonite at Kamaishi Minecomparison of field results to predictions of four finite element codes, International Journal of Rock Mechanics and Mining Sciences 38 (1) (2001) 129–142.
[7] L. Sanavia, B. François, R. Bortolotto, L. Luison, L. Laloui, Finite element modelling of thermo-elasto-plastic water saturated porous materials, Journal of Theoretical and Applied Mechanics 38 (1-2) (2008) 7–34.
[8] W. Wang, G. Kosakowski, O. Kolditz, A parallel finite element scheme for thermo-hydro-mechanical (THM) coupled problems in porous media, Computers & Geosciences 35 (8) (2009) 1631–1641.
[9] F. Tong, L. Jing, R. W. Zimmerman, A fully coupled thermo-hydro-mechanical model for simulating multiphase flow, deformation and heat transfer in buffer material and rock masses, International Journal of Rock Mechanics and Mining Sciences 47 (2) (2010) 205–217.
[10] S. Mu, B. Ladanyi, Modeling of coupled heat, moisture and stress-field in freezing soil, Cold Regions Science and Technology 14 (3) (1987) 237–246.
[11] A. Selvadurai, J. Hu, I. Konuk, Computational modelling of frost heave induced soil–pipeline interaction: I. modelling of frost heave, Cold Regions Science and Technology 29 (3) (1999) 215–228.
[12] N. Li, B. Chen, F. X. Chen, X. Z. Xu, The coupled heat-moisture-mechanic model of the frozen soil, Cold Regions Science and Technology 31 (3) (2000) 199–205.
[13] S. Nishimura, A. Gens, S. Olivella, R. J. Jardine, THM-coupled finite element analysis of frozen soil: formulation and application, Geotechnique 59 (3) (2009) 159–171.
[14] Z. Liu, X. Yu, Coupled thermo-hydro-mechanical model for porous materials under frost action: theory and implementation, Acta Geotechnica 6 (2) (2011) 51–65.
[15] K. M. Neaupane, T. Yamabe, A fully coupled thermo-hydro-mechanical nonlinear model for a frozen medium, Computers and Geotechnics 28 (8) (2001) 613–637.
[16] M. Dall'Amico, S. Endrizzi, S. Gruber, R. Rigon, A robust and energy-conserving model of freezing variably-saturated soil, The Cryosphere 5 (2) (2011) 469–484.
[17] Z. L. Wang, Q. Fu, Q. X. Jiang, T. X. Li, Numerical simulation of water-heat coupled movements in seasonal frozen soil, Mathematical and Computer Modelling 54 (3-4) (2011) 970–975.
[18] X. M. Peng, X. B. Chen, Y. Q. Wang, A model coupled heat, moisture and stress-field of saturated soil during freezing, Ground Freezing 91, Vol 1 1 (1991) 77–82.
[19] J. Qi, X. Yao, F. Yu, Consolidation of thawing permafrost considering phase change, KSCE Journal of Civil Engineering 17 (6) (2013) 1293–1301.
[20] M. M. Zhou, G. Meschke, A three-phase thermo-hydro-mechanical finite element model for freezing soils, International Journal for Numerical and Analytical Methods in Geomechanics 37 (18) (2013) 31733193.
[21] Y. Kang, Q. Liu, S. Huang, A fully coupled thermo-hydro-mechanical model for rock mass under freezing/thawing condition, Cold Regions Science and Technology 95 (2013) 19–26.
[22] K. Hansson, J. Simunek, M. Mizoguchi, L.-C. Lundin, M. T. Van Genuchten, Water flow and heat transport in frozen soil, Vadose Zone Journal 3 (2) (2004) 693–704.
[23] H. R. Thomas, P. Cleall, Y.-C. Li, C. Harris, M. Kern-Luetschg, Modelling of cryogenic processes in permafrost and seasonally frozen soils, Geotechnique 59 (3) (2009) 173–184.
[24] O. Coussy, Poromechanics of freezing materials, Journal of the Mechanics and Physics of Solids 53 (8) (2005) 1689–1718.
[25] G. P. Newman, G. W. Wilson, Heat and mass transfer in unsaturated soils during freezing, Canadian

Geotechnical Journal 34 (1) (1997) 63–70.
[26] R. L. Michalowski, M. Zhu, Frost heave modelling using porosity rate function, International Journal for Numerical and Analytical Methods in Geomechanics 30 (8) (2006) 703–722.
[27] J. Cote, J. M. Konrad, A generalized thermal conductivity model for soils and construction materials, Canadian Geotechnical Journal 42 (2) (2005) 443–458.
[28] J. P. G. Loch, Thermodynamic-equilibrium between ice and water in porous-media, Soil Science 126 (2) (1978) 77–80.
[29] R. D. Miller, Freezing phenomena in soils, Applications of Soil Physics (Hillel, D.) (1980) 254–298.
[30] M. T. Vangenuchten, A closed-form equation for predicting the hydraulic conductivity of unsaturated soils, Soil Science Society of America Journal 44 (5) (1980) 892–898.
[31] T. J. R. Hughes, J. A. Cottrell, Y. Bazilevs, Isogeometric analysis: CAD, finite elements, NURBS, exact geometry and mesh refinement, Computer Methods in Applied Mechanics and Engineering 194 (3941) (2005) 4135–4195.
[32] J. A. Cottrell, T. J. R. Hughes, Y. Bazilevs, Isogeometric Analysis : Toward Integration of CAD and FEA, Wiley, Chichester, West Sussex, U.K., Hoboken, NJ, 2009.
[33] H. Kyokawa, Y. W. Bekele, Numerical simulation of thermo-hydro-mechanically coupled processes during ground freezing and thawing, Computer Methods and Recent Advances in Geomechanics (2014) 379–384.
[34] M. Smith, D. Patterson, Detailed observations on the nature of frost heaving at a field scale, Canadian Geotechnical Journal 26 (2) (1989) 306–312.
[35] A. Selvadurai, J. Hu, I. Konuk, Computational modelling of frost heave induced soil–pipeline interaction: II. modelling of experiments at the Caen test facility, Cold Regions Science and Technology 29 (3) (1999) 229–257.
[36] M. Mikkola, J. Hartikainen, Mathematical model of soil freezing and its numerical implementation, International Journal for Numerical Methods in Engineering 52 (5-6) (2001) 543–557.
[37] O. B. Andersland, B. Ladanyi, Frozen ground engineering, John Wiley & Sons, 2004.

Part III

Summary

"It is strange that only extraordinary men make the discoveries, which later appear so easy and simple."

– Georg Lichtenberg

Chapter 4

Conclusions and Outlook

This chapter presents a summary of the research work in the thesis and the main findings as conclusions. A list of recommendations for future work is also made.

4.1 Summary

Computational modeling of physical phenomena that occur in porous media requires detailed mathematical formulations describing the processes and a robust numerical method for simulation. The mathematical formulations governing various physical processes are based on porous media theory. The fundamental state-of-the-art concepts in this theory are summarized in a general form that may be applicable to any porous material. The applications of interest in this thesis were porous media flow, hydro-mechanically and thermo-hydro-mechanically coupled problems. With these applications in mind, formulation of the governing equations for specific cases is discussed in detail such that the assumptions and limitations of the formulations in each case are evident.

The computational method that is applied here is IGA which relies on B-Spline and NURBS basis functions that are used in CAD. IGA was first introduced to bridge the gap between CAD and FEA. It has been applied to various computational mechanics problems with commendable success and has shown several advantages over FEA. In the context porous media problems, the features of IGA that are especially attractive are the controllable smoothness of the basis functions and its unique refinement capability that can be used to achieve high regularity meshes. The ability to represent CAD geometries in an 'exact' manner during analysis is another feature that is useful for particular application problems.

Application of IGA to the porous media problems studied here resulted in the papers presented in Part II. Each of the papers contain a summary of their respective applications. A shorter summary of each paper is presented here.

Paper I

Adaptive IGA of steady-state groundwater flow problems, which are governed by Darcy's law, is studied in this paper. The numerical challenges in the simulation of these problems, for instance due to complex boundary conditions, motivated the application of adaptive refinement using LR B-Splines. The numerical implementation is verified based on problems with analytical solutions. A posteriori error estimates are calculated based on analytical solutions, whenever available, and L^2 projection of the primary solution. The groundwater flow problems simulated are flow around an impervious corner, flow around a cutoff wall and flow in a heterogeneous medium.

Paper II

The second paper deals with the application of mixed IGA to classical poroelasticity problems. The finite element method has been applied to such problems and the numerical behavior of the governing equations has been discussed by several researchers, as documented in the introduction of this paper. Pressure oscillations at small time steps have been known to be an issue in the simulation of these problems. Several measures have been put forward to alleviate this, of which the critical time step concept is one which is widely used in finite element packages. The performance of mixed IGA for smaller time steps is investigated by revisiting Terzaghi's classical consolidation problem. A numerical study is also performed on the consolidation of a layered soil with a pressure oscillation susceptible very low permeability layer.

Paper III

Fully coupled THM processes during ground freezing are studied in this paper. The governing linear momentum, mass and energy balance equations are formulated by assuming saturated conditions. Strain due to phase change is incorporated into the equilibrium equation through the constitutive equations. A simple thermoelastic constitutive model with temperature dependent strength parameters is presented. The mathematical model is completed by defining a soil-water characteristic curve and a hydraulic conductivity model, both adopted from literature. Mixed IGA is applied and Galerkin formulation of the governing equations resulted in a highly nonlinear coupled system of equations, which are solved using Newton-Raphson iterations. Numerical studies are performed on one-dimensional freezing and a frost heave problem where experimental data is available.

4.2 Conclusions

Application of IGA to coupled problems in porous media is presented. The work here mainly initiates application of IGA to THM coupled problems in porous media to take advantage of the features of IGA that are computationally attractive in this context. This is achieved by developing a fully coupled THM numerical framework for ground freezing based on mixed IGA. Good agreements were observed between the mixed IGA based simulation of a THM coupled problem of frost heave and the

corresponding experimental data found from literature.

Classical steady-state groundwater flow and poroelasticity problems are revisited from a computational perspective. Numerical studies are performed to study the accuracy of the IGA based simulations. It is shown that adaptive and higher-order simulations can improve the accuracy of the numerical results. This emphasizes that there is some room for improvement in the efficiency and robustness of traditional FEA of such problems.

The specific observations made from the research work are listed below in the order of the application problems studied.

- ⋆ Adaptive isogeometric analysis of steady-state groundwater flow problems using LR B-Splines improves the accuracy of the primary solution, by recovering the spatial errors, compared to simulations with uniform refinement.
- ⋆ The convergence rates for flow problems with strong discontinuities, such as flow around a cutoff wall, were found to be optimal and observed to improve with increasing polynomial degrees.
- ⋆ Adaptive simulation of flow problems with weak discontinuities, such as flow in a heterogeneous medium, may not result in optimal convergence rates. Adaptive refinement, however, still outperformed simulations with uniform refinement.
- ⋆ Extrapolation of the observations from the adaptive simulations implies that adaptive refinement could especially be more useful for large-scale groundwater flow problems where uniform refinement may be computationally expensive.
- ⋆ Mixed IGA of classical poroelasticity problems, using different polynomial orders for displacement and pore pressure, improves the accuracy of the pore pressure results compared to equal order simulations, as is known from standard FEA.
- ⋆ Investigation of the accuracy of the pore pressure results at very small time steps disclosed that mixed IGA may not completely remove the oscillations. The results were, however, noticed to improve with increasing polynomial degrees.
- ⋆ IGA of poroelasticity problems with graded mesh refinement was observed to reduce the pore pressure oscillations, revealing the potential of adaptive refinement for such problems. This should be studied further.
- ⋆ Frost heave due to a pipeline transporting chilled gas in a cold environment is predicted with a reasonable accuracy by incorporating strain due to phase change and a simple thermoelastic constitutive model into the mixed IGA based THM framework.

- ⋆ The continuity of the basis functions in mixed IGA of THM coupled problems implies that derived quantities, such as fluxes, will be continuous between knot spans (analogous to elements in FEA). This is qualitatively discussed to imply local conservation of the derived quantities. This should be studied further quantitatively.

Further numerical studies are required to quantify the specific advantages of IGA over traditional FEA when applied to THM coupled problems in porous media.

In general, the numerical implementation work resulted in H, HM and THM frameworks for simulation of poro/geomechanics problems using IGA. The frameworks are developed based on IFEM - an object-oriented isogeometric toolbox for the solution of partial differential equations. The developed numerical codes may be used and extended further.

4.3 Possible Future Work

The following recommendations for further work are made based on the observations in this research.

- ⋆ Adaptive IGA of porous media flow problems such as transient groundwater flow, free-surface seepage and multi-phase flow.
- ⋆ Extension of the mixed IGA HM and THM frameworks for unsaturated conditions i.e. incorporation gas phases in both cases.
- ⋆ Incorporation of advanced constitutive models, such as elastoplastic and viscoplastic models, into the HM and THM frameworks and investigation of the performance of mixed IGA.
- ⋆ Generalization of the coupled frameworks to dynamic porous media problems; IGA has been successfully applied to dynamic problems in other fields and the possibility of having mass matrices with non-negative entries (owing to the non-negative basis functions) is anticipated to be particularly advantageous.
- ⋆ Adaptive IGA of HM and THM coupled problems in porous media.
- ⋆ Investigation of sequentially and fully coupled solution approaches to THM coupled problems under the IGA framework.
- ⋆ Parallelization of flow, HM and THM implementations in IFEM to reduce computation times and improve efficiency, especially for large-scale problems.

Part IV

Appendix

"*Everything is a work in progress.*"
– Anonymous

Appendix A

Mixed Isogeometric Analysis of THM Coupled Processes in Saturated Porous Media

The isogeometric analysis numerical implementation work in this thesis followed a strategic procedure starting with hydraulic processes followed by hydro-mechanical coupling and then fully coupled thermo-hydro-mechanical (THM) implementation. The development of the fully coupled code for ground freezing started with the simplest possible THM processes in saturated porous media for easier debugging, verification and validation of the final implementation. The governing equations, final system of equations and numerical tests performed during this intermediate THM implementation are discussed in this appendix.

A.1 Governing Equations

The main governing equations for THM coupled processes in a fluid-saturated porous medium are the linear momentum, mass and energy balance equations.

The linear momentum balance equation for the mixture is given by

$$\boldsymbol{L}^{\intercal}\boldsymbol{\sigma} + \rho\boldsymbol{b} = \boldsymbol{0} \tag{A.1}$$

where $\boldsymbol{\sigma}$ is the total stress tensor in Voigt notation, ρ is the total density of the mixture, $\boldsymbol{b}$ represents body forces and $\boldsymbol{L}$ is a differential operator corresponding to Voigt notation given by

$$\boldsymbol{L}^{\intercal} = \begin{bmatrix} \frac{\partial}{\partial x} & 0 & 0 & \frac{\partial}{\partial y} & 0 & \frac{\partial}{\partial z} \\ 0 & \frac{\partial}{\partial y} & 0 & \frac{\partial}{\partial x} & \frac{\partial}{\partial z} & 0 \\ 0 & 0 & \frac{\partial}{\partial z} & 0 & \frac{\partial}{\partial y} & \frac{\partial}{\partial x} \end{bmatrix}. \tag{A.2}$$

The total stress $\boldsymbol{\sigma}$ and the effective stress $\boldsymbol{\sigma}'$ are related by

$$\boldsymbol{\sigma} = \boldsymbol{\sigma}' + \alpha p^{\mathrm{w}} \tilde{\boldsymbol{I}} \tag{A.3}$$

where p^{w} is the pore water pressure, α is Biot's coefficient and for stresses in Voigt notation and a general three-dimensional case $\tilde{\boldsymbol{I}} = \{1\ 1\ 1\ 0\ 0\ 0\}^{\intercal}$. The constitutive stress-strain relation for linear elasticity is given by

$$\boldsymbol{\sigma}' = \tilde{\boldsymbol{D}} : (\boldsymbol{\varepsilon} - \boldsymbol{\varepsilon}^{\mathrm{T}}) \tag{A.4}$$

where $\tilde{\boldsymbol{D}}$ is the tangent stiffness for linear elasticity, $\boldsymbol{\varepsilon}$ is the total strain tensor and $\boldsymbol{\varepsilon}^{\mathrm{T}}$ represents thermal strains and is expressed as

$$\boldsymbol{\varepsilon}^{\mathrm{T}} = \alpha_{\mathrm{s}} T \tilde{\boldsymbol{I}}. \tag{A.5}$$

Here α_{s} is the thermal expansion coefficient of the solid and T is the temperature. Based on (A.3), (A.4) and (A.5), we can now rewrite (A.1) as

$$\boldsymbol{L}^{\intercal} \left[\tilde{\boldsymbol{D}} \boldsymbol{L} \boldsymbol{u} - \alpha p^{\mathrm{w}} \tilde{\boldsymbol{I}} - \tilde{\boldsymbol{D}} \alpha_{\mathrm{s}} T \tilde{\boldsymbol{I}} \right] + \rho \boldsymbol{b} = \boldsymbol{0} \tag{A.6}$$

where $\boldsymbol{u}$ is the displacement vector and we have used the small deformation strain-displacement relation

$$\boldsymbol{\varepsilon} = \frac{1}{2} (\nabla \boldsymbol{u} + \nabla^{\intercal} \boldsymbol{u}). \tag{A.7}$$

The mass balance equation is given by

$$\alpha \nabla \cdot \dot{\boldsymbol{u}} + c \frac{\partial p^{\mathrm{w}}}{\partial t} + \nabla \cdot \boldsymbol{w} = 0 \tag{A.8}$$

where c is the specific storage coefficient given by

$$c = \frac{\alpha - n}{K_{\mathrm{s}}} + \frac{n}{K_{\mathrm{w}}} \tag{A.9}$$

with n being the porosity, K_{s} the bulk modulus of the solid and K_{w} the bulk modulus of water. Darcy's velocity $\boldsymbol{w}$ is expressed as

$$\boldsymbol{w} = -\frac{1}{\gamma_{\mathrm{w}}} \boldsymbol{k} (\nabla p^{\mathrm{w}} - \rho_{\mathrm{w}} \boldsymbol{b}) \tag{A.10}$$

where γ_{w} is the unit weight of water, $\boldsymbol{k}$ is the hydraulic conductivity matrix and ρ_{w} is the density of water.

The energy balance equation is given by

$$(\rho c)_{\mathrm{eff}} \frac{\partial T}{\partial t} + \rho_{\mathrm{w}} c_{\mathrm{w}} \boldsymbol{w} \cdot \nabla T + \nabla \cdot \mathbf{q} = Q \tag{A.11}$$

where Q is the external heat supply and $(\rho c)_{\mathrm{eff}}$ is the effective heat capacity of the mixture expressed as the sum of the heat capacities of the constituents:

$$(\rho c)_{\mathrm{eff}} = (1 - n) \rho_{\mathrm{s}} c_{\mathrm{s}} + n \rho_{\mathrm{w}} c_{\mathrm{w}}. \tag{A.12}$$

In the equation above, c_s and c_w are the specific heat capacities of the solid and water, respectively, and ρ_s is the density of the solid. The conductive heat flux $\boldsymbol{q}$ is defined by Fourier's law as

$$\boldsymbol{q} = -\lambda \nabla T \tag{A.13}$$

where λ is the overall thermal conductivity of the mixture, which may be approximated as the geometric mean of the individual thermal conductivities of the solid and water, λ_s and λ_w, as

$$\lambda = \lambda_\mathrm{s}^{1-n} \lambda_\mathrm{w}^{n}. \tag{A.14}$$

The governing equations may be summarized in terms of the field variables $\boldsymbol{u}$, p^w and T as

$$\begin{cases} \boldsymbol{L}^\intercal \left[\tilde{\boldsymbol{D}} \boldsymbol{L} \boldsymbol{u} - \alpha p^\mathrm{w} \tilde{\boldsymbol{I}} - \tilde{\boldsymbol{D}} \alpha_\mathrm{s} T \tilde{\boldsymbol{I}} \right] + \rho \boldsymbol{b} = \boldsymbol{0} \\ \alpha \tilde{\boldsymbol{I}}^\intercal \boldsymbol{L} \dfrac{\partial \boldsymbol{u}}{\partial t} + c \dfrac{\partial p^\mathrm{w}}{\partial t} + \nabla \cdot \left[-\dfrac{1}{\gamma_\mathrm{w}} \boldsymbol{k} (\nabla p^\mathrm{w} - \rho_\mathrm{w} \boldsymbol{b}) \right] = 0 \\ (\rho c)_\mathrm{eff} \dfrac{\partial T}{\partial t} + \rho_\mathrm{w} c_\mathrm{w} \left[-\dfrac{1}{\gamma_\mathrm{w}} \boldsymbol{k} (\nabla p^\mathrm{w} - \rho_\mathrm{w} \boldsymbol{b}) \right] \cdot \nabla T + \nabla \cdot (-\lambda \nabla T) = Q. \end{cases} \tag{A.15}$$

A.2 Mixed Isogeometric Implementation

A.2.1 Initial and Boundary Conditions

The initial conditions for the displacement, pore water pressure and temperature at time $t = 0$ are:

$$\boldsymbol{u} = \boldsymbol{u}_\mathrm{o} \qquad p^\mathrm{w} = p_\mathrm{o}^\mathrm{w} \qquad T = T_\mathrm{o} \qquad \text{in } \Omega \text{ and on } \Gamma \tag{A.16}$$

where Ω and Γ are the domain and its boundary, respectively. We denote the Dirichlet boundaries by Γ_D and the Neumann boundaries by Γ_N, where $\Gamma_D \cup \Gamma_N = \Gamma$. The Dirichlet boundary conditions may be defined as:

$$\begin{cases} \boldsymbol{u} = \overline{\boldsymbol{u}} & \text{on } \Gamma_D^\mathrm{u} \\ p^\mathrm{w} = \overline{p}^\mathrm{w} & \text{on } \Gamma_D^\mathrm{p} \\ T = \overline{T} & \text{on } \Gamma_D^\mathrm{T}. \end{cases} \tag{A.17}$$

The Neumann boundary conditions are defined as:

$$\begin{cases} \boldsymbol{\sigma} \cdot \boldsymbol{n} = \overline{\boldsymbol{t}} & \text{on } \Gamma_N^\mathrm{u} \\ \boldsymbol{w} \cdot \boldsymbol{n} = \overline{q}^\mathrm{w} & \text{on } \Gamma_N^\mathrm{p} \\ \boldsymbol{q} \cdot \boldsymbol{n} = \overline{q}^\mathrm{T} & \text{on } \Gamma_N^\mathrm{T} \end{cases} \tag{A.18}$$

where $\overline{\boldsymbol{t}}$ is the traction boundary condition and $\boldsymbol{n}$ is the outward unit normal vector to the boundary. The water and heat fluxes at the boundary are represented by $\overline{q}^\mathrm{w}$ and $\overline{q}^\mathrm{T}$, respectively.

A.2.2 Variational Formulation

To derive the variational formulations of the governing equations we introduce a vector-valued test function $\delta\boldsymbol{u}$, which vanishes on Γ_D^{u}, and scalar test functions δp and δT, which vanish on Γ_D^{p} and Γ_D^{T}, respectively. The weak form of the linear momentum balance equation in $(\mathrm{A}.15)_1$ is obtained by multiplying it with $\delta\boldsymbol{u}$ and integrating over the domain Ω i.e.

$$\int_\Omega \delta\boldsymbol{u}\left\{\boldsymbol{L}^\intercal\left[\tilde{\boldsymbol{D}}\boldsymbol{L}\boldsymbol{u}-\alpha p^{\mathrm{w}}\tilde{\boldsymbol{I}}-\tilde{\boldsymbol{D}}\alpha_{\mathrm{s}}T\tilde{\boldsymbol{I}}\right]+\rho\boldsymbol{b}\right\}\mathrm{d}\Omega=\boldsymbol{0}. \tag{A.19}$$

Similarly, the weak form of the mass balance equation $(\mathrm{A}.15)_2$ is obtained as

$$\int_\Omega \delta p\left\{\alpha\tilde{\boldsymbol{I}}^\intercal\boldsymbol{L}\frac{\partial\boldsymbol{u}}{\partial t}+c\frac{\partial p^{\mathrm{w}}}{\partial t}+\nabla\cdot\left[-\frac{1}{\gamma_{\mathrm{w}}}\boldsymbol{k}(\nabla p^{\mathrm{w}}-\rho_{\mathrm{w}}\boldsymbol{b})\right]\right\}\mathrm{d}\Omega=0 \tag{A.20}$$

The weak form of the energy balance equation $(\mathrm{A}.15)_3$

$$\int_\Omega \delta T\left\{(\rho c)_{\mathrm{eff}}\frac{\partial T}{\partial t}+\rho_{\mathrm{w}}c_{\mathrm{w}}\left[-\frac{1}{\gamma_{\mathrm{w}}}\boldsymbol{k}(\nabla p^{\mathrm{w}}-\rho_{\mathrm{w}}\boldsymbol{b})\right]\cdot\nabla T+\nabla\cdot(-\lambda\nabla T)-Q\right\}\mathrm{d}\Omega=0 \tag{A.21}$$

The weak forms in (A.19), (A.20) and (A.21) are further simplified by applying Green's theorem to relax second derivatives. The details are omitted here.

A.2.3 Galerkin Formulation

Choosing the basis functions $\boldsymbol{N}_{\mathrm{u}}$,$\boldsymbol{N}_{\mathrm{p}}$ and $\boldsymbol{N}_{\mathrm{T}}$ for the displacement, pore water pressure and temperature, respectively, we write the approximations:

$$\begin{aligned}
\boldsymbol{u}&=\boldsymbol{N}_{\mathrm{u}}\boldsymbol{u}^{\mathrm{c}}, & \frac{\partial\boldsymbol{u}}{\partial t}&=\boldsymbol{N}_{\mathrm{u}}\frac{\partial\boldsymbol{u}^{\mathrm{c}}}{\partial t}\\
p^{\mathrm{w}}&=\boldsymbol{N}_{\mathrm{p}}\boldsymbol{p}^{\mathrm{c}}, & \frac{\partial p^{\mathrm{w}}}{\partial t}&=\boldsymbol{N}_{\mathrm{p}}\frac{\partial\boldsymbol{p}^{\mathrm{c}}}{\partial t}\\
T&=\boldsymbol{N}_{\mathrm{T}}\boldsymbol{T}^{\mathrm{c}}, & \frac{\partial T}{\partial t}&=\boldsymbol{N}_{\mathrm{T}}\frac{\partial\boldsymbol{T}^{\mathrm{c}}}{\partial t}
\end{aligned} \tag{A.22}$$

where $\boldsymbol{u}^{\mathrm{c}}$, $\boldsymbol{p}^{\mathrm{c}}$ and $\boldsymbol{T}^{\mathrm{c}}$ are the control point displacement, pore water pressure and temperature values.

Application of (A.22) to the weak form of the linear momentum balance equation in (A.19) results in the matrix equation

$$\boldsymbol{C}_{\mathrm{uu}}\frac{\partial\boldsymbol{u}^{\mathrm{c}}}{\partial t}+\boldsymbol{C}_{\mathrm{up}}\frac{\partial\boldsymbol{p}^{\mathrm{c}}}{\partial t}+\boldsymbol{C}_{\mathrm{uT}}\frac{\partial\boldsymbol{T}^{\mathrm{c}}}{\partial t}=\boldsymbol{f}_{\mathrm{u}} \tag{A.23}$$

where

$$\begin{aligned}\boldsymbol{C}_{\mathrm{uu}} &= \int_{\Omega} \boldsymbol{B}^{\intercal}\tilde{\boldsymbol{D}}\boldsymbol{B}\mathrm{d}\Omega \\ \boldsymbol{C}_{\mathrm{up}} &= \int_{\Omega} \boldsymbol{B}^{\intercal}\alpha\tilde{\boldsymbol{I}}\boldsymbol{N}_{\mathrm{p}}\mathrm{d}\Omega \\ \boldsymbol{C}_{\mathrm{uT}} &= \int_{\Omega} \boldsymbol{B}^{\intercal}\tilde{\boldsymbol{D}}\alpha_{\mathrm{s}}\tilde{\boldsymbol{I}}\boldsymbol{N}_{\mathrm{T}}\mathrm{d}\Omega \\ \boldsymbol{f}_{\mathrm{u}} &= \int_{\Gamma^{\mathrm{u}}_{N}} \boldsymbol{N}_{\mathrm{u}}^{\intercal}\dot{\bar{\boldsymbol{t}}}\mathrm{d}\Gamma.\end{aligned} \tag{A.24}$$

Here $\boldsymbol{B} = \boldsymbol{L}\boldsymbol{N}_u$ is the strain-displacement matrix. Similarly, Galerkin formulation of the weak form of the mass balance equation (A.20) results in

$$\boldsymbol{K}_{\mathrm{pp}}\boldsymbol{p}^{\mathrm{c}} + \boldsymbol{C}_{\mathrm{pu}}\frac{\partial \boldsymbol{u}^{\mathrm{c}}}{\partial t} + \boldsymbol{C}_{\mathrm{pp}}\frac{\partial \boldsymbol{p}^{\mathrm{c}}}{\partial t} = \boldsymbol{f}_{\mathrm{p}} \tag{A.25}$$

where

$$\begin{aligned}\boldsymbol{K}_{\mathrm{pp}} &= \int_{\Omega} \nabla\boldsymbol{N}_{\mathrm{p}}^{\intercal}\frac{1}{\gamma_{\mathrm{w}}}\boldsymbol{k}\nabla\boldsymbol{N}_{\mathrm{p}}\mathrm{d}\Omega \\ \boldsymbol{C}_{\mathrm{pu}} &= \boldsymbol{C}_{\mathrm{up}}^{\intercal} \\ \boldsymbol{C}_{\mathrm{pp}} &= \int_{\Omega} \boldsymbol{N}_{\mathrm{p}}^{\intercal}c\boldsymbol{N}_{\mathrm{p}}\mathrm{d}\Omega \\ \boldsymbol{f}_{\mathrm{p}} &= \int_{\Omega} \nabla\boldsymbol{N}_{\mathrm{p}}^{\intercal}\frac{1}{\gamma_{\mathrm{w}}}\boldsymbol{k}\rho_{\mathrm{w}}\boldsymbol{b}\mathrm{d}\Omega - \int_{\Gamma^{\mathrm{p}}_{N}} \boldsymbol{N}_{\mathrm{p}}^{\intercal}\bar{q}^{\mathrm{w}}\mathrm{d}\Gamma.\end{aligned} \tag{A.26}$$

Galerkin approximation of the weak form of the energy balance equation (A.21) gives

$$\boldsymbol{K}_{\mathrm{TT}}\boldsymbol{T}^{\mathrm{c}} + \boldsymbol{C}_{\mathrm{TT}}\frac{\partial \boldsymbol{T}^{\mathrm{c}}}{\partial t} = \boldsymbol{f}_{\mathrm{T}} \tag{A.27}$$

where

$$\begin{aligned}\boldsymbol{K}_{\mathrm{TT}} &= \int_{\Omega} \nabla\boldsymbol{N}_{\mathrm{T}}^{\intercal}\rho_{\mathrm{w}}c_{\mathrm{w}}\boldsymbol{w}\boldsymbol{N}_{\mathrm{T}}\mathrm{d}\Omega + \int_{\Omega} \nabla\boldsymbol{N}_{\mathrm{T}}^{\intercal}\lambda\nabla\boldsymbol{N}_{\mathrm{T}}\mathrm{d}\Omega \\ \boldsymbol{C}_{\mathrm{TT}} &= \int_{\Omega} \boldsymbol{N}_{\mathrm{T}}^{\intercal}(\rho c)_{\mathrm{eff}}\boldsymbol{N}_{\mathrm{T}}\mathrm{d}\Omega \\ \boldsymbol{f}_{\mathrm{T}} &= -\int_{\Gamma^{\mathrm{T}}_{N}} \boldsymbol{N}_{\mathrm{T}}^{\intercal}\bar{q}^{\mathrm{T}}\mathrm{d}\Gamma\end{aligned} \tag{A.28}$$

Combining (A.23), (A.25) and (A.27) results in the coupled system of equations

$$\begin{bmatrix}\boldsymbol{0} & \boldsymbol{0} & \boldsymbol{0} \\ \boldsymbol{0} & \boldsymbol{K}_{\mathrm{pp}} & \boldsymbol{0} \\ \boldsymbol{0} & \boldsymbol{0} & \boldsymbol{K}_{\mathrm{TT}}\end{bmatrix}\begin{Bmatrix}\boldsymbol{u}^{\mathrm{c}} \\ \boldsymbol{p}^{\mathrm{c}} \\ \boldsymbol{T}^{\mathrm{c}}\end{Bmatrix} + \begin{bmatrix}\boldsymbol{C}_{\mathrm{uu}} & \boldsymbol{C}_{\mathrm{up}} & \boldsymbol{C}_{\mathrm{uT}} \\ \boldsymbol{C}_{\mathrm{pu}} & \boldsymbol{C}_{\mathrm{pp}} & \boldsymbol{0} \\ \boldsymbol{0} & \boldsymbol{0} & \boldsymbol{C}_{\mathrm{TT}}\end{bmatrix}\frac{\partial}{\partial t}\begin{Bmatrix}\boldsymbol{u}^{\mathrm{c}} \\ \boldsymbol{p}^{\mathrm{c}} \\ \boldsymbol{T}^{\mathrm{c}}\end{Bmatrix} = \begin{Bmatrix}\boldsymbol{f}_{\mathrm{u}} \\ \boldsymbol{f}_{\mathrm{p}} \\ \boldsymbol{f}_{\mathrm{T}}\end{Bmatrix} \tag{A.29}$$

which can be written in a more compact form as:

$$\boldsymbol{K}\boldsymbol{X} + \boldsymbol{C}\frac{\partial \boldsymbol{X}}{\partial t} = \boldsymbol{F} \tag{A.30}$$

where the coefficient matrices $\boldsymbol{K}$ and $\boldsymbol{C}$, the external load vector $\boldsymbol{F}$ and the vector of unknowns $\boldsymbol{X}$ are evident from (A.29). The equation system is nonlinear due to the convective term in the coefficient matrix $\boldsymbol{K}_{\mathrm{TT}}$ and a fully coupled solution requires the use of iterative methods like the Newton-Raphson method.

A.2.4 Temporal Discretization

Temporal discretization of the system of matrix equations is performed using the Generalized Trapezoidal Rule (GTR). For the rate of change of the unknown vector $\boldsymbol{X}$, we have the approximation:

$$\begin{aligned} \left.\frac{\partial \boldsymbol{X}}{\partial t}\right|_{n+\theta} &= \frac{\boldsymbol{X}_{n+1} - \boldsymbol{X}_n}{\Delta t} \\ \boldsymbol{X}_{n+\theta} &= (1-\theta)\boldsymbol{X}_n + \theta \boldsymbol{X}_{n+1} \end{aligned} \tag{A.31}$$

where θ is a time integration parameter which has limits $0 \leq \theta \leq 1$. The system of matrix equations at time $t_{n+\theta}$ is then:

$$\boldsymbol{K}\boldsymbol{X}_{n+\theta} + \boldsymbol{C}\left.\frac{\partial \boldsymbol{X}}{\partial t}\right|_{n+\theta} = \boldsymbol{F}_{n+\theta}. \tag{A.32}$$

Using the approximation in Eq. (A.31) into Eq. (A.32) and adopting a fully implicit time integration scheme with $\theta = 1$, we get the residual at time step t_{n+1} as:

$$\boldsymbol{R}_{n+1} = [\Delta t \boldsymbol{K} + \boldsymbol{C}]_{n+1}\, \boldsymbol{X}_{n+1} - \boldsymbol{C}_{n+1}\boldsymbol{X}_n - \Delta t \boldsymbol{F}_{n+1}. \tag{A.33}$$

After Taylor series expansion of the residual, we solve for the increment of the unknown vector $\Delta \boldsymbol{X}_{n+1}^{i+1}$ using Newton-Raphson iterations from:

$$\left.\frac{\partial \boldsymbol{R}}{\partial \boldsymbol{X}}\right|_{n+1}^{i} \Delta \boldsymbol{X}_{n+1}^{i+1} \cong -\boldsymbol{R}_{n+1}^{i} \tag{A.34}$$

where i is the iteration number and we have the Jacobian matrix in the above equation as:

$$\boldsymbol{J} = \frac{\partial \boldsymbol{R}}{\partial \boldsymbol{X}}. \tag{A.35}$$

The vector of unknowns at time step t_{n+1} is updated after each iteration using:

$$\boldsymbol{X}_{n+1}^{i+1} = \boldsymbol{X}_{n+1}^{i} + \Delta \boldsymbol{X}_{n+1}^{i+1}. \tag{A.36}$$

A.3 Numerical Example

Non-isothermal consolidation of a linearly elastic soil column is considered; see Aboustit et al. (1985). The computational domain and boundary conditions are shown in Figure A.1. The soil column is loaded with a surface pressure of 1000 Pa and is subjected to a temperature change of $\Delta T = 50\,^{\circ}\mathrm{C}$ at the top boundary. The lateral boundaries are constrained from moving in the horizontal direction and the bottom

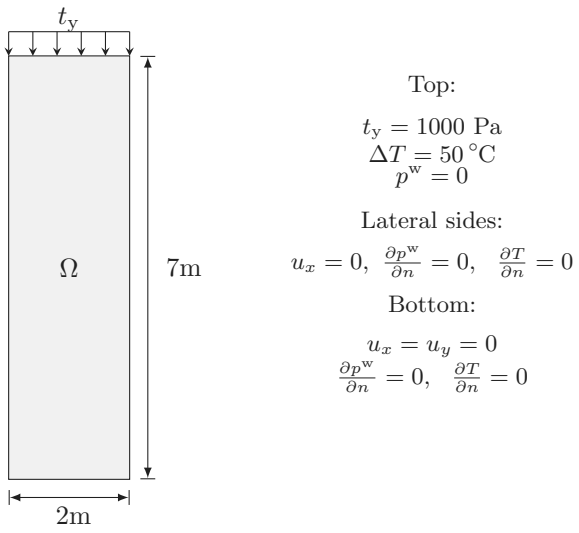

Figure A.1: Non-isothermal consolidation: Computational domain and boundary conditions.

boundary is fixed. The top boundary is permeable. The lateral and bottom boundaries are sealed and insulated. The material parameters used for the simulation are given in Table A.1, which are slightly different from the reference cited above.

Mixed isogeometric analysis is performed where quadratic basis functions are used for the pressure and temperature ($p_p = p_T = 2$) and cubic basis functions for the displacement ($p_u = 3$). The vertical displacement versus time results at randomly selected points along the height of the soil column are shown in Figure A.2. The corresponding pore water pressure and temperature results versus time are shown in Figures A.3 and A.4, respectively. The settlement of the soil column due to the surface load can be observed to be reversed due to thermal expansion as the temperature in the domain increases with time.

A.4 Summary

An isogeometric analysis based numerical implementation for fully coupled THM processes in saturated porous media is presented. The numerical implementation is verified by performing simulation of non-isothermal consolidation of a linearly elastic soil column, a well-known problem in literature. The specific advantages of using isogeometric analysis for this class of problems requires further theoretical and numerical investigations. This will be a subject for a future work with a possible outcome in the form of a publication.

Table A.1: Non-isothermal consolidation: Material parameters.

Parameter	Value	Unit
Thermal properties:		
Thermal conductivity of soil, λ_s	1.0×10^5	W/m/°C
Thermal conductivity of water, λ_w	0.6	W/m/°C
Specific heat capacity of soil, c_s	61	J/kg/°C
Specific heat capacity of water, c_w	200	J/kg/°C
Thermal expansion coeff. of soil, α_s	0.9×10^{-6}	/°C
Hydraulic properties:		
Hydraulic conductivity, k	8.04×10^{-6}	m/s
Mechanical properties:		
Young's modulus of soil, E	6.0	MPa
Poisson's ratio of soil, ν	0.4	–
Biot's coefficient, α	1.0	–
Mass and volume properties:		
Initial porosity, n	0.4	–
Density of soil, ρ_s	2200	kg/m^3
Density of water, ρ_w	1000	kg/m^3

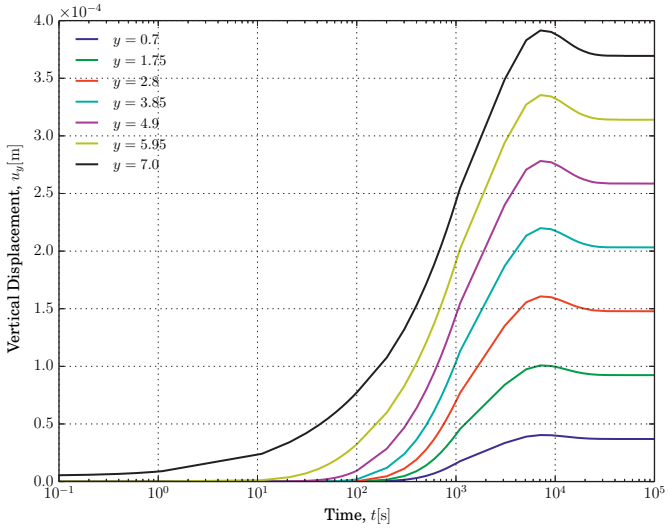

Figure A.2: Vertical displacement versus time at selected points along the height of the soil column ($y = 0$ at the bottom boundary).

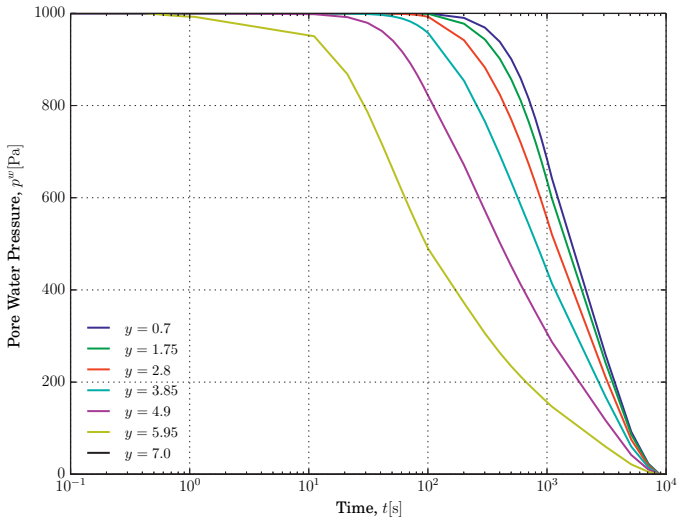

Figure A.3: Pore water pressure versus time at selected points along the height of the soil column ($y = 0$ at the bottom boundary). $p^{\mathrm{w}} = 0$ at $y = 7.0$, the top boundary.

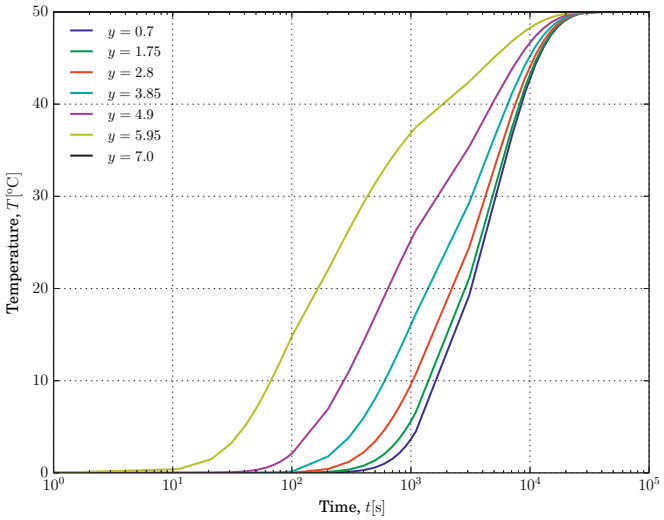

Figure A.4: Temperature versus time at selected points along the height of the soil column ($y = 0$ at the bottom boundary). $T = 50\,^{\circ}\mathrm{C}$ at $y = 7.0$, the top boundary.

"*Mathematics takes us still further from what is human, into the region of absolute necessity, to which not only the world, but every possible world, must conform.*"

– Bertrand Russel

Appendix B

Integral Theorems

The integral theorems that are mentioned and used in the theoretical and numerical formulations in this thesis are presented in this appendix as a quick reference.

Divergence Theorem

The divergence theorem, also known as Gauss's theorem, is stated as: Given a volume region V with boundary ∂V, the volume integral of the divergence $\nabla \cdot \boldsymbol{F}$ of a continuously differentiable vector field $\boldsymbol{F}$ and the surface integral of $\boldsymbol{F}$ over ∂V satisfy the relationship

$$\int_V (\nabla \cdot \boldsymbol{F}) \mathrm{d}V = \int_{\partial V} \boldsymbol{F} \cdot \boldsymbol{n} \mathrm{d}A \tag{B.1}$$

where $\boldsymbol{n}$ is the outward unit normal to the boundary ∂V. The physical statement of the divergence theorem is that the density in a given space changes only when there is an inflow or outflow through its boundary, assuming there is no creation or destruction of matter.

Reynold's Transport Theorem

The rate of change of integrated quantities is obtained using Reynold's transport theorem, which is briefly presented in Section 2.3. This theorem is used in formulating the conservations laws. It is clarified further here to give insight into the physical meanings of the terms involved.

For a given quantity $\boldsymbol{f}(\boldsymbol{x}, t)$ (which may be tensor-, scalar- or vector-valued) over a time-dependent volume $V(t)$ with boundary $\partial V(t)$, Reynold's transport theorem is given by

$$\frac{d}{dt} \int_{V(t)} \boldsymbol{f} \mathrm{d}V = \int_{V(t)} \frac{\partial \boldsymbol{f}}{\partial t} \mathrm{d}V + \int_{\partial V(t)} \boldsymbol{f} (\boldsymbol{v}^A \cdot \boldsymbol{n}) \, \mathrm{d}A \tag{B.2}$$

where $\boldsymbol{n}(\boldsymbol{x}, t)$ is the outward unit normal to the boundary, $\mathrm{d}A$ is the surface area

at position vector $\boldsymbol{x}$ and $\boldsymbol{v}^A(\boldsymbol{x}, t)$ is the velocity of the area element. In terms of the velocity $\boldsymbol{v}(\boldsymbol{x}, t)$ of material elements, we have

$$\frac{d}{dt}\int_{V(t)} \boldsymbol{f}\mathrm{d}V = \int_{V(t)} \frac{\partial \boldsymbol{f}}{\partial t}\mathrm{d}V + \int_{\partial V(t)} \boldsymbol{f}(\boldsymbol{v}\cdot\boldsymbol{n})\mathrm{d}A \tag{B.3}$$

where at the boundary $\boldsymbol{v}^A \cdot \boldsymbol{n} = \boldsymbol{v} \cdot \boldsymbol{n}$ is satisfied.

Green's Theorem

Given a region D in a plane with a closed boundary ∂D, Green's theorem states that

$$\oint_{\partial D} \boldsymbol{F}\cdot\boldsymbol{n}\mathrm{d}s = \iint_D (\nabla\cdot\boldsymbol{F})\mathrm{d}A \tag{B.4}$$

where $\boldsymbol{F}$ is a two-dimensional vector field, $\boldsymbol{n}$ is the outward unit normal on the boundary and $\mathrm{d}s$ is the length of the boundary. Green's theorem is the two-dimensional equivalent of the divergence theorem.

"*Problems worthy of attack prove their worth by fighting back.*"
– Paul Erdős

Appendix C

Conference Papers and Presentations

The following conference papers and presentations have been part of the thesis work. The abstracts and papers are not included here as the journal papers expand based on them.

1. Bekele, Y.W.*, Fonn, E., Kvarving, A.M., Kvamsdal, T., and Nordal, S. *On mixed isogeometric analysis of poroelasticity*†: 13th US National Congress on Computational Mechanics - USNCCM13, 26-30 July 2015, San Diego, CA, USA.

2. Bekele, Y.W.*, Kvamsdal, T., Kvarving, A.M., and Nordal, S. *On adaptive isogeometric analysis of steady-state groundwater flow with LR B-splines*†: III International Conference on Isogeometric Analysis - IGA2015, 1-3 June 2015, Trondheim, Norway.

3. Fonn, E.*, Bekele, Y.W., Kvarving, A.M., Kvamsdal, T., and Nordal, S. *A mixed-order isogeometry solver for poroelasticity problems*†: III International Conference on Isogeometric Analysis - IGA2015, 1-3 June 2015, Trondheim, Norway.

4. Bekele, Y.W.*, Kvamsdal, T., Kvarving, A.M., and Nordal, S. *Adaptive isogeometric finite element analysis of groundwater flow in heterogeneous porous media*†: VI International Conference on Coupled Problems in Science and Engineering - COUPLED2015, 18-20 May 2015, San Servolo Island, Venice, Italy.

*Presenting author
†Abstract + Presentation

5. Kyokawa, H.* and Bekele, Y.W. *Numerical simulation of thermo-hydro-mechanically coupled processes during ground freezing and thawing*‡: 14th International Conference of the International Association for Computer Methods and Advances in Geomechanics - 14IACMAG, September 22-25, 2014, Kyoto, Japan.

6. Bekele, Y.W.*, Kvarving, A.M., Nordal, S., Kvamsdal, T., and G. Grimstad. *Isogeometric finite element analysis of single-phase Darcy flow in porous media*†: 11th World Congress on Computational Mechanics - WCCM XI, 5th European Conference on Computational Mechanics - ECCM V, 6th European Conference on Computational Fluid Dynamics - ECFD VI, 20-25 July 2014, Barcelona, Spain.

7. Bekele, Y.W.* and Kyokawa, H. *On thermo-hydro-mechanically (THM) coupled finite element modeling of ground freezing and thawing*§: 8th European Conference on Numerical Methods in Geotechnical Engineering - NUMGE2014, 18-20 June, 2014, Delft, The Netherlands.

8. Bekele, Y.W.* *Finite element modeling of thermo-hydro-mechanically (THM) coupled problems in frozen ground engineering: state-of-the-art*‡: V International Conference on Coupled Problems in Science and Engineering - COUPLED2015, 17-19 June 2013, Ibiza, Spain.

‡Paper + Presentation
§Paper + Poster

Bibliography

Aboustit, B., Advani, S., and Lee, J. Variational principles and finite element simulations for thermo-elastic consolidation. *International Journal for Numerical and Analytical Methods in Geomechanics*, 9(1):49–69, 1985.

Akkerman, I., Bazilevs, Y., Kees, C., and Farthing, M. Isogeometric analysis of free-surface flow. *Journal of Computational Physics*, 230(11):4137–4152, 2011.

Ames, W. F. *Numerical Methods for Partial Differential Equations*. Academic press, 2014.

Andersland, O. B. and Ladanyi, B. *Frozen Ground Engineering*. John Wiley & Sons, 2004.

Bazilevs, Y., Calo, V., Zhang, Y., and Hughes, T. J. R. Isogeometric fluid–structure interaction analysis with applications to arterial blood flow. *Computational Mechanics*, 38(4-5):310–322, 2006.

Bazilevs, Y., Calo, V. M., Cottrell, J. A., Evans, J. A., Hughes, T. J. R., Lipton, S., Scott, M. A., and Sederberg, T. W. Isogeometric analysis using T-splines. *Computer Methods in Applied Mechanics and Engineering*, 199(5):229–263, 2010.

Bedford, A. and Drumheller, D. S. Theories of immiscible and structured mixtures. *International Journal of Engineering Science*, 21(8):863–960, 1983.

Bluhm, J. and de Boer, R. The volume fraction concept in the porous media theory. *ZAMM-Journal of Applied Mathematics and Mechanics/Zeitschrift für Angewandte Mathematik und Mechanik*, 77(8):563–577, 1997.

Bowen, R. M. Incompressible porous media models by use of the theory of mixtures. *International Journal of Engineering Science*, 18(9):1129–1148, 1980.

Bowen, R. M. Compressible porous media models by use of the theory of mixtures. *International Journal of Engineering Science*, 20(6):697–735, 1982.

Bressan, A. Some properties of LR-splines. *Computer Aided Geometric Design*, 30 (8):778–794, 2013.

Buffa, A., Sangalli, G., and Vázquez, R. Isogeometric analysis in electromagnetics: B-splines approximation. *Computer Methods in Applied Mechanics and Engineering*, 199(17):1143–1152, 2010.

Collier, N., Pardo, D., Dalcin, L., Paszynski, M., and Calo, V. M. The cost of continuity: a study of the performance of isogeometric finite elements using direct solvers. *Computer Methods in Applied Mechanics and Engineering*, 213: 353–361, 2012.

Collier, N., Dalcin, L., Pardo, D., and Calo, V. M. The cost of continuity: performance of iterative solvers on isogeometric finite elements. *SIAM Journal on Scientific Computing*, 35(2):A767–A784, 2013.

Colombo, G., Lunardi, P., Cavagna, B., Cassani, G., and Manassero, V. The artificial ground freezing technique application for the Naples underground. In *Proceedings of Word Tunnel Congress*, pages 910–921, 2008.

Cottrell, J., Reali, A., Bazilevs, Y., and Hughes, T. J. R. Isogeometric analysis of structural vibrations. *Computer Methods in Applied Mechanics and Engineering*, 195(41):5257–5296, 2006.

Cottrell, J. A., Hughes, T. J. R., and Bazilevs, Y. *Isogeometric Analysis: Toward Integration of CAD and FEA*. John Wiley & Sons, 2009.

Coussy, O. *Poromechanics*. John Wiley & Sons, 2004.

Coussy, O., Dormieux, L., and Detournay, E. From mixture theory to Biot's approach for porous media. *International Journal of Solids and Structures*, 35(34): 4619–4635, 1998.

de Boer, R. Thermodynamics of phase transitions in porous media. *Applied Mechanics Reviews*, 48(10):613–622, 1995.

de Boer, R. Theory of porous media - past and present. *ZAMM-Journal of Applied Mathematics and Mechanics/Zeitschrift für Angewandte Mathematik und Mechanik*, 78(7):441–466, 1998.

de Boer, R. Reflections on the development of the theory of porous media. *Applied Mechanics Reviews*, 56(6):R27–R42, 2003.

de Boer, R. *Trends in Continuum Mechanics of Porous Media*, volume 18. Springer Science & Business Media, 2006.

de Boer, R. and Bluhm, J. Phase transitions in gas-and liquid-saturated porous solids. *Transport in Porous Media*, 34(1-3):249–267, 1999.

de Boer, R. and Ehlers, W. A historical review of the formulation of porous media theories. *Acta Mechanica*, 74(1-4):1–8, 1988.

de Boer, R. and Ehlers, W. The development of the concept of effective stresses. *Acta Mechanica*, 83(1-2):77–92, 1990.

de Boer, R. and Kowalski, S. Thermodynamics of fluid-saturated porous media with a phase change. *Acta Mechanica*, 109(1-4):167–189, 1995.

De Lorenzis, L., Temizer, I., Wriggers, P., and Zavarise, G. A large deformation frictional contact formulation using NURBS-based isogeometric analysis. *International Journal for Numerical Methods in Engineering*, 87(13):1278–1300, 2011.

de Souza Neto, E. A., Peric, D., and Owen, D. R. J. *Computational Methods for Plasticity: Theory and Applications*. John Wiley & Sons, 2011.

Dedè, L., Borden, M. J., and Hughes, T. J. R. Isogeometric analysis for topology optimization with a phase field model. *Archives of Computational Methods in Engineering*, 19(3):427–465, 2012.

Deng, Z.-S. and Liu, J. Numerical simulation of 3-D freezing and heating problems for combined cryosurgery and hyperthermia therapy. *Numerical Heat Transfer, Part A: Applications*, 46(6):587–611, 2004.

Dokken, T., Lyche, T., and Pettersen, K. F. Polynomial splines over locally refined box-partitions. *Computer Aided Geometric Design*, 30(3):331–356, 2013.

Ehlers, W. and Bluhm, J. *Porous Media: Theory, Experiments and Numerical Applications*. Springer Science & Business Media, 2013.

Eiksund, G. R., Berggren, A. L., and Svanø, G. Stabilisation of a glacifluvial zone in the Oslofjord subsea tunnel with ground freezing. In *Proceedings of the International Conference on Soil Mechanics and Geotechnical Engineering*, volume 3, pages 1731–1736. AA Balkema Publishers, 2001.

Felippa, C. A., Park, K., and Farhat, C. Partitioned analysis of coupled mechanical systems. *Computer Methods in Applied Mechanics and Engineering*, 190(24): 3247–3270, 2001.

Frémond, M. *Phase Change in Mechanics*, volume 13. Springer Science & Business Media, 2012.

French, H. M. Past and present permafrost as an indicator of climate change. *Polar Research*, 18(2):269–274, 1999.

Gómez, H., Calo, V. M., Bazilevs, Y., and Hughes, T. J. R. Isogeometric analysis of the Cahn–Hilliard phase-field model. *Computer Methods in Applied Mechanics and Engineering*, 197(49):4333–4352, 2008.

Green, A. E. and Naghdi, P. M. A theory of mixtures. *Archive for Rational Mechanics and Analysis*, 24(4):243–263, 1967.

Harris, J. S. *Ground Freezing in Practice*. Thomas Telford, 1995.

Hassanizadeh, M. and Gray, W. G. General conservation equations for multi-phase systems: 3. constitutive theory for porous media flow. *Advances in Water Resources*, 3(1):25–40, 1980.

Hassanizadeh, S. M. Derivation of basic equations of mass transport in porous media, part 1. macroscopic balance laws. *Advances in Water Resources*, 9(4): 196–206, 1986.

Hughes, T. J. R. *The Finite Element Method: Linear Static and Dynamic Finite Element Analysis*. Courier Corporation, 2012.

Hughes, T. J. R., Cottrell, J. A., and Bazilevs, Y. Isogeometric analysis: CAD, finite elements, NURBS, exact geometry and mesh refinement. *Computer Methods in Applied Mechanics and Engineering*, 194(39):4135–4195, 2005.

Hughes, T. J. R., Reali, A., and Sangalli, G. Efficient quadrature for NURBS-based isogeometric analysis. *Computer Methods in Applied Mechanics and Engineering*, 199(5):301–313, 2010.

Irzal, F., Remmers, J., Verhoosel, C., and Borst, R. An isogeometric analysis bézier interface element for mechanical and poromechanical fracture problems. *International Journal for Numerical Methods in Engineering*, 97(8):608–628, 2014.

Johannessen, K. A., Kvamsdal, T., and Dokken, T. Isogeometric analysis using LR B-splines. *Computer Methods in Applied Mechanics and Engineering*, 269: 471–514, 2014.

Johannessen, K. A., Kumar, M., and Kvamsdal, T. Divergence-conforming discretization for stokes problem on locally refined meshes using LR B-splines. *Computer Methods in Applied Mechanics and Engineering*, 293:38–70, 2015a.

Johannessen, K. A., Remonato, F., and Kvamsdal, T. On the similarities and differences between classical hierarchical, truncated hierarchical and LR B-splines. *Computer Methods in Applied Mechanics and Engineering*, 291:64–101, 2015b.

Johansson, T. *Artificial Ground Freezing in Clayey Soils: Laboratory and Field Studies of Deformations during Thawing at the Bothnia Line*. PhD thesis, KTH Royal Institute of Technology, Stockholm, Sweden, 2009.

Kadapa, C. *Mixed Galerkin and Least-squares Formulations for Isogeometric Analysis*. PhD thesis, Swansea University, Wales, UK, 2014.

Kiendl, J., Bletzinger, K.-U., Linhard, J., and Wüchner, R. Isogeometric shell analysis with Kirchhoff–Love elements. *Computer Methods in Applied Mechanics and Engineering*, 198(49):3902–3914, 2009.

Lewis, R. W. and Schrefler, B. A. *The Finite Element Method in the Static and Dynamic Deformation and Consolidation of Porous Media*. Wiley, 1998.

Li, S., Lai, Y., Zhang, M., and Zhang, S. Minimum ground pre-freezing time before excavation of Guangzhou subway tunnel. *Cold regions science and technology*, 46(3):181–191, 2006.

Loch, J. Thermodynamic equilibrium between ice and water in porous media. *Soil Science*, 126(2):77–80, 1978.

Moraga, N. O. and Salinas, C. H. Numerical model for heat and fluid flow in food freezing. *Numerical Heat Transfer: Part A: Applications*, 35(5):495–517, 1999.

Piegl, L. and Tiller, W. *The NURBS Book*. Springer Science & Business Media, 2012.

Prévost, J. H. Mechanics of continuous porous media. *International Journal of Engineering Science*, 18(6):787–800, 1980.

Reali, A. An isogeometric analysis approach for the study of structural vibrations. *Journal of Earthquake Engineering*, 10(spec01):1–30, 2006.

Rebellato, L., Giudice, S., and Comini, G. Finite element analysis of freezing processes in foodstuffs. *Journal of Food Science*, 43(1):239–243, 1978.

Rubinsky, B. and Pegg, D. A mathematical model for the freezing process in biological tissue. *Proceedings of the Royal Society of London B: Biological Sciences*, 234(1276):343–358, 1988.

Sederberg, T. W., Zheng, J., Bakenov, A., and Nasri, A. T-splines and T-NURCCs. *ACM Transactions on Graphics (TOG)*, 22(3):477–484, 2003.

Segerlind, L. J. and Saunders, H. *Applied Finite Element Enalysis*. American Society of Mechanical Engineers, 1987.

Skempton, A. W. Terzaghi's discovery of effective stress. *From Theory to Practice in Soil Mechanics: Selections from the Writings of Karl Terzaghi*, pages 42–53, 1960.

Temizer, I., Wriggers, P., and Hughes, T. J. R. Contact treatment in isogeometric analysis with NURBS. *Computer Methods in Applied Mechanics and Engineering*, 200(9):1100–1112, 2011.

Vadász, P. *Emerging Topics in Heat and Mass Transfer in Porous Media: From Bioengineering and Microelectronics to Nanotechnology*, volume 22. Springer Science & Business Media, 2008.

Verhoosel, C. V., Scott, M. A., Hughes, T. J. R., and De Borst, R. An isogeometric analysis approach to gradient damage models. *International Journal for Numerical Methods in Engineering*, 86(1):115–134, 2011.

Verruijt, A. *Theory and Problems of Poroelasticity*. Delft University of Technology, 2013.

Whitaker, S. Advances in theory of fluid motion in porous media. *Industrial & Engineering Chemistry*, 61(12):14–28, 1969.

Whitaker, S. Simultaneous heat, mass, and momentum transfer in porous media: a theory of drying. *Advances in Heat Transfer*, 13:119–203, 1977.

Whitaker, S. Flow in porous media I: A theoretical derivation of Darcy's law. *Transport in Porous Media*, 1(1):3–25, 1986.

Yortsos, Y. C. and Stubos, A. K. Phase change in porous media. *Current Opinion in Colloid & Interface Science*, 6(3):208–216, 2001.

Zhang, Y., Bazilevs, Y., Goswami, S., Bajaj, C. L., and Hughes, T. J. R. Patient-specific vascular NURBS modeling for isogeometric analysis of blood flow. *Computer Methods in Applied Mechanics and Engineering*, 196(29):2943–2959, 2007.

Zienkiewicz, O. C. and Taylor, R. L. *The Finite Element Method, Vol. 1.* McGraw-Hill, London, 1989.